Theory and Application of Strong Field Ionization in Atomic Systems

by

S. R. Walker

B.S., University of Delaware, 2018

A thesis submitted to the

Faculty of the Graduate School of the

University of Colorado in partial fulfillment

of the requirements for the degree of

Doctor of Philosophy

Department of Physics

2023

Committee Members:

Andreas Becker, Chair

Michael Litos

David Jonas

Thomas Schibli

Andy Lucas

Walker, S. R. (Ph.D., Physics)

Theory and Application of Strong Field Ionization in Atomic Systems

Thesis directed by Prof. Andreas Becker

Throughout this thesis we explore ionization processes ranging from the single photon x-ray and ultraviolet limit to the opposite adiabatic infrared limit where large numbers of photons are required for ionization. We will summarize criteria responsible for the breakdown of perturbation theory and outline key aspects of the non-perturbative theory. Our numerical calculations bridge the short wavelength limit of single photon perturbative ionization to the long wavelength limit of non-perturbative multiphoton ionization to demonstrate an optimal wavelength regime for generation of electron pulses for probing chiral systems in rare gas atoms.

Breakdown of the widely used asymptotic saddle point approximation in strong-field physics is analyzed for ionization of electrons bound to $p-$states. We resolve this issue by evaluating Keldysh's ionization amplitude exactly. Finally, we present an analytic model for the perturbative two-photon ionization of atoms by arbitrary fields. As an application we reconstruct isolated attosecond pulses and pulse trains from a provided autocorrelation trace generated in a pump probe ionization measurement. The results are generalized to the non-perturbative limit.

Dedication

To my grandparents John and Lori as well as my mom Amy and siblings Cody and Kelsi.

Acknowledgements

I would like to express gratitude to everyone who has helped me get to this point. I would like to thank my advisor Andreas Becker, current group membrs: Yonas Gebre, Bejan Ghomashi, Keegan Finger, Rex Planalp and Noah Welikson, former group memebers: Joel Venzke, Brynn Reiff, and Lucas Kolanz and all of my friends and family for their support before, during and after the pandemic.

Contents

Chapter

Tables

Table

Figures

Figure

Chapter 1

Introduction

1.1 Background

The interaction of atoms with radiation fields is qualitatively different depending on the intensity of the applied radiation and energy of constituent photons. Electrons with binding energy I_p exposed to very weak radiation with photon energies $\hbar\omega > I_p$ behave differently than the same electrons interacting with intense fields comprised of photons with energy $\hbar\omega \ll I_p$ (ω is the angular frequency of each photon and $\hbar$ is the reduced Plank constant). When weak fields comprised of highly energetic photons strike an atom, there is some small, but finite probability that the initially bound electron will absorb a single quanta and ionize, where all additional energy is translated into the kinetic motion of the ejected electron:

$$E_k = \hbar\omega - I_p. \tag{1.1}$$

This single-photon ionization process was first explored by Einstein [54] in 1905.

If the weak field is now comprised of photons containing energy $\hbar\omega < I_p$, then multiple quanta must be absorbed simultaneously for ionization, which was first discussed by Dirac in 1927 [46,153]. In this early work it was stated that "These (two-photon) terms correspond to processes in which two light-quanta are emitted or absorbed simultaneously, and cannot arise in a light-quantum theory in which there are no forces between the light quanta. The effects of these terms will be found to be negligible, so that this disagreement with the light-quantum theory is not serious." Dirac claimed that multi-photon processes were an artifact of his theory and not a true physical process.

Over time this has been proven untrue. Four years later the full theory of two-photon absorption was developed by Göppert-Mayer in 1931 [67] with experimental verification three decades later by Kaiser [91] in 1961.

In subsequent decades Dirac's perspective changed until in 1958 [48] he stated that "Similarly for a more general radiative process in which two or more photons are simultaneously emitted or absorbed, the probability is proportional to (an intensity) factor I for each absorbed photon and $I + h\nu^3/c^2$ for each emitted photon (where h is the Plank constant, c is the speed of light, $h\nu$ is the photon energy and I is the field intensity). Thus, the process is stimulated by incident radiation in the same direction and with the same frequency and polarization as any of the emitted photons." These ideas outline the most fundamental principles of perturbative multi-photon processes. When weak radiation interacts with an atom the probability of absorbing n quanta is proportional to $(I/I_{\text{a.u.}})^n \ll 1$, where $I_{\text{a.u.}}$ is a characteristic value defined as the intensity associated with the electric field binding an electron within the Hydrogen atom (see section 2.3). Ionization in this regime is dominated by the lowest-order ($n_{\text{th}} = \lceil I_p/\hbar\omega \rceil$) photon process.

The advent of the first Ruby laser by Maiman in 1960 [120] allowed experiments to utilize stronger coherent radiation than was possible before and allowed for serious investigations into processes involving a large number of field quanta. This advancement allowed Agostini et al. in 1979 [3] to irradiate xenon atoms with high enough intensity to not only observe the dominant lowest-order (n_{th}) ionization process, but an additional perturbative ($n_{\text{th}}+1$) photon process corresponding to a single free-free transition in the continuum. This process is known as above threshold ionization (ATI). As technology improved over the following years, higher order ATI peaks were observed where the largest probability for emission was surprisingly found for the absorption of $n > n_{\text{th}}$ photons and not the lowest order process predicted from perturbation theory [2, 138]. These were some of the earliest explorations of non-perturbative multi-photon processes. Transitions are still described by the absorption and emission of field quanta, but the framework of perturbation theory breaks down.

Theoretical models for these processes have been available decades before these experimental

observations. These models originate from Oppenheimer's model of ionization of Hydrogen by a static field in 1928 [132]. Here, the initial Hydrogen ground-state perturbatively interacts with the applied field once before transitioning into a final state described by an otherwise free electron propagating in a static electric field. The framework of perturbation theory is still used, but the final-state includes all orders of the field-interaction. Subsequently in 1965 Keldysh [98] applied Oppenheimer's model to ionization of atoms by linearly-polarized alternating fields. The final state describes the motion of an otherwise free electron in a dynamical field. Both of these models are able to determine largely the correct ionization behavior in terms of physical parameters, but are missing a proportionality factor due to the fact that the final state in this first-order amplitude does not include the long-range Coulomb potential during and after ionization.

In subsequent years Keldysh's model was extended by Perelomov, Popov and Terent'ev [135–137] to include arbitrary initial states and both circular and elliptical polarization. These earliest Keldysh-like theories employed asymptotic approximations most accurate for long-wavelength radiation. Faisal and Reiss [57, 146] extended the model into the short-wavelength limit by evaluating the amplitude exactly in the vector-potential (velocity) gauge opposed to the electric field (length) gauge used in earlier works. This method pushes the theory of strong field ionization into the short-wavelength limit, but fails for initial states with orbital angular momentum $l > 0$ due to the use of the velocity-gauge [20, 146].

1.2 Structure of the thesis

The thesis is structured as follows. Starting in Chapter 2, we will outline fundamental principles of the perturbative theory of light-matter interaction. Here, electrons propagate as they do in atomic systems and applied weak radiation fields kick the electron a finite number of times between atomic states before finally transitioning in the continuum. We will finish the Chapter by discussing necessary conditions for the applicability of the theory.

Subsequently in Chapter 3, we will summarize key aspects of the non-perturbative theory of light-matter interaction, where both atomic reference-states and reference-states of an elec-

tron propagating in the field are required to determine a low-order expansion which describes the non-perturbative ionization process. We will start by describing accurate numerical methods for modeling the ionization of atoms. Afterwards we will describe the analytic models of Oppenheimer and Keldysh [98, 132] and briefly summarize the influential models of Perelomov, Popov and Terent'ev as well as Reiss. As an application we will outline difficulties associated with the long-range Coulomb interaction and applicability to "real" atoms.

In Chapter 4 we present results of numerical calculations describing ionization where we explore the transition from single photon to perturbative and non-perturbative multi-photon ionization. We explore optimal wavelength regimes for how atto- or femtosecond laser pulses may potentially provide the opportunity to generate ultrashort spin-polarized electron pulses for probing chiral systems and magnetic properties of materials. A key element in the generation of spin-polarized electrons is a selectivity in ionization to the sense of the electron's rotation in the initial state with respect to the rotation direction of the laser field. We will therefore identify mechanisms which increase the ionization from a specific magnetic sublevel over the others.

In Chapter 5 we demonstrate the breakdown of the asymptotic approximations used in the ionization amplitude of Keldysh as well as Perelomov, Popov and Terent'ev for initial p-states irradiated by circularly polarized fields. To overcome this challenge we expand the ionization amplitude for an arbitrary initial angular momentum state exactly in terms of partial wave components for both circularly and elliptically polarized fields. Our spherical expansion has been motivated by the cylindrical expansion employed by Reiss [146] in velocity-gauge and Bauer [23] in length-gauge, however we believe our complementary method is more convenient for initial states consisting of higher angular momentum components.

In Chapter 6 we will derive semi-analytic perturbative two-photon amplitudes for the ionization of atoms by arbitrary polychromatic fields. These formulas are applied to reconstruct isolated attosecond pulses and pulse trains from a provided autocorrelation trace. A feedback loop is used and ionization is determined from a model laser parameterized by a set of variational parameters. The field is recovered when variational parameters are determined such that the exact autocorre-

lation trace agrees with the trace generated by the parameterized field. The amplitude is extended to the non-perturbative limit where time is partitioned into slices $(t_{m-1}, t_m]$ $(m \in \mathbb{Z})$ [63] narrow enough such that perturbative formulas may be applied over each interval. We believe that this approach may be a useful alternative to the earlier non-perturbative methods in applications requiring short pulses and long-range interactions.

We will complete the thesis with a brief summary.

Chapter 2

Perturbative Theory of Light-Matter Interaction

The theory section of this thesis is intended to systematically introduce concepts such as Green's functions, perturbation theory and non-perturbative approaches to ionization in a way that bridges standard upper-division undergraduate quantum mechanics, first year graduate quantum mechanics [125, 151, 152], more advanced Green's function approaches to strong field ionization [5,57,98,107,132,146] and finally our own non-perturbative approach that generalizes the amplitude of [98,132] by expanding the final scattering-state in partial waves [27,29,107] which will be discussed in Chapter 5. We will try our best to honor the original texts, but may find our own way to their results. The present Chapter will focus on the perturbative theory while the subsequent Chapter will discuss the nonperturbative approaches.

The first section will focus on Green's functions and the Lippmann-Schwinger equation. We will use reference states of a free particle scattering off of a Yukawa potential to motivate the idea of a reference Green's function and perturbation theory. In the second section we will describe multi-photon ionization of an atom interacting with a weak laser field. Here, field-free atomic states will take the place of the plane-wave reference Green's function and the (dipole) laser interaction will take the place of the Yukawa potential described in the earlier section. We will focus on one- and two-photon ionization. In the third section we will discuss the breakdown of perturbation theory and motivate the subsequent Chapter on nonperturbative approaches. Throughout this thesis we will use cgs units and switch to the system of atomic units (a.u.), where $m = |e| = \hbar = 1$, when convenient.

2.1 Green's functions and the Lippmann-Schwinger equation

The time-dependent Schrödinger equation

$$\left[i\hbar\frac{\partial}{\partial t} - H(x)\right]\Psi_j(x) = 0 \tag{2.1}$$

describes the time-evolution of a physical state $\Psi_j(x)$ under the influence of the Hamiltonian

$$H(x) = \frac{\mathbf{p}^2}{2m} + V(x) \tag{2.2}$$

for a single particle. Here, $\mathbf{p} = -i\hbar\nabla_{\mathbf{r}}$ determines the momentum of a state and $V(x)$ represents an external potential with $x \equiv \{\mathbf{r}, t\}$. The index j is included to emphasize that a system of orthogonal states satisfies Eq. (2.1).

One may relate some known initial state $\Psi(x)$ of the system to the state of the same system at a later time through

$$\Psi(x) = i\hbar \int_{\mathbb{R}^3} d\mathbf{r}_0\, G(x; \mathbf{r}_0, t_0)\Psi(\mathbf{r}_0, t_0)\,, \tag{2.3}$$

where the Green's function

$$G(x; x') = -\frac{i}{\hbar}\theta(t - t') \sum_j \Psi_j(x)\overline{\Psi_j(x')} \tag{2.4}$$

is determined from *all* states Ψ_j satisfying Eq. (2.1). Since we do not know the set of $\Psi_j(x)$ it is often convenient to suppose we have a complete set of eigenstates $\{\phi_j(x)\}_{j=1,2,\ldots}$ corresponding to a simpler closely related Schrödinger equation with Hamiltonian $H_{i/f}(x)$ where

$$\left[i\hbar\frac{\partial}{\partial t} - H_{i/f}(x)\right]\phi_j(x) = 0. \tag{2.5}$$

Using

$$\left[i\hbar\frac{\partial}{\partial t} - H(x)\right]G(x; x') = \delta^{(4)}(x - x') \tag{2.6}$$

from Eq. (2.1) and

$$\left[i\hbar\frac{\partial}{\partial t} - H_{i/f}(x)\right]G_{i/f}(x; x') = \delta^{(4)}(x - x') \tag{2.7}$$

it is clear that

$$\Psi(x) = \phi_i(x) + \int d^4 x_1 G(x; x_1)V(x_1)\phi_i(t_1). \tag{2.8}$$

with

$$\int d^4x_1 \equiv \int_{t_i}^{t} dt_1 \int d\mathbf{r}_1 \tag{2.9}$$

and

$$\delta^{(4)}(x - x') \equiv \delta(t - t')\delta^{(3)}(\mathbf{r} - \mathbf{r}') \tag{2.10}$$

where t_1 describes the moment where the initial state $\phi_i(x)$ is set. This is called the Lippmann-Schwinger equation [112]. Continuing along these lines the full Green's function can be expanded as

$$\begin{aligned} G(x;x_0) = G_i(x;x_0) + \int d^4x_1 G(x;x_1)V_i(x_1)G_i(x_1;x_0) \\ = G_f(x;x_0) + \int d^4x_1 G_f(x;x_1)V_f(x_1)G(x_1;x_0) \end{aligned} \tag{2.11}$$

with respect to the reference states where i/f are referred to as an initial- and final-state expansion.

2.1.1 Scattering off an external potential

As a concrete example, consider the Hamiltonian

$$H_0(t) = \frac{\mathbf{p}^2}{2m} \tag{2.12}$$

corresponding to a free particle with states

$$\phi_{\mathbf{k}}(x) = e^{-(i/\hbar)\frac{\hbar^2k^2}{2m}t}\phi_{\mathbf{k}}(\mathbf{r}) \quad \text{and} \quad \phi_{\mathbf{k}}(\mathbf{r}) = \frac{e^{i\mathbf{k}\cdot\mathbf{r}}}{(2\pi)^{3/2}}. \tag{2.13}$$

The reference Green's function becomes

$$G_i(x;x') = -\frac{i}{\hbar}\theta(\Delta t)\int \frac{d\mathbf{k}}{(2\pi)^3} e^{i\mathbf{k}\cdot\Delta\mathbf{r} - (i/\hbar)\frac{\hbar^2k^2}{2m}\Delta t} = -\frac{i}{\hbar}\theta(\Delta t)\left(\frac{m}{2\pi i\hbar\Delta t}\right)^{3/2} e^{-\frac{m(\Delta r)^2}{2i\hbar\Delta t}}. \tag{2.14}$$

where in the Fourier basis

$$\tilde{\Phi}(\mathbf{k}) = \int d\mathbf{r}\,\overline{\phi_{\mathbf{k}}(\mathbf{r})}\Phi(\mathbf{r}) \quad \text{with} \quad \Phi(\mathbf{r}) = \int d\mathbf{k}\,\tilde{\Phi}(\mathbf{k})\phi_{\mathbf{k}}(\mathbf{r}). \tag{2.15}$$

one may find a simpler representation of the Green's function by transforming $\mathbf{r}$ and $\mathbf{r}'$ to give the representation in the momentum space

$$\tilde{G}_i(\mathbf{k},t;\mathbf{k}',t') = -\frac{i}{\hbar}\theta(\Delta t)\int d\mathbf{q}\,\tilde{\phi}_{\mathbf{q}}(\mathbf{k},t)\overline{\tilde{\phi}_{\mathbf{q}}(\mathbf{k}',t')}. \tag{2.16}$$

Transforming the states we have

$$\tilde{\phi}_{\mathbf{q}}(\mathbf{k}) = \delta^{(3)}(\mathbf{k}-\mathbf{q}) \tag{2.17}$$

which gives

$$\tilde{G}_0(\mathbf{k},t;\mathbf{k}',t') = -\frac{i}{\hbar}\theta(\Delta t)\delta^{(3)}(\Delta\mathbf{k})e^{-(i/\hbar)\frac{\hbar^2}{2m}\Delta t} \tag{2.18}$$

and the trivial equation of motion

$$\mathbf{F} = \frac{\Delta\mathbf{p}}{\Delta t} = \hbar\frac{\Delta\mathbf{k}}{\Delta t} = 0. \tag{2.19}$$

Individual momentum states $\phi_{\mathbf{k}}(x)$ exactly follow the classical equation of motion and quantum mechanics describes the interferences between momentum components $\mathbf{k}$ and $\mathbf{k}'$ within a single state.

Considering now Eq. (2.1) with potential

$$V(x) = -\frac{Z|e|^2}{r}e^{-\mu r} \tag{2.20}$$

and truncating at first order

$$\Psi(x) = \phi_{\mathbf{k}_i}(x) + \int d^4x_1 G_i(x;x_1)V(x_1)\phi_{\mathbf{k}_i}(x_1) = \Psi^{(\mathrm{in})}(x) + \Psi^{(\mathrm{sc})}(x) \tag{2.21}$$

where the superscript (in) denotes the incoming plane-wave and (sc) the first-order scattered state.

The contribution to the scattered wave with momentum $\mathbf{k}$ is given by

$$\mathcal{M}^{(\mathrm{sc})}(\mathbf{k},t) = \int d^4x\,\overline{\phi_{\mathbf{k}}(x)}\Psi^{(\mathrm{sc})}(x) = -\frac{i}{\hbar}\int_0^t dt_1\, e^{(i/\hbar)\frac{\hbar^2}{2m}(k^2-k_i^2)t_1}\,\tilde{V}(\mathbf{k};\mathbf{k}_i) \tag{2.22}$$

where

$$\int_0^t dt_1 e^{(i/\hbar)\Delta\varepsilon t} = e^{(i/\hbar)\Delta\varepsilon t/2}\mathrm{sinc}((1/\hbar)\Delta\varepsilon t/2)t \equiv \delta_t((1/\hbar)\Delta\varepsilon/2)$$
$$\xrightarrow{t\to\infty} \delta^{(1)}((1/\hbar)\Delta\varepsilon/2) = \frac{2m}{\hbar k}\delta^{(1)}(k-k_i) \tag{2.23}$$

enforces $k = k_i$ in the $t \to \infty$ limit and

$$\tilde{V}(\mathbf{k};\mathbf{k}_i) = \int d\mathbf{r}_1\,\overline{\phi_{\mathbf{k}}(\mathbf{r}_1)}\left[-\frac{Z|e|^2}{r_1}e^{-\mu r_1}\right]\phi_{\mathbf{k}_i}(\mathbf{r}_1) = \frac{-Z|e|^2}{2\pi^2(q^2+\mu^2)} \tag{2.24}$$

with $q = \|\mathbf{k} - \mathbf{k}_i\| = 2k\sin(\theta/2)$ yielding

$$\mathcal{M}^{(\mathrm{sc})}(\mathbf{k}, t) = \frac{iZ|e|^2}{2\pi^2\hbar}\frac{\delta_t((1/\hbar)\Delta\varepsilon/2)}{(q^2+\mu^2)} \tag{2.25}$$

with the scattered rate

$$w^{(sc)}(\mathbf{k}) = \lim_{t\to\infty} t^{-1}|\mathcal{M}^{(\mathrm{sc})}(\mathbf{k}, t)|^2 = \frac{Z^2|e|^4 m}{4\pi^4\hbar^3 k}\frac{\delta^{(1)}(k-k_i)}{(q^2+\mu^2)^2} \tag{2.26}$$

and angular distribution

$$\frac{d\lambda^{(\mathrm{sc})}}{d\Omega} = \int_0^\infty dk\, k^2\, w(k\hat{k}) = \frac{1}{4\pi^4\hbar^3}\frac{Z^2|e|^4 mk}{(4k^2\sin^2(\theta/2)+\mu^2)^2} \tag{2.27}$$

which is the Rutherford scattering angular distribution as $\mu \to 0$.

In Fig. 2.1 an example of an angular distribution is shown for a plane-wave (electron) scattering of a Yukawa potential with $Z = 1$, $\mu = 1/5$ a.u. and $k = 1/8$ a.u..

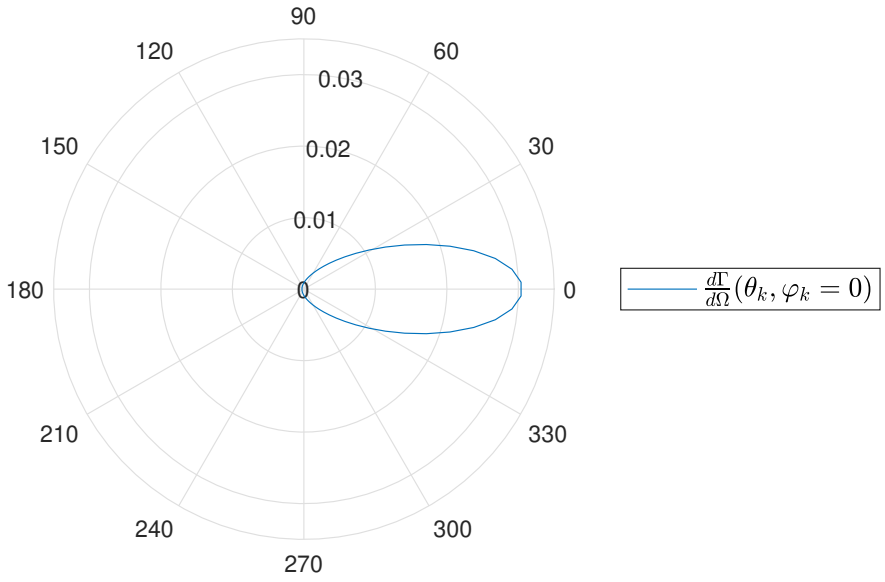

Figure 2.1: Angular distribution (with $\Gamma \equiv w$) in arbitrary units for a plane-wave (electron) scattering of a Yukawa potential with $Z = 1$, $\mu = 1/5$ a.u. and $k = 1/8$ a.u.

The Lippmann-Schwinger equation recursively relates the solution of a simple problem to a more complicated problem of interest. In the next section we describe atomic reference states and

subsequently apply the ideas from this section to discuss ionization of an atom by the perturbation of a weak electric field.

2.1.2 Atomic states

Atomic states are often represented in spherical-polar coordinates

$$x = r\sin\theta\cos\phi, \quad y = r\sin\theta\sin\phi \quad \text{and} \quad z = r\cos\theta \tag{2.28}$$

with some spherically symmetric potential $V_{\mathrm{a}}(\mathbf{r}) = V_{\mathrm{a}}(r)$. Using the Laplacian

$$\Delta = \frac{1}{r^2}\frac{\partial}{\partial r}\left(r^2\frac{\partial}{\partial r}\right) + \frac{L^2}{r^2} \tag{2.29}$$

the time-independent Schrödinger equation (TISE) in atomic units is written as

$$\frac{1}{r^2}\frac{\partial}{\partial r}\left(r^2\frac{\partial\psi(\mathbf{r})}{\partial r}\right) + \frac{L^2\psi(\mathbf{r})}{r^2} + 2(E - V_a(r))\psi(\mathbf{r}) = 0 \tag{2.30}$$

where the eigenspace of the angular momentum operator L^2 is given by

$$L^2 Y_l^m(\hat{\mathbf{r}}) = l(l+1)Y_l^m(\hat{\mathbf{r}}) \tag{2.31}$$

with spherical harmonics $Y_l^m(\hat{\mathbf{r}})$. Applying the separation

$$\psi = R(r)Y_l^m(\hat{\mathbf{r}}) \quad \text{with} \quad R(r) = \frac{\chi(r)}{r} \tag{2.32}$$

we are left with the radial equation

$$\frac{d^2\chi(r)}{dr^2} + \left[2(E - V_{\mathrm{a}}(r)) - \frac{l(l+1)}{r^2}\right]\chi(r) = 0. \tag{2.33}$$

Since ψ is finite everywhere in space we have $\chi(r) \xrightarrow{r\to 0} 0$ and $\frac{\chi(r)}{r}$ bounded for $r \to \infty$ [27, 107].

For the special case of Hydrogen the analytic solution may be determined. Using $V_{\mathrm{a}}(r) = -1/r$ and defining

$$n = 1/\sqrt{-2E} \quad \text{and} \quad \rho = 2r/n \tag{2.34}$$

the radial Schrödinger equation can be written as

$$R'' + \frac{2}{\rho}R' + \left[-\frac{1}{4} + \frac{n}{\rho} - \frac{l(l+1)}{\rho^2}\right]R = 0 \tag{2.35}$$

where primes indicate derivatives with respect to ρ. The solution R is found by taking the product of its solution for $\rho \to 0$ and for $\rho \to \infty$ with some other function which must be determined. Taking $\rho \to 0$ and setting $R \propto \rho^{\nu}$ one sees

$$\nu(\nu-1)r^{\nu-2} + 2\nu\rho^{\nu-2} - l(l+1)r^{\nu-2} \to 0 \Rightarrow \nu = l. \tag{2.36}$$

Similarly for $\rho \to \infty$ the TISE becomes

$$R'' - \frac{1}{4}R = 0 \Rightarrow R \propto e^{-\rho/2} \tag{2.37}$$

yielding

$$R = \rho^{l} e^{-\rho/2} w(\rho). \tag{2.38}$$

Inserting R back into the Schrödinger equation one obtains the hypergeometric differential equation

$$\rho w''(\rho) + (2l+2-\rho)w'(\rho) + (n-l-1)w(\rho) = 0 \tag{2.39}$$

which we will describe in the next subsection.

2.1.2.1 Hypergeometric functions

Eq. (2.39) is a particular case of the confluent hypergeometric differential equation

$$zu'' + (\gamma - z)u' - \alpha u = 0\,, \tag{2.40}$$

which is satisfied by the hypergeometric function

$${}_1F_1(\alpha;\gamma;z) = 1 + \frac{\alpha}{\gamma}\frac{z}{1!} + \frac{\alpha(\alpha+1)}{\gamma(\gamma+1)}\frac{z^2}{2!} + \cdots = \sum_{n=0}^{\infty}\frac{(\alpha)_n}{(\gamma)_n}\frac{z^n}{n!}\,, \tag{2.41}$$

where

$$(a)_n = \frac{\Gamma(a+n)}{\Gamma(a)} \tag{2.42}$$

is the Pochhammer symbol. Here, the sum converges for all finite z and α while γ cannot be zero or a negative integer.

Since the confluent hypergeometric differential equation is second order there must be an additional linearly independent solution which is determined by the substitution [107]

$$u = z^{1-\gamma} u_1 \ , \tag{2.43}$$

where

$$z u_1'' + (2 - \gamma - z) u_1' - (\alpha - \gamma + 1) u_1 = 0 \ , \tag{2.44}$$

which immediately yields the independent solution

$$z^{1-\gamma} {}_1F_1(\alpha - \gamma + 1; 2 - \gamma; z) \ , \tag{2.45}$$

where γ cannot be an integer greater than 1. The general solution is therefore

$$u = a \, {}_1F_1(\alpha; \gamma; z) + b \, z^{1-\gamma} {}_1F_1(\alpha - \gamma + 1; 2 - \gamma; z) \tag{2.46}$$

where a and b are arbitrary constants.

Returning now to the determination of electronic states for atomic hydrogen we have

$$w = a \, {}_1F_1(-n + l + 1; 2l + 2; \rho) \tag{2.47}$$

since solutions must be finite at the origin. Using the boundedness of R and properties of ${}_1F_1$ in the limit where $\rho \to \infty$ from Ref. [107] we have n to be an integer with $n - l - 1 \geq 0$. The bound-state solutions are therefore given by

$$R_{kl}(r) = \frac{2}{n^{l+2}(2l+1)!} \sqrt{\frac{(n+1)!}{(n-l-1)!}} (2r)^l e^{-r/n} {}_1F_1(-n + l + 1; 2l + 2; 2r/n). \tag{2.48}$$

Following the same steps for continuum states we have parameters

$$n = -i/\sqrt{2E} = -i/k, \quad \rho = 2ikr \tag{2.49}$$

and radial functions

$$R_{kl}(r) = \frac{C_k}{(2l+1)!} (2kr)^l e^{-ikr} {}_1F_1(i/k + l + 1; 2l + 2; 2ikr) \tag{2.50}$$

with normalization

$$C_k = \sqrt{\frac{2}{\pi}} k e^{\pi/2k} |\Gamma(l + 1 - i/k)| \tag{2.51}$$

on the k-scale.

2.1.3 Single active electron approximation

For atoms other than Hydrogen analytic solutions to Eq. (2.33) are in general not known. We assume each individual electron orbitals in an atom given by an averaged (fixed in time) atomic potential

$$V_{\rm a}(r) = V_{\rm long}(r) + V_{\rm short}(r) + V_{\rm shell}(r) \tag{2.52}$$

generated from density functional theory (see Ref. [143]). The numerical potential $V_{\rm a}(r)$ is fit to the functions

$$V_{\rm long}(r) = -\frac{Z|e|^2}{r} \tag{2.53}$$

which corresponds to the long-range interaction between an ionized electron and the residual charge $Z|e|$, while

$$V_{\rm short}(r) = -\frac{Z_c|e|^2}{r}e^{-cr} \tag{2.54}$$

and

$$V_{\rm shell}(r) = -\sum_j a_j e^{-b_j r} \tag{2.55}$$

approximate the average interaction of all other electrons at short distances.

To find the states in this case one defines a maximum radius $r_{\rm max}$ with boundary condition $\chi(r_{\rm max}) = 0$ and solves Eq. (2.33) numerically. The first approach we use involves expanding Eq. (2.33) in some basis and solving the eigenvalue problem

$$\mathbb{H}_l|\chi_l\rangle = E|\chi_l\rangle \tag{2.56}$$

for each l to determine a truncated set of both bound-states and discrete continuum states that span the finite box. The second approach we follow involves integrating the radial function χ from $r = 0$ to $r_{\rm max}$ using Eq. (2.33) where a boundary condition $\frac{d}{dr}\chi|_{r=0}$ is set to some small constant ϵ. For bound states a particular energy $E < 0$ is chosen as a lower bound. If $\chi(r_{\rm max}) = 0$ (up to some tolerance) then the associated state is a bound-state. If the boundary condition at $r_{\rm max}$ is not met, then E is increased by some increment and the boundary is checked yet again. For

continuum states the procedure is simpler. All $E > 0$ satisfy Eq. (2.33) and therefore one only needs to integrate the radial equation and normalize.

On the $k-$scale the parameter ϵ is determined by fitting each radial function to the asymptotic solution for $r \to \infty$ [27]

$$\chi_k(r) \sim \sqrt{\frac{2}{\pi}} \sin\left[kr + \log(2kr)/k - l\pi/2 + \eta_l(k)\right] , \tag{2.57}$$

where the additional fit parameter $\eta_l(k)$ describes the so-called scattering phase shifts relates radial functions $R_{kl}(r)$ to the scattering states

$$\phi_{\mathbf{k}}^{(-)}(\mathbf{r}) = \frac{1}{k} \sum_{l=0}^{\infty} \sum_{m=-l}^{l} i^l \, e^{-i\eta_l(k)} R_{k,l}(r) \, \overline{Y_l^m(\hat{\mathbf{k}})} Y_l^m(\hat{\mathbf{r}}) , \tag{2.58}$$

which describe the momentum of an electron in the continuum. For hydrogen atom we have

$$\eta_l(k) = \arg\left[\Gamma(l + 1 - i/k)\right] . \tag{2.59}$$

For short-range potentials the same procedure is applied to the asymptotic solution

$$\chi_k(r) \sim \sqrt{\frac{2}{\pi}} \sin\left[kr - l\pi/2 + \eta_l(k)\right] , \tag{2.60}$$

where

$$\eta_l(k) = 0 \tag{2.61}$$

for a zero-range potential. We almost always use the first method to determine a set of bound states and the second method to describe the continuum.

Diagonalization ensures orthogonality of the bound states, but produces a set of discretized continuum states. Assuming continuum wave-packets do not approach $r = r_{\max}$, the discrete basis is able to describe physical observables and represent the state well. Unfortunately, in the limit of $t \to \infty$, corresponding to states of ejected electrons ($r \to \infty$), determination and interpretation of the photo-electron distribution becomes difficult, but possible given the binning procedure of Ref. [84] as an example.

The shooting method proves to be an inexpensive straight-forward procedure for determining final scattering states with clear physical interpretation. When applied to bound states an

additional orthogonalization procedure is required and accuracy is not guaranteed. In practice the discretized continuum proves to be an efficient computational basis where the true scattering states determined through the shooting method may be projected onto the computational basis to describe properties of the photo-electron distribution at the end of a calculation. It is important to separate states corresponding to physical observables and convenient basis sets for numerical calculations.

2.2 Dirac and Fermi's golden rule

We will now consider the ionization of an atom initially occupying the atomic state

$$\phi_i(x) = R_i(r)\, Y_{l_i}^{m_i}(\hat{\mathbf{r}}) \tag{2.62}$$

by a single photon from the linearly-polarized monochromatic electric field

$$\mathbf{E}(t) = \frac{\mathbf{E}}{2}\left[e^{-i\omega t} + e^{i\omega t}\right]. \tag{2.63}$$

Using the first-order expansion [47, 62]

$$\Psi(x) \approx \phi_i(x) + \int d^4x_1 G_i(x;x_1) V_L(x_1)\phi_i(x_1) \tag{2.64}$$

and laser interaction

$$V_L(x) = |e|\mathbf{E}(t)\cdot\mathbf{r} \tag{2.65}$$

the distribution of ejected photo-electrons can be described by

$$\mathcal{M}(\mathbf{k},t) = \int d^4x\, \overline{\phi_{\mathbf{k}}^{(-)}(x)}\Psi(x) = -\frac{i}{2\hbar}\int_0^t dt_1\, e^{(i/\hbar)\left(\frac{\hbar^2k^2}{2m}+I_p-\hbar\omega\right)t_1}\, V_i(\mathbf{k})\ , \tag{2.66}$$

where

$$H_{\mathrm{a}}(x)\phi_i(x) = -I_p\phi_i(x), \tag{2.67}$$

$I_p \equiv \hbar^2\kappa^2/2m$ and

$$V_i(\mathbf{k}) \equiv \int d\mathbf{r}\, \overline{\phi_{\mathbf{k}}^{(-)}(\mathbf{r})}\,[|e|Ez]\,\phi_i(\mathbf{r}) = (|e|E/k)\sum_{l,m}(-i)^l e^{i\eta_l(k)} Y_l^m(\hat{\mathbf{k}})(z)_i^{(k,l,m)} \tag{2.68}$$

with

$$(z)_i^{(k,l,m)} = \sqrt{\frac{4\pi}{3}} \int_0^\infty dr\, r^2\, R_{k,l}(r) r R_i(r) \int d\Omega_k \overline{Y_l^m(\hat{\mathbf{r}})} Y_1^0(\hat{\mathbf{r}}) Y_{l_i}^{m_i}(\hat{\mathbf{r}}). \tag{2.69}$$

Since the energy of a final ionized state must be larger than the initial ground state we have only included the single photon absorption contribution

$$|e|\mathbf{E}(t)\cdot\mathbf{r} \mapsto \frac{1}{2}|e|Ee^{-i\omega t}z \tag{2.70}$$

and assumed polarization in the $\hat{\mathbf{z}}$-direction. Additionally the integral over three spherical harmonics

$$\int d\Omega_k \overline{Y_l^m(\hat{\mathbf{r}})} Y_1^0(\hat{\mathbf{r}}) Y_{l_i}^{m_i}(\hat{\mathbf{r}}) \tag{2.71}$$

enforces the angular momentum selection rule $m_i = m$ and $|l_i - 1| \le l \le l_i + 1$ for linearly polarized lasers in the $\hat{\mathbf{z}}$-direction. For elliptically polarized lasers (in the $x-y$ plane) the selection rules remain relating l and l_i while $m = m_i \pm 1$ due to the harmonic contributions $Y_1^{\pm 1}(\hat{\mathbf{r}})$. For higher-order photon processes corresponding to Eq. (2.11) these rules hold between photon orders.

For the simplest case of an s-state interacting with a zero-range potential one has [136]

$$R_i(r) \approx C_{\kappa,0}\kappa^{3/2}\frac{e^{-\kappa r}}{\kappa r} \tag{2.72}$$

and

$$\phi_k(\mathbf{r}) = \frac{e^{i\mathbf{k}\cdot\mathbf{r}}}{(2\pi)^{3/2}} = \sqrt{\frac{2}{\pi}} \sum_{l,m} i^l\, j_l(kr) \overline{Y_l^m(\hat{\mathbf{k}})} Y_l^m(\hat{\mathbf{r}}) \tag{2.73}$$

which immediately yields

$$V_i(\mathbf{k}) = \left[|e|\mathbf{E}\cdot(i\nabla_{\mathbf{k}})\right]\tilde{\phi}_i(\mathbf{k})\,, \tag{2.74}$$

where

$$\tilde{\phi}_i(\mathbf{k}) = \int d\mathbf{r}_1 \frac{e^{-i\mathbf{k}\cdot\mathbf{r}_1}}{(2\pi)^{3/2}}\phi_i(\mathbf{r}_1) \tag{2.75}$$

is the Fourier transform of the initial state and $C_{\kappa,0}$ is an asymptotic constant which describes the the ground-state for $\kappa r \gg 1$.

The matrix element becomes

$$V_i(\mathbf{k}) = \left[|e|\mathbf{E}\cdot(i\nabla_{\mathbf{k}})\right] \int d\mathbf{r}_1 \frac{e^{i\mathbf{k}\cdot\mathbf{r}}}{(2\pi)^{3/2}}\phi_i(\mathbf{r}_1) = \frac{-iC_{\kappa,0}(2\kappa)^{1/2}}{\pi(k^2+\kappa^2)^2}\left[|e|Ek_z\right] \tag{2.76}$$

after inserting

$$\tilde{\phi}_i(\mathbf{k}) = \sqrt{\frac{\kappa}{2}}\frac{C_{\kappa,0}}{\pi(k^2+\kappa^2)}. \tag{2.77}$$

The amplitude is completed by using

$$\int_0^t dt_1 e^{(i/\hbar)\Delta\varepsilon t} = e^{(i/\hbar)\Delta\varepsilon t/2}\mathrm{sinc}((1/\hbar)\Delta\varepsilon t/2)t \equiv \delta_t((1/\hbar)\Delta\varepsilon/2)$$
$$\xrightarrow{t\to\infty} 2\hbar\,\delta^{(1)}\left(\frac{\hbar^2k^2}{2m} + I_p - \hbar\omega\right) = \frac{2m}{\hbar k}\delta^{(1)}(k-k_f) \tag{2.78}$$

where $\hbar k_f = \sqrt{2m\left[\hbar\omega - I_p\right]}$ is the final momentum of the ejected electron.

The resulting amplitude is

$$\mathcal{M}(\mathbf{k},t) = -\frac{i}{2\hbar}\delta_t((1/\hbar)\Delta\varepsilon/2)\,\frac{-iC_{\kappa,0}(2\kappa)^{1/2}}{\pi(k^2+\kappa^2)^2}[|e|Ek_z] \tag{2.79}$$

with partial rate

$$w(\mathbf{k}) = \lim_{t\to\infty} t^{-1}|\mathcal{M}(\mathbf{k},t)|^2. \tag{2.80}$$

Using

$$\lim_{t\to\infty} t^{-1}\delta_t((1/\hbar)\Delta\varepsilon/2)^2 = \frac{2\pi}{v_f}\delta^{(1)}(k-k_f) \tag{2.81}$$

with

$$mv_f = \hbar k_f = \sqrt{2m(\hbar\omega - I_p)} \tag{2.82}$$

yields

$$w(\mathbf{k}) = \frac{m}{2\hbar^3}\delta^{(1)}(k-k_f)\frac{C_{\kappa,0}^2(2\kappa)}{\pi(k_f^2+\kappa^2)^4}[|e|^2E^2k_f\cos^2\theta_k]\,. \tag{2.83}$$

Hence, angular distributions are given by

$$\frac{d\lambda}{d\Omega} = \int_0^\infty dk\,k^2 w(\mathbf{k}) = \frac{m}{2\hbar^3}\frac{C_{\kappa,0}^2(2\kappa)}{\pi(k_f^2+\kappa^2)^4}[|e|^2E^2k_f^3\cos^2\theta_k] \tag{2.84}$$

and

$$\frac{d\lambda}{d(\cos\theta_k)} = \int_{-\pi}^{\pi} d\varphi_k \frac{d\lambda}{d\Omega} = \frac{m}{\hbar^3}\frac{C_{\kappa,0}^2(2\kappa)}{(k_f^2+\kappa^2)^4}[|e|^2E^2k_f^3\cos^2\theta_k] \tag{2.85}$$

where the ionization rate is determined by

$$\lambda = \frac{4m}{3\hbar^3}\frac{C_{\kappa,0}^2\kappa}{(k_f^2+\kappa^2)^4}[|e|^2E^2k_f^3] \xrightarrow{k_f\to 0} \frac{4mC_{\kappa,0}^2}{3\hbar^3\kappa^7}|e|^2E^2k_f^3 \propto k_f^{2l_f+1} \tag{2.86}$$

which follows the expected $k_f^{2l_f+1}$ ($l_f = 1$) near-threshold scaling [27, 29, 172]. Exactly the same steps are followed in the case of more complicated atomic potentials where $\phi_i(\mathbf{r})$ and $\phi_{\mathbf{k}}^{(-)}(\mathbf{r})$ are calculated numerically. This approach is taken in Chapter 6.

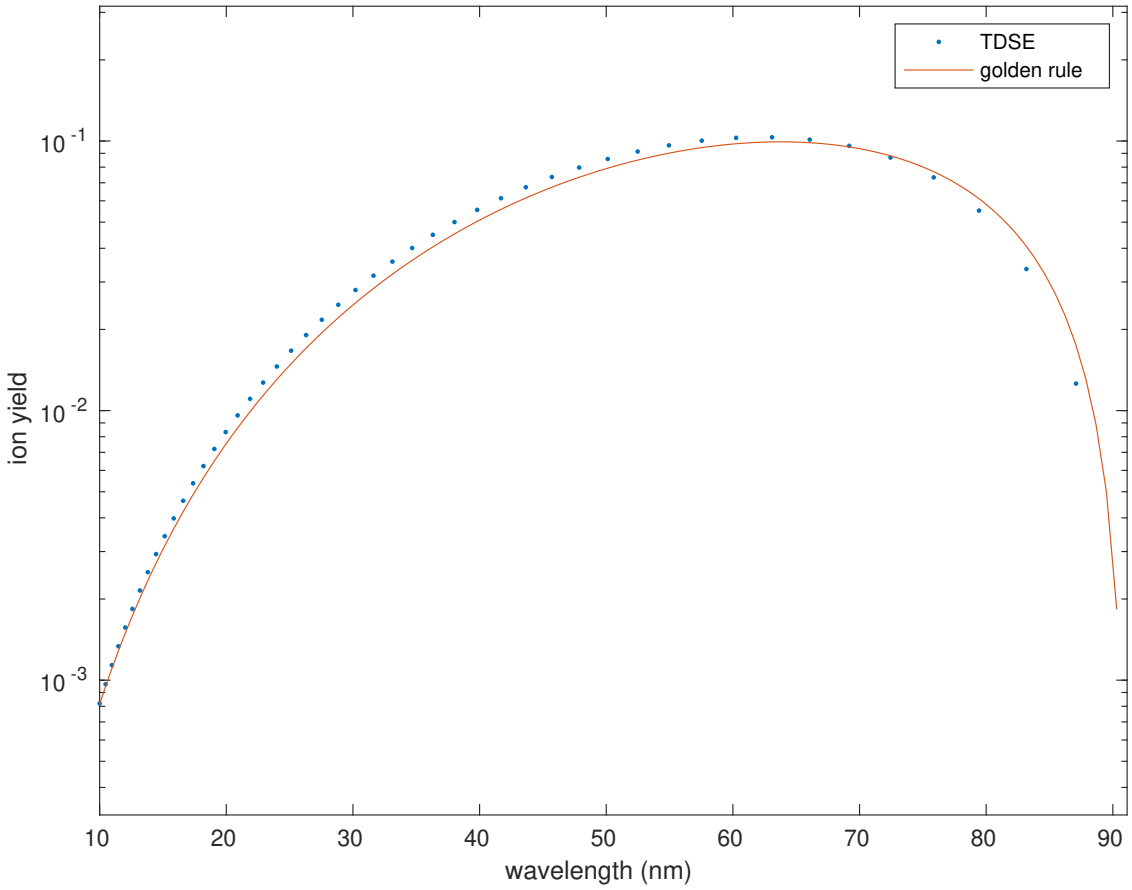

Figure 2.2: Comparison of the total ionization yield between Fermi and Dirac's golden rule and the time-dependent Schrödinger equation. The linearly polarized field has an intensity of $I = 1 \times 10^{14}$ W/cm^2, duration of 16 cycles and wavelengths between 10 nm and 91.928 nm.

In Fig. 2.2 we plot the zero-range total ionization yield

$$N_{\text{ion}} = 1 - \exp\left[-\lambda\left(N_{\text{cycles}}\frac{2\pi}{\omega}\right)\right] \tag{2.87}$$

(solid line) for a 16 cycle laser at $I = 1 \times 10^{14}$ W/cm^2 for wavelengths between 10 nm and 91.928 nm, with the longest wavelength corresponding to $\hbar\omega = I_p = 13.6$ eV. For comparison the blue dots

in Fig. 2.2 correspond to the numerical solution of the TDSE using 8th order B-splines (which will be discussed in Chapter 3) where the ground state is described by the Yukawa potential

$$V_{\rm a}(r) = -\frac{Z|e|^2}{r} e^{-r/a} \tag{2.88}$$

with a range of one fifth of a Bohr radii ($a = a_0/5$), Z chosen such that $I_p = 13.6$ eV and $C_{\kappa,0}$ is fit to the asymptotic tail of the exact ground state. The TDSE calculations use a monochromatic 16 cycle flat-top pulse which smoothly turns both on an off using a 2 cycle $\sin^2$ ramp function. Differences in the two plots correspond to errors introduced by the asymptotic ground state and the fact that we are not including the shape of the envelope in the analytic calculations.

2.2.1 Perturbative multi-photon ionization

Expanding Eq. (2.11) to second order

$$\begin{aligned}\Psi^{(2)}(x) &= \int d^4x_2\, G_0(x;x_2)\,[|e|\mathbf{E}(t_2)\cdot\mathbf{r}_2] \int d^4x_1\, G_0(x_2;x_1)[|e|\mathbf{E}(t_1)\cdot\mathbf{r}_1]\phi_i(x_1) \\ &= \int d^4x_2\, G_0(x;x_2)\,[|e|\mathbf{E}(t_2)\cdot\mathbf{r}_2]\,\Psi^{(1)}(x_2)\end{aligned} \tag{2.89}$$

describes the lowest-order two-photon correction where

$$\Psi^{(1)}(x) = \int d^4x_1\, G_0(x;x_1)[|e|\mathbf{E}(t_1)\cdot\mathbf{r}_1]\phi_i(x_1) \tag{2.90}$$

corresponds to the first order correction as before. In Chapter 6 we will apply these formulas to Helium in the case of a poly-chromatic field generated from high-order harmonic generation. Assuming conditions described in the next section are met, Eq. (2.11) can be applied iteratively to generate higher photon amplitudes where factors containing $e^{-i\omega t_j}$ ($e^{i\omega t_j}$) describe the absorption (emission) of a single photon during the $j-$th process.

2.3 Breakdown of perturbation theory

Several criteria exists which must all be simultaneously satisfied for the validity of perturbation theory. Following Ref. [101] we will outline some of the simplest ones.

2.3.1 Coulomb force

The first criterium for the applicability of perturbation theory corresponds to the fact that the force associated with the external (laser) field must be significantly weaker than the Coulomb force binding a free electron to the atomic core. Here, we approximate the Coulomb force at an electronic distance of one Bohr radius a_0 in Hydrogen as

$$|F_{\text{Coul}}(r)| = \frac{|e|^2}{r^2} \sim \frac{|e|^2}{a_0^2} \tag{2.91}$$

where the force applied by the electric field is

$$|F_L| = |e|E. \tag{2.92}$$

Setting these two quantities equal to one another, we obtain the characteristic electric field and intensity

$$E_{\text{a.u.}} \equiv \frac{|e|}{a_0^2} = 5.14 \times 10^9\,\text{V/cm} \Rightarrow I_{\text{a.u.}} = \frac{c}{8\pi} E_{\text{a.u.}}^2 = 3.51 \times 10^{16}\,\text{W/cm}^2 \tag{2.93}$$

binding the electron to the atomic core. For perturbation theory to be valid the external field amplitude E must satisfy

$$E \ll E_{\text{a.u.}} \tag{2.94}$$

and therefore not significantly distort the ground state orbital motion.

2.3.2 Bound state intensity parameter

The second parameter we will describe relates the energy of a single photon $\hbar\omega$ to the power broadening of a level due to the application of a strong field $|e|Ea_0$ where the characteristic scale a_0 is the Bohr radius of the atom related to the ionization potential by $I_{\text{p}} = \hbar^2/2ma_0^2$ and E is the field amplitude. The ratio

$$\gamma = \frac{\hbar\omega}{|e|Ea_0} \tag{2.95}$$

is referred to as the Keldysh parameter [98]. When this value is significantly greater than one ($\gamma \gg 1$) the level broadening is small compared to the energy contained in a single quanta. When

($\gamma \ll 1$) the level broadening is large compared to the photon energy and the number of photons needed to transition between levels is indefinite.

In the literature Reiss [146] has introduced a more convenient "bound-state" intensity parameter

$$z_1 = \frac{2U_p}{I_p} = \frac{1}{\gamma^2} \,, \tag{2.96}$$

which re-expresses the Keldysh parameter in a way that it relates the ionization potential of the initial bound state I_p to the time averaged quiver energy

$$U_\mathrm{p} \equiv \frac{1}{2} m\omega \langle x(t)^2 \rangle_T = \frac{|e|^2 E^2}{4m\omega^2} \tag{2.97}$$

of a free electron in an external field.

One typically refers to $\gamma \gg 1$ as the (perturbative) multi-photon regime since associating features with a particular photon process is possible. Here, processes involving fewer photons are most probable. The $\gamma \ll 1$ limit is referred to as tunneling ionization where many different photon orders (possibly infinite) contribute to processes. In this limit the field-free atomic system is no longer a good reference. It is important to recognize that multi-photon processes are still responsible for ionization, but perturbation theory fails. Processes involving a large number of photons can contribute more than lower order processes.

In the static limit ($\gamma = 0$), ionization becomes tunneling through a time-independent barrier [107]. The electronic ground state of an atom like Hydrogen [124] is shifted and broadened by the electric field F (in atomic units) as it increases. The energy follows the form

$$E(F) = \varepsilon(F) - \frac{i}{2}\Gamma(F) \tag{2.98}$$

where $\Gamma(F)/\hbar$ describes the tunneling rate out of the Coulomb potential [132]. Perturbatively correcting the Hydrogen ground state as in Ref. [142] one obtains the expansion

$$E(F) \sim -\frac{1}{2} \sum_{n=0}^{\infty} e_n \left(\frac{F}{4}\right)^{2n} \tag{2.99}$$

where e_n are real coefficients that grow factorially. This expansion is real and therefore cannot describe $\Gamma(F)$ and the ionization process.

2.3.3 Continuum state intensity parameter

The third parameter we will discuss relates the quiver energy of a free electron to the energy contained in a single field quanta

$$z = \frac{U_p}{\hbar\omega} \tag{2.100}$$

which Reiss has called the "continuum-state" intensity parameter [146]. A classical electron interacting with a time-dependent electric field accumulates a time-averaged kinetic energy U_p. If a large number of photons with energy $\hbar\omega$ are required to describe the classical motion, then the process is inherently non-perturbative. In Chapter 5 we will expand the non-perturbative amplitude for ionization in a strong circularly polarized field in a series with respect to z_1 and z, and show that as the laser wavelength increases so do z_1 and z necessitating increasingly higher order terms.

In Fig. 2.3 we plot shaded regions where $E < E_{\text{a.u.}}$, $z_1 < 1$ and $z < 1$. For given laser parameters perturbation theory is limited by the continuum state intensity parameter z. The dark red shaded region corresponds to $z < 0.1$ corresponding to a region where perturbation theory should be valid. An intensity estimate of 2.6×10^{12} W/cm^2 for ionization by a Ti-sapphire laser (800 nm) is noted by a horizontal and vertical line within the Figure.

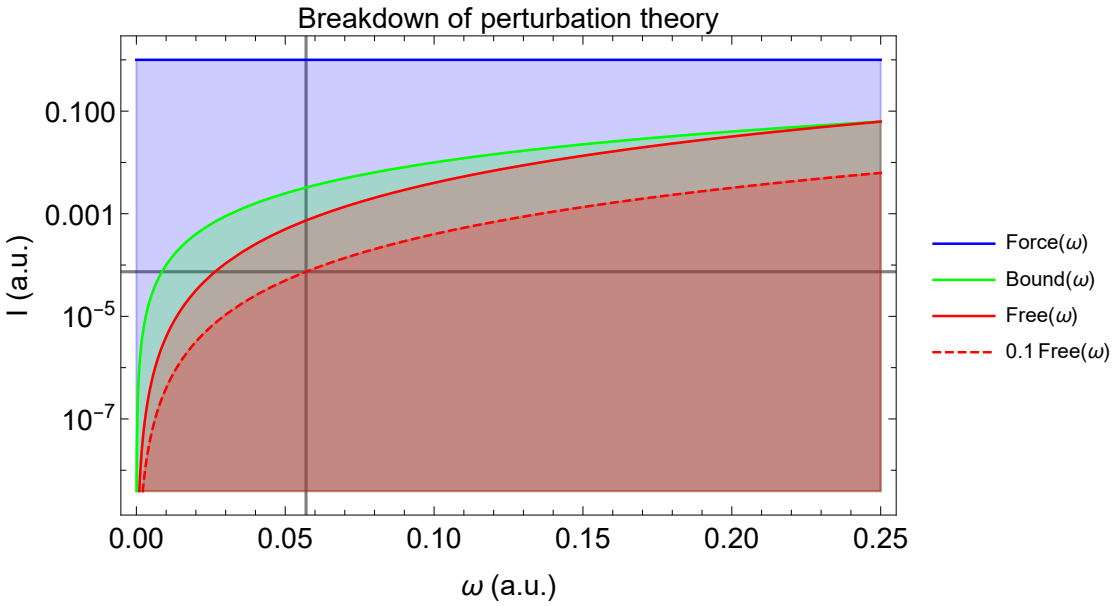

Figure 2.3: Shaded regions correspond to regions where $E < E_{\text{a.u.}}$ (blue), $z_1 < 1$ (green), $z < 1$ (red) and $z < 0.1$ (dark red). An estimate for the applicability of perturbation theory is given by the dark red region. The vertical grey line corresponds to a laser wavelength of 800 nm, at which an intensity of $2.6 \times 10^{12}\text{W/cm}^2$ (horizontal line) marks the limit where perturbation theory would approximately break down for a Ti-sapphire laser.

Chapter 3

Non-perturbative Theory of Light-Matter Interaction

Attempts made at modeling (non-perturbative) strong field ionization dates back to at least Oppenheimer in 1928 [132] where an expansion similar to the golden rule [47, 62] was generated for the ionization of Hydrogen by a strong static field where the final scattering states of Sec. 2.2 have been replaced by states of an otherwise free electron in a static field (Airy functions). Later in 1964 Keldysh applied essentially the same method to time-dependent fields and derived the ionization amplitude [98]. In Keldysh's work the quasi-classical method of steepest descent was applied to approximate time-integration and the final continuum states have been replaced by states of a free electron propagating in a dynamic electric field (Volkov states [98, 165]). The quasi-classical approximation allows for a clear classical interpretation, but fails in the ultraviolet limit where exact (fully quantum) time integration must be performed. In Chapter 5 we discard the quasi-classical approximation in our own work where we have further extended Oppenheimer's and Keldysh's amplitude into the ultraviolet limit. Our first-order amplitude is valid for arbitrary initial and final states, but just as in Refs. [98, 132] higher order approximations are required to describe long-range potentials. We will focus on the first-order expansion for this thesis, but the exact same method can be applied recursively to generate higher order corrections.

In the first section of this Chapter we will describe numerical solutions to the time-dependent problem of ionization by a finite pulse which will be used in subsequent Chapters. Afterwards we will discuss the main ingredients required to build the strong field approximation [57,98,107,132,136,146] and key models that have motivated us to form our own approach. The goal here is to summarize

the points that have influenced our own work and not to determine which models are "best" or provide a complete review. We will try our best to respect the original works and emphasize key points, but our derivation may deviate at times.

Our starting point is the idea of contour deformation and asymptotic approximations of oscillatory integrals. Direct integration of integrals encountered in strong-field ionization are either cumbersome or not available. Asymptotic approximations are able to extract simplified properties of a system in some reduced parameter space. These ideas are immediately applied to the quantum propagation of a free electron in a static external field where we will recover the classical equations of motion and describe quantum turning point behavior. Next, we will apply Oppenheimer's model [132] to describe the transition of a bound electron into the before mentioned states of an electron propagating in an external field. For hydrogen atom (and all long-range potentials) the final state must somehow include the influence of the atomic potential. Although mostly correct, Oppenheimer's rate [132] is missing a constant proportionality factor recovered by the s-state Landau and Lifshitz model [107] which includes the influence of both the Coulomb and laser interaction in the final state. Afterwards, we will average the static ionization rate of a long-wavelength field over a laser cycle to generate the so-called adiabatic ionization rate [5, 136]. At shorter wavelengths the adiabatic approximation breaks down and the ionized electron must be described by a final (Volkov) state which is determined by the full time-dependent electric field as we will discuss. We will finally discuss the non-adiabatic rate given in Ref. [98] on which our own method is based on and the complementary methods of Perelomov, Popov and Terent'ev [136] as well as of Reiss [146] which have also influenced our approach.

3.1 Numerical solution

The most straightforward way of modeling strong-field problems for which perturbation theory fails is the direct numerical solution of the time-dependent Schrödinger equation. $\Psi(x)$ is

represented in spherical-polar coordinates where the state is expanded as

$$\Psi(x) = \sum_{l,m} \frac{\chi_{l,m}(r,t)}{r} Y_l^m(\hat{\mathbf{r}}) \tag{3.1}$$

in the basis of spherical harmonics over θ and ϕ and the radial function $\chi_{l,m}(r,t)$ is either represented on a grid or expanded in some basis.

Finite-difference methods correspond to approaches where $\chi_{l,m}(r,t)$ is represented on a grid with points at $r_j = j\delta r$ where $j = 1, 2, \ldots, N_r$ and $r_{\max} = r_{N_r}$ represents the edge of a finite "box". r and functions $f(r)$ are represented by a diagonal matrix evaluated at each r_j. To cope with outgoing ionized wave-packets that would otherwise reflect off the edge of the "box" at $r = r_{\max}$, exterior complex scaling [78] is used where $\delta r \mapsto e^{i\eta}\delta r$ at points $r_{\text{ECS}} \leq r \leq r_{\max}$ where, the derivative

$$\frac{d^2}{dr^2} \mapsto e^{-2i\eta} \frac{d^2}{dr^2} \tag{3.2}$$

and $\eta = -\pi/4$ has been used. Oscillatory functions e^{ikr} corresponding to the kinetic energy $k^2/2$ are replaced by $-ik^2/2$ and exponentially suppressed. Assuming the region $r_{\text{ECS}} \leq r \leq r_{\max}$ is wide enough and η is chosen appropriately the wave-packet is exponentially diminished as a function of time.

For derivatives multiple different Taylor series are taken about some point r_j which are added together with appropriate weights such that all terms lower than the desired derivative vanish and higher order terms correspond to some truncation error. The general procedure is referred to as Fornberg's method [64]. Using a second-order approximation in the case of the second derivative centered about r_j one has

$$\frac{d^2}{dr^2} f(r) \mapsto \frac{f(r_{j-1}) - 2f(r_j) + f(r_{j+1})}{(\delta r)^2} \tag{3.3}$$

where $f(0)$ and $f(r_{N_r+1})$ are equal to zero and omitted. At fourth order the central difference becomes

$$\frac{d^2}{dr^2} f(r) \mapsto \frac{-(1/12)f(r_{j-2}) + (4/3)f(r_{j-1}) - (5/2)f(r_j) + (4/3)f(r_{j+1}) - (1/12)f(r_{j+2})}{(\delta r)^2} \tag{3.4}$$

for points corresponding to $j = 2, \cdots, N_r - 1$ and the forward difference

$$\left.\frac{d^2}{dr^2} f(r)\right|_{r=r_1} \mapsto \frac{-20f(r_1) + 6f(r_2) + 4f(r_3) - f(r_4)}{12(\delta r)^2} \tag{3.5}$$

at r_1 and a similar backward difference at r_{N_r} to deal with the end of the box.

For the radial functions we have used both approximate states of the field-free atomic Hamiltonian [36] or B-splines. For the basis of atomic states,

$$\left[-\frac{1}{2}\frac{d^2}{dr^2} + \frac{l(l+1)}{2r^2} + V_{\rm a}(r) - iW(r)\right]\chi_{n,l}(r) = E_{n,l}\chi_{n,l}(r) \tag{3.6}$$

is diagonalized (as a finite-difference representation) within a finite box where the complex absorbing potential $W(r)$ [178] suppresses wave-packets in the absorbing region at the end of the box.

Since the Hamiltonian is no longer Hermitian the energy

$$E_{n,l} = \varepsilon_{n,l} - \frac{i}{2} w_{n,l} \tag{3.7}$$

is now complex where $w_{n,l}$ corresponds to the rate with which each state leaves the box and states are normalized as

$$\int_0^{r_{\rm max}} dr\, \chi_{n,l}(r)^2 = 1 \tag{3.8}$$

with $\chi_{n,l}(r) \in \mathbb{C}$ [129]. For deeply bound states $w_{n,l} \approx 0$ and $\chi_{n,l}(r)$ is approximately a real function. For the B-spline method we expand the radial coordinate similarly as in Refs. [1, 10, 15] where exterior complex scaling has been implemented as in Ref. [123].

For time-integration of all methods described in this section, we have applied the Crank-Nicolson method where the known state $|\Psi(t)\rangle$ at time t is used to determine the state $|\Psi(t+\delta t)\rangle$ at a later time from the solution of

$$[\mathbb{S} + (i\delta t/2)\mathbb{H}(t)]\,|\Psi(t+\delta t)\rangle = [\mathbb{S} - (i\delta t/2)\mathbb{H}(t)]\,|\Psi(t)\rangle, \tag{3.9}$$

where $|\Psi(t)\rangle$ is a numerical representation of the state (column vector), $\mathbb{H}(t)$ is the discritized Hamiltonian (matrix) and $\mathbb{S}$ is an overlap matrix between states of the numerical expansion. $\mathbb{S}$

is exactly the identity matrix $\mathbb{I}$ for basis sets corresponding to orthonormal atomic states or grid-points. In contrast, off-diagonal elements of $\mathbb{S}$ are nonzero for non-orthogonal basis-sets such as B-splines.

Although methods discussed in this section are nearly exact in the limit of converged parameters difficulties arise from both the amount of time and computing resources needed for converged calculations. In view of this as well as the need for approximate analytic models to physically interpret numerical results, in the following sections as well as in Chapter 5 we will discuss perturbation-like approximations to strong-field problems which are able to help interpret numerical results and give a clear physical picture.

3.2 Contour deformation

Often when computing amplitudes, integrals of the form

$$I(s) = \int_C dz\, e^{-sf(z)} \tag{3.10}$$

are encountered where, in general, the function f is complex valued and C is some arbitrary contour. In the limit of large s the imaginary part of f causes the integrand to oscillate rapidly where the resulting cancellations obscure the behavior of $I(s)$. When f is analytic one can deform the contour of integration such that the function f is almost entirely real-valued over the new deformed contour C'. On this new deformed contour the now slowly oscillating integrand allows for a clearer interpretation. As an example, we now apply this idea to extract the asymptotic behavior of a Bessel function $J_\nu(s)$ $(\nu > -1/2)$ in the large s limit.

3.2.1 Application to Bessel functions

Before applying this method to derive amplitudes we will sketch the simplest example presented in Appendix A of Ref. [155]. Intuition gained in this part is important to define the rate [98] from which our own method is derived. For index $\nu > -1/2$ we may define the Bessel function as

$$J_\nu(s) = \frac{(s/2)^\nu}{\Gamma(\nu + 1/2)\Gamma(1/2)} \int_{-1}^{1} dx\, e^{isx}(1 - x^2)^{\nu - 1/2} \tag{3.11}$$

which only provides a simple representation in terms of elementary functions for half-integer ν [107] where

$$J_{n+1/2}(s) = \sqrt{\frac{2s}{\pi}} j_n(s) \tag{3.12}$$

with

$$j_n(s) = (-s)^n \left(\frac{1}{s}\frac{d}{ds}\right)^n \frac{\sin s}{s} \tag{3.13}$$

for integer n.

For arbitrary $\nu > -1/2$ we may extract the $s \to \infty$ behavior by defining

$$I(s) = \int_{-1}^{1} dx\, e^{isx}(1-x^2)^{\nu-1/2}\,, \tag{3.14}$$

where we immediately recognize that the e^{isx} product in the integrand rapidly oscillates obscuring the asymptotic behavior of $I(s)$. Realizing that $f(z) = e^{isz}(1-z^2)^{\nu-1/2}$ is an analytic function we may further define the closed loop contour $C_{R,\epsilon}$ which contains no singularities for all $R, \epsilon > 0$ (c.f., Fig. 3.1). Taking the limit $R \to \infty$, $\epsilon \to 0^+$ we may define the closed loop contour $C = \lim_{R\to\infty,\,\epsilon\to 0^+} C_{R,\epsilon}$ where the contribution from the line segment $z = -1$ to $z = 1$ describes the desired integral $I(s)$. $I_\pm(s)$ describes the integrand from $z = 1$ to $z = 1 + i\infty$ ($I_+(s)$) and the integrand from $z = -1 + i\infty$ to $z = -1$ ($I_-(s)$). Finally, the contribution $I_R(s)$ is defined from $z = 1 + i\infty$ to $z = -1 + i\infty$, which closes the loop. Since $f(z)$ is an analytic function we immediately see that $I(s) + I_+(s) + I_-(s) + I_R(s) = 0$. Furthermore, there exists some $A, c > 0$ such that $|f(z)| = e^{-sR}|(1-(x+iR)^2)^{\nu-1/2}| < Ae^{-cR}$, and we immediately see that the contribution $I_R(s)$ tends towards zero as $R \to 0$ yielding $I(s) = -I_+(s) - I_-(s)$. Here, $I_\pm(s)$ has a simpler asymptotic behavior since the integrand oscillates slowly with an exponential decay factor $|e^{isz}| = e^{-sy}$.

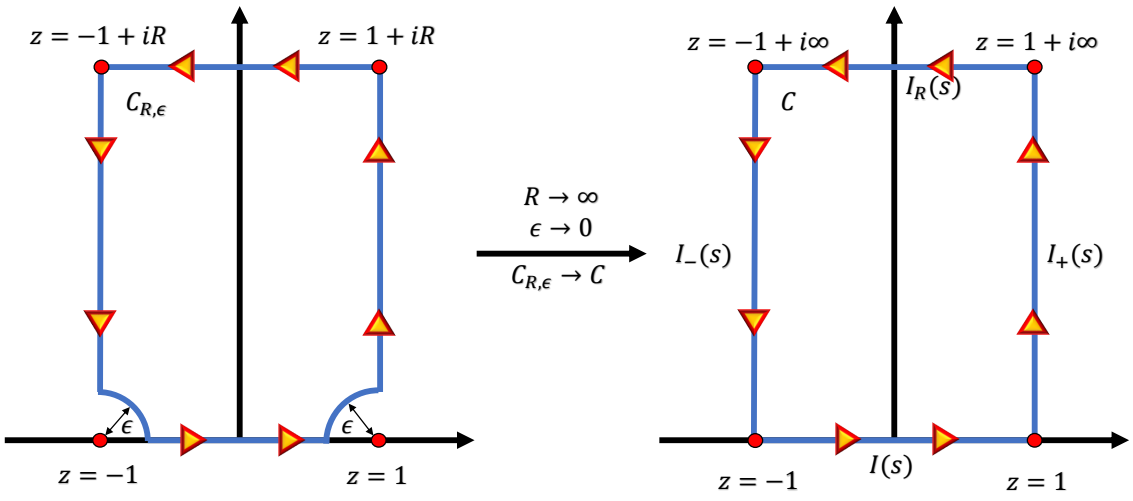

Figure 3.1: Contour of integration $C_{R,\epsilon}$ (left). Taking the limit as $R\to\infty$ and $\epsilon\to 0^+$ defines the contour C from which $I(s)$, $I_\pm(s)$ and $I_R(s)$ are defined (right). Taking the limit $R\to\infty$ forces $I_R(s)\to 0$ and taking the limit $\epsilon\to 0^+$ allows C to avoid the branch points $z=\pm 1$ of $(1-z^2)^{\nu-1/2}$.

Writing

$$I_\pm(s) = ie^{\pm is}\int_0^\infty dy\, e^{-sy}(1-(\pm 1+iy)^2)^{\nu-1/2} \tag{3.15}$$

we may now approximate the integrand $f(z)$ to extract the asymptotic behavior of $I_\pm(s)$ yielding the behavior of $I(s)$. To this end, we may expand the polynomial factor as

$$(1-(\pm 1+iy)^2)^{\nu-1/2} = \begin{cases} (\mp 2iy)^{\nu-1/2}+O(y^{\nu+1/2}) & 0\le y\le 1 \\ O(y^{2\nu-1}+y^{\nu-1/2}) & 1<y. \end{cases} \tag{3.16}$$

Since as $s\to\infty$, e^{-sR} falls off faster than all polynomial orders we may replace the polynomial factor with the $0\le y\le 1$ contribution alone yielding the Laplace transform

$$I_\pm(s) = \int_0^\infty dy\, e^{-sy}\left[(\mp 2iy)^{nu-1/2}+O(y^{\nu+1/2})\right] = \frac{2^{\nu-1/2}}{s^{\nu+1/2}}\Gamma(\nu+1/2)e^{\pm i(s-\nu\frac{\pi}{2}+\frac{3\pi}{4})}+O(s^{-\nu-3/2}). \tag{3.17}$$

Combining these contributions we immediately see that

$$J_\nu(s) = \sqrt{\frac{2}{\pi s}} \cos\left(s - \nu\frac{\pi}{2} - \frac{\pi}{4}\right) + O(s^{-3/2}). \tag{3.18}$$

Although determining the exact behavior of $J_\nu(x)$ is difficult, we were able to extract the behavior in the limit $s \to \infty$ for arbitrary $\nu > -1/2$. This idea is essential when approximating Green's functions in the long-wavelength limit. As an example in Fig. 3.2 both the approximate and exact form of $J_3(s)$ are plotted.

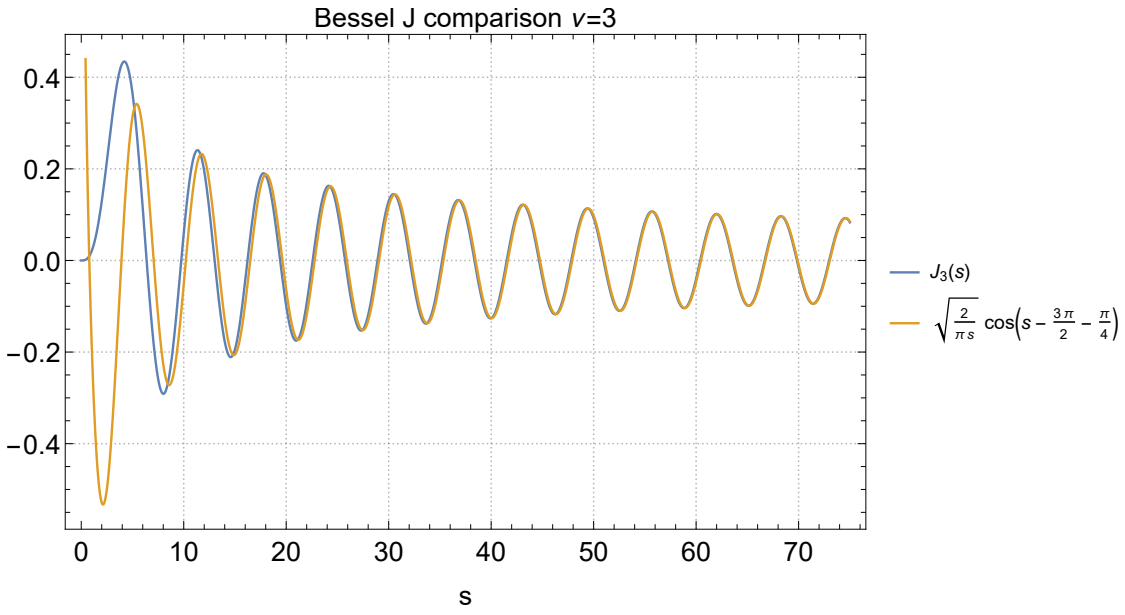

Figure 3.2: Comparison of $J_3(s)$ with its asymptotic approximation, Eq. (3.18).

3.3 Motion in a static field: Airy functions

In a static field the motion of an otherwise free electron is described by the time-independent Schrödinger equation

$$\left[\frac{\mathbf{p}^2}{2m} + |e|\mathbf{E}\cdot\mathbf{r}\right]\Phi(\mathbf{r}) = \varepsilon\Phi(\mathbf{r}) \tag{3.19}$$

with energy eigenvalue ε and field $\mathbf{E} = E\hat{\mathbf{z}}$ in the case of linear polarization. States are determined by separation of variables where

$$\Phi(\mathbf{r}) = \Phi_\perp(\mathbf{r}_\perp)\Phi_\parallel(z), \qquad \varepsilon = \varepsilon_\perp + \varepsilon_z \tag{3.20}$$

describes partitioning of the wave function into a part parallel to the field ($\parallel$) along the z–axis and perpendicular ($\perp$) part within the x-y plane. Inserting the state into Eq. (3.19) we have

$$\frac{1}{\Phi_\parallel(z)}\left[\frac{p_{\mathrm{op},\parallel}^2}{2m}+|e|Ez\right]\Phi_\parallel(z)=\frac{1}{\Phi_\perp(\mathbf{r}_\perp)}\left[\varepsilon-\frac{\mathbf{p}_{\mathrm{op},\perp}^2}{2m}\right]\Phi_\perp(\mathbf{r}_\perp) \tag{3.21}$$

which immediately yields the perpendicular ($\perp$) plane-wave solution

$$\Phi_\perp(\mathbf{r}_\perp)=\Phi_{\mathbf{k}_\perp}(\mathbf{r}_\perp)=\frac{e^{i\mathbf{k}_\perp\cdot\mathbf{r}_\perp}}{(2\pi)}\qquad \varepsilon_\perp=\frac{\hbar^2k_\perp^2}{2m} \tag{3.22}$$

that describes the expected free propagation.

The left-hand side of Eq. (3.21) describes the motion in the parallel direction and can be written as Airy's differential equation [4]

$$\left[\frac{\partial^2}{\partial z^2}-\frac{(z-z_{\mathrm{cl}})}{L^3}\right]\Phi_\parallel(z)=0 \tag{3.23}$$

with

$$z_{\mathrm{cl}}\equiv\varepsilon_\parallel/(|e|E),\quad \text{and}\quad L\equiv[\hbar^2/(2m|e|E)]^{1/3}. \tag{3.24}$$

Here it is clear that for values of z to the left of the classical turning point z_{cl} ($z<z_{\mathrm{cl}}$) solutions are locally oscillatory and to the right of the turning point, solutions either tend towards zero or are exponentially divergent. Here, we will only concern ourselves with the solutions which tend towards zero.

Since Airy's differential equation takes the form

$$\sum_{m=0}^{n}(a_m+b_mx)\frac{d^my}{dx^m}=0 \tag{3.25}$$

Laplace's method may be applied [68]. The solution [107]

$$y(x)=\int_C dt\,Z(t)e^{xt} \tag{3.26}$$

is formed from the polynomials

$$P(t)=\sum_{m=0}^{n}a_mt^m,\qquad Q(t)=\sum_{m=0}^{n}b_mt^m \tag{3.27}$$

and the function

$$Z(t) = \frac{1}{Q(t)} e^{\int dt\, P(t)/Q(t)}, \tag{3.28}$$

where the contour C is chosen such that the integral is nonzero and finite. Note that

$$V(t) = e^{xt} Q(t) Z(t) \tag{3.29}$$

returns to its original value where the contour can either be open or closed.

Starting with

$$\left[\frac{\partial^2}{\partial x^2} - x\right] y(x) = 0 \tag{3.30}$$

and identifying

$$P(t) = t^2, \quad Q(t) = -1, \quad Z(t) = -e^{-t^3/3} \quad \text{and} \quad V(t) = e^{xt - t^3/3} \tag{3.31}$$

the solution becomes

$$y(x) = A \int_C dt\, e^{xt - t^3/3} \tag{3.32}$$

where the integrand goes to zero ($\mathrm{Re}\, t^3 > 0$) at each of its endpoints corresponding to the shaded region in Fig. 3.3 and A is an arbitrary constant. In Fig. 3.3 the three most important contributions correspond to contours C_A, C_{B_+} and C_{B_-} where C_A results in a solution $y(x) \equiv \mathrm{Ai}(x)$ that goes to zero at $x \to \pm\infty$ and $C_{B_\pm}$ results in a divergent solution for $x \to \infty$.

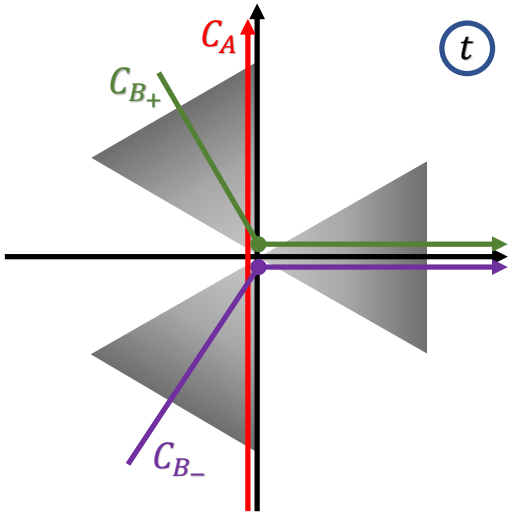

Figure 3.3: Contours of integration for the integrand $e^{xt-x^3/3}$. The dark triangular regions correspond to zones where the contour may begin or end ($e^{-t^3/3} \to 0$). C_A corresponds to a convergent solution as $x \to \infty$, while $C_{B_\pm}$ correspond to divergent solutions as $x \to \infty$.

Here we choose the bounded solutions along the imaginary axis (contour C_A in Fig. 3.3, where $t = i\varphi$) corresponding to

$$y(x) = \mathrm{Ai}(x) = \frac{1}{2\pi}\int_{\mathbb{R}} d\varphi\, e^{i\varphi^3/3 + i\varphi x} \tag{3.33}$$

where we have used the normalization convention

$$\int_{\mathbb{R}} dz\, \mathrm{Ai}(z-x)\mathrm{Ai}(z-y) = \delta^{(1)}(x-y) \tag{3.34}$$

yielding

$$\Phi_z(z) = \Phi_{z_{\mathrm{cl}}}(z) = \frac{1}{L}\mathrm{Ai}[(z - z_{\mathrm{cl}})/L]. \tag{3.35}$$

and finally [28]

$$\Phi_{\mathbf{k}_\perp z_{\mathrm{cl}}}(\mathbf{r}) = \frac{1}{2\pi L} e^{i\mathbf{k}_\perp \cdot \mathbf{r}_\perp} \mathrm{Ai}\left[(z - z_{\mathrm{cl}})/L\right]. \tag{3.36}$$

In the next subsection we will use solutions to Eq. (3.19) to describe the motion of a free particle in a static field.

3.3.1 Newton's second law

In this subsection we will use the momentum-space Green's function $\tilde{G}(\mathbf{k},t;\mathbf{k}',t')$ of Eq. (3.19) to recover the classical equation of motion

$$m\mathbf{a} = -|e|\mathbf{E}. \tag{3.37}$$

Starting with the states in the Schrödinger picture

$$\Phi_{\mathbf{k}_\perp z_{\rm cl}}(x) = e^{-(i/\hbar)\varepsilon(\mathbf{k}_\perp z_{\rm cl})t}\,\Phi_{\mathbf{k}_\perp z_{\rm cl}}(\mathbf{r}) \tag{3.38}$$

we may write the position-basis Green's function as

$$G(x;x') = -\frac{i}{\hbar}\theta(t-t')\int_{\mathbb{R}^2} d\mathbf{q}_\perp \int_{\mathbb{R}} dz_{\rm cl}\,\Phi_{\mathbf{q}_\perp z_{\rm cl}}(x)\overline{\Phi_{\mathbf{q}_\perp z_{\rm cl}}(x')} \tag{3.39}$$

and Fourier transform with respect to each coordinate $\mathbf{r}$ and $\mathbf{r}'$ to determine the momentum basis representation

$$\tilde{G}(\mathbf{k},t;\mathbf{k}',t') = -\frac{i}{\hbar}\theta(t-t')\int_{\mathbb{R}^2} d\mathbf{q}_\perp \int_{\mathbb{R}} dz_{\rm cl}\,\tilde{\Phi}_{\mathbf{q}_\perp z_{\rm cl}}(\mathbf{k},t)\overline{\tilde{\Phi}_{\mathbf{q}_\perp z_{\rm cl}}(\mathbf{k}',t')}. \tag{3.40}$$

Evaluating

$$\tilde{\Phi}_{\mathbf{q}_\perp z_{\rm cl}}(\mathbf{k},t) \equiv \int_{\mathbb{R}^3} d\mathbf{r}\frac{e^{-i\mathbf{k}\cdot\mathbf{r}}}{(2\pi)^{3/2}}\Phi_{\mathbf{q}_\perp z_{\rm cl}}(x) = \delta^{(2)}(\mathbf{k}_\perp - \mathbf{q}_\perp)\frac{e^{i(k_\parallel L)^3/3}}{(2\pi)^{1/2}}e^{-(i/\hbar)\varepsilon(\mathbf{q}_\perp z_{\rm cl})t} \tag{3.41}$$

yields

$$\tilde{G}(\mathbf{k},t;\mathbf{k}',t') = -\frac{i}{\hbar}\theta(\Delta t)\,\delta^{(1)}(\Delta k_\parallel + (|e|/\hbar)E\Delta t)\,\delta^{(2)}(\Delta\mathbf{k}_\perp) \times \exp\left[-(i/\hbar)\frac{\hbar^2}{2m}\left(\frac{k_\parallel^2 + k_\parallel k_\parallel' + k_\parallel'^2}{3} + \mathbf{k}_\perp^2\right)\Delta t\right] \tag{3.42}$$

after integration. $\hbar\mathbf{k}'$ describes the momentum of a free electron at time t' in the past and $\hbar\mathbf{k}$ describes the resulting momentum at time t after the influence of $\mathbf{E}$. The displacement in time is written as $\Delta t \equiv t - t'$ and momentum $\hbar\Delta\mathbf{k} = \hbar(\mathbf{k} - \mathbf{k}')$.

Using properties of the δ-distribution one immediately recognizes the expected classical equations of motion

$$\mathbf{F}_\perp = \frac{\Delta\mathbf{p}_\perp}{\Delta t} = \hbar\frac{\Delta\mathbf{k}_\perp}{\Delta t} = 0 \quad \text{and} \quad F_\parallel = \frac{\Delta p_\parallel}{\Delta t} = \hbar\frac{\Delta k_\parallel}{\Delta t} = -|e|E. \tag{3.43}$$

The δ-functions in Eq. (3.42) describe classical evolution of a single momentum state, while the phase factors correspond to quantum interferences due to initial states composed of multiple plane wave contributions (for example in an isolated wave-packet).

3.3.2 Asymptotic behavior

Determining the properties of an electron under the influence of a constant field far from the turning point is an important pre-requisite for describing strong field ionization. Since the Airy function (as we will soon see) tends towards zero as $e^{-\frac{2}{3}|x|^{3/2}}$, where $x = (z - z_{\mathrm{cl}})/L$, and therefore faster than the bound states which fall off as $e^{-\kappa r}$ one immediately recognizes that the asymptotic tail of the ground-state wave-function is most important for tunneling ionization. Steps taken here to describe the Airy function will later be applied to determine ionization rates in an alternating field [98, 136]. We may note that we intend to get results and gain intuition and not to provide a rigorous proof.

Defining

$$f(t) = tx - t^3/3 \tag{3.44}$$

we may apply the saddle point approximation to determine the behavior of $\mathrm{Ai}(x)$ in the limit of $x \to \pm\infty$. In section 3.2 we extracted the asymptotic behavior of an integral with an oscillatory integrand by finding a new contour where the integrand was slowly changing and decayed exponentially. Here we will do the same by deforming the contour of integration such that it passes through each value $t = t_s$ where $f'(t_s) = 0$. The exponent is approximated as $f(t) \approx f(t_s) + \frac{1}{2}f''(t_s)(\delta t)^2$ where $\delta t = t - t_s = \eta e^{i\phi_s}$ and ϕ_s is chosen such that the coefficient of η^2 becomes real. This corresponds to selecting contours such that $\mathrm{Im} f(t)$ is essentially constant (removing oscillations) and the integrand is built based on sharply-peaked Gaussian contributions corresponding to the approximation

$$y(z) = \sum_s e^{f(t_s)+i\phi_s} \int_{\mathbb{R}} d\eta\, e^{(\eta^2/2)f''(t_s)e^{2i\phi_s}} \tag{3.45}$$

for complex z. It is assumed that the integrand is sharply peaked at each t_s, where the precise shape of the contour is unimportant as long as it passes through the saddle points at an angle ϕ_s.

This procedure causes difficulties for the Airy function since

$$f'(t_s) = x - t_s^2 = 0 \to t_{s\pm} = \pm\sqrt{x}, \quad f''(t_{s\pm}) = \mp 2\sqrt{x}, \quad \text{and} \quad f(t_{s\pm}) = \pm\frac{2}{3}x^{3/2} \tag{3.46}$$

corresponds to a multi-valued integrand with branch cuts, where the original integrand was entire. Qualitatively, this imposes restrictions on which contours are allowed.

Starting with the relatively simple case of $x \to -\infty$ with

$$t_{s\pm} = \pm i\sqrt{|x|}, \quad f''(t_{s\pm}) = \pm 2i\sqrt{|x|}, \quad \text{and} \quad f(t_{s\pm}) = \mp i\frac{2}{3}|x|^{3/2} \tag{3.47}$$

we want the contour to start in the bottom-left shaded region and end up in the top-left shaded region of Fig. 3.4 while traveling along steepest descent curves through t_s defined by ϕ_s. Letting $x \to -\infty$ we have $\phi_{s-} = \pi/4$ and $\phi_{s+} = 3\pi/4$ where we may easily draw a contour from the bottom-left dark region through the saddle point t_{s-} at an angle of $\pi/4$ to $\sqrt{|x|}$ and then through the saddle point t_{s+} at an angle of $3\pi/4$ described in Fig. 3.4.

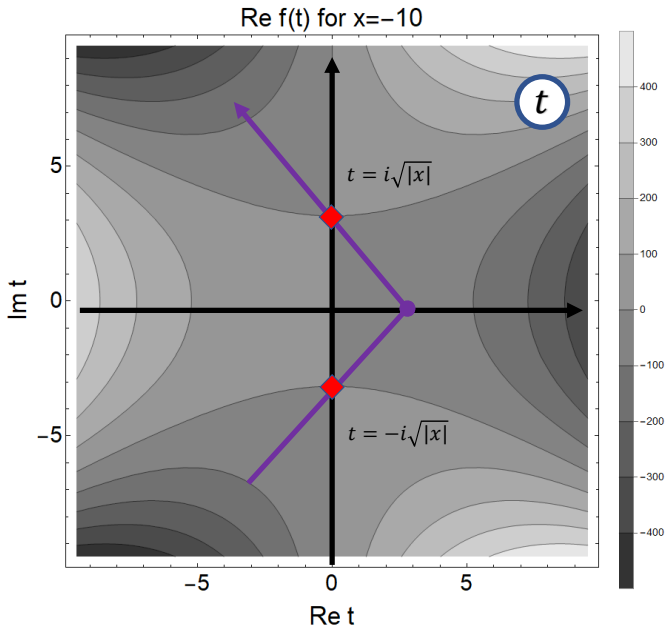

Figure 3.4: Plot of the real part of $f(t)$ where $t = t_r + it_i$. Integration contours connecting the bottom-left and top-left regions are chosen such that they pass through the saddle points in a direction that the imaginary part of the exponent is constant.

Near the origin of the contour, the real part of $f(t)$ is large and negative resulting in a small contribution to the total integral compared to contributions from the points $t_{s\pm}$ meaning that the precise orientation of the contour is unimportant far from the saddle points as long as they locally pass through the saddle points at an angle ϕ_s with respect to the real-axis. Along this first segment the integral therefore accumulates a partial contribution

$$\frac{1}{2\sqrt{\pi}i}|x|^{-1/4}\exp\left[i\left(\frac{2}{3}|x|^{3/2}+\frac{\pi}{4}\right)\right] \tag{3.48}$$

where we have assumed that the Gaussian is so sharply peaked that the bounds of integration for η may extend from minus infinity to infinity. The contour of integration lies between the large positive valued "ridges" of $\mathrm{Re}f(t)$.

After passing through t_{s-} the contour now resides in the right-most dark region where again the integrand is small and contributions can be neglected. To arrive at the desired top left shaded region we must pass through t_{s+} along a contour described by the angle ϕ_{s+} between the "ridges" of $\mathrm{Re}f(t)$ yielding the contribution

$$-\frac{1}{2\sqrt{\pi}i}|x|^{-1/4}\exp\left[-i\left(\frac{2}{3}|x|^{3/2}+\frac{\pi}{4}\right)\right]. \tag{3.49}$$

and the overall approximation

$$\mathrm{Ai}(x)\xrightarrow{x\to-\infty}\frac{1}{\sqrt{\pi}}|x|^{-1/4}\sin\left(\frac{2}{3}|x|^{3/2}+\frac{\pi}{4}\right). \tag{3.50}$$

For $x\to\infty$ the situation becomes more complicated. From

$$f'(t_s)=|x|-t_s^2=0\to t_{s\pm}=\pm\sqrt{|x|},\quad f''(t_{s\pm})=\mp2\sqrt{|x|},\quad\text{and}\quad f(t_{s\pm})=\pm\frac{2}{3}|x|^{3/2} \tag{3.51}$$

we immediately have that $\phi_{s+}=0$ and $\phi_{s-}=\pi/2$ corresponding to the yellow and purple curves in Fig. 3.5 where we again want to determine a suitable contour connecting the top left and bottom left triangular regions of Fig. 3.3. To achieve this goal we will determine contours where the imaginary part of the exponent is zero and which connect the two regions.

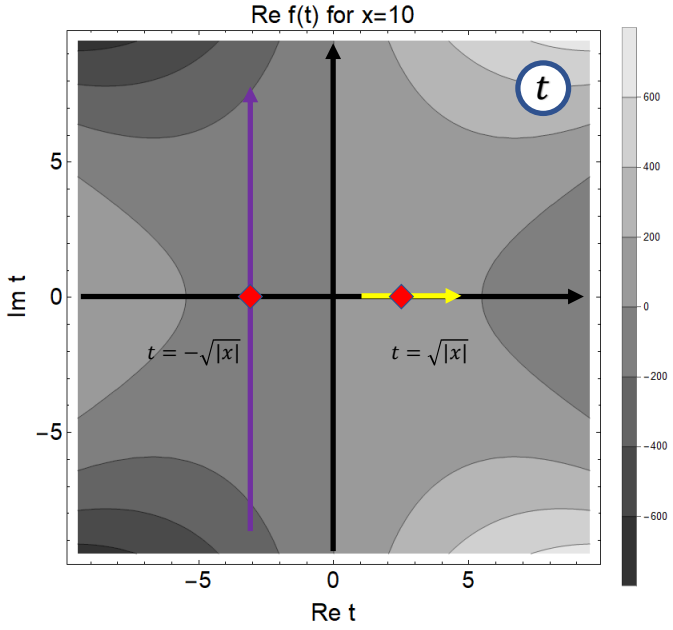

Figure 3.5: Plot of the real part of $f(t)$ where $t = t_r + it_i$. Integration contours connecting the bottom-left and top-left regions are chosen such that they pass through the saddle points in a direction that the imaginary part of the exponent is constant. Here only the saddle point at $t = -\sqrt{|x|}$ contributes to the integral since $t = \sqrt{|x|}$ connects the bottom left region to the right-most region describing divergent solutions.

Writing $t = t_r + it_i$ $(t_r, t_i \in \mathbb{R})$ we have

$$\mathrm{Im} f(t) = 0 \Rightarrow t_r = \pm\sqrt{x + t_i^2/3} \quad \text{or} \quad t_i = 0 \tag{3.52}$$

where only the solution $t_r = -\sqrt{x + t_i^2/3}$ connects the desired regions. Defining a contour which accumulates a contribution from $t = -\sqrt{|x|}$ connecting the bottom-left and top-left regions is straight forward. We may use the contour mentioned above to pass through the saddle point $t = -\sqrt{|x|}$. Since the integrand is essentially zero everywhere except through the saddle point we may replace the contour with a vertical line passing through t_{s-} and the job is done.

Deforming the contour such that it passes through $t = \sqrt{|x|}$ we are stuck in the right-most shaded region in Fig. 3.3, which describes exponentially divergent solutions to Airy's differential equation. The only way to return the contour back to the top-left region is by crossing "ridges"

perpendicular to $t = \sqrt{|x|}$ which is "forbidden". The approximation therefore only includes the solution corresponding to the saddle point $t = -\sqrt{|x|}$ along the path of "steepest descent" forming the approximation

$$\mathrm{Ai}(x) \xrightarrow{x->\infty} \frac{1}{2\sqrt{\pi}}|x|^{-1/4}e^{-\frac{2}{3}|x|^{3/2}} \tag{3.53}$$

Plotting $\mathrm{Ai}(x)$ with each of its asymptotic solutions, we see acceptable agreement as early as $|x| \gtrsim 2$ in Fig. 3.6.

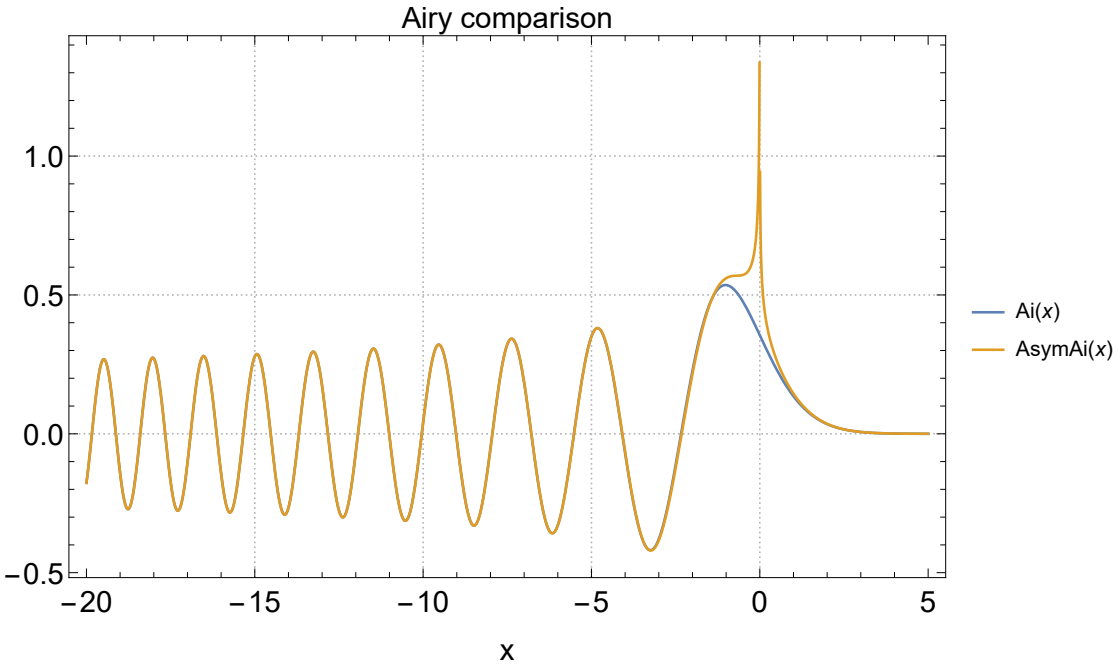

Figure 3.6: Airy function (blue), compared with the asymptotic approximations for $x \to \infty$ (Eq. (3.53), orange $x > 0$) and $x \to -\infty$ (Eq. (3.50), orange $x < 0$).

3.4 Ionization by a static field

In section 2.3 we have shown that modeling the ionization of Hydrogen by a static electric field is not possible at any order of (the standard) perturbation theory. In this section we will describe two different approaches towards ionization of an atom by a static electric field.

The first approach given by Oppenheimer essentially follows the golden rule expansion of

section 2.2 where the final scattering state has been replaced with states of an electron in a static field, as discussed in the prior section. Methods we will discuss later for ionization by dynamic fields follow this idea. The Airy functions in section 3.3 are replaced by the time-dependent states of an electron in a time-dependent field (section 3.5). For long-range potentials these methods require higher order corrections or additional modifications since the final state does not see the atomic potential.

The second approach which is able to predict the correct ionization rate for Hydrogen is given by Landau and Lifshitz. The final ionized state is described by the atomic ground-state whenever the atomic potential is significantly stronger than the field-interaction. The Wentzel–Kramers–Brillouin (WKB) approximation is used to include both the field-interaction and atomic potential wherever both contribute.

3.4.1 Oppenheimer's rate

In this section we will use states of the electron in a static field discussed in the prior section to approximate the static field rate. The original work [132] contained errors in the derivation. Later in Ref. [177] the corrected version was reported with no derivation. We will therefore systematically derive the corrected rate and find our own way to the results of Ref. [177]. Keldysh [98] (section 3.6.1) uses the exact same method to describe ionization of an atom in an alternating field where the Airy functions of section 3.3 are replaced by the Volkov states of section 3.5 which describe motion of an electron in a dynamic field. In Ref. [98] and similarly in Ref. [136] the ionization rate was derived using a similar contour deformation approach as discussed in section 3.2 and the saddle point approximation (see section 3.3.2) which is valid for sufficiently low laser frequencies. In our own work (chapter 5) we will generalize the work in Refs. [98, 132, 136] to arbitrary frequencies.

We start with the Hamiltonian

$$H(x) = H_{\mathrm{a}}(x) + V_{\mathrm{DC}}(\mathbf{r}) \tag{3.54}$$

which is partitioned into an atomic contribution and a field interaction

$$H_a(x) = \frac{\mathbf{p}^2}{2m} - Z\frac{|e|^2}{r}, \quad V_{\mathrm{DC}}(\mathbf{r}) = |e|\mathbf{E}\cdot\mathbf{r} \quad \text{and} \quad \mathbf{E} = E\hat{\mathbf{z}} \tag{3.55}$$

as before where the initial $1s$ state is given as

$$\phi_i(x) = e^{(i/\hbar)I_p t}\phi_i(\mathbf{r}) \quad \text{and} \quad \phi_i(\mathbf{r}) = \frac{\kappa^{3/2}}{\sqrt{\pi}}e^{-\kappa r}. \tag{3.56}$$

with ionization potential and bound-state κ-vector

$$I_p = \frac{\hbar^2\kappa^2}{2m} \quad \text{and} \quad \kappa \equiv mZ|e|^2/\hbar^2. \tag{3.57}$$

The rate is determined by expressing the exact wave function $\Psi(x)$ with the initial-state Lippmann Schwinger equation where

$$\Psi(x) = \phi_i(x) + \int d^4x_1 G(x;x_1)[|e|\mathbf{E}\cdot\mathbf{r}_1]\phi_i(x_1). \tag{3.58}$$

In the standard perturbation theory one would continue by expanding the exact Green's function $G(x;x_1)$ up to higher orders with respect to the atomic Green's function $G_{\mathrm{a}}(x;x')$ of $H_{\mathrm{a}}(x)$ and rest interaction $[|e|\mathbf{E}\cdot\mathbf{r}]$. Unfortunately, such a perturbation series breaks down as described in the prior section and therefore an alternative expansion is required.

Oppenheimer's approach involved now expressing $G(x;x_1)$ by the final-state Lippmann Schwinger equation

$$G(x;x_1) = G_{\mathrm{DC}}(x;x_1) + \int d^4x_2\, G_{\mathrm{DC}}(x;x_2)\left[-Z\frac{|e|^2}{r_2}\right]G(x_2;x_1) \tag{3.59}$$

where $G_{\mathrm{DC}}(x;x')$ describes the otherwise free propagation of an electron in a static field corresponding to

$$H_{\mathrm{DC}}(x) = \frac{\mathbf{p}^2}{2m} + |e|\mathbf{E}\cdot\mathbf{r} \tag{3.60}$$

as discussed in a prior section.

Setting $G(x_2;x_1) \approx G_{\mathrm{DC}}(x_2;x_1)$ we immediately arrive at the first and second order correction

$$\Psi^{(1)}(x) = \int d^4x_1\, G_{\mathrm{DC}}(x;x_1)[|e|\mathbf{E}\cdot\mathbf{r}_1]\phi_i(x_1) \tag{3.61}$$

and

$$\Psi^{(2)}(x) = \int d^4x_2\, G_{\rm DC}(x;x_2)\left[-Z\frac{|e|^2}{r_2}\right]\int d^4x_1\, G_{\rm DC}(x_2;x_1)[|e|\mathbf{E}\cdot\mathbf{r}_1]\phi_i(x_1) \tag{3.62}$$

as given in Ref. [132]. Here, $\Psi^{(1)}(x)$ intuitively describes the transition of the initial ground state $\phi_i(x)$ into a free particle state accelerating down the $|e|\mathbf{E}\cdot\mathbf{r}$ potential surface, while $\Psi^{(2)}(x)$ describes the same exact process where the ejected electron may scatter once of the atomic potential $-Z|e|^2/r$ before again propagating as a free particle down the surface $|e|\mathbf{E}\cdot\mathbf{r}$. $G(x;x')$ can be expanded up to arbitrary order in $-Z|e|^2/r$ although convergence is not guaranteed (just as in any perturbation series). Although the first and second order terms were introduced in Ref. [132] only the first order contribution was considered.

The rate is determined by considering

$$\mathcal{M}(\mathbf{k}_\perp, z_{\rm cl}, t) \equiv \int_{\mathbb{R}^3} d\mathbf{r}\,\overline{\Phi_{\mathbf{k}_\perp z_{\rm cl}}(x)}\,[\Psi(x)-\phi_i(x)] \approx \mathcal{M}^{(1)}(\mathbf{k}_\perp, z_{\rm cl}, t) \tag{3.63}$$

which corresponds to

$$\begin{aligned}\mathcal{M}^{(1)}(\mathbf{k}_\perp, z_{\rm cl}, t) &= \left(-\frac{i}{\hbar}\right)\int d^4x_1\,\overline{\Phi_{\mathbf{k}_\perp z_{\rm cl}}(x_1)}\,[|e|\mathbf{E}\cdot\mathbf{r}_1]\,\phi_i(x_1)\\ &= \left(-\frac{i}{\hbar}\right)\int_0^t dt_1 V_i(\mathbf{k}_\perp, z_{\rm cl})\, e^{(i/\hbar)\Delta\varepsilon(\mathbf{k}_\perp, z_{\rm cl})t_1}\end{aligned} \tag{3.64}$$

where

$$\Delta\varepsilon(\mathbf{k}_\perp, z_{tp}) \equiv \varepsilon_\perp + \varepsilon_\parallel + I_p \tag{3.65}$$

and

$$V_i(\mathbf{k}_\perp, z_{\rm cl}) \equiv \int d\mathbf{r}\,\overline{\Phi_{\mathbf{k}_\perp z_{\rm cl}}(\mathbf{r})}\,[|e|\mathbf{E}\cdot\mathbf{r}]\,\phi_i(\mathbf{r}). \tag{3.66}$$

Time-integration may be immediately performed as

$$\int_0^t dt_1 e^{(i/\hbar)\Delta\varepsilon t} = e^{(i/\hbar)\Delta\varepsilon t/2}\mathrm{sinc}((1/\hbar)\Delta\varepsilon t/2)t \equiv \delta_t((1/\hbar)\Delta\varepsilon/2)\,, \tag{3.67}$$

where in the $t\to\infty$ limit the energy conservation law

$$z_{\rm cl} = -\frac{1}{|e|E}\left(\varepsilon_\perp + I_p\right) < 0 \tag{3.68}$$

is satisfied. Electrons have zero parallel velocity at the tunnel exit and as the perpendicular momentum at ionization, $\mathbf{k}_\perp^2$, increases, states corresponding to the classical turning points $z_{\rm cl}$ are pushed further away from the Coulomb potential. For $\varepsilon_\perp = 0$, Fig. 3.7 shows the atomic potential and the laser interaction as well as the initial- and final-state wave-functions for $F = 0.05$ a.u..

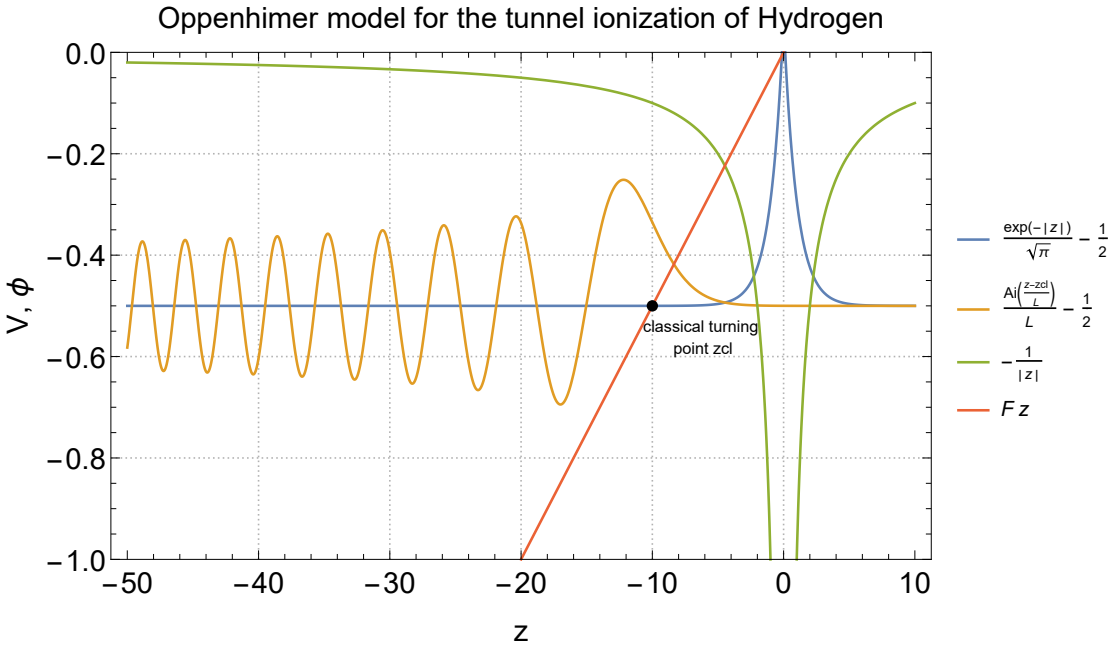

Figure 3.7: Sketch of components required to compute the Oppenheimer rate. Blue represents the initial $1s$ state of hydrogen atom, orange shows the final continuum state $\Phi_{\mathbf{k}_\perp, z_{\rm cl}}(\mathbf{r})$ (with $\mathbf{k}_\perp = 0$), green represents the field free Coulomb potential and red depicts the DC Stark potential. The classical turning point $z_{\rm cl} = -10$ a.u. is noted for a field-strength of $F = 0.05$ a.u.. For $F \to 0$ ionization is determined by the tail of the initial bound-state alone (Eq. (3.92)).

Completing the amplitude involves computing the overlap matrix element

$$V_i(\mathbf{k}_\perp, z_{\rm cl}) = \int_{\mathbb{R}^2} d\mathbf{r}_\perp \frac{e^{-i\mathbf{k}_\perp\cdot\mathbf{r}_\perp}}{(2\pi)} \int_{\mathbb{R}} dz \frac{1}{L} \mathrm{Ai}\left[(z - z_{\rm cl})/L\right] \left[|e|Ez\right] \frac{\kappa^{3/2}}{\sqrt{\pi}} e^{-\kappa\sqrt{r_\perp^2 + z^2}}. \tag{3.69}$$

For the $1s$-state of Hydrogen, the ionization amplitude in the perpendicular $\mathbf{r}_\perp$ direction has cylin-

drical symmetry around the z-axis allowing for the simplification

$$\int_{\mathbb{R}^2} d\mathbf{r}_\perp \frac{e^{-i\mathbf{k}_\perp\cdot\mathbf{r}_\perp}}{(2\pi)} = \sum_{m=-\infty}^{\infty}(-i)^m \int_0^\infty dr_\perp r_\perp J_m(k_\perp r_\perp)\int_{-\pi}^{\pi}\frac{d\varphi_r}{(2\pi)}e^{im(\varphi_k-\varphi_r)} = \int_0^\infty dr_\perp r_\perp J_0(k_\perp r_\perp). \tag{3.70}$$

Utilizing Ref. [69]

$$\int_1^\infty dx\, J(\alpha\sqrt{x^2-1})e^{-\beta x} = \frac{1}{\sqrt{\alpha^2+\beta^2}}e^{-\sqrt{\alpha^2+\beta^2}}, \tag{3.71}$$

the perpendicular contribution

$$\begin{aligned}\int_0^\infty dr_\perp r_\perp J_0(k_\perp r_\perp)e^{-\kappa\sqrt{r_\perp^2+z^2}} &= \left(-\frac{\partial}{\partial\kappa}\right)\int_{|z|}^\infty dr\, J_0(k_\perp\sqrt{r^2-z^2})e^{-\kappa r}\\ &= |z|\left(-\frac{\partial}{\partial\kappa}\right)\int_1^\infty du\, J_0(k_\perp|z|\sqrt{u^2-1})e^{-\kappa|z|u} = \frac{\kappa}{k_\perp^2+\kappa^2}\left[|z|+\frac{1}{\sqrt{k_\perp^2+\kappa^2}}\right]e^{-\sqrt{k_\perp^2+\kappa^2}|z|}\end{aligned} \tag{3.72}$$

is complete.

Defining $K \equiv \sqrt{k_\perp^2+\kappa^2}$, the final parallel contribution

$$V_i(\mathbf{k}_\perp, z_{\rm cl}) = \frac{|e|E}{\sqrt{\pi}}\frac{\kappa^{5/2}}{K^2}\left(\frac{1}{K}-\frac{\partial}{\partial K}\right)\int_{\mathbb{R}} dz\, z\,\frac{1}{L}\mathrm{Ai}\left[(z-z_{\rm cl})/L\right]e^{-K|z|}\Big|_{K=\sqrt{k_\perp^2+\kappa^2}} \tag{3.73}$$

must now be computed. The integral over z is evaluated by using the variable substitution $u = (z-z_{\rm cl})/L$:

$$\int_{\mathbb{R}} dz\, z\,\frac{1}{L}\mathrm{Ai}\left[(z-z_{\rm cl})/L\right]e^{-K|z|} = \int_{\mathbb{R}} du\,(Lu-|z_{\rm cl}|)\mathrm{Ai}(u)e^{-K|Lu+z_{\rm cl}|} \tag{3.74}$$

and partitioning the integral into two parts:

$$\begin{aligned}&\int_{\mathbb{R}} du\,(Lu-|z_{\rm cl}|)\mathrm{Ai}(u)e^{-K|Lu+z_{\rm cl}|}\\ &\qquad = \frac{\partial}{\partial K}\left[e^{-K|z_{\rm cl}|}\int_{-\infty}^{|z_{\rm cl}|/L} du\,\mathrm{Ai}(u)e^{KLu} - e^{K|z_{\rm cl}|}\int_{|z_{\rm cl}|/L}^{\infty} du\,\mathrm{Ai}(u)e^{-KLu}\right]\end{aligned} \tag{3.75}$$

corresponding to each piecewise portion of $|z|$. The second integral from $|z_{\rm cl}|/L$ to infinity may be neglected in the weak field $E\to 0$ limit where the bound of integration $|z_{\rm cl}|/L$ goes to positive infinity and the magnitude of the Airy function falls off faster than $Ae^{-\alpha u}$ for all $A,\alpha>0$ as $u\to\infty$ since

$$\mathrm{Ai}(u) \xrightarrow{u\to-\infty} \frac{1}{2\sqrt{\pi}}|u|^{-1/4}e^{-\frac{2}{3}|u|^{3/2}}. \tag{3.76}$$

The first integral is evaluated with the help of the Heaviside step function

$$\theta(|z_{\rm cl}| - Lu) = \lim_{\eta\to 0^+} \frac{1}{2\pi i}\int_{\mathbb{R}} \frac{d\tau}{\tau - i\eta} e^{i(|z_{\rm cl}|-Lu)\tau} \tag{3.77}$$

to give

$$\int_{\mathbb{R}} du\, \mathrm{Ai}(u) e^{pu} = e^{p^3/3} \tag{3.78}$$

where

$$\int_{-\infty}^{|z_{\rm cl}|/L} du\, \mathrm{Ai}(u) e^{KLu} = \lim_{\eta\to 0^+} \frac{1}{2\pi i}\int_{\mathbb{R}} \frac{d\tau}{\tau - i\eta} e^{i|z_{\rm cl}|\tau} e^{[(K-i\tau)L]^3/3} = \frac{1}{2} e^{(KL)^3/3}. \tag{3.79}$$

In Eq. (3.79) the integral over τ was determined using the Sokhotski–Plemelj theorem [125,139,154]

$$\lim_{\eta\to 0^+} \frac{-i}{x - i\eta} = \pi\delta(x) - i\,\mathrm{p.v.}\frac{1}{x}. \tag{3.80}$$

where we will show that the term corresponding to the Cauchy principal value (p.v.) is negligible in the $E \to 0$ limit.

Here

$$\mathrm{p.v.}\int_{\mathbb{R}} \frac{d\tau}{\tau} e^{i|z_{\rm cl}|\tau} e^{[(K-i\tau)L]^3/3} = e^{(KL)^3/3}\,\mathrm{p.v.}\int_{\mathbb{R}} \frac{d\tau}{\tau}\, e^{i(|z_{\rm cl}|-K^2L^3)\tau} e^{i(\tau L)^3/3} e^{-L^3K\tau^2}. \tag{3.81}$$

To show that this term is negligible one must consider that the p.v. integral after the $e^{(KL)^3/3}$ factor on the right hand side is significantly smaller than $1/2$. Since the overall integral is real we should expect that the real part of the p.v. integral is identically zero. Explicitly writing it out we have

$$\begin{aligned}\mathrm{Re}\left[\mathrm{p.v.}\int_{\mathbb{R}} \frac{d\tau}{\tau}\, e^{i(|z_{\rm cl}|-K^2L^3)\tau} e^{i(\tau L)^3/3} e^{-L^3K\tau^2}\right] \\ = \mathrm{p.v.}\int_{\mathbb{R}} \frac{d\tau}{\tau}\, \cos[(|z_{\rm cl}| - K^2L^3)\tau + (\tau L)^3/3] e^{-L^3K\tau^2}\end{aligned} \tag{3.82}$$

which is zero since we have an odd integrand over an even interval.

Investigating the imaginary part we have

$$\begin{aligned}\mathrm{Im}\left[\mathrm{p.v.}\int_{\mathbb{R}} \frac{d\tau}{\tau}\, e^{i(|z_{\rm cl}|-K^2L^3)\tau} e^{i(\tau L)^3/3} e^{-L^3K\tau^2}\right] \\ = \int_{\mathbb{R}} \frac{d\tau}{\tau}\, \sin[(|z_{\rm cl}| - K^2L^3)\tau + (\tau L)^3/3] e^{-L^3K\tau^2}.\end{aligned} \tag{3.83}$$

Since the sin-function has a zero at $\tau = 0$, the first order pole exactly cancels out.

To the best of our knowledge, there is no analytic solution to this integral, therefore we will bound it from above and show that as $E \to 0$ the integral goes to zero. Starting with the triangle inequality

$$\left| \int_{\mathbb{R}} \frac{d\tau}{\tau} \sin[(|z_{\rm cl}| - K^2L^3)\tau + (\tau L)^3/3] e^{-L^3 K\tau^2} \right| \leq \int_{\mathbb{R}} \frac{d\tau}{|\tau|} \left| \sin[(|z_{\rm cl}| - K^2L^3)\tau + (\tau L)^3/3] \right| e^{-L^3 K\tau^2} \tag{3.84}$$

and replacing the $|\sin(\cdots)/\tau|$ factor by its maximum value M we have

$$\int_{\mathbb{R}} \frac{d\tau}{|\tau|} \left| \sin[(|z_{\rm cl}| - K^2L^3)\tau + (\tau L)^3/3] \right| e^{-L^3 K\tau^2} \leq M \int_{\mathbb{R}} d\tau e^{-L^3 K\tau^2} = M\sqrt{\frac{\pi}{KL^3}}. \tag{3.85}$$

Taking $E \to 0$ we have $L \to \infty$ and therefore the principal value contribution is negligble.

Applying Eq. (3.68) the matrix element is given by

$$V_i(\mathbf{k}_\perp, z_{\rm cl}) = -\frac{\kappa^{1/2}}{\sqrt{\pi}} \frac{I_p}{K} e^{-\frac{2}{3}K|z_{\rm cl}|} \equiv V_i(k_\perp). \tag{3.86}$$

Computing then the ionization rate

$$w = \lim_{t\to\infty} \int_{\mathbb{R}^2} d\mathbf{k}_\perp \int_{\mathbb{R}} dz_{\rm cl} \frac{\partial}{\partial t} |\mathcal{M}^{(1)}(\mathbf{k}_\perp, z_{\rm cl}, t)|^2 \tag{3.87}$$

we have

$$\begin{aligned} w = \frac{2\pi}{\hbar} \int_{\mathbb{R}^2} d\mathbf{k}_\perp \int_{\mathbb{R}} dz_{\rm cl} \, |V_i(\mathbf{k}_\perp, z_{\rm cl})|^2 \, \delta(\varepsilon_\perp + \varepsilon_\parallel + I_p) &= \frac{(2\pi)^2}{|e|E\hbar} \int_0^\infty dk_\perp k_\perp \, |V_i(k_\perp)|^2 \\ &= \frac{4\pi^2 m}{|e|E\hbar^3} \int_0^\infty d\varepsilon_\perp |V_i(k_\perp)|^2 \approx \frac{4\pi m}{|e|E\hbar^3} \frac{I_p^2}{\kappa} \int_0^\infty d\varepsilon_\perp e^{-\frac{4}{3}K|z_{\rm cl}|} \end{aligned} \tag{3.88}$$

where in the prefactor we set $K \approx \kappa$ since the exponential factor is sharply peaked at $\varepsilon_\perp = 0$.

Integration is now performed by writing

$$\frac{4}{3}K|z_{\rm cl}| \approx \frac{4}{3}\frac{I_p}{|e|Ea} + 2\frac{\varepsilon_\perp}{|e|Ea} \tag{3.89}$$

which yields

$$w = \pi \left(\frac{I_p}{\hbar}\right) e^{-\frac{4}{3}\frac{I_p}{|e|Ea}} \text{"}=\text{"} \frac{\pi}{2} e^{-2/3F} \tag{3.90}$$

where the "=" symbol denotes that the right-hand side is expressed in atomic units. Here the total ionization rate, as shown in Fig. 3.8, is exponentially proportional to $1/F$.

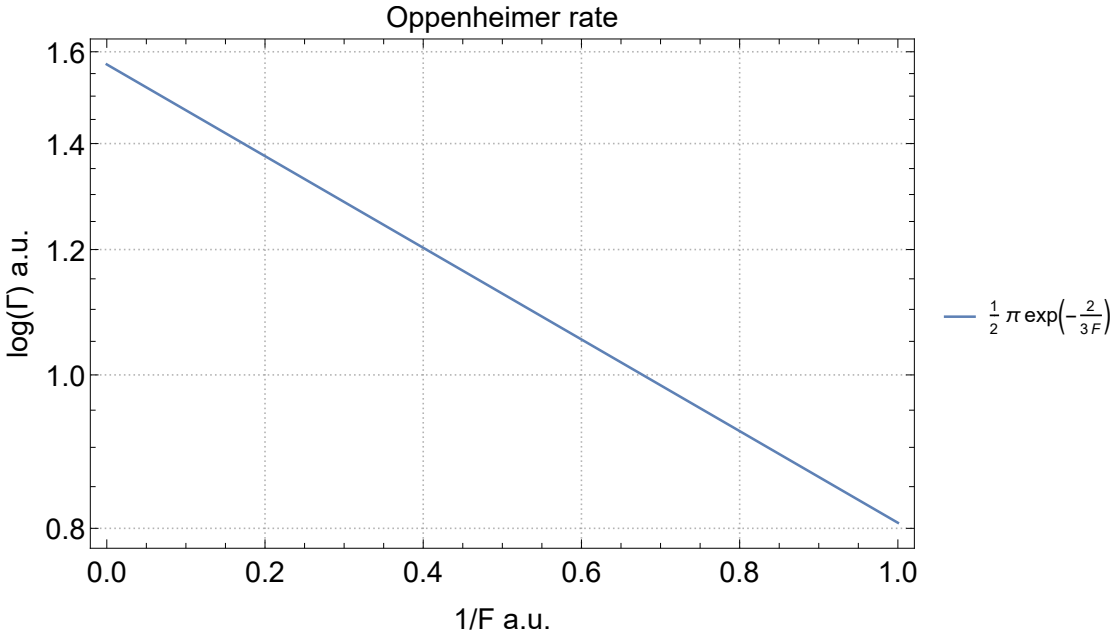

Figure 3.8: Ionization rate $\Gamma \equiv w$ of Oppenheimer as a function of $1/F$ in atomic units.

This first approximation of at an ionization rate in a static field predicts the correct exponential dependence in the $F \to 0$ limit, but contains an incorrect pre-factor since the Coulomb potential is neglected in the final continuum states, which will be explored further in section 3.4.2.

3.4.1.1 Final state form

In section 3.6.2 we will discuss a so-called final state ionization amplitude which uses $-Z|e|^2/r$ as a perturbation instead of $|e|\mathbf{E}\cdot\mathbf{r}$ in the case of an alternating field. Here,

$$\mathcal{M}^{(1)}(\mathbf{k}_\perp, z_{\rm cl}, t) = \left(-\frac{i}{\hbar}\right)\int d^4x_1\, \overline{\Phi_{\mathbf{k}_\perp z_{\rm cl}}(x_1)}\left[-Z\frac{|e|^2}{r_1}\right]\phi_i(x_1)$$
$$= \left(-\frac{i}{\hbar}\right)\int_0^t dt_1 V_i(\mathbf{k}_\perp, z_{\rm cl})\, e^{(i/\hbar)\Delta\varepsilon(\mathbf{k}_\perp, z_{\rm cl})t_1}. \quad (3.91)$$

represents the equivalent final state amplitude for the case of a static electric field. Setting $Z|e|^2 = 2I_p/\kappa$ we have

$$V_i(\mathbf{k}_\perp, z_{\rm cl}) \equiv \int d\mathbf{r}\, \overline{\Phi_{\mathbf{k}_\perp z_{\rm cl}}(\mathbf{r})}\left[-2\frac{I_p}{\kappa r}\right]\phi_i(\mathbf{r}) \tag{3.92}$$

and

$$\begin{aligned} V_i(\mathbf{k}_\perp, z_{\rm cl}) &= \int_{\mathbb{R}^2} d\mathbf{r}_\perp \frac{e^{-i\mathbf{k}_\perp\cdot\mathbf{r}_\perp}}{(2\pi)} \int_{\mathbb{R}} dz \frac{1}{L}\mathrm{Ai}\left[(z-z_{\rm cl})/L\right]\left[-2\frac{I_p}{\kappa\sqrt{r_\perp^2+z^2}}\right]\frac{\kappa^{3/2}}{\sqrt{\pi}} e^{-\kappa\sqrt{r_\perp^2+z^2}} \\ &= \int_{\mathbb{R}} dz \frac{1}{L}\mathrm{Ai}\left[(z-z_{\rm cl})/L\right]\left[-2\frac{I_p}{\kappa K}\right]\frac{\kappa^{3/2}}{\sqrt{\pi}} e^{-K|z|} = -\frac{\kappa^{1/2}}{\sqrt{\pi}}\frac{I_p}{K} e^{-\frac{2}{3}K|z_{\rm cl}|} \end{aligned} \tag{3.93}$$

exactly as before leading to the same rate

$$w = \frac{\pi}{\hbar} I_p\, e^{-\frac{4}{3}\frac{I_p}{|e|Ea}}. \tag{3.94}$$

In section 3.6.2.1 we show that initial state and final state amplitudes will also be identical for the case of an arbitrary alternating electric field. If the final state is modified to account for the atomic potential, this property does not hold in general.

3.4.2 Landau and Lifshitz rate: Correcting the pre-factor

The rate derived by Oppenheimer predicted the correct weak-field exponential factor with an incorrect proportionality constant. Landau and Lifshitz improved the pre-factor by including both the atomic Coulomb potential and the applied field within the final state through the quasi-classical WKB approximation [34,72,89,103,111,171]. The method requires determining the ground state of hydrogen atom in parabolic coordinates and then determining regions of the wave function modified with the quasi-classical approximation by the applied field.

3.4.2.1 Parabolic coordinates

The transformation to parabolic coordinates from the Cartesian system [107] involves

$$\xi = r + z, \quad \eta = r - z, \quad \varphi = \tan^{-1}(y/x). \tag{3.95}$$

with backwards transformation

$$x = \sqrt{\xi\eta}\cos\varphi, \quad y = \sqrt{\xi\eta}\sin\varphi, \quad z = \frac{1}{2}(\xi - \eta) \tag{3.96}$$

and

$$r = \sqrt{x^2 + y^2 + z^2} = \frac{1}{2}(\xi + \eta). \tag{3.97}$$

In this system the length element is determined by

$$(dl)^2 = \frac{\xi + \eta}{4\xi}(d\xi)^2 + \frac{\xi + \eta}{4\eta}(d\eta)^2 + \xi\eta(d\varphi)^2 \tag{3.98}$$

and the volume element is given by

$$d\mathbf{r} = \frac{1}{4}(\xi + \eta)d\xi d\eta d\varphi. \tag{3.99}$$

Determining the atomic states requires the Laplacian

$$\nabla^2 = \frac{4}{\xi + \eta}\left[\frac{\partial}{\partial\xi}\left(\xi\frac{\partial}{\partial\xi}\right) + \frac{\partial}{\partial\eta}\left(\eta\frac{\partial}{\partial\eta}\right)\right] + \frac{1}{\xi\eta}\frac{\partial^2}{\partial\varphi^2} \tag{3.100}$$

which gives for the Schrödinger equation

$$\frac{4}{\xi + \eta}\left[\frac{\partial}{\partial\xi}\left(\xi\frac{\partial\phi(\mathbf{r})}{\partial\xi}\right) + \frac{\partial}{\partial\eta}\left(\eta\frac{\partial\phi(\mathbf{r})}{\partial\eta}\right)\right] + \frac{1}{\xi\eta}\frac{\partial^2\phi(\mathbf{r})}{\partial\varphi^2} + 2\left(E + \frac{2}{\xi + \eta}\right)\phi(\mathbf{r}) = 0. \tag{3.101}$$

Writing

$$\phi(\mathbf{r}) = f_1(\xi)f_2(\eta)e^{im\varphi} \tag{3.102}$$

separation of variables may be applied giving

$$\frac{d}{d\xi}\left(\xi\frac{df_1(\xi)}{d\xi}\right) + \left[\frac{1}{2}E\xi - \frac{1}{4}m^2/\xi + \beta_1\right]f_1(\xi) = 0 \tag{3.103}$$

and

$$\frac{d}{d\eta}\left(\eta\frac{df_2(\eta)}{d\eta}\right) + \left[\frac{1}{2}E\eta - \frac{1}{4}m^2/\eta + \beta_2\right]f_2(\eta) = 0 \tag{3.104}$$

with separation parameters described by

$$\beta_1 + \beta_2 = 1. \tag{3.105}$$

Defining parameters

$$n = 1/\sqrt{-2E}, \quad \rho_1 = \xi/n, \quad \rho_2 = \eta/n \tag{3.106}$$

we have

$$\frac{d^2 f_1(\xi)}{d\xi^2} + \frac{1}{\rho_1}\frac{df_1(\xi)}{d\xi} + \left[-\frac{1}{4} + \frac{1}{\rho_1}\left(\frac{|m|+1}{2} + n_1\right) - \frac{m^2}{4\rho_1^2}\right] f_1(\xi) = 0 \tag{3.107}$$

and a similar expression for $f_2(\eta)$.

Solving exactly as in the spherical-polar case before we get

$$\phi_{n_1,n_2,m}(\mathbf{r}) = \frac{\sqrt{2}}{n^2} f_{n_1,m}\left(\frac{\xi}{n}\right) f_{n_2,m}\left(\frac{\eta}{n}\right)\frac{e^{im\varphi}}{\sqrt{2\pi}} \tag{3.108}$$

with

$$f_{p,m}(\rho) = \frac{1}{|m|!}\sqrt{\frac{(p+|m|)!}{p!}}\,{}_1F_1(-p;|m|+1;\rho)e^{-\rho/2}\rho^{|m|/2} \tag{3.109}$$

and the ground state given by

$$\phi_{1s}(\mathbf{r}) = \frac{1}{\sqrt{\pi}} e^{-\frac{1}{2}(\xi+\eta)} \tag{3.110}$$

3.4.2.2 Hydrogen rate

The initial state

$$\psi(\mathbf{r}) = \frac{1}{\sqrt{\pi}} e^{-\frac{1}{2}(\xi+\eta)} \tag{3.111}$$

from the earlier subsection is the starting point of the approximation. Far from the atom the Schrödinger equation

$$\frac{d^2\chi}{d\eta^2} + \left[-\frac{1}{4} + \frac{1}{2\eta} + \frac{1}{4\eta^2} + \frac{1}{4}F\eta\right]\chi = 0 \tag{3.112}$$

now includes the laser interaction where $\chi = \sqrt{\eta}\psi$. Choosing some point $1 \ll \eta_0 \ll 1/F$ within the barrier and applying the WKB approximation one has

$$\chi = \sqrt{\frac{\eta_0|p_0|}{\pi p}}\exp\left(\frac{\chi+\eta_0}{2} + i\int_{\eta_0}^{\eta_1} p\,d\eta + \frac{1}{4}i\pi\right) \tag{3.113}$$

with momentum $p(\eta_1) = 0$ at the tunnel exit and

$$p(\eta) = \sqrt{-\frac{1}{4} + \frac{1}{2\eta} + \frac{1}{4\eta^2} + \frac{1}{4}F\eta} \approx \frac{1}{2}\sqrt{F\eta - 1} - \frac{1}{2\eta\sqrt{F\eta - 1}} \tag{3.114}$$

within the barrier.

Taking the square

$$|\chi|^2 = \frac{\eta_0}{\pi} e^{-\xi} \frac{|p_0|}{p} \exp\left[-2\int_{\eta_0}^{\eta_1} |p(\eta')| d\eta' - \eta_0\right] \tag{3.115}$$

and using $|p_0| \approx \frac{1}{2}$ one has

$$|\chi|^2 = \frac{\eta_0}{\pi\sqrt{F\eta - 1}} e^{-\xi} \exp\left[-\int_{\eta_0}^{\eta_1} \sqrt{1 - F\eta'} d\eta' + \int_{\eta_0}^{\eta_1} \frac{d\eta'}{\eta'\sqrt{1 - F\eta'}} - \eta_0\right] \tag{3.116}$$

where the first term of Eq. 3.114 has been used to approximate p in the prefactor and both terms have been retained within the exponent.

Integrating and using $F\eta_0 \ll 1$ whenever possible

$$|\chi|^2 = \frac{4}{\pi F} e^{-2/3F} \frac{e^{-\xi}}{\sqrt{F\eta - 1}} \tag{3.117}$$

may be used to give the total rate

$$w = 2\pi \int_0^\infty dr\, r\, v_z |\psi|^2 \tag{3.118}$$

where

$$dr \approx \frac{1}{2}\sqrt{\frac{\eta}{\xi}} d\xi, \quad v_z = \sqrt{F\eta - 1} \tag{3.119}$$

and

$$w = \frac{4}{F} e^{-2/3F}. \tag{3.120}$$

Restoring units the ionization becomes ($a = 1/\kappa$)

$$w = 16\left(\frac{I_p}{\hbar}\right)\left(\frac{I_p}{|e|Ea}\right) \exp\left(-\frac{4}{3}\frac{I_p}{|e|Ea}\right) \tag{3.121}$$

which has the same exponential factor as the ionization rate of section 3.4.1 with the correct weak-field prefactor $4/F$ [177].

3.4.2.3 Short-range rate

The same procedure may now be followed for short-range potentials. The short-range asymptotic ground state

$$\psi(\mathbf{r}) = \frac{1}{2} C_{\kappa,0} \sqrt{\frac{\kappa}{\pi}} \frac{e^{-\kappa r}}{r} = C_{\kappa,0} \sqrt{\frac{\kappa}{\pi}} \frac{e^{-\frac{\kappa}{2}(\xi+\eta)}}{\xi + \eta} \approx C_{\kappa,0} \sqrt{\frac{\kappa}{\pi}} \frac{e^{-\frac{\kappa}{2}(\xi+\eta)}}{\eta} \tag{3.122}$$

is used and gives

$$w = \frac{1}{4}C_{\kappa,0}^2 F e^{-2/3F} = \frac{1}{4}C_{\kappa,0}^2 \frac{|e|E}{\hbar\kappa}\exp\left(-\frac{4}{3}\frac{I_p}{|e|Ea}\right) \tag{3.123}$$

where $C_{\kappa,0}$ is fit to the asymptotic tail of the field-free ground-state. The exponential factor is a general property of ionization of particles bound by both long- and short-range potentials, while the prefactor is determined by properties of the binding potential.

3.5 Motion in a dynamic field: Volkov states

In section 3.3 we solved Airy's differential equation to determine the dynamics of an otherwise free electron in an external electric field. These states were applied by Oppenheimer [132] (section 3.4.1) to determine an estimate for the ionization rate of Hydrogen. We now will follow the same steps as in section 3.3 to determine the behavior of a free electron experiencing an arbitrary time-dependent field. In the next subsection 3.6.1 we will follow the derivation by Keldysh [98] to apply exactly the same method as in Ref. [132] and determine an estimate for the ionization of Hydrogen by a linearly polarized field. The so-called Volkov states form the basis for many standard non-perturbative approaches [57, 98, 136, 146] including our own generalization of Ref. [98] which will be discussed in Chapter 5.

Motion of an otherwise free electron interacting with a time-dependent electric field is described by the Schrödinger equation

$$i\hbar\frac{\partial}{\partial t}\Phi(\mathbf{r}) = \left[\frac{\mathbf{p}^2}{2m} + |e|\mathbf{E}(t)\cdot\mathbf{r}\right]\Phi(\mathbf{r}). \tag{3.124}$$

Recognizing that

$$\mathbf{E}(t) = -\frac{1}{c}\frac{\partial}{\partial t}\mathbf{A}(t) \quad \text{and} \quad i\hbar\frac{\partial}{\partial t}e^{\frac{i|e|}{\hbar c}\mathbf{A}(t)\cdot\mathbf{r}} = \left[|e|\mathbf{E}(t)\cdot\mathbf{r}\right]e^{\frac{i|e|}{\hbar c}\mathbf{A}(t)\cdot\mathbf{r}} \tag{3.125}$$

we immediately see that the set of solutions must follow the form

$$\Phi_{\mathbf{k}}(x) = T(t)\frac{e^{i\mathbf{k}(t)\cdot\mathbf{r}}}{(2\pi)^{3/2}} \tag{3.126}$$

where

$$\mathbf{k}(t) = \mathbf{k} + \frac{|e|}{\hbar c}\mathbf{A}(t) \tag{3.127}$$

is the kinetic momentum of an electron in the field. Inserting this solution one obtains the Schrödinger equation

$$i\hbar\frac{\partial}{\partial t}T(t) = \frac{\hbar^2 k(t)^2}{2m}T(t) \tag{3.128}$$

and the states

$$\Phi_{\mathbf{k}}(x) = e^{-(i/\hbar)\int_0^t d\tau \frac{\hbar^2 k^2(\tau)}{2m}} \frac{e^{i\mathbf{k}(t)\cdot\mathbf{r}}}{(2\pi)^{3/2}}. \tag{3.129}$$

3.5.1 Newton's second law

In this subsection we will use the momentum-space Green's function $\tilde{G}(\mathbf{k},t;\mathbf{k}',t')$ of Eq. 3.19 to recover the classical equation of motion

$$m\mathbf{a}(t) = -|e|\mathbf{E}(t). \tag{3.130}$$

Starting with the Volkov states $\Phi_{\mathbf{k}}(x)$ we may write the position-basis Green's function as

$$G(x;x') = -\frac{i}{\hbar}\theta(t-t')\int_{\mathbb{R}^3} d\mathbf{q}\,\Phi_{\mathbf{q}}(x)\overline{\Phi_{\mathbf{q}}(x')} \tag{3.131}$$

and Fourier transform with respect to each coordinate $\mathbf{r}$ and $\mathbf{r}'$ to determine the momentum basis representation

$$\tilde{G}(\mathbf{k},t;\mathbf{k}',t') = -\frac{i}{\hbar}\theta(t-t')\int_{\mathbb{R}^3} d\mathbf{q}\,\tilde{\Phi}_{\mathbf{q}}(\mathbf{k},t)\overline{\tilde{\Phi}_{\mathbf{q}}(\mathbf{k}',t')}. \tag{3.132}$$

Evaluating

$$\tilde{\Phi}_{\mathbf{q}}(\mathbf{k},t) \equiv \int_{\mathbb{R}^3} d\mathbf{r}\frac{e^{-i\mathbf{k}\cdot\mathbf{r}}}{(2\pi)^{3/2}}\Phi_{\mathbf{q}}(x) = \delta^{(3)}(\mathbf{k}-\mathbf{q}(t))\,e^{-(i/\hbar)\int_0^t d\tau\frac{\hbar^2 q^2(\tau)}{2m}} \tag{3.133}$$

yields

$$\tilde{G}(\mathbf{k},t;\mathbf{k}',t') = -\frac{i}{\hbar}\theta(\Delta t)\,\delta^{(3)}(\Delta\mathbf{k} - (|e|/\hbar c)\Delta\mathbf{A})\exp\left[-(i/\hbar)\int_{t'}^{t} d\tau\frac{\hbar^2 q^2(\tau)}{2m}\right] \tag{3.134}$$

after integration. $\hbar\mathbf{k}'$ describes the momentum of a free electron at time t' in the past and $\hbar\mathbf{k}$ describes the resulting momentum at time t after the influence of $\mathbf{E}(t)$. Displacements are defined as $\Delta t \equiv t - t'$ in time, $\hbar\Delta\mathbf{k} = \hbar(\mathbf{k}-\mathbf{k}')$ in momentum and $\Delta\mathbf{A} = \mathbf{A}(t) - \mathbf{A}(t')$ in vector potential.

Using properties of the δ-distribution one immediately recognizes the expected classical equations of motion

$$\mathbf{F}_{\text{avg}} = \frac{\Delta \mathbf{p}}{\Delta t} = \hbar \frac{\Delta \mathbf{k}}{\Delta t} = \frac{|e|}{c} \frac{\Delta \mathbf{A}}{\Delta t} = -|e| \mathbf{E}_{\text{avg}} \quad \text{where} \quad \mathbf{E}_{\text{avg}} \equiv -\frac{1}{c} \frac{\Delta \mathbf{A}}{\Delta t}. \tag{3.135}$$

The δ-functions in Eq. (3.134) describe classical evolution of a single momentum state, while the phase factors given by

$$\mathbf{q}(\tau) = \mathbf{k} + \frac{|e|}{\hbar c} \left[\mathbf{A}(\tau) - \mathbf{A}(t) \right] = \mathbf{k}' + \frac{|e|}{\hbar c} \left[\mathbf{A}(\tau) - \mathbf{A}(t') \right] \tag{3.136}$$

relate to quantum interferences due to initial states composed of multiple plane wave contributions (for example, in an isolated wave-packet).

3.6 Ionization by a dynamic field

We will now describe some of the standard golden-rule-like approaches to strong field ionization in a dynamic field. The earliest one is by Keldysh [98] to describe ionization of a hydrogen-like atom in which the saddle point approximation for ionization is introduced. Additionally, we will use the parameter γ described in section 2.3 to connect the $\gamma \gg 1$ regime where perturbation theory is valid to the static-field case ($\gamma \ll 1$) where the exponential factor $\exp\left(-\frac{4}{3}\frac{I_p}{|e|Ea}\right)$ is recovered. Afterwards we will show the equivalence of Keldysh's amplitude with the complementary amplitude of Perelomov, Popov and Terent'ev [136] where the results of Ref. [98] were generalized to arbitrary initial states and additional laser configurations. We will focus on the case of short-range potentials and circular polarization to show agreement with the TDSE in the long-wavelength limit. Finally, we will discuss the velocity-gauge amplitude given by Reiss [146], where the saddle point method is abandoned and the amplitude is integrated exactly.

3.6.1 Keldysh rate

Ionization is modeled for a hydrogen atom interacting with the linearly polarized field

$$\mathbf{E}(t) = \mathbf{E} \cos(\omega t) \tag{3.137}$$

and prepared in the initial state

$$R_i(r) \approx C_{\kappa,0}\kappa^{3/2}e^{-\kappa r}. \tag{3.138}$$

Following steps given in Refs. [30, 98] we will use the saddle point approximation to determine a rate accurate for a large range of γ-values. In the limit of tunnel and multi-photon ionization we will simplify the rate.

The approximation starts by expanding the exact Green's function in the initial state Lippmann-Schwinger equation

$$\Psi(x) = \phi_i(x) + \int d^4x_1\ G(x;x_1)V_L(x_1)\phi_i(x_1) \tag{3.139}$$

to zeroth order in Volkov states

$$\Phi_{\mathbf{k}}^{(-)}(x) = e^{-(i/\hbar)\int_{t_0}^{t}\frac{(\hbar\mathbf{k}+\frac{|e|}{c}\mathbf{A}(\tau))^2}{2m}d\tau+\frac{i|e|}{\hbar c}\mathbf{A}(t)\cdot\mathbf{r}}\phi_{\mathbf{k}}^{(-)}(\mathbf{r}). \tag{3.140}$$

Here, we will choose $\phi_{\mathbf{k}}^{(-)}(\mathbf{r})$ to be plane waves as it was done in Keldysh's original paper [98], which has been recently generalized to exact atomic scattering states [58]. When the (plane-wave) Volkov Green's function

$$G^{(V)}(x;x') = -\frac{i}{\hbar}\theta(t-t')\int d\mathbf{k}\,\Phi_{\mathbf{k}}(x)\,\overline{\Phi_{\mathbf{k}}(x')} \tag{3.141}$$

is inserted into Eq. (3.139) we get the approximation

$$\Psi(x) \approx \phi_i(x) + \int d^4x_1\,G^{(V)}(x;x_1)V_L(x_1)\phi_i(x_1). \tag{3.142}$$

Emission of electrons is described by the outgoing partition

$$\Psi^{(\mathrm{out})}(x) = \int d\mathbf{k}\,\mathcal{M}(\mathbf{k},t)\Phi_{\mathbf{k}}^{(-)}(x) \tag{3.143}$$

with coefficients

$$\mathcal{M}(\mathbf{k},t) = \int d\mathbf{r}\,\overline{\Phi_{\mathbf{k}}^{(-)}(x)}\Psi(x). \tag{3.144}$$

The zeroth order contribution

$$\mathcal{M}^{(0)}(\mathbf{k},t) = \int d\mathbf{r}\,\overline{\Phi_{\mathbf{k}}^{(-)}(x)}\phi_i(x) \tag{3.145}$$

is identically zero for finite-range Volkov states and vanishes for plane-wave Volkov states in the long pulse limit [136]. The lowest order contribution therefore arises from

$$\mathcal{M}^{(1)}(\mathbf{k},t) = -\left(\frac{i}{\hbar}\right)\int d^4x_1 \overline{\Phi_{\mathbf{k}}^{(-)}(x_1)}[|e|\mathbf{E}(t_1)\cdot\mathbf{r}_1]\phi_i(x_1), \tag{3.146}$$

where the ionization rate is determined by

$$\begin{aligned} w &= \lim_{t\to\infty}\int d\mathbf{k}\frac{\partial}{\partial t}|\mathcal{M}^{(1)}(\mathbf{k},t)|^2 \\ &= \lim_{t\to\infty}\left(\frac{2}{\hbar^2}\right)\mathrm{Re}\int d\mathbf{k}\,\cos(\omega t)\overline{L(\mathbf{k},t)}\int_0^t dt_1\cos(\omega t_1)L(\mathbf{k},t_1) \end{aligned} \tag{3.147}$$

in the long pulse limit ($t_i \to 0$, $t\to\infty$) with

$$L(\mathbf{k},t) \equiv V_i\left(\mathbf{k} - \frac{|e|\mathbf{E}}{\hbar\omega}\sin(\omega t)\right)e^{(i/\hbar)S(\mathbf{k},t)}, \tag{3.148}$$

the matrix element

$$V_i(\mathbf{k}) \equiv \int d\mathbf{r}_1\phi_{\mathbf{k}}^{(-)}(\mathbf{r}_1)[|e|\mathbf{E}(t)\cdot\mathbf{r}]\phi_i(\mathbf{r}) \tag{3.149}$$

and the action

$$S(\mathbf{k},t) \equiv \int_{t_i}^t d\tau\left[\frac{(\hbar\mathbf{k} - \frac{|e|}{c}\mathbf{A}(\tau))^2}{2m} + I_p\right]. \tag{3.150}$$

The rate, Eq. (3.147), is evaluated by expanding $L(\mathbf{k},t)$ in the Fourier components

$$L(\mathbf{k},t) = \sum_{n=-\infty}^{\infty}\exp\left[(i/\hbar)\left(E_k + \tilde{I}_p - n\hbar\omega\right)t\right]L_n(\mathbf{k}) \tag{3.151}$$

where $\tilde{I}_p = I_p + U_p$ is the shifted ionization threshold, $E_k = \frac{\hbar\mathbf{k}^2}{2m}$ is the ionized kinetic energy,

$$U_p = \frac{|e|^2}{2mc^2}\langle\mathbf{A}_\pm(t)^2\rangle_T \tag{3.152}$$

is the ponderomotive or cycle-averaged quiver energy and the Fourier component corresponding to $n\hbar\omega$ can be interpreted as the contribution determined by the absorption of n photons. Inserting this expansion we have

$$w = \lim_{t\to\infty}\frac{\pi}{\hbar}\int d\mathbf{k}\sum_{n=-\infty}^{\infty}|L_{n+1}(\mathbf{k}) + L_{n-1}(\mathbf{k})|^2\delta(E_k + \tilde{I}_p - n\hbar\omega) \tag{3.153}$$

with

$$L_n(\mathbf{k}) = \frac{1}{2\pi}\int_{-\pi}^{\pi}d\varphi\,\exp\left[-(i/\hbar\omega)(E_k + \tilde{I}_p - n\hbar\omega)\varphi\right]L(\mathbf{k},\varphi/\omega) \tag{3.154}$$

and $\hbar k_n = \sqrt{2m(n\hbar\omega - \tilde{I}_p)}$.

Using properties of the δ-distribution the rate simplifies to

$$w = \lim_{t\to\infty} \frac{2\pi}{\hbar} \int d\mathbf{k} \sum_{n=-\infty}^{\infty} |L(\mathbf{k})|^2 \delta(E_k + \tilde{I}_p - n\hbar\omega) \tag{3.155}$$

with

$$L(\mathbf{k}) = \frac{1}{2\pi} \int_{-\pi}^{\pi} d\varphi \cos\varphi \, L(\mathbf{k}, \varphi/\omega) = \frac{1}{2\pi} \oint_C du \, V_i\left(\mathbf{k} - \frac{|e|\mathbf{E}}{\hbar\omega} u\right) e^{(i/\hbar\omega)S(u)} \tag{3.156}$$

where the Fourier integral is expressed as a contour integral around the dog-bone contour C surrounding branch points $u = \pm 1$ and cut connecting the two [30]. The effective action is given by

$$S(u) = \int_0^u \frac{dv}{\sqrt{1-v^2}} \left[\frac{\left(\hbar\mathbf{k} - \frac{|e|}{\omega}\mathbf{E}v\right)^2}{2m} + I_p \right]. \tag{3.157}$$

Concepts from sections 3.2 and 3.3 are applied to determine the Fourier coefficients when $\hbar\omega \ll I_p$ and $\hbar\omega \ll U_p$. The action $S(u)$ is expanded to second order and the contour is deformed such that it passes through saddle points u_s (determined from $S'(u_s) = 0$) along the path of steepest descent. The slowly changing pre-exponential factor $V_i\left(\mathbf{k} - \frac{|e|}{\omega}\mathbf{E}u\right)$ may be evaluated at $u = u_s$ and Gaussian integration is performed to evaluate $L(\mathbf{k})$.

In Ref. [98] the rate is evaluated for a Hydrogen-like initial state

$$R_i(r) \approx 2C_{\kappa,0}\kappa^{3/2} e^{-\kappa r} \tag{3.158}$$

with plane-wave Volkov states yielding

$$V_i(\mathbf{k}) = [|e|\mathbf{E}\cdot(i\nabla_{\mathbf{k}})] \int d\mathbf{r}_1 \frac{e^{i\mathbf{k}\cdot\mathbf{r}}}{(2\pi)^{3/2}} \phi_i(\mathbf{r}_1) = \frac{-iC_{\kappa,0}(2\kappa)^{5/2}}{\pi(k^2+\kappa^2)^3}[|e|Ek_{\|}] \tag{3.159}$$

where $k_{\|}$ is the momentum component parallel to the field $\mathbf{E}$. The matrix element contains a pole at $k = \pm i\kappa$ corresponding to the initial bound state [27, 107]. Setting $S'(u)|_{u=u_s} = 0$ and defining $\gamma \equiv (\hbar\omega\kappa/|e|E)$ the two saddle points

$$u_{s\pm} = \gamma \left[\frac{k_{\|}}{\kappa} \pm i\sqrt{1 + \left(\frac{k_{\perp}}{\kappa}\right)^2} \right] \tag{3.160}$$

are obtained which correspond exactly to the poles of $V_i(\mathbf{k})$ after the substitution $\mathbf{k} \to \mathbf{k} - \frac{|e|\mathbf{E}}{\hbar\omega}u$.

Expanding $S(u)$ to second order and assuming $k^2 \ll \kappa^2$ the integral is evaluated with deformed contour passing through the saddle points $u_{s\pm}$ (without crossing them) yielding

$$w = \frac{C_{\kappa,0}^2}{2}\sqrt{\omega\frac{2I_p}{\hbar}}\left(\frac{\gamma}{\sqrt{1+\gamma^2}}\right)^{3/2}\mathcal{S}\left(\gamma,\frac{\tilde{I}_p}{\hbar\omega}\right)\exp\left[-\frac{2\tilde{I}_p}{\hbar\omega}\left(\sinh^{-1}\gamma-\gamma\frac{\sqrt{1+\gamma^2}}{1+2\gamma^2}\right)\right] \tag{3.161}$$

after integration [30, 98] with

$$\mathcal{S}(\gamma,x) \equiv \sum_{a=0}^{\infty}\exp\left[-2(\langle x+1\rangle - x + a)\left(\sinh^{-1}\gamma - \frac{\gamma}{\sqrt{1+\gamma^2}}\right)\right] \times D_+\left\{\left[\frac{2\gamma}{\sqrt{1+\gamma^2}}(\langle x+1\rangle - x + a)\right]^{1/2}\right\}. \tag{3.162}$$

a describes the number of quanta absorbed above the ionization threshold $\tilde{I}_p$, $\langle x\rangle$ corresponds to the integer part of x and $D_+(z) \equiv \int_0^z e^{y^2-z^2}dy$ is the Dawson function. When performing the final integral over k interference effects between the two saddle points $u = u_{s\pm}$ are neglected. Errors introduced by this approximation are small for the total rate w, but must be included to describe the angular emission rate $\frac{dw}{d\Omega}$ [30]. $C_{\kappa,0}$ is numerically fit to the asymptotic tail of the initial state. Here we follow Ref. [98] and set $C_{\kappa,0} = 2$ for the $1s$ state of Hydrogen.

3.6.1.1 Multiphoton limit

Keldysh's amplitude has been approximated in the weak-field multiphoton limit. Here the lowest near-threshold order $a = 0$ dominates and the rate

$$w = 2\sqrt{\omega\frac{2I_p}{\hbar}}\left(\frac{1}{4\gamma^2}\right)^{\langle \tilde{I}_p/\hbar\omega+1\rangle}\exp\left(2\left\langle\frac{\tilde{I}_p}{\hbar\omega}+1\right\rangle - \frac{\tilde{I}_p}{\hbar\omega}\right)D_+\left[\sqrt{2\left(\left\langle\frac{\tilde{I}_p}{\hbar\omega}+1\right\rangle - \frac{\tilde{I}_p}{\hbar\omega}\right)}\right] \tag{3.163}$$

is determined by taking $\gamma \gg 1$ in the rate, truncating the sum and approximating $\sinh^{-1}\gamma \approx \log(2\gamma)$. Portions containing $\langle \tilde{I}_p/\hbar\omega + 1\rangle$ describe the influence of ionization thresholds and quanta absorbed in the perturbative limit. Care must be taken since the saddle point approximation may not be valid. We will discuss this further in Chapter 5.

3.6.1.2 Tunnel Limit

For very long wavelengths and/or very strong fields where $\gamma \ll 1$ the sum in Eq. (3.162) is approximated as an integral since large a are the dominant contributions yielding $\mathcal{S}(\gamma, \tilde{I}_p/\hbar\omega) \approx$

$\sqrt{3\pi}/4\gamma^2$. Expanding the exponent to 3rd order in γ the rate of tunnel ionization is given by

$$w = \frac{\sqrt{6\pi}}{2}\sqrt{\frac{\omega I_p}{\hbar\gamma}}\exp\left[-\frac{4I_p\gamma}{3\hbar\omega}\left(1-\frac{\gamma^3}{10}\right)\right]. \tag{3.164}$$

Taking $\omega \to 0$ the exponent in Eq. (3.164) corresponds to the ionization rate of atoms in a quasi-static field. Here, one has

$$w = \frac{\sqrt{6\pi}}{2}\sqrt{\frac{|e|EI_p}{\hbar^2\kappa}}\exp\left[-\frac{4}{3}\frac{I_p\kappa}{|e|E}\right] = \frac{\sqrt{6\pi}}{2}\sqrt{|e|Ea\frac{I_p}{\hbar^2}}\exp\left[-\frac{4}{3}\frac{I_p}{|e|Ea}\right]. \tag{3.165}$$

Averaging the static Landau and Lifshitz rate w_{stat} from section 3.4.2 over a laser cycle [5, 136] an adiabatic rate

$$w_{\text{adiabatic}} = \sqrt{\frac{3}{2\pi}\frac{|e|Ea}{I_p}}w_{\text{stat}} = 16\left(\frac{I_p}{\hbar}\right)\sqrt{\frac{3}{2\pi}\frac{I_p}{|e|Ea}}\exp\left[-\frac{4}{3}\frac{I_p}{|e|Ea}\right] \tag{3.166}$$

is determined.

The Keldysh rate [98] is unable to recover the correct adiabatic pre-factor since the final (ionized) Volkov state does not include the Coulomb potential as in Ref. [132]. In later sections as well as in Chapter 5 we will show that the approximation is accurate for short-range potentials. Often semi-classical long-range Coulomb corrections are applied in the limit of long wavelength radiation. We will discuss one of the simplest Coulomb corrections [102] to give an idea of how one might better approximate the long-range rate.

3.6.2 PPT rate

In this section we will show that the first order Keldysh ionization amplitude is equivalent to the PPT amplitude [136] up to boundary terms for zero-range final states and all applied fields $\mathbf{E}(t)$. After establishing equivalence with the Keldysh rate we will quickly summarize the rate of $s-$ and $p-$state ionization in circularly polarized fields [20]. Numerical solutions of the TDSE will be used to establish accuracy of the rate for s-states and in Chapter 5 we will use the $p-$state rate to discuss breakdown of the saddle point approximation and when asymptotic approximations to the initial state become inappropriate.

3.6.2.1 Equivalence with the Keldysh amplitude for zero-range Volkov states

We may write Keldysh's amplitude as

$$\mathcal{M}^{(1)}(\mathbf{k},t) = -(i/\hbar)\int d^4x_1\,\overline{\Phi_{\mathbf{k}}(x)}\,[|e|\mathbf{E}(t_1)\cdot\mathbf{r}_1]\,\phi_i(x_1)$$
$$= \int_{t_0}^{t} dt_1 e^{(i/\hbar)S(\mathbf{k},t_1)}\left(-\frac{\partial}{\partial t_1}\right)\tilde{\phi}_i\left(\mathbf{k}(t_1)\right) \quad (3.167)$$

where

$$\tilde{\phi}_i(\mathbf{k},\mathbf{A}(t)) = \int d\mathbf{r}_1\overline{\phi_{\mathbf{k}+\frac{|e|}{\hbar c}\mathbf{A}(t)}(\mathbf{r}_1)}\phi_i(\mathbf{r}_1) \equiv \tilde{\phi}_i\left(\mathbf{k}(t)\right) \quad (3.168)$$

and

$$\hbar\mathbf{k}(t) \equiv \hbar\mathbf{k} + \frac{|e|}{c}\mathbf{A}(t) \equiv \mathbf{p}(t). \quad (3.169)$$

Acting on both sides with $i\hbar\frac{\partial}{\partial t}$ we see that

$$i\hbar\frac{\partial}{\partial t}\left[\mathcal{M}^{(1)}(\mathbf{k},t) + e^{(i/\hbar)S(\mathbf{k},t)}\tilde{\phi}_i\left(\mathbf{k}(t)\right)\right] = -\left(\frac{\partial S}{\partial t}\right)e^{(i/\hbar)S(\mathbf{k},t)}\tilde{\phi}_i\left(\mathbf{k}(t)\right) \quad (3.170)$$

and solving for the amplitude we get

$$\mathcal{M}^{(1)}(\mathbf{k},t) = -\left[\mathcal{M}^{(0)}(\mathbf{k},t_1)\right|_{t_1=t_0}^{t} + \left(\frac{i}{\hbar}\right)\int_{t_0}^{t} dt_1\left(\frac{\partial S}{\partial t_1}\right)e^{(i/\hbar)S(\mathbf{k},t_1)}\tilde{\phi}_i\left(\mathbf{k}(t_1)\right) \quad (3.171)$$

where we recognize that the boundary term

$$\mathcal{M}^{(0)}(\mathbf{k},t) = e^{(i/\hbar)S(\mathbf{k},t)}\tilde{\phi}_i\left(\mathbf{k}(t)\right), \quad (3.172)$$

can be neglected. Using

$$\left(\frac{\partial S}{\partial t}\right) = \frac{\mathbf{p}^2(t)}{2m} + I_p \quad (3.173)$$

the remaining term is written as

$$\mathcal{M}^{(1)}(\mathbf{k},t) = \left(\frac{i}{\hbar}\right)\int d^4x_1\overline{\Phi_{\mathbf{k}}(x_1)}\left[\frac{\mathbf{p}^2(t_1)}{2m} + I_p\right]\phi_i(x_1). \quad (3.174)$$

To arrive at the plane-wave PPT formulas we recognize

$$-I_p\phi_i(x) = \left[\frac{\hat{\mathbf{p}}^2}{2m} + V_a(\mathbf{r})\right]\phi_i(x) \quad (3.175)$$

which gives us

$$\mathcal{M}^{(1)}(\mathbf{k},t) = -\left(\frac{i}{\hbar}\right)\int d^4x_1 \overline{\Phi_{\mathbf{k}}(x_1)}\left[\frac{\hat{\mathbf{p}}_1^2 - \mathbf{p}^2(t_1)}{2m} + V_a(\mathbf{r}_1)\right]\phi_i(x_1). \tag{3.176}$$

Integrating by parts we see that

$$\frac{\hat{\mathbf{p}}^2}{2m}\Phi_{\mathbf{k}}(x_1) = \frac{\mathbf{p}^2(t)}{2m}\Phi_{\mathbf{k}}(x_1) \tag{3.177}$$

yields the desired result

$$\mathcal{M}^{(1)}(\mathbf{k},t) = -\left(\frac{i}{\hbar}\right)\int d^4x_1 \overline{\Phi_{\mathbf{k}}(x_1)}V_a(\mathbf{r}_1)\phi_i(x_1). \tag{3.178}$$

For finite-range final states the situation is different. Writing down the PPT amplitude and substituting in finite-range states gives a different rate than using the equivalent Keldysh amplitude with the same states. Starting with Eq. (3.176) we separate the amplitude into a PPT-like contribution and a perturbation

$$\mathcal{M}^{(1)}(\mathbf{k},t) = \mathcal{M}^{(1,\mathrm{PPT})}(\mathbf{k},t) + \delta\mathcal{M}^{(1)}(\mathbf{k},t) \tag{3.179}$$

where

$$\mathcal{M}^{(1,\mathrm{PPT})}(\mathbf{k},t) = -\left(\frac{i}{\hbar}\right)\int d^4x_1 \overline{\Phi_{\mathbf{k}}^{(-)}(x_1)}V_a(\mathbf{r}_1)\phi_i(x_1) \tag{3.180}$$

and

$$\delta\mathcal{M}^{(1)}(\mathbf{k},t) = -\left(\frac{i}{\hbar}\right)\int d^4x_1 \overline{\Phi_{\mathbf{k}}^{(-)}(x_1)}\left[\frac{\hat{\mathbf{p}}_1^2 - \mathbf{p}^2(t_1)}{2m}\right]\phi_i(x_1). \tag{3.181}$$

Using the Fourier representation

$$\phi_i(x) = (2\pi)^{-3/2}\int d\mathbf{k}' e^{i\mathbf{k}'\cdot\mathbf{r}}\tilde{\phi}_i(\mathbf{k}',t) \tag{3.182}$$

and

$$\Phi_{\mathbf{k}}^{(-)}(x) = (2\pi)^{-3/2}\int d\mathbf{k}'' e^{i\mathbf{k}''\cdot\mathbf{r}}\tilde{\Phi}_{\mathbf{k}}^{(-)}(\mathbf{k}'',t) \tag{3.183}$$

we see that the perturbation becomes

$$\delta\mathcal{M}^{(1)}(\mathbf{k},t) = \\ -\left(\frac{i}{\hbar}\right)\int_{t_0}^{t} dt_1 \int d\mathbf{q}\, \overline{\tilde{\Phi}_{\mathbf{k}}^{(-)}(\mathbf{k}+\mathbf{q},t_1)}\left[\frac{(\hbar\mathbf{q})^2 + 2(\hbar\mathbf{k})\cdot(\hbar\mathbf{q} - \frac{|e|}{c}\mathbf{A}(t_1)) - (\frac{|e|}{c}\mathbf{A}(t_1))^2}{2m}\right]\tilde{\phi}_i(\mathbf{k}+\mathbf{q},t_1). \tag{3.184}$$

If $\phi_{\mathbf{k}}^{(-)}$ is a plane wave then the corresponding Volkov state contains a single Fourier component corresponding to $\hbar\mathbf{q} = \frac{|e|}{c}\mathbf{A}(t)$ and gives $\delta\mathcal{M}^{(1)} = 0$ as before. Atomic scattering states are described by a distribution of vectors $\mathbf{q}$ which leads to $\delta\mathcal{M}^{(1)} \neq 0$ in general and therefore a different result.

3.6.2.2 Ionization by circularly polarized fields

In Refs. [135–137] the amplitude was generalized to the case of arbitrary initial states and extended to both circular and elliptical polarizations. Additional quasi-classical Coulomb corrections have been applied to the PPT formulas. We will instead describe the simpler Coulomb corrections [23, 102] which are closely related to the WKB corrections used by Landau and Lifshitz in their static rate (Sec.3.4.2).

Starting with the right-/left- handed ($\pm$) circularly polarized field

$$\mathbf{A}_{\pm}(t) = -A\left[\sin(\omega t)\mathbf{e}_x \mp \cos(\omega t)\mathbf{e}_y\right] \tag{3.185}$$

the final state Lippmann-Schwinger equation is applied to determine the first order expansion

$$\mathcal{M}^{(1)}(\mathbf{k},t) = -\left(\frac{i}{\hbar}\right)\int d^4x_1 \overline{\Phi_{\mathbf{k}}(x_1)} V_a(\mathbf{r}_1)\phi_i(x_1). \tag{3.186}$$

Using

$$V_a(\mathbf{r})\phi_i(x) = \left(i\hbar\frac{\partial}{\partial t} - \frac{\hat{\mathbf{p}}^2}{2m}\right)\phi_i(x) \tag{3.187}$$

and integrating by parts the amplitude becomes

$$\mathcal{M}^{(1)}(\mathbf{k},t) = \left(\frac{i}{\hbar}\right)\int_0^t dt_1\left[\frac{\hbar^2\mathbf{k}(t_1)^2}{2m} + I_p\right]e^{(i/\hbar)S(\mathbf{k},t_1)}\tilde{\phi}_i(\mathbf{k}(t_1)). \tag{3.188}$$

with $\mathbf{k}(t) \equiv \mathbf{k} + \frac{|e|}{\hbar c}\mathbf{A}(t)$ and

$$\tilde{\phi}_i(\mathbf{k}) \equiv \int d\mathbf{r}\frac{e^{-i\mathbf{k}\cdot\mathbf{r}}}{(2\pi)^{3/2}}\phi_i(\mathbf{r}). \tag{3.189}$$

The rate can then be determined as

$$w = \lim_{t\to\infty}\int d\mathbf{k}\frac{\partial}{\partial t}|\mathcal{M}^{(1)}(\mathbf{k},t)|^2 = \lim_{t\to\infty}\left(\frac{2}{\hbar^2}\right)\mathrm{Re}\int d\mathbf{k}\,\overline{L(\mathbf{k},t)}\int_0^t dt_1 L(\mathbf{k},t_1) \tag{3.190}$$

in the long pulse limit ($t_i \to 0$, $t \to \infty$) with

$$L(\mathbf{k},t) \equiv \left[\frac{\hbar^2 \mathbf{k}(t_1)^2}{2m} + I_p\right] e^{(i/\hbar)S(\mathbf{k},t_1)} \tilde{\phi}_i(\mathbf{k}(t_1)). \tag{3.191}$$

Expanding $L(\mathbf{k},t)$ again as a Fourier series the rate is represented as

$$w = \frac{2\pi}{\hbar} \int d\mathbf{k} \sum_{n=-\infty}^{\infty} |L_n(\mathbf{k})|^2 \delta(E_k + \tilde{I}_p - n\hbar\omega) \tag{3.192}$$

with

$$L_n(\mathbf{k}) \equiv \frac{\omega}{2\pi} \int_{-\pi/\omega}^{\pi/\omega} dt \left[\frac{\hbar^2 \mathbf{k}(t)^2}{2m} + I_p\right] e^{(i/\hbar)S(\mathbf{k},t)} \tilde{\phi}_i(\mathbf{k}(t))\Big|_{k=k_n}. \tag{3.193}$$

Switching now to atomic units

$$|L_{n\pm}(\mathbf{k})|^2 = \left|\frac{1}{2\pi} \int_{-\pi}^{\pi} d\varphi \, \Xi_i(\mathbf{k}_\pm(\varphi/\omega)) e^{iS_\pm(\mathbf{k},\varphi/\omega)}\right|^2_{k=k_n} \tag{3.194}$$

with

$$\Xi_i(\mathbf{k}_\pm(t)) \equiv \left[\frac{\mathbf{k}_\pm(t)^2}{2} + I_p\right] \tilde{\phi}_i(\mathbf{k}_\pm(t)) \tag{3.195}$$

where the integral is approximated using the saddle point approximation to obtain [20]

$$|L_{n\pm}(\mathbf{k})|^2_{k=k_n} = \frac{|\Xi_i(\mathbf{k}(t_i))|^2_{k=k_n}}{2\pi n\sqrt{1-1/\chi_n(k_z)^2}} e^{-2n[\operatorname{arcosh}\chi_n(k_z) - \sqrt{1-1/\chi_n(k_x)^2}]} \tag{3.196}$$

from the zero-range initial state Eq. (2.72) with saddle points

$$\omega t_i = \frac{\pi}{2} \pm \phi_k + 2\pi N + i \operatorname{arcosh}\chi_n(k_z) \tag{3.197}$$

which gives

$$w_\pm^{(l_i=0)} = \frac{C_{\kappa,0}^2 \kappa}{2\pi} \sum_{n=n_{\text{th}}}^{\infty} \frac{1}{n} \int_0^{k_n} dk_z \frac{e^{-2n[\operatorname{arcosh}\chi_n(k_z) - \sqrt{1-1/\chi_n(k_z)^2}]}}{\sqrt{1-1/\chi_n(k_z)^2}} \tag{3.198}$$

for an s-state,

$$w_\pm^{(l_i=1,m_i=0)} = \frac{3C_{\kappa,1}^2}{2\pi\kappa} \sum_{n=n_{\text{th}}}^{\infty} \frac{1}{n} \int_0^{k_n} dk_z \frac{k_z^2 e^{-2n[\operatorname{arcosh}\chi_n(k_z) - \sqrt{1-1/\chi_n(k_z)^2}]}}{\sqrt{1-1/\chi_n(k_z)^2}} \tag{3.199}$$

for a p_0-state and

$$\begin{aligned} w_\pm^{(l_i=1,|m_i|=1)} = \frac{3C_{\kappa,1}^2 A_0^2}{16\pi\kappa} \sum_{n=n_{\text{th}}}^{\infty} \frac{1}{n} \int_0^{k_n} dk_z \frac{e^{-2n[\operatorname{arcosh}\chi_n(k_z) - \sqrt{1-1/\chi_n(k_z)^2}]}}{\chi_n(k_z)^2\sqrt{1-1/\chi_n(k_z)^2}} \\ \times \left[2\chi_n(k_z)^2(1 \mp \operatorname{sgn}(m_i)\sqrt{1-1/\chi_n(k_z)^2}) - (1+(\kappa/A_0)^2)n/n_0\right]^2 \end{aligned} \tag{3.200}$$

for a $p_{\pm 1}$-state where

$$\chi_n(k_z) = \frac{n\omega}{A_0\sqrt{k_n^2 - k_z^2}}, \tag{3.201}$$

$n_{\rm th} = \lceil n_0 \rceil$, $n_0 = \tilde{I}_p/\omega$ and $A_0 \equiv (1/\omega)\sqrt{I/2}$ with I is the laser intensity in atomic units.

Results for the s-state yield:

$$N_{\rm ion} = 1 - \exp\left[-w\left(N_{\rm cycles}\frac{2\pi}{\omega}\right)\right] \tag{3.202}$$

are compared with those of numerical solutions of the TDSE (8'th-order B-splines) in Fig. 3.9 for the Yukawa potential

$$V_{\rm a}(r) = -\frac{Z}{r}e^{-r/a} \tag{3.203}$$

with $a = 1/5$ a.u. and Z are chosen such that $I_p = 1/2$ a.u.. TDSE calculations are performed for a 16 cycle flat-top pulse with a 2 cycle $\sin^2$ ramp on and off. The laser intensity is fixed at $I = 1\times10^{14}$ W/cm^2 and wavelengths are chosen in the interval from 10 nm to 800 nm. Jumps at 91.928 nm and longer wavelengths correspond to the single photon and higher order ionization thresholds.

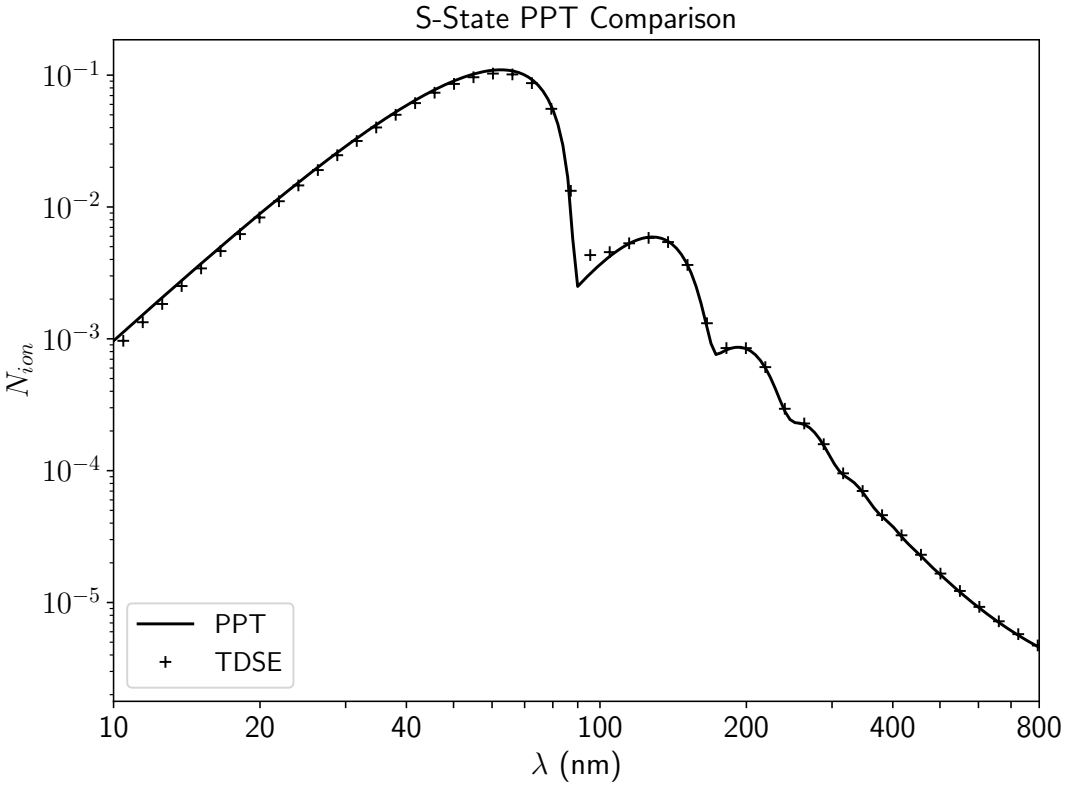

Figure 3.9: Comparison of results for the total ionization yield obtained by the time-dependent Schrödinger equation and the $s-$state PPT formulas [20]. The circularly polarized field has an intensity of $I = 1 \times 10^{14}$ W/cm^2, duration of 16 cycles and wavelengths between 10 nm and 800 nm. Properties of the Yukawa potential are discussed in the main text.

At the first threshold (91.928 nm) disagreement between the results of TDSE calculations and those for the PPT formulas are due to the use of a short pulse in the TDSE calculations and the approximate long-pulse rate in the PPT formulas. For longer pulse durations errors of this form diminish. At the short wavelength (10 nm) limit the PPT rate starts to deviate from the TDSE data set due to breakdown of the saddle point approximation. For zero-range $s-$ states and current laser parameters the approximation works well even for single-photon ionization. In Chapter 5 we show that this disagreement greatly increases in the case of p-states where we will derive our own complementary rate.

3.6.2.3 Coulomb corrections

In the long-wavelength limit the Landau and Lifshitz ionization rate [107] may be recovered by applying a similar quasi-classical correction to the final ionized Volkov state. We will stick to one of the simplest [23, 102] where

$$\Phi_{\mathbf{k}}(x) \mapsto \exp\left[i \int_r^{1/2F} dr'\, \delta p(r')\right] \Phi_{\mathbf{k}}(x), \tag{3.204}$$

with $\delta p(r) = \frac{1}{r p_0(r)}$ and $p_0(r) \approx i\sqrt{1 - 2Fr}$. We assume sufficiently weak fields giving:

$$\exp\left[i \int_r^{1/2F} dr'\, \delta p(r')\right] \approx \frac{2}{Fr} \tag{3.205}$$

where the long-range Hydrogen rate may be approximated as

$$w_{\text{Hydrogen}} \sim Q w_{\text{zero-range}} \tag{3.206}$$

with $Q = (2/F)^2$ and $C_{\kappa,0} = 2$. The WKB-like Coulomb correction relates the Hydrogen rate to a closely related zero-range rate. In Ref. [140] improvements were made to the correction with acceptable, but not perfect agreement with results of ab-initio numerical calculations. The lack of fully quantum Coulomb corrections for ionization of atoms where $\gamma \gtrsim 1$ proves to be one of the largest difficulties associated with the theory of strong field ionization.

In Fig. 3.10 we show a comparison of the PPT yield [20, 136] with the simplified WKB-like Coulomb correction given in Refs. [23, 102] and the TDSE results for ionization of hydrogen atom by a 16-cycle flat top laser pulse with a two cycle $\sin^2$ ramp up and down with an intensity of $I = 1 \times 10^{14}$ W/cm^2 and wavelengths between 10 and 800 nm. In the long wavelength ($\sim$ 800 nm) limit where γ is smallest the approximation performs well, while for the shortest wavelengths ($\sim$ 350 nm and shorter) the approximation fails completely.

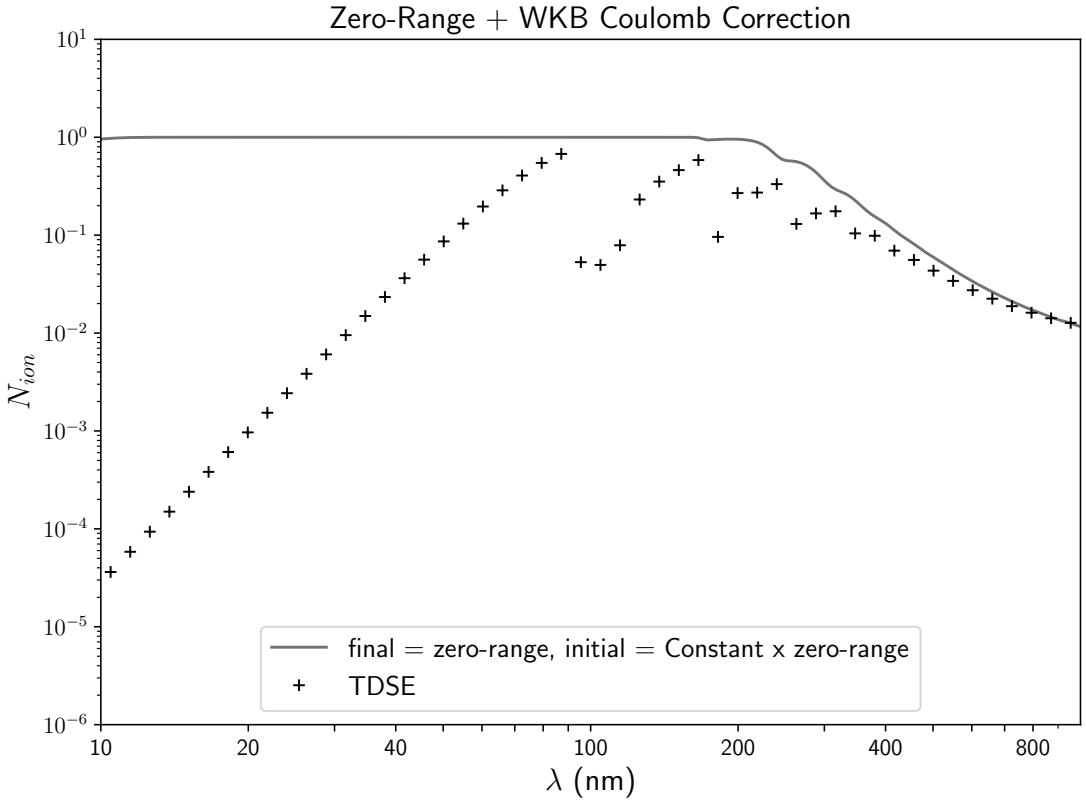

Figure 3.10: Comparison of the total ionization yield for hydrogen atom between results of the time-dependent Schrödinger equation (+ symbols) and the $s-$state PPT formulas (solid line). The circularly polarized field has an intensity of $I = 1 \times 10^{14}$ W/cm^2, duration of 16 cycles and wavelengths between 10 nm and 800 nm. The black curve represents application of the Coulomb correction [23,102] to the circular s-state PPT rate [20,136]. The approximation only agrees in the limit of $\gamma \ll 1$ and outlines difficulties associated with Coulomb corrections when $\gamma \gtrsim 1$.

For the remainder of the thesis we will apply the amplitude in the short-range case and consider only this simplest correction. In Chapter 4 we will compare p-state ionization ratios N_{+1}/N_{-1}, and N_0/N_{-1} between its three magnetic projections $m = -1, 0$ and 1. Approximating

$$N_{\text{ion}} = 1 - \exp\left[-w\left(N_{\text{cycles}}\frac{2\pi}{\omega}\right)\right] \approx w\left(N_{\text{cycles}}\frac{2\pi}{\omega}\right) \tag{3.207}$$

the Coulomb pre-factor Q vanishes in ionization ratios and it is clear that zero-range estimates of long-range properties are valid in the long-wavelength limit where $N_{\text{ion}} \lesssim 0.1$.

3.6.3 Velocity-gauge approach

When solving the TDSE exactly, all observables are gauge-independent. In other words exact solutions to the TDSE within the dipole approximation should yield the same observables when either

$$V_L(x) = |e|\mathbf{E}(t)\cdot\mathbf{r} \tag{3.208}$$

or

$$V_L(x) = \frac{|e|}{mc}\mathbf{A}(t)\cdot\mathbf{p} + \frac{\mathbf{A}(t)^2}{2mc^2} \tag{3.209}$$

is used to describe interactions between an electron and an external field [151, 152]. However, both perturbative approximations [33] and nonperturbative approaches [23, 146] are, in general, gauge dependent unless expanded to infinite order.

We will outline the most common velocity-gauge amplitude given by Reiss [146] and note that Faisal [57] has produced a similar rate which allows for more general final states. The amplitude starts with the velocity-gauge version of the same initial state Lippmann-Schwinger expansion as used in Keldysh's amplitude. The first order contribution is

$$\mathcal{M}_{\pm}^{(1,\mathrm{VG})}(\mathbf{k},t) = -\left(\frac{i}{\hbar}\right)\int d^4x_1\,\overline{\Phi_{\mathbf{k}\pm}^{(\mathrm{VG})}(x_1)}V_{L\pm}^{(\mathrm{VG})}(x_1)\phi_i(x_1), \tag{3.210}$$

where

$$V_{L\pm}^{(\mathrm{VG})}(x) = \frac{|e|}{mc}\mathbf{A}_{\pm}(t)\cdot\hat{\mathbf{p}} + \frac{|e|^2}{2mc^2}\mathbf{A}_{\pm}(t)^2 \tag{3.211}$$

and

$$\Phi_{\mathbf{k}\pm}^{(\mathrm{VG})}(x) = e^{-(i/\hbar)\int_{t_0}^{t}\frac{(\hbar\mathbf{k}+\frac{|e|}{c}\mathbf{A}_{\pm}(\tau))^2}{2m}d\tau}\frac{e^{i\mathbf{k}\cdot\mathbf{r}}}{(2\pi)^{3/2}}. \tag{3.212}$$

Using

$$i\hbar\frac{\partial}{\partial t}\Phi_{\mathbf{k}\pm}^{(\mathrm{VG})}(x) = \frac{(\hbar\mathbf{k}+\frac{|e|}{c}\mathbf{A}_{\pm}(t))^2}{2m}\Phi_{\mathbf{k}\pm}^{(\mathrm{VG})}(x) \tag{3.213}$$

with

$$\hat{\mathbf{p}}\,\Phi_{\mathbf{k}\pm}^{(\mathrm{VG})}(x) = (\hbar\mathbf{k})\,\Phi_{\mathbf{k}\pm}^{(\mathrm{VG})}(x) \quad\text{and}\quad i\hbar\frac{\partial}{\partial t}\phi_i(x) = -I_p\,\phi_i(x) \tag{3.214}$$

we have

$$\mathcal{M}_{\pm}^{(1,\mathrm{VG})}(\mathbf{k},t) = \left(\frac{i}{\hbar}\right)(E_k+I_p)\int d^4x_1\,\overline{\Phi_{\mathbf{k}\pm}^{(\mathrm{VG})}(x_1)}\phi_i(x_1) \tag{3.215}$$

where vanishing boundary terms have been omitted.

Proceeding as before

$$\int d^4x_1 \overline{\Phi^{(\mathrm{VG})}_{\mathbf{k}\pm}(x_1)}\phi_i(x_1) = \tilde{\phi}_i(\mathbf{k}) \int_0^t dt_1 e^{(i/\hbar)S_\pm(\mathbf{k},t_1)} \tag{3.216}$$

where

$$\tilde{\phi}_i(\mathbf{k}) = \int d\mathbf{r}_1 \frac{e^{-i\mathbf{k}\cdot\mathbf{r}_1}}{(2\pi)^{3/2}}\phi_i(\mathbf{r}_1) \tag{3.217}$$

is the Fourier transform of the initial state and using the asymptotic state

$$\phi_i(\mathbf{r}) = C_{\kappa,l_i}\kappa^{3/2}(\kappa r)^{\nu-1}e^{-\kappa r}Y^{m_i}_{l_i}(\hat{\mathbf{r}}), \tag{3.218}$$

the momentum representation is given as

$$\tilde{\phi}_i(\mathbf{k}) = (-i)^{l_i}\frac{C_{\kappa,l_i}\kappa^{\nu+1/2}}{\sqrt{k}}Y^{m_i}_{l_i}(\hat{\mathbf{k}})\frac{\Gamma(l_i+\nu+2)}{(\sqrt{k^2+\kappa^2})^{\nu+3/2}}P^{-(l_i+1/2)}_{\nu+1/2}\left(\frac{\kappa}{\sqrt{k^2+\kappa^2}}\right) \equiv \tilde{R}_i(k)Y^{m_i}_{l_i}(\hat{\mathbf{k}}), \tag{3.219}$$

which simplifies to

$$\tilde{\phi}_i(\mathbf{k}) = \sqrt{\frac{\kappa}{2}}\frac{C_{\kappa,0}}{\pi(k^2+\kappa^2)} \tag{3.220}$$

in the case of a zero-range ($\nu = 0$) s-state.

To complete the amplitude the $\mathbf{k}\cdot\boldsymbol{\xi}_\pm(t)$ term in $e^{(i/\hbar)S_\pm(\mathbf{k},t_1)}$ is expanded using the Jacobi-Anger expansion

$$e^{i\mathbf{k}\cdot\boldsymbol{\xi}_\pm(t)} = e^{ik_\rho\xi\cos(\pm\varphi_k-\omega t)} = \sum_{n=-\infty}^{\infty} i^n e^{-in\omega t}J_n(k_\rho\xi)e^{\pm in\varphi_k} \tag{3.221}$$

which gives

$$\int_0^t dt_1 e^{(i/\hbar)S_\pm(\mathbf{k},t_1)} = e^{-i\mathbf{k}\cdot\boldsymbol{\xi}_\pm(0)}\sum_{n=-\infty}^{\infty} i^n J_n(k_\rho\xi)e^{\pm in\varphi_k}\delta_t([N(k)-n]\omega/2) \tag{3.222}$$

and

$$\mathcal{M}^{(1,\mathrm{VG})}_\pm(\mathbf{k},t) = \left(\frac{i}{\hbar}\right)(E_k+I_p)\,\tilde{\phi}_i(\mathbf{k})e^{-i\mathbf{k}\cdot\boldsymbol{\xi}_\pm(0)}\sum_{n=-\infty}^{\infty} i^n J_n(k_\rho\xi)e^{\pm in\varphi_k}\delta_t([N(k)-n]\omega/2) \tag{3.223}$$

after time integration. Taking the long pulse limit as before we have

$$\frac{dw_n}{d\Omega} = \frac{(2\pi)mk_n}{\hbar^3}(n\hbar\omega-U_p)^2|\tilde{\phi}_i(\mathbf{k}_n)|^2J_n^2(k_n\xi\sin\theta_k) \tag{3.224}$$

and

$$w_n = \frac{(2\pi)^2 m k_n}{\hbar^3}(n\hbar\omega - U_p)^2 \int_0^\pi d\theta_k \ \sin\theta_k |\tilde{\phi}_i(\mathbf{k}_n)|^2 J_n^2(k_n \xi \sin\theta_k) \tag{3.225}$$

where we assumed that $\tilde{\phi}_i(\mathbf{k}_n)$ contains a single spherical harmonic component which removes the φ_k dependence from the angular integral ($|e^{im_i\varphi_k}|^2 = 1$).

Additionally, as given the velocity-gauge formulas incorrectly predict an identical ionization rate for co- and counter-rotating electrons [166, 167] since $|Y_{l_i}^{m_i}(\hat{\mathbf{k}})|^2 = |Y_{l_i}^{-m_i}(\hat{\mathbf{k}})|^2$ in the $|\tilde{\phi}_i(\mathbf{k}_n)|^2$ product. The inclusion of $e^{-i\frac{|e|}{c}\mathbf{A}(t)\cdot\mathbf{r}}$ in the length-gauge Volkov states resolves this issue, as shown in Refs. [20, 136]. In Fig. 3.9 we compare the yield from Reiss' rate

$$w = \sum_{n=n_{\text{th}}}^{\infty} w_n \tag{3.226}$$

(with $n_{\text{th}} = \lceil \tilde{I}_p/\omega \rceil$) to the numerical data produced by simulations of the TDSE, as discussed in the PPT section 3.6.2. Again differences persist near ionization thresholds since we have modeled the total yield using a long pulse rate.

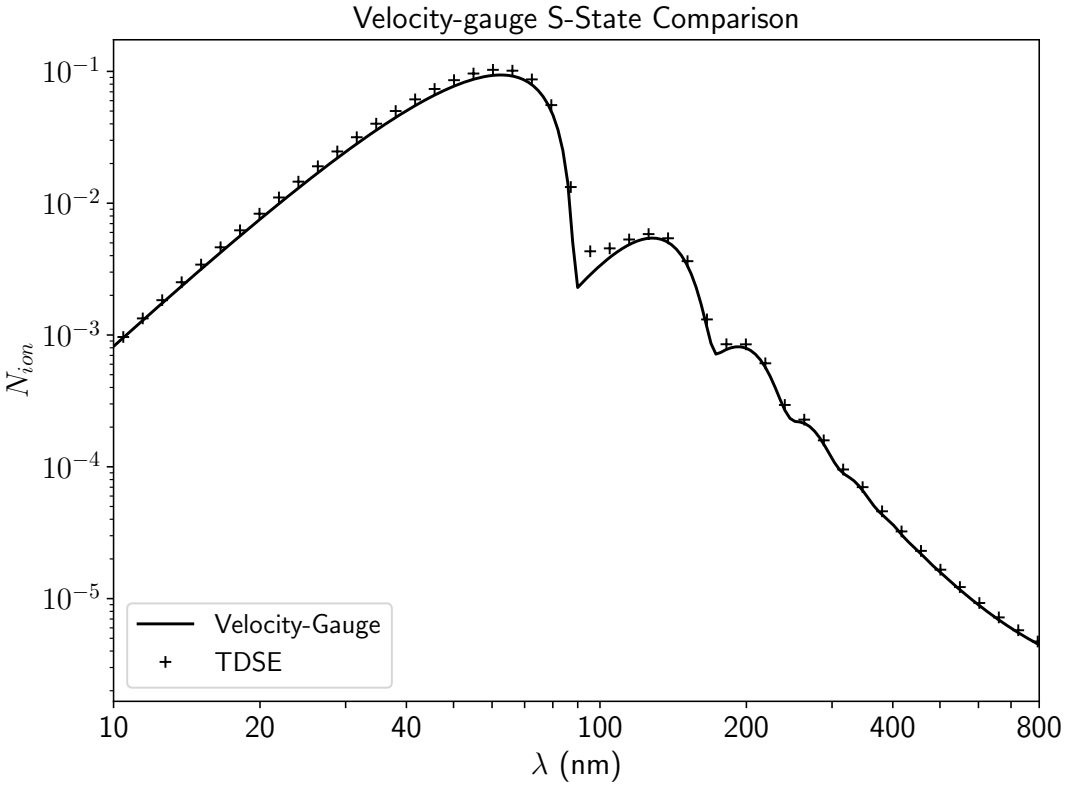

Figure 3.11: Comparison of the total ionization yield between the time-dependent Schrödinger equation (data from Fig. 3.9) and $s-$state Reiss' formulas [146]. The circularly polarized field has an intensity of $I = 1 \times 10^{14}$ W/cm^2, duration of 16 cycles and wavelengths between 10 nm and 800 nm.

For zero-range s-states and laser parameters considered, both the velocity-gauge expansion discussed here as well as the PPT expansions of section 3.6.2 are able to accurately describe the ionization yield. In Chapter 5 we will show that for ionization of an initial $p-$state, the velocity-gauge formulas discussed here fail at all wavelengths and the saddle point approximation applied to the PPT formulas is unable to accurately predict ionization across a large range of wavelengths. We will resolve this issue by integrating the length gauge rate of Keldysh [98] exactly using a similar expansion as used in this section.

Chapter 4

Selectivity in electron emission induced by ultrashort circularly polarized laser pulses

4.1 Introduction[1]

Spin polarization of atomic photo-electrons is an important aspect in exploring the structure of atoms, molecules and solids [99]. The generation of ultrashort spin-polarized electron pulses can be achieved by ionizing a gaseous atomic target with ultrashort circularly polarized laser pulses. These electron pulses are useful tools to characterize and probe chiral systems and magnetic properties of materials on an ultrafast time scale. Towards an understanding of the mechanisms behind the generation of spin-polarized electrons it is essential to study the sensitivity of the ionization probability on the sense of the electron's rotation in the initial state of the atom with respect to the helicity of the applied circularly polarized laser field [18, 77]. Thus, it is interesting to identify laser parameter regimes in which the ionization rate strongly depends on the number and/or the sign of the magnetic quantum number in the initial state.

Spin polarization of photo-electrons and the related dependence of atomic photoionization on the relative rotation between electrons in the initial state and the applied field has first been studied for single-photon ionization. While it was first believed that spin polarization of photo-electrons is a relativistic effect [141], Fano showed that electrons can be spin polarized in the nonrelativistic energy region as well [59]. In general, for single-photon ionization the emission

[1] Part of the material presented in this Chapter has been previously published in S. Walker, L. Kolanz, J. Venzke, and A. Becker, Physical Review A **103**, L061101 (2021) and in S. Walker, L. Kolanz, J. Venzke, and A. Becker, Physical Review Research **3**, 043051 (2021).

of electrons co-rotating with respect to the rotation of the electric field of the applied field is more likely than that of counter-rotating electrons. Stronger spin polarization was predicted for energy regions near Cooper minima. Experimental [26,79] and further theoretical [38] investigations supported these predictions by Fano. Preference of the emission of co-rotating over counter-rotating electrons has also been found in the ionization of atoms prepared in Rydberg states with microwave radiation [150, 180]. In the seventies and eighties of last century the quest for sources generating spin-polarized electrons continued along with the development of laser technology. Significant electron spin polarization has been predicted and observed in two- and three-photon ionization of atomic targets [8, 16, 49, 50, 60, 61, 70, 71, 104–106, 157]. At the corresponding laser frequencies the mechanism for spin polarization is related to intermediate resonances. The cross sections for near-resonant two- or three-photon ionization can be large if high-power lasers with narrow spectral bandwidth are available.

Using ultrashort laser pulses fine-tuning of the laser frequency to specific resonances is generally not possible and (near-)resonant effects, previously observed with lasers having a long pulse duration, are often less pronounced in the ultrashort pulse regime. However, in the highly non-perturbative tunneling regime of strong-field ionization a different selectivity in the emission of electrons on the sense of the electron rotation in the initial state has been predicted recently [18]. In contrast to the general observations in the single-photon ionization regime, strong-field tunnel ionization yields larger ionization probabilities for counter-rotating electrons than for those co-rotating with respect to the helicity of the applied field. The effect is due to nonadiabatic tunneling in which the two kind of electrons have, contrary to the standard assumption in strong-field tunneling theory, nonzero velocities at the exit of the tunnel barrier. This prediction sparked significant experimental [45, 52, 53, 77, 80, 85, 118, 158, 176] and theoretical [11–14, 17, 19–22, 24, 25, 35, 40, 44, 45, 74, 76, 82, 88, 90, 92–97, 110, 113–118, 122, 128, 166, 169, 170, 174–176, 179, 181, 182] interest over the last decade, including the observation of spin polarization of electrons of about 30%-50% for the interaction of atoms with laser pulses at 800 nm [21, 77, 158] and even larger one at about 400 nm [176].

The role of excited states on the selectivity in the emission of counter- versus co-rotating electrons has been investigated in a few studies [13, 25, 44, 82, 90, 166, 176, 182]. It has been shown that resonant excitation can lead to peaks in the helicity dependent enhancement of ionization at wavelengths in the deep multiphoton regime [182]. On- and off-resonance two-photon ionization of an inner p-sub-shell electron has been discussed in the context of fluorescence polarization [82]. More recently, experimental and theoretical work has demonstrated that at wavelengths of about 400 nm Freeman resonances [65] provide a scheme to separate counter-rotating electrons from co-rotating electrons in the photo-electron energy spectrum of xenon atoms [176]. In this case resonant ionization via an intermediate state close to the threshold, which is accessible to the counter-rotating electrons only, leads to a selection in the electron emission at a specific kinetic energy. Therefore, the scheme provides an opportunity to generate spin-polarized electrons by energy gating. Furthermore, strong asymmetries in the ionization with left- and right-handed circularly polarized light for the lithium atom prepared in the polarized $2p(m = +1)$ state has been observed [44]. In that combined experimental-theoretical study the emission of counter-rotating electrons is found to be favored when the wavelength is tuned to the $2p$–$3s$ transition. We have more generally analyzed the impact of resonant transitions via excited states, that – due to the selection rules – can only be accessed by counter-rotating electrons. As we will show below, these states act as doorway states in the few-photon ionization regime and are responsible for a dependence of the total ionization probability on the magnetic quantum number of the initial state which is stronger than those in both the single-photon and the tunneling regimes. The maximum ratios of total ionization of counter- over co-rotating electrons, found in the numerical calculations, are about ten to one, indicating the possibility to achieve a large selectivity in the overall electron emission.

More specifically, based on numerical solutions of the time-dependent Schrödinger equation we predict a surprisingly large enhancement in the emission of electrons, that are initially counter-rotating with respect to rotation of the applied field, during the interaction of rare-gas atoms with ultrashort circular polarized laser pulses in a previously unexplored wavelength regime [166, 167]. In order to determine the mechanism behind this surprising enhancement we performed additional

numerical calculations where specific emphasis was given to the intermediate-wavelength regime where the trend in the ionization probability of counter-rotating electrons strongly differs from those for electrons in the other two initial magnetic sub-levels. Theoretical analysis and numerical results indicate that the enhanced emission of counter-rotating electrons occurs via photon absorption channels, which are only accessible for electrons rotating opposite to the rotation direction of the external electric field. Physical mechanisms behind the enhancement are identified as threshold effects, in which the emission into continuum states with low angular momentum quantum numbers is favored, and resonant enhanced ionization involving transitions via specific excited states in the atom [166, 167].

4.2 Numerical methods

To study the dependence of strong-field ionization on the value and the sign of the magnetic quantum number, we have solved the TDSE for the interaction of an atom with an intense laser pulse in atomic units, where

$$i\frac{\partial}{\partial t}\Psi(\mathbf{r},t) = \left[-\frac{\nabla^2}{2} + \mathbf{E}(t)\cdot\mathbf{r} + V(r)\right]\Psi(\mathbf{r},t)\ . \tag{4.1}$$

Here, $V(r)$ is a single-active electron (SAE) model potential for an electron in the $2p$-shell in Neon and in the $3p$ shell in Argon given by:

$$V(r) = -\frac{1}{r} - \frac{Z_c e^{-cr}}{r} - \sum_j a_j e^{-b_j r}\ , \tag{4.2}$$

where for Neon, Z_C = 9, c = 2.0872, a_1 = −5.4072, a_2 = 1.0374, b_1 = 4.1537 and b_2 = 67.1114. Similarly for Argon Z_C = 17, c = 0.8472, a_1 = −15.3755, a_2 = −27.7431, a_3 = 2.1705, b_1 = 1.2484, b_2 = 4.3924 and b_3 = 87.9345. The potential has been constructed using a method for benchmarking tests between TDSE and time-dependent density functional theory calculations [143]. We will discuss general features in detail for Neon [167] and note that we have observed the exact same trends in Argon [166].

For the circularly polarized laser pulse we set the vector potential of the applied field as:

$$\mathbf{A}(t) = A_0 \sin^2\left(\frac{\pi t}{\tau}\right)\left[\sin(\omega_A t)\,\hat{\mathbf{x}} - \epsilon\cos(\omega_A t)\hat{\mathbf{y}}\right] \tag{4.3}$$

where $A_0 = \sqrt{c^2 I/(1+\epsilon^2)\omega_A^2}$, $\tau = \frac{2\pi N}{\omega_A}$, c is the speed of light, I is the peak intensity, N is the number of cycles in the pulse, and ω_A is the central frequency of the vector potential. This ensures that the electric field integrates to zero. ω_A is determined such that the spectral distribution of the E-field matches the given physical central frequency ω_E [164]. The electric field is obtained by

$$\mathbf{E}(t) = -\frac{1}{c}\frac{\partial}{\partial t}\mathbf{A}(t)\,. \tag{4.4}$$

We have considered a wavelength regime from 10 nm, which corresponds to ionization by a single-photon, to 1000 nm, corresponding to tunneling ionization. At all wavelengths we have applied intense laser pulses with a duration of 10-cycles and a peak intensity of 5×10^{14} W/cm^2. Without loss of generality we have chosen left-handed circularly polarized pulses (i.e. $\epsilon = -1$). In each calculation we have prepared the atomic system in one of the three magnetic sub-levels of the p-shell. Eq. (4.1) has been solved in three spatial dimensions by using previously discussed grid-based [163] and numerical basis-state methods [37, 168]. At the end of each simulation we have determined the population in the excited states, characterized by the quantum numbers n, l and m, via projection on the corresponding bound states of the atomic potential, which have been determined numerically. The ionization probability has then been evaluated as the difference between unity and the total probability left in the bound states.

In the grid-based method we have expanded $\Psi(\mathbf{r},t)$ in spherical harmonics up to $l_{max} = |m_{max}| = 40$ and discretized the radius using fourth order finite difference. The wave function has been propagated in time with a time step of 0.05 a.u., on a grid with spacing of 0.05 a.u., maximum radius of 500 a.u., and exterior complex scaling on the outer 25 a.u. of the grid using the Crank-Nicolson method to propagate the wave function in time. This method was mainly used for the simulations at long wavelengths.

In the numerical basis state method we have also expanded $\Psi(\mathbf{r},t)$ in spherical harmonics with $l_{max} = |m_{max}| = 40$ in a box with maximum radius of 500 a.u. The basis was generated by

diagonalizing the field-free Hamiltonian including a double-exponential complex absorbing potential [78] on the outer 50 a.u. of the domain using a second order finite difference method with a grid spacing of 0.03 a.u. In the calculations we have chosen a maximum principal quantum number n_{max} = 500 corresponding to a maximum energy per angular momentum block of about 4.9 a.u. The wave function is propagated in time using the Crank-Nicolson method with a time step of 0.05 a.u. We account for outgoing boundary conditions and the results have been checked against those of the grid-based approach. Transitions to occupied states other than the initial state have been prohibited in the basis code calculations.

4.3 Selectivity in electron emission

We first discuss concepts to enhance the emission probability of electrons from initial atomic states with different magnetic quantum numbers via photon absorption. The absorption of a photon from a left-handed circularly polarized field leads to changes of orbital angular and magnetic quantum numbers of $\Delta l = \pm 1$ and $\Delta m = -1$. The schematic representations in Fig. 4.1 show the allowed pathways for the absorption of the first three photons from initial (a) p and (b) d states.

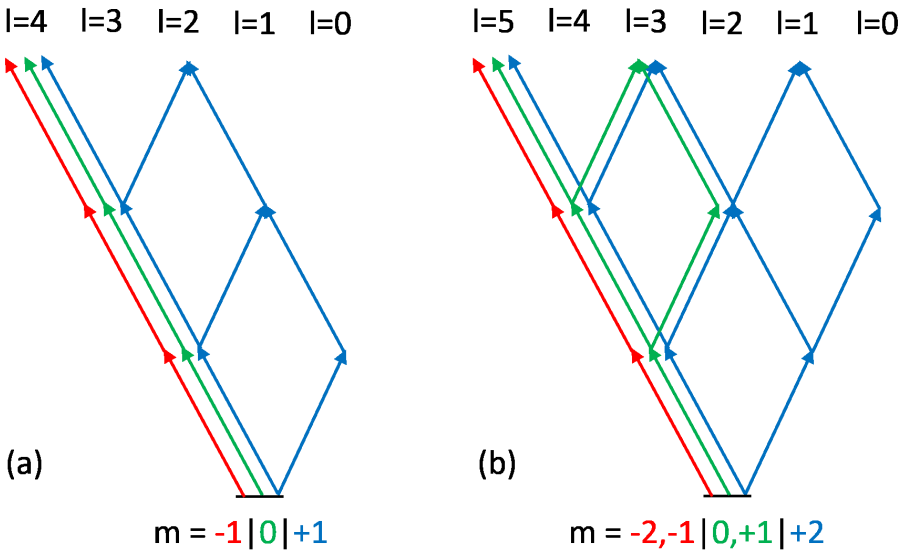

Figure 4.1: Photon absorption channels for interaction of a left-handed circularly polarized laser field ($\Delta l = \pm 1$, $\Delta m = -1$) with an atom in initial (a) p (red: $m = -1$, green: $m = 0$, blue: $m = 1$) and (b) d state (red: $m = -2, -1$, green: $m = 0, 1$, blue: $m = 2$) [167].

In the case of an initial p state (Fig. 4.1(a)) for electrons in each of the three magnetic sub-levels transitions with $\Delta l = 1$ are allowed leading to a successive increase of the orbital angular quantum number with the absorption of each photon, where additional photon absorption channels are accessible for the counter-rotating electrons (here, electrons in the initial $m = 1$ level, blue arrows). For example, for a counter-rotating electron the absorption of a (left-handed circularly polarized) photon induces a change in magnetic quantum number to $m = 0$ and therefore transitions into both $l = 2$- and $l = 0$-levels are allowed. In contrast, for the other two initial sub-levels only the transition to $l = 2$ is possible. Similar considerations hold for the absorption of additional photons. If the probability via these additional channels can be enhanced, we should therefore expect a strong selectivity of the emission of counter-rotating electrons in the interaction with a circularly polarized laser field. As our results below indicate this can be achieved either near the thresholds of photon absorption (section 4.3.2) or via intermediate resonances which act as doorway states accessible for the counter-rotating electrons only (section 4.3.3). These additional pathways

to ionization have been also mentioned in Refs. [13, 25, 44, 82, 90, 166, 176]. Resonant transitions via different pathways for counter-rotating electrons in two-photon ionization has been discussed in Refs. [82, 90]. Since selective emission via these additional pathways does not rely on a splitting of energy levels, the enhancement can be achieved independent of the duration of the applied laser pulse, which is interesting for the generation of ultrashort spin-polarized electron pulses.

With our numerical results presented below we study the applicability of these concepts for the initial $2p$ state in the neon atom, similar results have been found for argon atom as well [166]. Reasoning along similar lines as above can be however done for initial states with a larger orbital angular momentum number as well, as it is illustrated for an initial d state in Fig. 4.1(b). Besides the $\Delta l = 1$ pathway, which is open for electrons from each of the five initial m-levels, additional pathways are available for electrons from the initial levels with $m = 0, 1$ (red arrows) and even more for those from the $m = 2$ state (blue arrows). Thus, by identifying specific frequency regions in which the transition probability via one or some of these additional pathways is large one can expect an enhancement in the emission of certain groups of electrons.

4.3.1 General trends

In Fig. 4.2 we present the numerical results for the ionization probability from the three $2p$ orbitals of neon-like atom as a function of wavelength in a 10-cycle left-handed circularly polarized laser pulse at peak intensity of 5×10^{14} W/cm^2. P_+, where the index denotes the magnetic quantum number of the initial orbital ($m = 1$, $2p_+$, stars with line), corresponds to the ionization probability for counter-rotating electrons, while P_- (circles with line) is the one for co-rotating electrons and P_0 (squares with line) denotes the ionization probability for the initial state with $m = 0$.

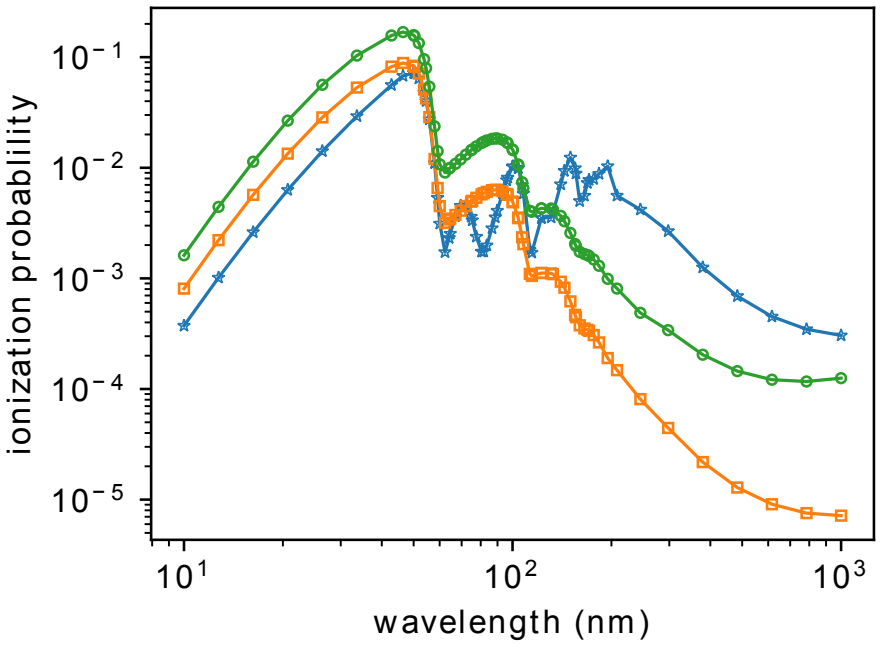

Figure 4.2: Ionization probabilities P_+ (stars with line), P_0 (squares with line), and P_- (circles with line) as function of wavelength for neon-like atom at 5×10^{14} W/cm^2 interacting with 10-cycle left-handed circularly polarized laser pulses [167].

There are a few general trends which we will discuss before we further analyze more specific features in the next subsections. In the short wavelength regime the single-photon ionization probability for each of the three sub-shells increases approximately proportional to $\lambda^{7/2}$, as it is expected at large photon energies based on the Born approximation [32]. In agreement with earlier work [59, 104] for single-photon transitions co-rotating electrons are easier to ionize than counter-rotating electrons, while the ionization probability for the initial orbital with $m = 0$ remains in between those for the other two sub-shells (section 4.3.2). The differences in the trends of the ionization probabilities near the one-photon threshold will be discussed in section 4.3.2.

In the two-, few- and multiphoton ionization regime the dependencies of P_- and P_0 on the wavelength remain rather similar. As discussed out the outset of section 4.3 (c.f., Fig. 4.1(a)), for electrons in initial p_- and p_0 states absorption of photons is allowed through the pathway with

$\Delta l = 1$ only. Therefore, the absorption of N photons results in the final state with $l_f = N + l$ and $m_f = m - N$, where l is the angular momentum quantum number of the initial state. In lowest order perturbation theory the transition amplitudes for both initial states share identical intermediate reduced matrix elements and differ from each other only by a $3j$ symbol. A perturbative scaling law for the ratio of ionization probabilities via the $\Delta l = +1$ pathway for electrons in initial states (l, m) and (l, m') is therefore given by

$$\frac{P_m}{P_{m'}} = \prod_{k=1}^{N_{min}} \frac{\begin{pmatrix} l+k & 1 & l+k-1 \\ k-m & -1 & m+1-k \end{pmatrix}^2}{\begin{pmatrix} l+k & 1 & l+k-1 \\ k-m' & -1 & m'+1-k \end{pmatrix}^2}, \tag{4.5}$$

where $N_{min} = \lceil I_p/\omega \rceil$ is the minimum number of photons absorbed and I_p is the field free ionization potential. Using

$$\begin{pmatrix} l+k & 1 & l+k-1 \\ k-m & -1 & m+1-k \end{pmatrix} = (-1)^{l-m} \sqrt{\frac{(2k+l-m-1)(2k+l-m)}{(2k+2l-1)(2k+2l)(2k+2l+1)}}, \tag{4.6}$$

we get

$$\frac{P_m}{P_{m'}} = \prod_{k=1}^{N_{min}} \frac{(2k+l-m-1)(2k+l-m)}{(2k+l-m'-1)(2k+l-m')} = \frac{(l-m')!(2N_{min}+l-m)!}{(l-m)!(2N_{min}+l-m')!}. \tag{4.7}$$

Thus, for an initial p state with $l = 1$ we have

$$\frac{P_0}{P_-} = \frac{1}{N_{min}+1} \tag{4.8}$$

and

$$\frac{P_+(l_f = N_{min}+1)}{P_-} = \frac{1}{(N_{min}+1)(2N_{min}+1)}, \tag{4.9}$$

where $P_+(l_f = N_{min}+1)$ is the perturbative ionization probability for counter-rotating electrons along the $\Delta l = +1$ pathway only.

The comparison in Fig. 4.11(a) shows that the numerical results for P_0/P_- (circles with line) overall agree well with the perturbative scaling law (solid line, Eq. (4.8)) at the shorter wavelengths. The differences near the photon absorption thresholds are due to the bandwidth of the short pulse

used in the calculations. The deviation at large wavelengths indicates the transition to the tunneling regime. In this regime the numerical results for P_0/P_- agree rather well with predictions based on nonadiabatic tunneling theory (dotted line in Fig. 4.11(a), [18, 20]):

$$\frac{P_0}{P_-} = \sqrt{\frac{I}{16 I_p^3}\frac{1+\gamma^2}{\zeta_0^2+\gamma^2}}\frac{\gamma^3(\zeta_0-1)^2(\zeta_0+1)}{\left(\sqrt{\zeta_0^2+\gamma^2}-\zeta_0\sqrt{1+\gamma^2}\right)^2}\,, \tag{4.10}$$

where I is the laser intensity, γ is the Keldysh parameter and ζ_0 is determined by

$$\sqrt{\frac{\zeta_0^2+\gamma^2}{1+\gamma^2}} = \tanh\left(\frac{1}{1-\zeta_0}\sqrt{\frac{\zeta_0^2+\gamma^2}{1+\gamma^2}}\right). \tag{4.11}$$

In contrast, the results for P_+/P_- (circles with line) in Fig. 4.11(b) show a deviation from both the perturbative scaling law (solid line, Eq. (4.9)) and the prediction of the nonadiabatic tunneling theory (dotted line, [18, 20]):

$$\frac{P_+}{P_-} = \left(\frac{\sqrt{\zeta_0^2+\gamma^2}+\zeta_0\sqrt{1+\gamma^2}}{\sqrt{\zeta_0^2+\gamma^2}-\zeta_0\sqrt{1+\gamma^2}}\right)^2 \tag{4.12}$$

in the intermediate two- and few-photon ionization regime. Here, P_+/P_- changes by two orders of magnitude, reversing from 1:10 to 10:1. An enhancement of the emission of counter-rotating electrons in the few-photon ionization regime has also been observed in numerical results for strong-field detachment of F^- [13]. As we will discuss in the next subsections, for the present results the strong variation in the ratio can be explained as due to the impact of the additional pathways available for the counter-rotating electrons (c.f., Fig. 4.1(a)). From the results in Fig. 4.11(b) we can identify that these pathways should have a strong impact at the one- and two-photon ionization thresholds, the region at about 70 nm and the few-photon ionization regime.

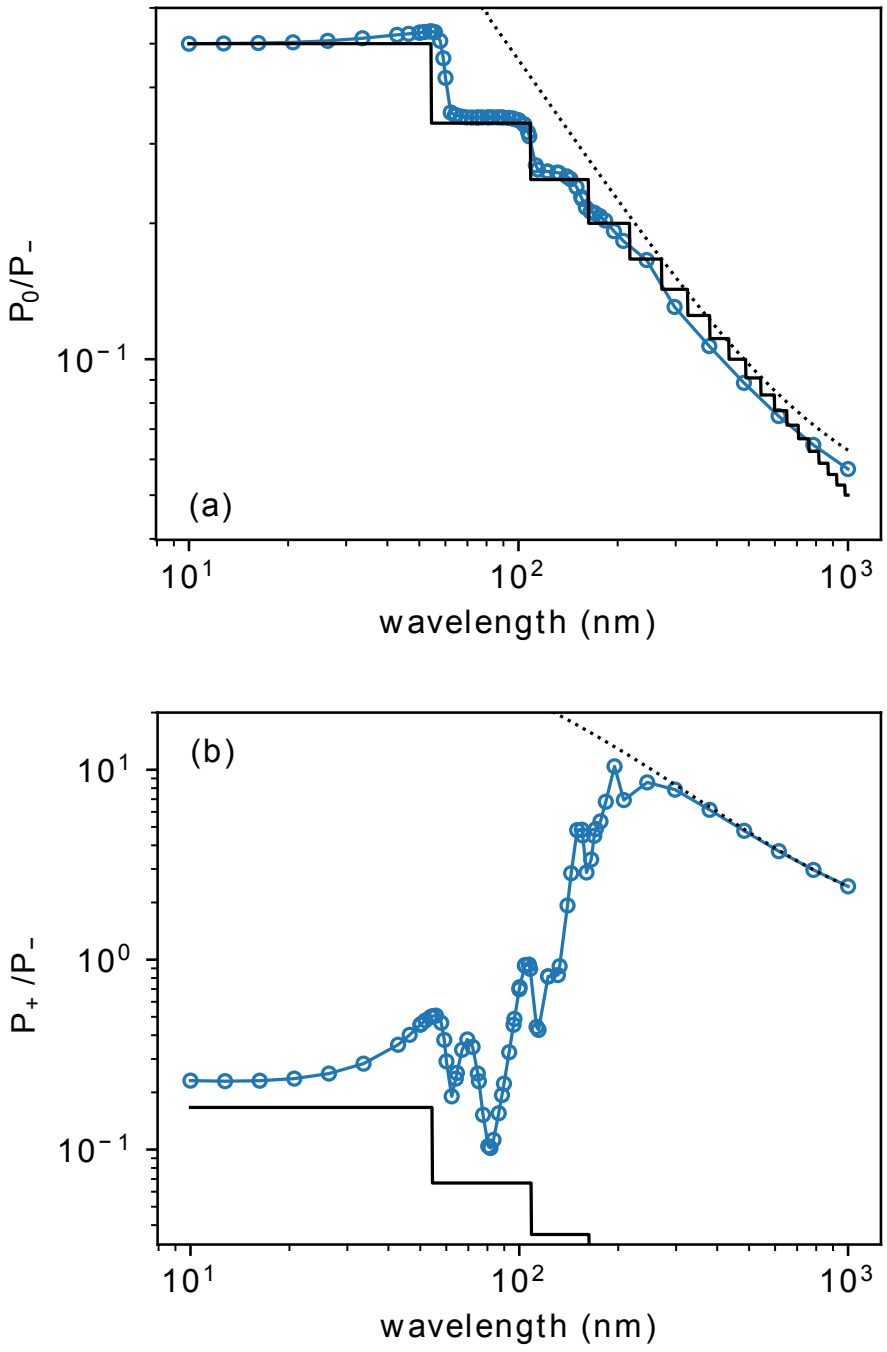

Figure 4.3: Comparison of numerical results (circles with line) for the ratios (a) P_0/P_- and (b) $P_+(l_f = N_{min} + 1)/P_-$ with the scaling laws from lowest order perturbation theory for $\Delta l = 1$ pathway (solid lines, Eqs. (4.8,4.9)) and those from nonadiabatic tunneling predictions (dotted lines, Eqs. (4.10,4.12)) as function of wavelength. Laser parameters are the same as in Fig. 4.2 [167].

Before proceeding, we note that the present numerical results agree well with the predictions of the nonadiabatic tunneling theory at long wavelengths. A similar degree of agreement has been reported before for results from an analytical R-matrix theory [94], 2D-TDSE calculations [17] and the R-matrix with time dependence method [13]. Furthermore, the results of the analytical R-matrix theory [94] indicate a maximum in the P_+/P_- ratio as well, which occurs in a wavelength regime close to that one where the maximum is found in the present results. Finally, we note that the trend of the results for P_+ and P_- in Figs. 4.2 and 4.11(b) near 1000 nm may indicate that the relative emission probability of counter- versus co-rotating electrons reverses at even longer wavelengths. Such a reversal has been predicted in past theoretical studies [174, 182].

4.3.2 Ionization thresholds and two-photon ionization

At wavelengths near the one-photon ionization threshold the relative probability for emission of counter-rotating electrons increases as compared to those from the initial levels with $m = -1$ and $m = 0$. This can be seen from the ratios P_+/P_- (Fig. 4.4(b), stars with line) and P_+/P_0 (Fig. 4.4(c), stars with line). The enhancement is due to the fact that for small photo-electron energies the transition in the continuum is favored for final states with low angular momentum quantum numbers [32]. Since transitions into continuum states with $l_f = 0$ are only allowed for counter-rotating electrons (Fig. 4.4(a)) the emission of those electrons is enhanced near the threshold, which raises the two ratios. This interpretation is verified by the comparison with reduced ratios, in which we deliberately neglected the probability for the channel to one of the final states in the P_+ results. To this end, we have computed the continuum populations for a certain angular momentum by projecting the wave function onto the corresponding continuum functions used in the basis method and adding these coefficients squared. The reduced ratios show the dominant emission in the $l_f = 2$-channel (squares with line) and the $l_f = 0$-channel (circles with line) at short wavelengths and near the threshold, respectively.

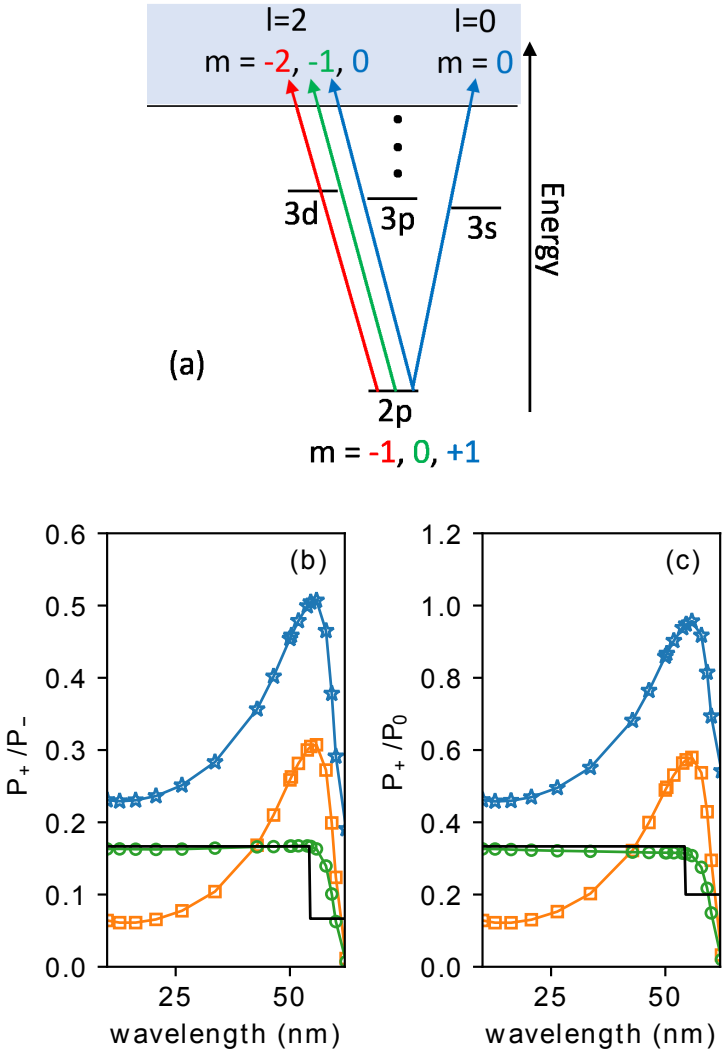

Figure 4.4: Upper row: (a) Channels for single-photon ionization. Lower row: Comparison of ratios (b) P_+/P_- (stars with line), $P_+(l=2)/P_-$ (circles with line), and $P_+(l=0)/P_-$ (squares with line), and (c) P_+/P_0 (stars with line), $P_+(l=2)/P_0$ (circles with line) and $P_+(l=0)/P_0$ (squares with line) as function of wavelength. Also shown are the predictions based on lowest order perturbation theory for the $\Delta l = 1$ channels (solid lines without symbols, Eqs. (4.8,4.9)) [167].

The same effect explains the enhancement in the emission of counter-rotating electrons for wavelengths near and just above 100 nm, at which the two-photon ionization channel closes. Since the pathway into the $l_f = 1$-channel is allowed for the counter-rotating electrons only (Fig. 4.5(a)),

predominant emission of counter-rotating electrons into the final channel with the lowest possible angular momentum quantum number enhances the ratio of P_+/P_- and P_+/P_0 near the threshold (Fig. 4.5(b,c)).

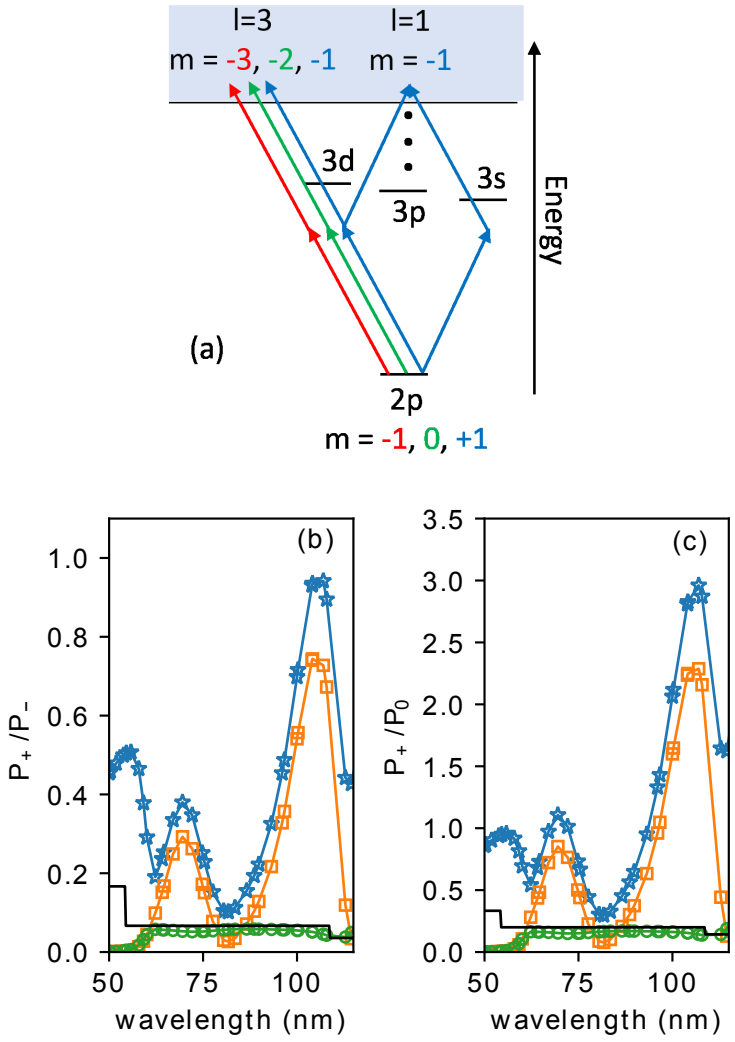

Figure 4.5: Upper row: (a) Channels for two-photon ionization. Lower row: Comparison of ratios (b) P_+/P_- (stars with line), $P_+(l = 3)/P_-$ (circles with line), and $P_+(l = 1)/P_-$ (squares with line), as well as (c) P_+/P_0 (stars with line), $P_+(l = 3)/P_0$ (circles with line) and $P_+(l = 1)/P_0$ (squares with line) as function of wavelength. Also shown are the predictions in lowest order perturbation for the $\Delta l = 1$ channels (lines without symbols) [167].

The impact of the channels with lowest angular momentum quantum number in the final state can be also investigated via photo-electron angular distributions. For ionization along the $\Delta l = 1$ pathway, available for all electrons, we expect an angular distribution proportional to the spherical harmonics $|Y_2^{m-1}|^2$ (for single photon ionization) and $|Y_3^{m-2}|^2$ (for two-photon ionization). As can be seen, from the comparison of the numerical results in Fig. 4.6, obtained at the one-photon (left column, 53.8 nm) and the two-photon threshold (right column, 104.12 nm), this is the case for ionization from both $2p_0$ (panels (b) and (e)) and $2p_{-1}$ (panels (c) and (f)). In contrast, the angular distributions for the counter-rotating electrons at the one-photon threshold (Fig. 4.6(a)) show signatures of an interference. Specifically, in the projections it is seen that the node that would occur for a pure $|Y_2^0|^2$ distribution is not present. This indicates the presence of an interference with a spherical harmonic having a different, here lower, angular momentum, as expected. At the two-photon threshold the contribution from $l = 3$ is significantly smaller than that from $l = 1$ so interference is barely visible in the photo-electron angular distributions (Fig. 4.6(d)).

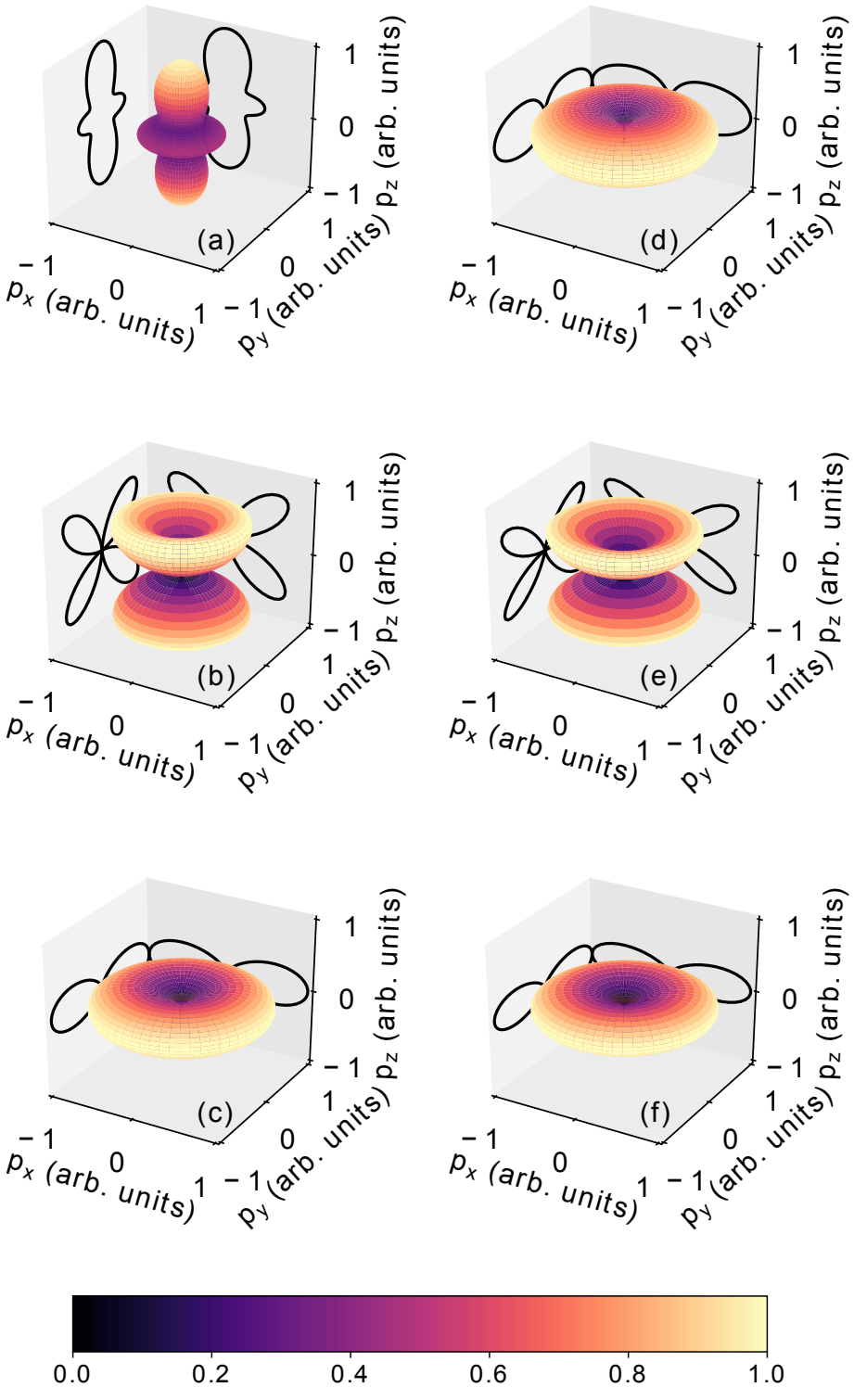

Figure 4.6: Comparison of photo-electron angular distributions for ionization from initial state $m = 1$ (a,d), $m = 0$ (b,e) and $m = -1$ (c,f) near one-photon (a-c: 53.8 nm) and two-photon (d-f: 104.12 nm) threshold [167].

The enhancement in the P_+-yield and the corresponding ratios at a wavelength of about 70 nm in the two-photon ionization regime is due to resonant ionization via the intermediate $3s$ doorway state. While transition into the $3d$ state is allowed from all three initial states via the absorption of one left-handed circularly polarized photon, the $3s$ state is only accessible for electrons in the initial $2p_{-1}$ state (c.f., Fig. 4.1(a)). Indications for the impact of the doorway state are given by the ratios $P_+(l_f = 1)/P_-$ and $P_+(l_f = 1)/P_0$ in Fig. 4.5(b,c) and the large population in the $3s$ state for ionization from the initial $2p_+$ state at the end of the pulse (Fig. 4.7(a)). The relative importance of resonant transition via s and d states in the two-photon ionization regime has also been discussed for interaction of counter-rotating electrons prepared in excited $2p$ state in hydrogen atom [90]. Similarly, an enhancement in the emission of counter-rotating electrons has been observed for a resonant $2p-3s$ transition in the three-photon ionization of lithium atoms, prepared in the polarized $2p(m = +1)$ state [44]. Together, the data clearly support the interpretation that the resonant ionization pathway, which is accessible for the counter-rotating electrons only, is the origin for the enhancement in the P_+-yield. The comparison with the final populations in the states of the $n = 3$-level for the other two initial states in Fig. 4.7(b,c) show that in those cases only the $3d$ state is populated and the population decreases as a function of wavelength in the two-photon ionization regime.

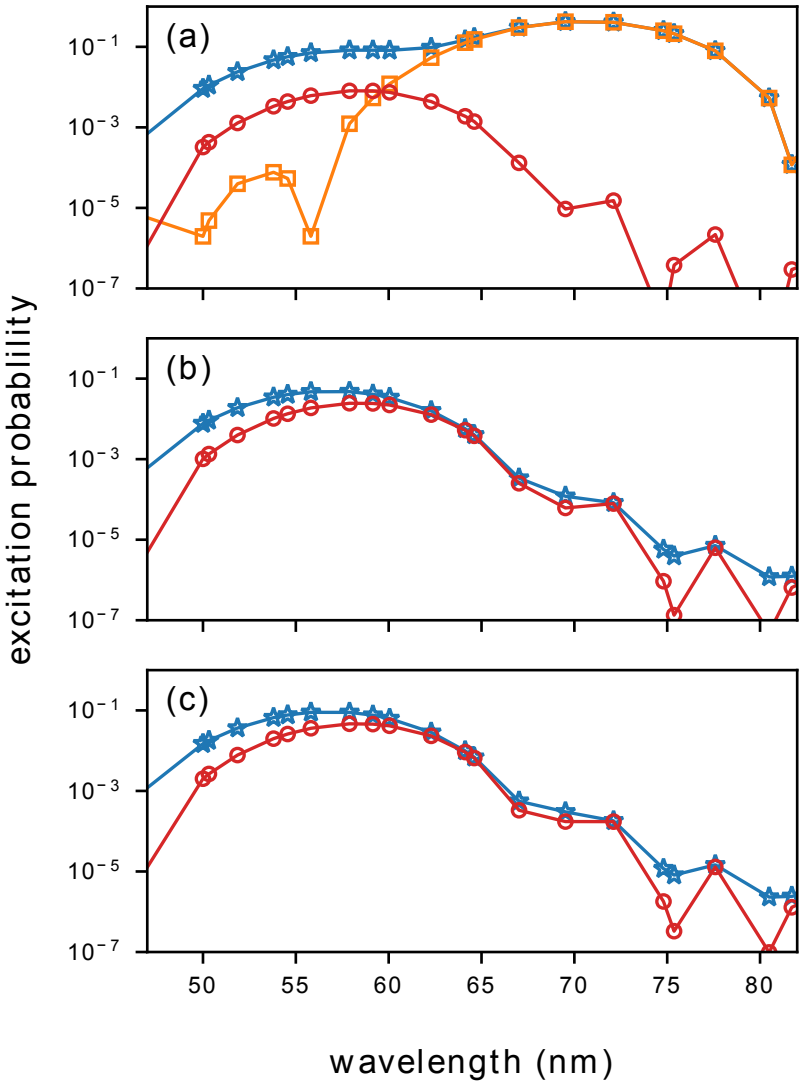

Figure 4.7: Excitation probabilities in $3s$ (orange squares), $3d$ (red circles) and all states (blue stars) for ionization from initial states (a) $2p_1$, (b) $2p_0$ and (c) $2p_{-1}$ for neon-like atom at 5×10^{14} W/cm^2) interacting with 10-cycle laser pulses [167].

4.3.3 Doorway states in few-photon ionization regime

In contrast to the two-photon ionization regime, for few-photon ionization states in the $n = 3$-level can only be accessed by the counter-rotating electrons, as shown in the two schemes in Fig. 4.8. Corresponding to each of these additional pathways one can expect resonant enhanced ionization in the P_+-yield. In contrast, there are no pathways for resonant enhanced ionization via the $n = 3$

states for electrons in the other initial states.

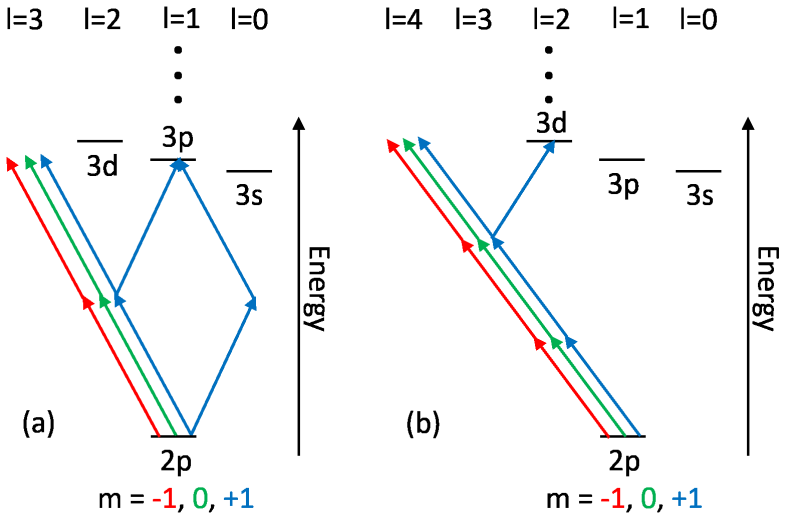

Figure 4.8: (a) Two- and (b) three-photon transitions into doorway states in the n = 3 shell from initial $2p_1$ state. Other non-resonant transitions are also shown using same arrow styles as in Fig. 4.1 [167].

The importance of the resonant transitions is supported by the results of our numerical calculations in Fig. 4.9. The comparison of the total and $3l$-excitation probabilities for the three initial states at the end of the pulse shows the stronger role of the overall excitation for counter-rotating electrons (Fig. 4.9(a)) as compared to the other initial states (Fig. 4.9(b,c)) in the wavelength regime between 100 nm and 200 nm. It is also seen that a major part of the total excitation arises from populations in either the $3p$-level (two photon resonant transition) or the $3d$-level (three photon resonant absorption). In contrast, there is only very small final population in the $3d$ state for the other two initial states. This population arises from one-photon transitions due to the broad bandwidth of the ultrashort pulse. Similarly, we see some small population in the $3s$ state due to one-photon absorption for the initial $2p_1$ state.

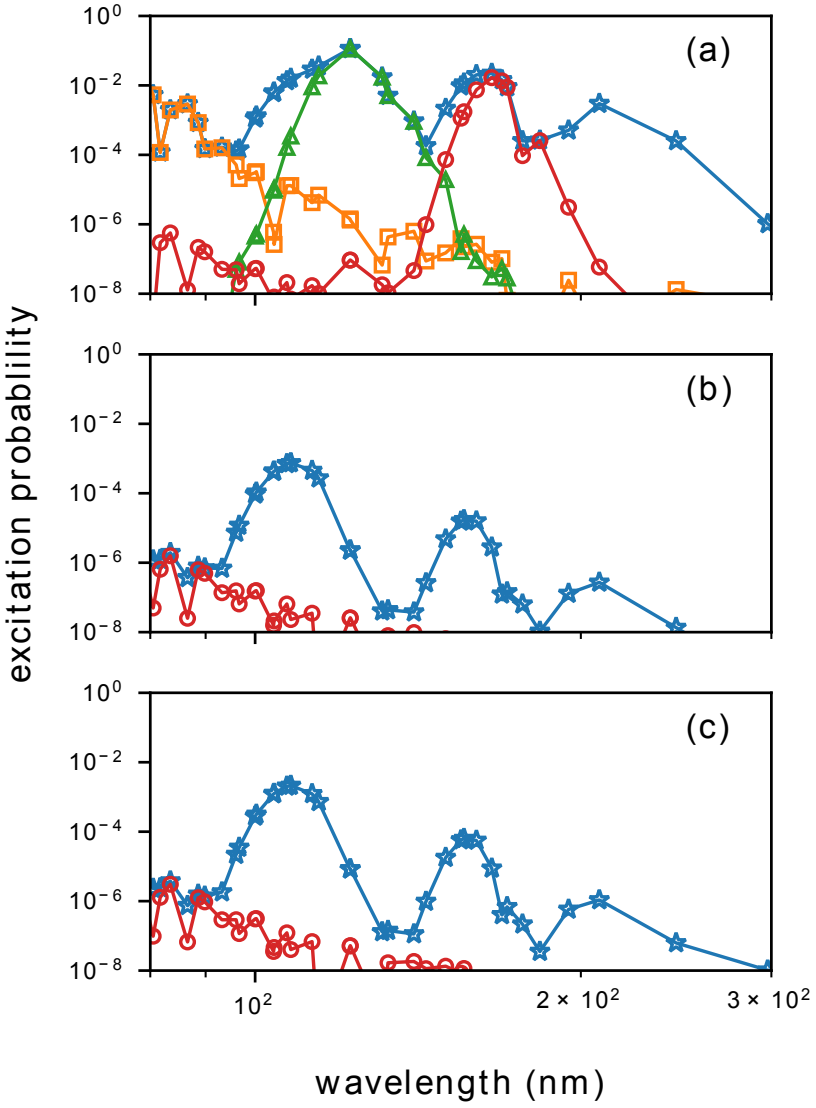

Figure 4.9: Comparison of excitation probabilities in $3s$ (orange squares), $3p$ (green triangles), $3d$ (red circles) with total excitation probability (blue stars) from initial states (a) $2p_1$, (b) $2p_0$ and (c) $2p_{-1}$ for neon-like atom with 10-cycle laser pulses at peak intensity 5×10^{14} W/cm^2) [167].

The remaining part of the total excitation probabilities for the counter-rotating electrons as well as the contributions for the other initial states arise from higher excited states. This is shown in Fig. 4.10, where we present the corresponding populations in states with $n \geq 4$, separately for each l-quantum number up to $l = 6$ (i states). The excitation for the initial states with (b) $m = 0$ and (c) $m = -1$ both solely arise from the f- (at about 110 nm), g- (~ 170 nm), h- (~ 200 nm), and i–levels

(~ 240 nm), confirming that mechanism and pathway to excitation and ionization from these two states are similar. The population of levels with successively larger l-value in separate regimes, as the wavelength increases, is in agreement with the interpretation of a resonant enhancement along the $\Delta l = 1$ pathway. In contrast, the results for the counter-rotating electrons (Fig. 4.10(a)) again indicate the strong impact of the additional pathways. In this case the populations in the excited states along the $\Delta l = 1$ pathway do not provide significant contributions to the total excitation probability. For example, the population in the nf states (purple crosses) at about 110 nm for initial state $m = 1$ is smaller than the populations in the corresponding states for the interaction with the other two initial states. However, its contribution to the total excitation probability is negligible. Instead, the populations in the excited states with lower l are, in general, by about two orders of magnitude stronger than those with the higher l's. This observation agrees with theoretical results for on-resonance two-photon ionization of an inner atomic np-sub-shell by a circularly polarized light field [82].

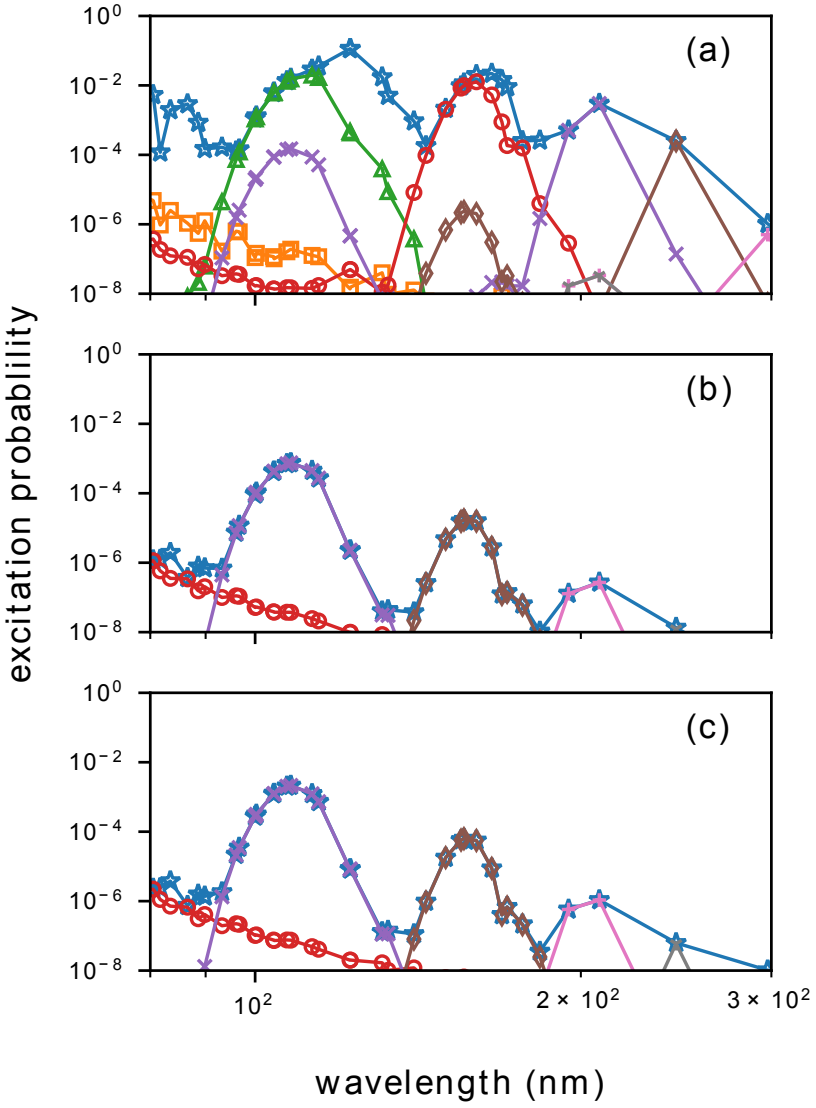

Figure 4.10: Same as Fig. 4.9 but for ns (orange squares), np (green triangles), nd (red circles), nf (purple crosses), ng (brown diamonds), nh (pink plus signs), and ni (grey 3 pointed stars) states with $n \geq 4$. Total excitation probabilities are represented by blue 5 pointed stars [167].

4.3.4 Application to Argon atoms

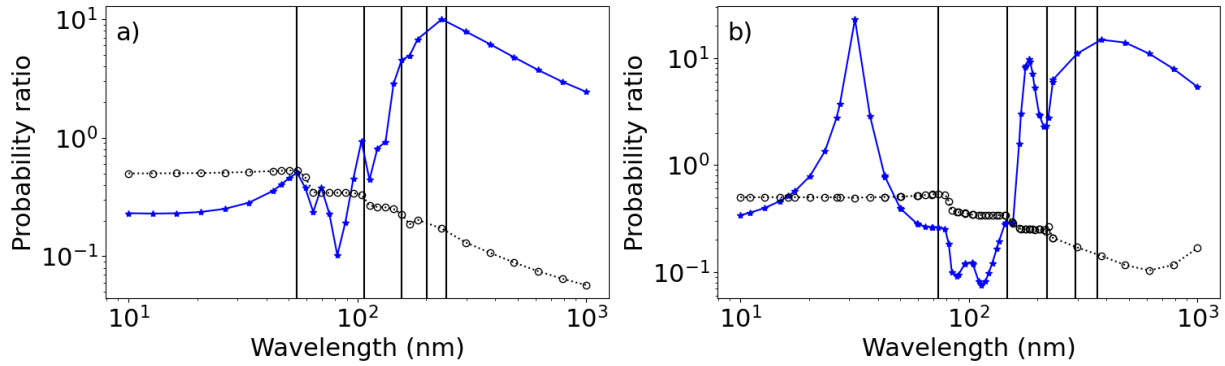

Figure 4.11: Ratio P_+/P_- (stars with solid lines) and P_0/P_- (open circles with dotted lines) as a function of wavelength for (a) neon-like atom (5×10^{14} W/cm^2) and (b) argon-like atom (5×10^{13} W/cm^2) interacting with 10-cycle laser pulses [166].

In general, the results for an argon-like atom can be interpreted in the same way as those for the neon-like atom. A few additional features arise due to the more complex level structure among the doorway states closest in energy to the initial $3p$-levels.

In Fig. 4.11, we plot the P_+/P_- ratio (solid blue line) and P_0/P_- ionization ratio (solid black line) now for both neon atoms (panel a) and argon atoms (panel b), where all laser parameters in the case for argon have been chosen identically to the neon-like case except the use of a reduced laser intensity of 5×10^{13} W/cm^2. The large maximum in the single-photon regime for the argon-like atom at about 30 nm and several of the small maxima in the two-photon regime for both atoms are due to the Cooper minimum and resonant transitions, respectively. These signals are therefore short-pulse features of the effects studied for continuous lasers or long pulses in earlier studies [59, 104]. Here, the vertical solid lines correspond to ionization thresholds where a maxima in the co- vs. counter-rotating ratio for both neon and argon atoms again lies approximately at the five-photon ionization threshold corresponding to the transition between tunneling and multiphoton ionization.

When analyzing the P_0/P_- ratio we again see the perturbative scaling law, Eq.(4.8), where the effects of resonances and Cooper minima are not observed. We must note that the upward slope of the ratio in Fig.(4.11 b) above 600 nm is likely a convergence error in the numerical results but does not alter our results and analysis.

4.4 Summary

To summarize, we have performed ab-initio numerical calculations of the time-dependent Schrödinger equation to study the dependence of the interaction of argon- and neon-like atoms [166, 168] with an intense ultrashort circularly polarized laser pulse on the magnetic quantum number of the initial state. In our analysis we have considered a broad wavelength regime, ranging from single-photon to tunneling ionization. The numerical results for ionization of electrons co-rotating with respect to the rotation direction of the field and those from the initial level with $m = 0$ agree well with the predictions from lowest order perturbation theory at short and nonadiabatic tunneling theory [18,20] at long wavelengths. In contrast, the data for the counter-rotating electrons deviate significantly from both these predictions in the intermediate wavelength regime.

At the one- and two-photon ionization thresholds the enhancement in the emission of counter-rotating electrons can be explained via the transition into channels with low angular momentum quantum number in the continuum, which are accessible for these type of electrons only. Further increase in the ionization yield for counter-rotating electrons (Fig. 4.2) and in the ionization ratio of counter- over co-rotating electrons (Fig. 4.11(b)) in the two- and few-photon ionization regime comes along with much stronger excitation probabilities found for the interaction of counter-rotating electrons with a circularly polarized short laser pulse. Together with the finding that the population is mainly in excited states with lower angular momentum quantum number our results indicate that resonant enhanced ionization via specific pathways and doorway states, which are accessible for the counter-rotating electrons only, is the physical mechanism behind the enhancement. The overall similar trends in ionization and excitation probabilities for initial states with $m = 0$ and $m = 1$, from which none of the doorway states can be excited, further support this interpretation.

The additional pathways for counter-rotating electrons exist in all atoms with ground states having $l \geq 1$ and may therefore provide an alternative route towards the generation of ultrashort spin-polarized electron pulses. Energy gating of the photo-electrons, as proposed and demonstrated in Ref. [176], can even further enhance the selectivity in the ionization process. Increasing the wavelength beyond the few-photon ionization regime, the excitation probability becomes less relevant due to the large number of photons needed for resonant transitions into excited states close to the threshold. Correspondingly, the relative strength of the emission of counter-rotating over co-rotating electrons gets significantly smaller, decreasing from a ratio of ten to one at 250 nm to less than three to one in the tunneling regime at 1000 nm (Fig. 4.11(b)).

Chapter 5

Extending the theory of strong-field ionization into the UV limit

Our recent work [166,167] discussed in the previous Chapter motivated us to seek out accurate models of strong field ionization from a general initial state at arbitrary photon energies. The current approach involves expanding the Keldysh ionization amplitude [98] in Fourier components (in time) and partial waves (in space). We are able to describe the strong field process in terms of photon absorption pathways and angular momentum selection rules. Almost exact results for the ionization of electrons bound to short range potentials in the presence of a strong circularly polarized field at an intensity of $I = 1 \times 10^{14}$ W/cm^2 and with wavelengths between 10 and 800 nm are found in comparison with ab-initio numerical TDSE simulations. We will, in particular, discuss the correct choice of states in the 10-200 nm wavelength regime where the asymptotic tail of the wave-function alone cannot describe ionization.

5.1 Circular polarization

In section 3.6.2, we summarized the results of Refs. [20, 136], for the ionization of electrons bound by short-range potentials for the case of a strong circularly polarized field. The success of these formulas was then demonstrated in Fig. 3.9, where satisfactory agreement was found with numerical solutions of the TDSE applied to a 16-cycle laser pulse with an intensity of $I = 1 \times 10^{14}$ W/cm^2 and wavelengths between 10 nm and 800 nm. Discrepancies were observed near ionization thresholds since we did not include the pulse envelope, and at the short (10 nm) limit due to the use of the quasi-classical saddle point approximation. Errors of the first kind are well understood and

may be resolved using rate equations and numerical time integration including the pulse envelope. In this section we will discuss errors of the second kind introduced by the use of saddle points.

5.1.1 Short-wavelength breakdown of the saddle point approximation

In Fig. 5.1 we integrate the length gauge amplitude exactly in time (Eq. (5.42)) to demonstrate short-wavelength errors introduced by the saddle-point approximation. The exact results will be derived in the subsequent section. In the left panel of Fig. 5.1 we compare the saddle point PPT result of section 3.6.2, as also shown in Fig. 3.9, to the exact same amplitude without the approximation for an initial s-state. It is clear that for nearly all wavelengths longer than the single photon ionization threshold (~ 92 nm), both the exact (black curve) and the approximate amplitude (red dashed curve) predict essentially the same results.

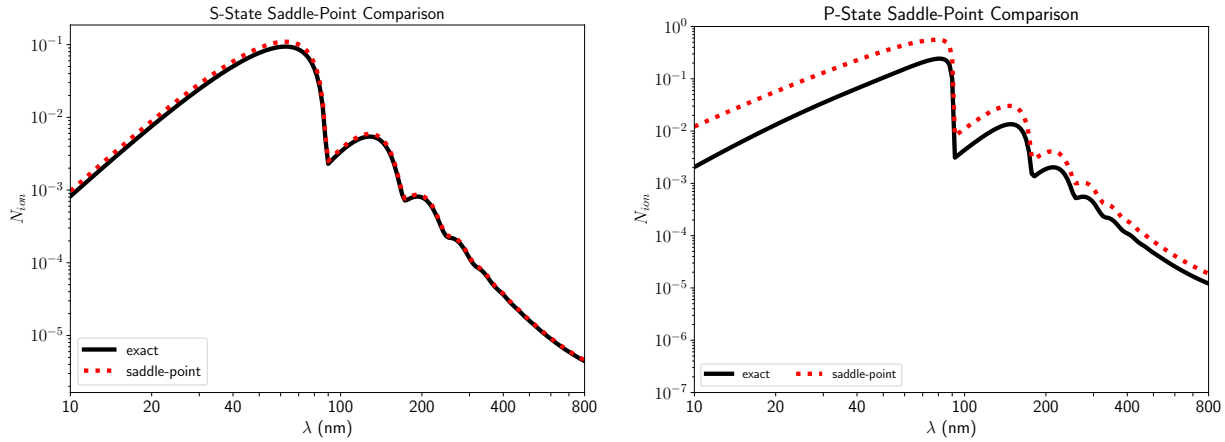

Figure 5.1: Total ionization yield for the length gauge amplitude (sections 3.6.1 and 3.6.2) corresponding to a 16 cycle laser pulse with an intensity of 10^{14} W/cm^2. Results are compared between the saddle-point approximation (red dashed curve) and the exact time integration (solid black curve) for s-states (left panel) and p-states (right-panel).

In contrast, in the right panel of Fig. 5.1 the same comparison is done for initial p-states, where it is clear that the exact (black curve) and the approximate amplitude (red dashed curve)

disagree over almost the entire wavelength regime considered. To further explore this behavior we decompose the ionization yield into contributions corresponding to each of the three initial states $m = -1, 0$ and 1 where the field is assumed to be right handed circularly polarized.

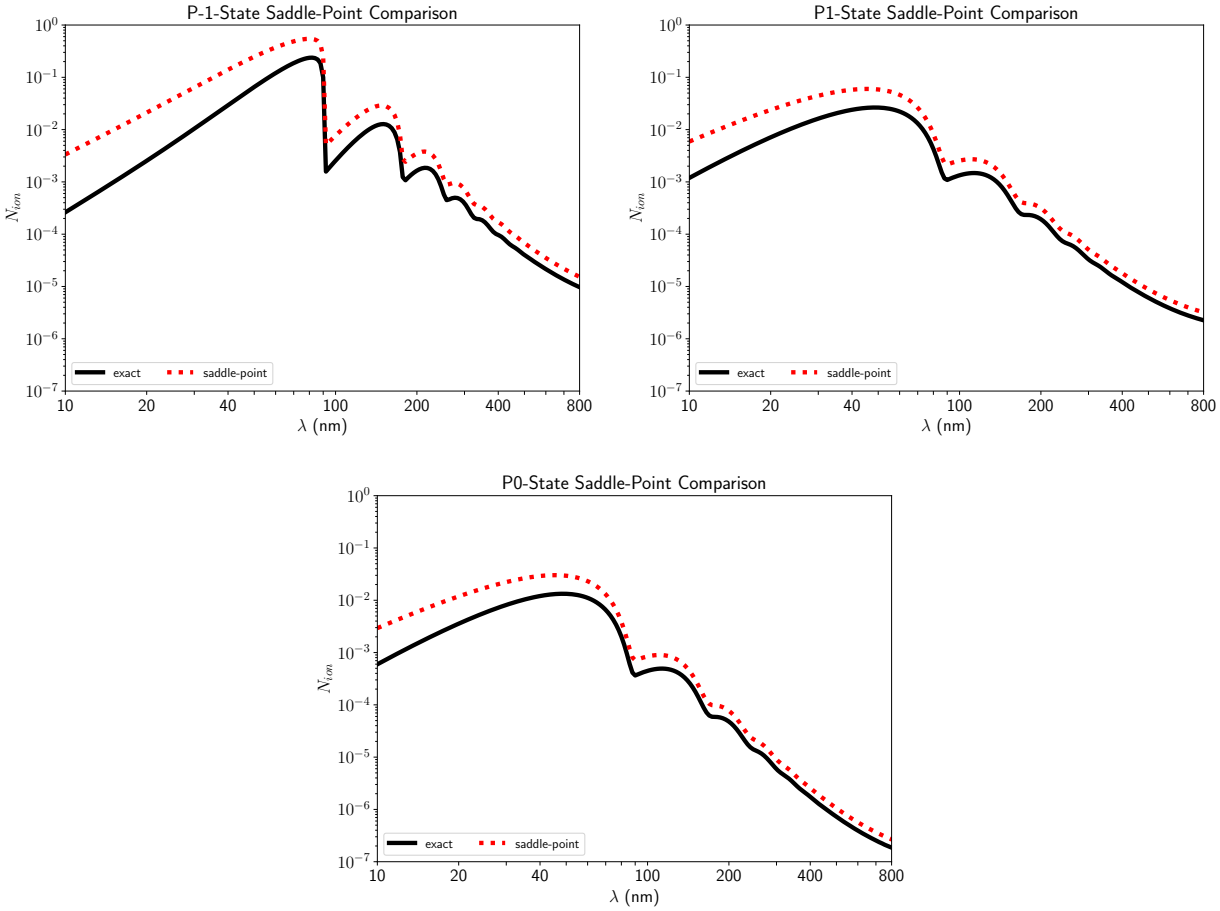

Figure 5.2: Total ionization yield for the length gauge amplitude (sections 3.6.1 and 3.6.2) corresponding to a 16 cycle laser pulse with an intensity of 10^{14} W/cm^2. The yield is compared between the saddle-point approximation (red dashed curve) and exact time integration (solid black curve). Top-left, bottom and top-right panels correspond to initial magnetic quantum number $m_i = -1$, 0 and 1, respectively.

From this comparison it is obvious that the saddle-point approximation overestimates the yield for each magnetic sub-level, where the worst agreement is observed near the short wavelength

10 nm limit, while the best agreement is found at the 800 nm long wavelength limit. To verify that the correct pre-factor has been used, the p_0−yield was calculated exactly from the s−yield used in the left panel of Fig. 5.1, where the s−state factor $\kappa/2\pi$ was replaced with $3k_z^2/2\pi\kappa$ with the appropriate term for C_{κ,l_i}.

5.1.2 Ionization amplitude

We will now discuss the accurate ionization amplitude used in Figs. 5.1 and 5.2 for the case of circular polarization with application to elliptically and linearly polarized pulses in a later section. The exact solution to the TDSE can be expressed as a Lippmann-Schwinger-type integral equation

$$\Psi_{\pm}(x) = \phi_i(x) + \int d^4x_1 \; G_{\pm}(x;x_1)V_{L\pm}(x_1)\phi_i(x_1), \tag{5.1}$$

where we use the notation

$$\int d^4x_1 \equiv \int_{t_0}^{t} dt_1 \int d\mathbf{r}_1 \tag{5.2}$$

for integration over intermediate coordinates and + and − in ± correspond to right- and left-handed polarized fields. Here, t_0 is the moment when the field is turned on and t is the time instant when the field is turned off and measurements are made.

The initial atomic state is either chosen to be the exact numerical eigenstates for a SAE potential

$$\phi_i(x) \equiv e^{(i/\hbar)I_p t}\phi_i(\mathbf{r}) = e^{(i/\hbar)I_p t}R_i(r)Y_{l_i}^{m_i}(\mathbf{r}) \tag{5.3}$$

with R_i given by

$$\hat{H}_a(\mathbf{r})\phi_i(\mathbf{r}) = \left[\frac{\hat{\mathbf{p}}^2}{2m} + V_a(\mathbf{r})\right]\phi_i(\mathbf{r}) = -I_p\phi_i(\mathbf{r}) \tag{5.4}$$

or the approximate asymptotic states from Ref. [136], where

$$R_i(r) \approx C_{\kappa l_i}\kappa^{3/2}(\kappa r)^{\nu-1}e^{-\kappa r} \tag{5.5}$$

which is accurate for calculations at long wavelengths, where ionization is dominated by the tail ($\kappa r \gg 1$) of the ground state. As before, I_p is the ionization potential, $\hbar\kappa \equiv \sqrt{2mI_p}$ is the bound

state momentum and we obtain $C_{\kappa l_i}$ by fitting the asymptotic state to the $\kappa r \gg 1$ part of the exact state.

We will investigate accurate solutions for the case of short range potentials where the solution to the atomic Schrödinger equation for $\kappa r \gg 1$ gives $\nu = 0$. For long range potentials (which we will treat in a later work) the power law becomes $\nu \equiv (\kappa_C/\kappa)$ with the Coulomb momentum $\hbar\kappa_C = mZ|e|^2/\hbar$ and residual ionic charge $Z|e|$. To derive the first order amplitude we expand the full Green's function in Eq. (5.1) to zeroth order in Volkov states

$$\Phi^{(-)}_{\mathbf{k}\pm}(x) = e^{-(i/\hbar)\int_{t_0}^{t} \frac{(\hbar\mathbf{k}+\frac{|e|}{c}\mathbf{A}_\pm(\tau))^2}{2m} d\tau + \frac{i|e|}{\hbar c}\mathbf{A}_\pm(t)\cdot\mathbf{r}} \phi^{(-)}_{\mathbf{k}}(\mathbf{r}). \tag{5.6}$$

Here, $\phi^{(-)}_{\mathbf{k}}(\mathbf{r})$ is chosen to either be plane-waves or atomic continuum states obtained through the shooting method. The earlier correspond to the usual zero-range Volkov states and the latter correspond to the finite-range atom Volkov states with properties given in Ref. [58].

When the Volkov Green's function

$$G^{(V)}_{\pm}(x;x') = -\frac{i}{\hbar}\theta(t-t') \sum\!\!\!\!\!\!\int_{\mathbf{k}} \Phi^{(-)}_{\mathbf{k}\pm}(x)\, \overline{\Phi^{(-)}_{\mathbf{k}\pm}(x')} \tag{5.7}$$

is inserted in Eq. (5.1) we arrive at the approximation

$$\Psi_\pm(x) \approx \phi_i(x) + \int d^4x_1\, G^{(V)}_{\pm}(x;x_1) V_{L\pm}(x_1)\phi_i(x_1). \tag{5.8}$$

To determine ionization properties we restrict ourselves to the outgoing part of the wave-function spanned by continuum Volkov states

$$\Psi^{(\mathrm{out})}_{\pm}(x) = \int d\mathbf{k}\, \mathcal{M}_\pm(\mathbf{k},t)\Phi^{(-)}_{\mathbf{k}\pm}(x) \tag{5.9}$$

with the coefficient given by

$$\mathcal{M}_\pm(\mathbf{k},t) = \int d\mathbf{r}\, \overline{\Phi^{(-)}_{\mathbf{k}\pm}(x)}\Psi_\pm(x). \tag{5.10}$$

The zeroth order contribution

$$\mathcal{M}^{(0)}_{\pm}(\mathbf{k},t) = \int d\mathbf{r}\, \overline{\Phi^{(-)}_{\mathbf{k}\pm}(x)}\phi_i(x) \tag{5.11}$$

is identically zero for finite-range Volkov states and dies off for plane-wave Volkov states in the long pulse limit [136]. The lowest order contribution therefore comes from

$$\mathcal{M}_{\pm}^{(1)}(\mathbf{k},t) = -\left(\frac{i}{\hbar}\right)\int d^4x_1 \overline{\Phi_{\mathbf{k}\pm}^{(-)}(x_1)}[|e|\mathbf{E}_{\pm}(t_1)\cdot\mathbf{r}_1]\phi_i(x_1) \tag{5.12}$$

and is the well known Keldysh amplitude [98].

5.1.3 Photon Absorption/Emission

We select $t_0 = 0$ and write the amplitude as

$$\mathcal{M}^{(1)}(\mathbf{k},t) = \int_0^t dt_1 e^{(i/\hbar)S(\mathbf{k},t_1)}\left(-\frac{\partial}{\partial t_1}\right)\tilde{\phi}_i(\mathbf{k},\mathbf{A}(t_1)) \tag{5.13}$$

with

$$\tilde{\phi}_i(\mathbf{k},\mathbf{A}(t)) = \int d\mathbf{r}_1 \overline{\phi_{\mathbf{k}}^{(-)}(\mathbf{r}_1)} e^{-\frac{i|e|}{\hbar c}\mathbf{A}(t)\cdot\mathbf{r}_1}\phi_i(\mathbf{r}_1) \tag{5.14}$$

We then expand the terms in Eq. (5.13) in partial waves to determine the ionization amplitude. To evaluate time integrals via Fourier components we replace the sum over saddle points by a sum over discrete energy levels. The discrete states describe the total quanta absorbed (n) and the final energy after ionization.

Starting with the $\tilde{\phi}_i$ term we express the vector potential contribution as

$$e^{-\frac{i|e|}{\hbar c}\mathbf{A}_{\pm}(t)\cdot\mathbf{r}} = 4\pi\sum_{l_A=0}^{\infty}\sum_{n_A=-l_A}^{l_A}(-i)^{l_A} j_{l_A}(k_A r)\overline{Y_{l_A}^{\pm n_A}(\hat{\mathbf{A}}_{\pm}(0))}Y_{l_A}^{\pm n_A}(\hat{\mathbf{r}})e^{-in_A\omega t} \tag{5.15}$$

where $k_A \equiv \frac{|e|A}{\hbar c}$ is the vector potential momentum. $Y_{l_A}^{\pm n_A}(\hat{\mathbf{r}})$ represents the angular momentum transfer and $e^{-in_A\omega t}$ represents the total energy transfer $n_A\hbar\omega$. Since $l_A \geq |n_A|$, we note that, in general, n_A describes the net absorption or emission of energy and not necessarily an order of perturbation theory. This factor is completed by expanding the continuum state in the term as

$$\phi_{\mathbf{k}}^{(-)}(\mathbf{r}) = \frac{1}{k}\sum_{l_k=0}^{\infty}\sum_{m_k=-l_k}^{l_k} i^{l_k}e^{-i\eta_{l_k}(k)}R_{k,l_k}(r)\overline{Y_{l_k}^{m_k}(\hat{\mathbf{k}})}Y_{l_k}^{m_k}(\hat{\mathbf{r}}) \tag{5.16}$$

where R_{k,l_k} is the radial continuum state with phase shift $\eta_{l_k}(k)$. Here, $\phi_{\mathbf{k}}^{(-)}$ describes scattering states which are asymptotically given at $r \to \infty$ by a plane wave plus an ingoing spherical wave [107].

Putting it all together we have

$$\left(-\frac{\partial}{\partial t}\right)\tilde{\phi}_i(\mathbf{k},\mathbf{A}(t)) = (i/\hbar)\sum_{l_A,n_A}(n_A\hbar\omega)A_{l_A}^{\pm n_A}e^{-in_A\omega t} \times\sum_{l_k}K_{l_k}(k)I_{l_i}^{l_k,l_A}(k)\begin{bmatrix} l_k & l_A & l_i \\ -(m_i\pm n_A) & \pm n_A & m_i\end{bmatrix}Y_{l_k}^{m_i\pm n_A}(\hat{\mathbf{k}}) \quad (5.17)$$

with coefficients

$$A_{l_A}^{\pm n_A} \equiv 4\pi(-i)^{l_A}\overline{Y_{l_A}^{\pm n_A}(\hat{\mathbf{A}}_{\pm}(0))}, \quad (5.18)$$

and

$$K_{l_k}(k) \equiv (-i)^{l_k}e^{i\eta_{l_k}(k)}. \quad (5.19)$$

The Fourier component $e^{-in_A\omega t}$ describes the transfer of n_A quanta of energy to the ionized electron and the angular integrals are given by

$$\begin{bmatrix} l_3 & l_2 & l_1 \\ -m_3 & m_2 & m_1\end{bmatrix} \equiv \int d\Omega_{r_1}\overline{Y_{l_3}^{m_3}(\hat{\mathbf{r}}_1)}Y_{l_2}^{m_2}(\hat{\mathbf{r}}_1)Y_{l_1}^{m_1}(\hat{\mathbf{r}}_1) \quad (5.20)$$

which provides the corresponding angular momentum selection rules which are evaluated as Wigner-$3j$ symbols. The radial integral

$$I_{l_i}^{l_k,l_A}(k) \equiv \frac{1}{k}\int_0^\infty dr_1\, r_1^2\, R_{k,l_k}(r_1)j_{l_A}(k_Ar_1)R_i(r_1), \quad (5.21)$$

determines how the initial state influences the photo-electron distribution. We numerically evaluate this integral for all cases in this section and the subsequent section on numerical applications.

Using the expansion

$$j_l(x) = \sqrt{\frac{\pi}{2x}}J_{l+1/2}(x) = \frac{\sqrt{\pi}}{2}\frac{(x/2)^l}{\Gamma(l+3/2)}{}_0F_1(l+3/2;-x^2/4), \quad (5.22)$$

for asymptotic initial states and zero-range Volkov states the integral can be evaluated exactly as

$$I_{l_i}^{l_k,l_A}(k) = C_{\kappa,l_i}\frac{2^{\nu-1/2}}{\kappa^{3/2}}\frac{\Gamma([l_k+l_A+\nu+2]/2)\Gamma([l_k+l_A+\nu+3]/2)}{\Gamma(l_k+3/2)\Gamma(l_A+3/2)} \times\left(\frac{k}{\kappa}\right)^{l_k}\left(\frac{k_A}{\kappa}\right)^{l_A}F_4\left(\frac{l_k+l_A+\nu+2}{2},\frac{l_k+l_A+\nu+3}{2};l_k+\frac{3}{2},l_A+\frac{3}{2};-\left(\frac{k}{\kappa}\right)^2,-\left(\frac{k_A}{\kappa}\right)^2\right). \quad (5.23)$$

The Appell F_4 function [9] is defined as

$$F_4(a,b;c_1,c_2;x,y) = \sum_{m,n=0}^{\infty} \frac{(a)_{m+n}(b)_{m+n}}{(c_1)_m(c_2)_n} \frac{x^m}{m!} \frac{y^n}{n!} \tag{5.24}$$

with domain of convergence $\sqrt{|x|}+\sqrt{|y|} < 1$ (or $k+k_A < \kappa$) and can be extended to the entire domain via various analytic continuations [6, 7, 56, 83]. In section 5.3 we will find a simpler expansion in terms of orders of the intensity parameters z_1 and z, where lowest-order contributions correspond to the weak-field limit and progressively higher-order terms are required when transitioning into the strong-field limit.

To finish the derivation we expand the action term in partial waves and perform time integrals such that

$$S_{\pm}(\mathbf{k},t) = \int_0^t d\tau \left[\frac{(\hbar\mathbf{k} + \frac{|e|}{c}\mathbf{A}_{\pm}(\tau))^2}{2m} + I_p \right] = N(k)\hbar\omega\, t + \hbar\mathbf{k}\cdot(\boldsymbol{\xi}_{\pm}(t) - \boldsymbol{\xi}_{\pm}(0)), \tag{5.25}$$

$$N(k) \equiv \frac{1}{\hbar\omega}\left(E_k + \tilde{I}_p\right), \quad E_k = \frac{\hbar^2 k^2}{2m}, \quad U_p \equiv \frac{\hbar^2 k_A^2}{2m} \tag{5.26}$$

and

$$\boldsymbol{\xi}_{\pm}(t) \equiv \frac{|e|}{mc}\int^t \mathbf{A}_{\pm}(\tau)d\tau = \xi[\cos(\omega t)\hat{\mathbf{x}} \pm \sin(\omega t)\hat{\mathbf{y}}] \tag{5.27}$$

with $\xi \equiv \frac{|e|A}{\omega mc}$. Using the same partial wave expansion as before we have

$$e^{i\mathbf{k}\cdot\boldsymbol{\xi}_{\pm}(t)} = 4\pi \sum_{l_S=0}^{\infty} \sum_{n_S=-l_S}^{l_S} i^{l_S} j_{l_S}(k\,\xi)\overline{Y_{l_S}^{\pm n_S}(\hat{\boldsymbol{\xi}}_{\pm}(0))} Y_{l_S}^{\pm n_S}(\hat{\mathbf{k}}) e^{-in_S\omega t}. \tag{5.28}$$

For a given number of quanta n_A from the vector potential term we have

$$\int_0^t dt_1 e^{(i/\hbar)S_{\pm}(\mathbf{k},t_1) - in_A\omega t_1} = e^{-i\mathbf{k}\cdot\boldsymbol{\xi}_{\pm}(0)} \sum_{l_S=0}^{\infty} \sum_{n_S=-l_S}^{l_S} X_{l_S}^{\pm n_S}(k) Y_{l_S}^{\pm n_S}(\hat{\mathbf{k}}) \delta_t([N(k) - (n_A + n_S)]\omega/2) \tag{5.29}$$

with coefficient

$$X_{l_S}^{\pm n_S}(k) \equiv 4\pi i^{l_S} j_{l_S}(k\xi)\overline{Y_{l_S}^{\pm n_S}(\hat{\boldsymbol{\xi}}_{\pm}(0))}. \tag{5.30}$$

The shape term

$$\delta_t(x) \equiv e^{ixt}\mathrm{sinc}(xt)t \tag{5.31}$$

describes the distribution of final energy states after the absorption of $n_A + n_S$ photons by a finite flat-top pulse.

Combining all contributions we get for the ionization amplitude

$$\mathcal{M}_{\pm}^{(1)}(\mathbf{k},t) = (i/\hbar)e^{-i\mathbf{k}\cdot\boldsymbol{\xi}_{\pm}(0)} \sum_{l_A=0}^{\infty} \sum_{n_A=-l_A}^{l_A} (n_A\hbar\omega) A_{l_A}^{\pm n_A} \times \sum_{l_k=\max(|l_i-l_A|,|m_i\pm n_A|)}^{l_i+l_A} K_{l_k}(k)\, I_{l_i}^{l_k,l_A}(k) \begin{bmatrix} l_k & l_A & l_i \\ -(m_i \pm n_A) & \pm n_A & m_i \end{bmatrix} Y_{l_k}^{m_i\pm n_A}(\hat{\mathbf{k}}) \times \sum_{l_S=0}^{\infty} \sum_{n_S=-l_S}^{l_S} X_{l_S}^{\pm n_S}(k) Y_{l_S}^{\pm n_S}(\hat{\mathbf{k}}) \delta_t([N(k) - (n_A + n_S)]\omega/2) \quad (5.32)$$

with angular momentum components determined by

$$Y_{l_S}^{\pm n_S}(\hat{\mathbf{k}}) Y_{l_k}^{m_i\pm n_A}(\hat{\mathbf{k}}) = \sum_{l=\max(|l_k-l_S|,|m_i\pm[n_A+n_S]|)}^{l_k+l_S} \begin{bmatrix} l & l_S & l_k \\ -(m_i \pm [n_A + n_S]) & \pm n_S & m_i \pm n_A \end{bmatrix} Y_l^{m_i\pm(n_A+n_S)}(\hat{\mathbf{k}}) \quad (5.33)$$

and the yield given by

$$P_{\pm}^{(\mathrm{ion})}(t) = \int d\mathbf{k}\, |\mathcal{M}_{\pm}(\mathbf{k},t)|^2. \quad (5.34)$$

5.1.4 Long Pulse Limit

To determine the time-averaged rate for a long pulse we use

$$w_{\pm} = \lim_{t\to\infty} t^{-1} P_{\pm}^{(\mathrm{ion})}(t) \quad (5.35)$$

where it is useful to introduce the distribution

$$W_{\pm}(\mathbf{k}) = \lim_{t\to\infty} t^{-1} |\mathcal{M}_{\pm}(\mathbf{k},t)|^2 \approx \lim_{t\to\infty} t^{-1} |\mathcal{M}_{\pm}^{(1)}(\mathbf{k},t)|^2. \quad (5.36)$$

Taking the limit we see that the only time-dependence comes from cross terms involving $\delta_t(x)$. Using the sinc representation of the Dirac delta function we see that

$$\lim_{t\to\infty} t^{-1} \delta_t([N(k) - n]\omega/2) \overline{\delta_t([N(k) - n']\omega/2)} = 2\pi\hbar\, \delta([N(k) - n]\hbar\omega)\, \delta_{n,n'} = \frac{2\pi}{v_n}\, \delta(k - k_n)\, \delta_{n,n'} \quad (5.37)$$

which results in the quantized final state momenta

$$\hbar k_n \equiv \sqrt{2m\left(n\hbar\omega - \tilde{I}_p\right)} \equiv m v_n \tag{5.38}$$

and the distribution

$$W_\pm(\mathbf{k}) = \sum_{n=n_{\rm th}}^{\infty} |\mathcal{M}_\pm^{(1)}(\mathbf{k}_n)|^2 \delta(k - k_n) \tag{5.39}$$

after the absorption of n photons with threshold value $n_{\rm th} = \lceil \tilde{I}_p/\hbar\omega \rceil$ and effective ionization potential $\tilde{I}_p = I_p + U_p$.

The amplitude for each photon process becomes

$$\mathcal{M}_\pm^{(1)}(\mathbf{k}_n) = e^{-i\mathbf{k}_n\cdot\boldsymbol{\xi}_\pm(0)} \sum_{l=|m_i\pm n|}^{\infty} C_l^{m_i\pm n}(k_n) Y_l^{m_i\pm n}(\hat{\mathbf{k}}). \tag{5.40}$$

with components

$$\begin{aligned} C_l^{m_i\pm n}(k_n) \equiv (i/\hbar)\sqrt{\frac{2\pi}{v_n}} \sum_{l_A=0}^{\infty} \sum_{n_A=-l_A}^{l_A} (n_A\hbar\omega) A_{l_A}^{\pm n_A} \\ \times \sum_{l_k=\max(|l_i-l_A|,|m_i\pm n_A|)}^{l_i+l_A} K_{l_k}(k_n)\, I_{l_i}^{l_k,l_A}(k_n) \begin{bmatrix} l_k & l_A & l_i \\ -(m_i\pm n_A) & \pm n_A & m_i \end{bmatrix} \\ \times \sum_{l_S=|n-n_A|}^{\infty} X_{l_S}^{\pm(n-n_A)}(k_n) \begin{bmatrix} l & l_S & l_k \\ -(m_i\pm n) & \pm(n-n_A) & m_i \pm n_A \end{bmatrix}. \end{aligned} \tag{5.41}$$

Performing the sum of the contributions for each photon process we obtain the rate as

$$w_\pm = \int d\mathbf{k}\, W_\pm(\mathbf{k}) = \sum_{n=n_{\rm th}}^{\infty} \int d\Omega_k \frac{dw_{n\pm}}{d\Omega_k} = \sum_{n=n_{\rm th}}^{\infty} \sum_{l=|m_i\pm n|}^{\infty} w_{ln\pm} = \sum_{n=n_{\rm th}}^{\infty} w_{n\pm} \tag{5.42}$$

where we have introduced the partial rates

$$w_{ln\pm} = k_n^2 |C_l^{m_i\pm n}(k_n)|^2 \quad \text{and} \quad w_{n\pm} = \sum_{l=|m_i\pm n|}^{\infty} w_{ln\pm} \tag{5.43}$$

as well as the angular differential rates

$$\frac{dw_{n\pm}}{d\Omega_k} = k_n^2 |\mathcal{M}_\pm(\mathbf{k}_n)|^2 \quad \text{and} \quad \frac{dw_\pm}{d\Omega_k} = \sum_{n=n_{\rm th}}^{\infty} \frac{dw_{n\pm}}{d\Omega_k}. \tag{5.44}$$

5.2 Numerical Applications

5.2.1 Ionization Yield

As an initial test we compare predictions for the ionization of spinless Hydrogen-like and Neon-like anions using Eq. (5.42) with results of the time dependent Schrödinger equation. Our application involves using a Yukawa potential

$$V_a(\mathbf{r}) = -\frac{Z_a|e|^2}{r}e^{-r/a} \tag{5.45}$$

with valence binding energy of $I_p \approx 13.6$ eV and the electron interacting with a 16 cycle circular flat-top pulse with intensity 1×10^{14} W/cm^2 at wavelengths between 10 nm and 800 nm. The exponential factor a describes the range of the Yukawa potential while the prefactor Z_a is chosen such that the binding energy remains the same for all ranges considered.

Numerical comparisons with the TDSE results are performed for three selections of initial- and final-states. In the first set we use zero-range initial and final states to determine errors introduced by the saddle-point approximation. In the next set of calculations we replace the asymptotic initial states with numerical states of the atomic Hamiltonian to determine errors introduced by the use of asymptotic zero-range initial state. Finally, we report another set of calculations in which for the Volkov states the plane-wave scattering state has been replaced with scattering states of the atom [58].

In Fig. 5.3 we compare the predictions of the model rate to the TDSE results for the case of an s-state and exponential parameters $a = a_0/5$, $a_0/3$, a_0 and ∞ (a_0 is the Bohr radius) to show that the model can provide accurate results for short-range potentials at all wavelengths. For the TDSE calculations we use velocity gauge and expand the wave function in a basis of spherical harmonics for the angular dimensions ($l_{\max} = |m_{\max}| = 30$) and a basis of 8^{th} order B-splines in the radial dimension. The 600 B-spline nodes are placed such that the spacing between nodes is quadratic near the origin then becomes constant at a chosen radius (30 a.u.). The maximum radius of the box is 500 a.u., where exterior complex scaling has been applied to the last 50 a.u.. The

Crank-Nicolson method has been used to propagate the wave function in time with a step size of 0.1 a.u.. Additional two cycle $\sin^2$ ramp on and ramp off are included to the 16 cycle flat-top pulse to ensure that the vector potential smoothly goes to zero at $t \to \pm\infty$. The zero-range yield for s-states predicts essentially the same yield for all but the shortest wavelengths and agrees well with the TDSE results for the case $a = a_0/5$. Expanding the atomic range to $a = a_0/3$ and a_0 makes it clear that atomic initial and final states are required to obtain reliable results. The case of $a = \infty$ is included in the bottom-right panel of Fig. 5.3, where the quasi-classical Coulomb corrections from section 3.6.2.3 are applied (blue curve), but a break down is observed in the short wavelength limit. In contrast, Coulomb-Volkov states (solid black curve) predict the correct ionization yield for wavelengths shorter than the single photon ionization threshold. An additional green curve which disagrees for all wavelengths has been included showing the results for using an atomic initial state and a plane-wave Volkov state.

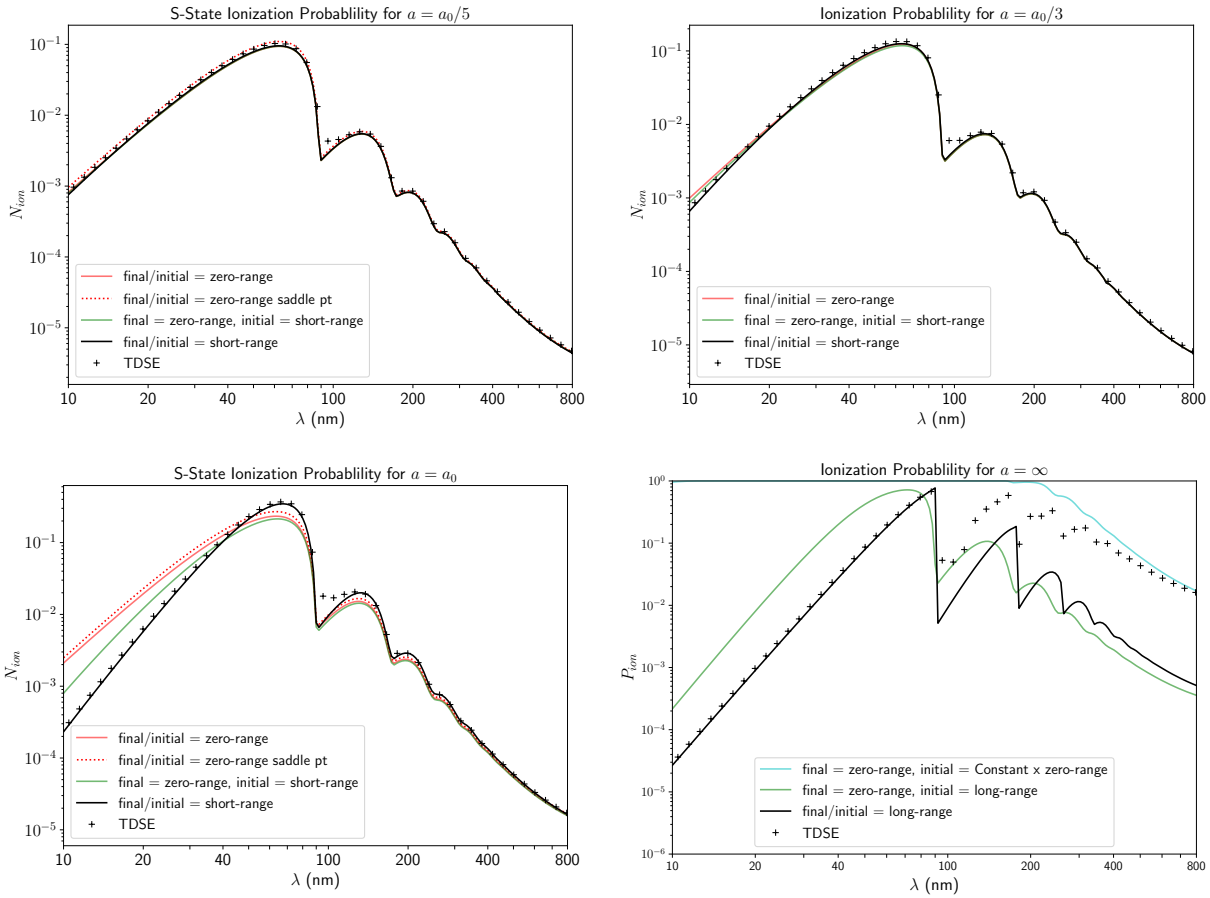

Figure 5.3: Comparison of predictions for the s-state model with the TDSE results for exponential parameters $a = a_0/5$, $a_0/3$, a_0 and ∞. The red solid (dashed) line corresponds to calculations using zero-range initial and final states without (with) the saddle-point approximation. The green curve in the calculations the asymptotic initial states are replaced by numerical states of the atomic Hamiltonian. The black curve corresponds to calculations with the same numerical initial state, but now with Volkov states where the plane-wave scattering state has been replaced with scattering states of the atom. $a = \infty$ is included for the initial Hydrogen ground-state and final Coulomb-corrected WKB Volkov state (blue curve) [23, 102].

For the case of a Neon-like anion we chose a valence ionization potential $I_p(2p) = 13.6$ eV to enable direct comparison with the Hydrogen-like data. The Yukawa range parameter of $a = a_0/2$ was chosen to obtain $1s$, $2s$ and $2p$ bound states with parameters given in Table 5.1. We will assume

all orbitals are occupied and neglect spin. Calculating the total ionization includes calculating the ionization for each occupied orbital and adding the results. This corresponds to the single active electron approximation. Although we work with Yukawa potentials, application to other potentials should be straightforward.

State	1s	2s	2p	$a = a_0/2$
I_p(Hartree)	33.9	1.32	0.50	$Z_c = 10.15$

Table 5.1: Table of bound-state energy levels and Yukawa parameters.

To obtain the total ionization yield for the Neon-like anion we calculate the single orbital yield

$$N_{\text{ion}}^{(j)} = 1 - e^{-w^{(j)}T} \tag{5.46}$$

as before and add those up

$$N_{\text{ion}} = N_{\text{ion}}^{(1s)} + N_{\text{ion}}^{(2s)} + N_{\text{ion}}^{(2p_1)} + N_{\text{ion}}^{(2p_0)} + N_{\text{ion}}^{(2p_{-1})} \tag{5.47}$$

to get the total yield. The results are shown in Fig. 5.4 for the case of a Yukawa potential with range parameter $a = a_0/2$.

As one can anticipate, the occupied core $1s$ orbital can be neglected since the yield is much smaller than all the other yields for all wavelengths considered. The TDSE results show reduced ionization in the co-rotating ($2p_1$) orbital due to transitions into the occupied 2s state. This is marked by the dashed $E_{2p} - E_{2s}$ line in the left panel of Fig. 5.4. At the same time, the $2s$ orbital experiences resonance enhanced ionization due to the occupied co-rotating state. The combination of these effects are negated and the model produces accurate predictions for the total ionization yield (right panel of Fig. 5.4). The effect of resonances can be included explicitly as shown in Ref. [98]. We have again plotted results for each initial/final state combination, as in Fig. 5.3. Ionization is best described by the use of initial and final atomic states, where some disagreement is observed near ionization thresholds since we have not included properties of the pulse envelope.

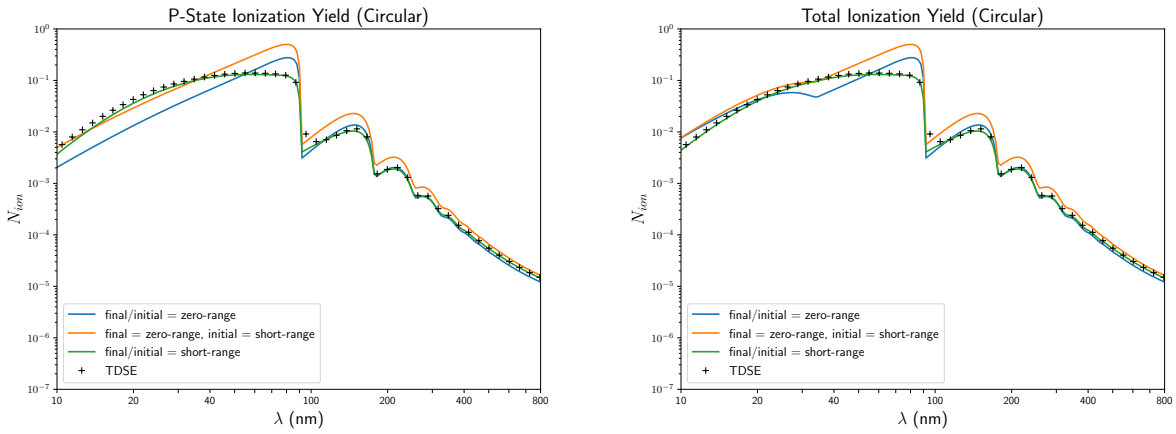

Figure 5.4: Comparison of the results of the p-state model with the TDSE results for exponential parameter $a = a_0/2$, where the left panel corresponds to the sum of all p-orbitals and the right panel corresponds to $2s$ ionization in addition to ionization by all p–states. The blue line corresponds to calculations using zero-range initial and final states. For the results presented by the orange curve the asymptotic initial states is replaced by numerical states of the atomic Hamiltonian. The results shown by the green curve correspond to calculations with the same numerical initial state, but now with Volkov states where the plane-wave scattering state has been replaced with scattering states of the atom.

5.2.2 Photoelectron Energy and Angular Distributions

After we have verified the accuracy of the formulas we will describe how to extract energy and angular photo-electron distributions with application to the before mentioned Neon-like anion. The population of the ground state and each energy level in the continuum is described by

$$\frac{d}{dt}\begin{bmatrix} N_i \\ N_{n_{\text{th}}} \\ N_{n_{\text{th}}+1} \\ \vdots \end{bmatrix} = \begin{bmatrix} -w \\ w_{n_{\text{th}}} \\ w_{n_{\text{th}}+1} \\ \vdots \end{bmatrix} N_i. \tag{5.48}$$

Inserting the solution into the rate equations we get the yield for each ATI peak n

$$N_n = \frac{w_n}{w} N_{\text{ion}}. \tag{5.49}$$

Using

$$w_n = \int d\Omega_k \frac{dw_n}{d\Omega_k} \tag{5.50}$$

we obtain the total angular distribution

$$\frac{dN_{\text{ion}}}{d\Omega_k} = \frac{1}{w} \frac{dw}{d\Omega_k} N_{\text{ion}} \tag{5.51}$$

and that for each photon process

$$\frac{dN_n}{d\Omega_k} = \frac{1}{w_n} \frac{dw_n}{d\Omega_k} N_n. \tag{5.52}$$

Angular distributions for ionization by a circularly polarized field and initial states that include a single $Y_{l_i}^{m_i}(\hat{\mathbf{r}})$-term have cylindrical symmetry in the φ_k direction. Integrating over this degree of freedom, one obtains the distributions

$$\frac{dN_{\text{ion}}}{d(\cos\theta_k)} \equiv \int_0^{2\pi} d\varphi_k \frac{dN_{\text{ion}}}{d\Omega_k} = 2\pi \left. \frac{dN_{\text{ion}}}{d\Omega_k} \right|_{\varphi_k=0} \tag{5.53}$$

and

$$\frac{dN_n}{d(\cos\theta_k)} \equiv \int_0^{2\pi} d\varphi_k \frac{dN_n}{d\Omega_k} = 2\pi \left. \frac{dN_n}{d\Omega_k} \right|_{\varphi_k=0}. \tag{5.54}$$

In Fig. 5.5 we plot the photo-electron energy and angular distributions corresponding to the Neon-like anion data with both atomic initial and final states as for the results presented in Fig. 5.4. Wavelengths of 10 nm, 100 nm and 800 nm are selected. The 10 nm and 100 nm data correspond to the perturbative multiphoton limit since the energy distribution is linear on a log scale. In contrast, the kinetic energy distribution at 800 nm is peaked at energies larger than the threshold value n_{th} demonstrating the expected behavior in the non-adiabatic limit [20]. The angular distributions become more localized at the equator as wavelengths increase since ionized electrons belong to higher-order spherical harmonic contributions with $l \approx m$ [167].

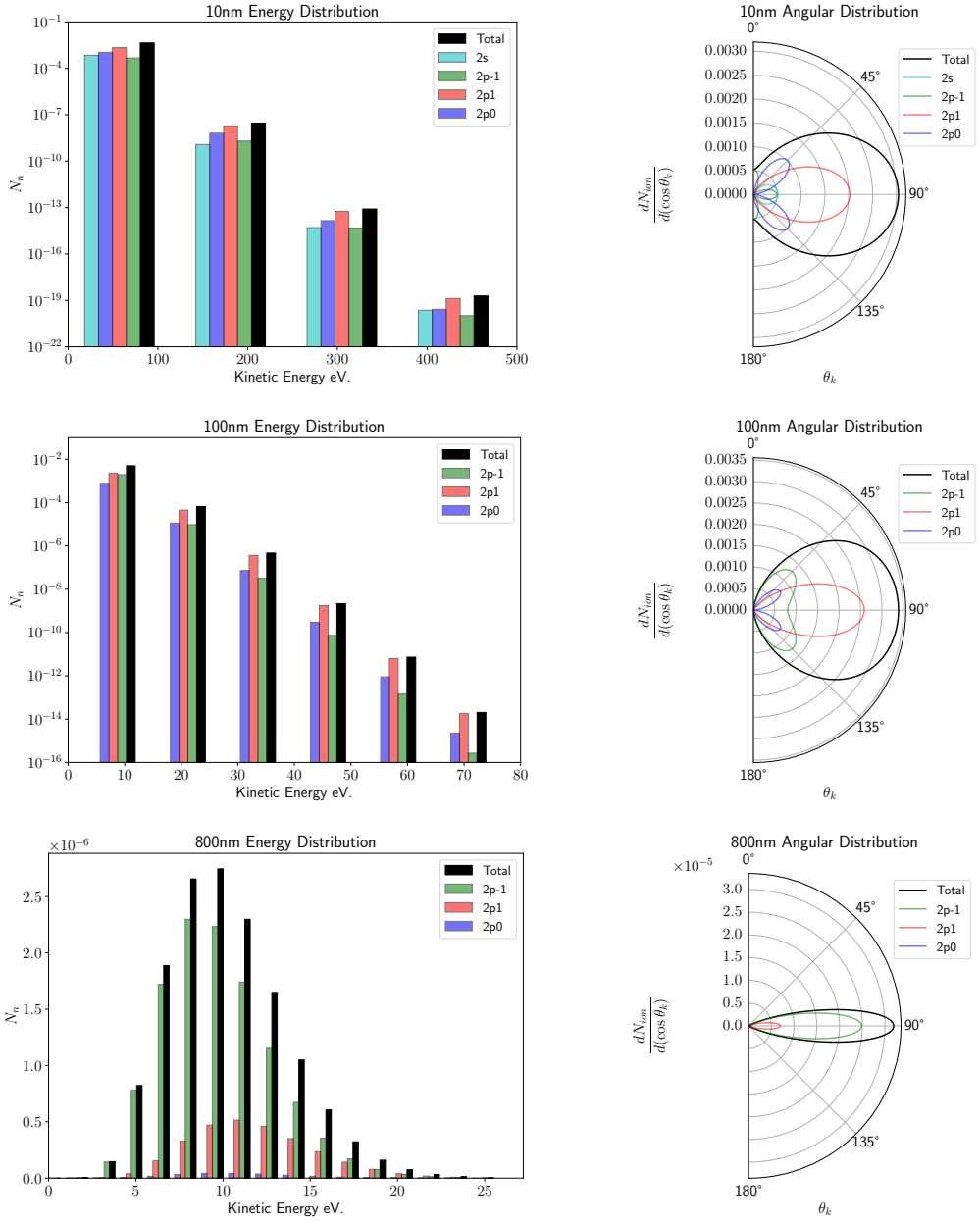

Figure 5.5: Photo-electron energy (left panels) and angular distributions (right panels) for the Neon-like anion data given in Fig. 5.4. Both atomic initial and final states are chosen and wavelengths of 10 nm (top panels), 100 nm (middle panels) and 800 nm (bottom panels) are selected.

5.3 Intensity parameters

The general ionization formula can be accurately approximated as a two-step process for laser parameters used in the current work. The initial state is promoted to a small set of intermediate momentum states via the absorption of n_A photons before an additional $n-n_A$ photons is absorbed to transfer in a final state. We will consider an initial s-state and use these ideas to determine dominant pathways for ionization. Furthermore, we will determine a simplified weak-field description and discuss successive corrections required when transitioning into the strong-field limit.

Starting with an initial s-state ($l_i = m_i = 0$) we immediately recognize the rule $l_k = l_A$ from

$$\begin{bmatrix} l_k & l_A & 0 \\ -(m_i \pm n_A) & \pm n_A & 0 \end{bmatrix} = \frac{\delta_{l_k,l_A}}{\sqrt{4\pi}} \tag{5.55}$$

which yields the coefficient

$$C_l^{\pm n}(k_n) = (i/\hbar)\frac{1}{\sqrt{2v_n}} \sum_{n_A=-\infty}^{\infty} (n_A\hbar\omega) \sum_{l_A=|n_A|}^{\infty} A_{l_A}^{\pm n_A} K_{l_A}(k_n)\, I_0^{l_A}(k_n) \times \sum_{l_S=|n-n_A|}^{\infty} X_{l_S}^{\pm(n-n_A)}(k_n) \begin{bmatrix} l & l_S & l_A \\ \mp n & \pm(n-n_A) & \pm n_A \end{bmatrix}. \tag{5.56}$$

As l_A increases the integral $I_{l_i}^{l_A}(k_n) \equiv I_{l_i}^{l_A,l_A}(k_n)$ decreases due to decreased overlaps of both the continuum state $R_{k,l_A}(r)$ and the Bessel function $j_{l_A}(k_A r)$ with the initial bound state $R_i(r)$. The coefficient should therefore be dominated by the lowest order contribution $l_A = |n_A|$. Similarly, we should expect that for the intensity and wavelengths considered the sum over l_S should be dominated by the lowest order contribution ($|n-n_A|$) yielding

$$C_l^{\pm n}(k_n) = (i/\hbar)\frac{1}{\sqrt{2v_n}} \sum_{n_A=-\infty}^{\infty} (n_A\hbar\omega) A_{|n_A|}^{\pm n_A} K_{|n_A|}(k_n)\, I_0^{|n_A|}(k_n) \times X_{|n-n_A|}^{\pm(n-n_A)}(k_n) \begin{bmatrix} l & |n-n_A| & |n_A| \\ \mp n & \pm(n-n_A) & \pm n_A \end{bmatrix}. \tag{5.57}$$

Continuing along the same lines, the sum over n_A may be reduced by restricting ourselves to the largest contributions. This is done by choosing the set of n_A which minimizes $|n-n_A| + |n_A|$

for a particular n. Geometrically this amounts to identifying the set of n_A which minimizes the total distance ($|n - n_A| + |n_A|$) over which the magnetic quantum number changes from the initial state to the intermediate state ($|n_A|$) and then to the final state ($|n - n_A|$). This is achieved for all $0 \leq n_A \leq n$ for $l = n$. Thus, the $l > n$ contributions may be neglected for fixed n since the distance $|n_A| + |n - n_A|$ is larger than for $n = l$ yielding the approximation

$$w_{\pm} \approx \sum_{n=n_{\mathrm{th}}}^{\infty} w_{nn\pm}. \tag{5.58}$$

In Fig. 5.6 we show that approximating the rate as described above accurately determines the ionization yield for the case of $a = a_0/5$. For later comparison we use zero-range Volkov states and an asymptotic initial state, but the conclusion holds in general.

5.3.1 Weak-Field Limit

We will now apply the above mentioned selection rules to the special case of a zero-range potential for $k_A \ll \kappa$. The radial integral is approximated by

$$j_{l_A}(k_A r) \approx \frac{l_A!(2k_A r)^{l_A}}{(2l_A+1)!} \tag{5.59}$$

yielding

$$I_0^{n_A}(k_n) = \frac{C_{\kappa,l_i} n_A!}{\Gamma(n_A+3/2)} \sqrt{\frac{\kappa}{2}} \frac{(k_n k_A)^{n_A}}{(k_n^2+\kappa^2)^{n_A+1}}. \tag{5.60}$$

Using

$$Y_l^{\pm l}(\theta,\varphi) = \frac{1}{l!}\sqrt{\frac{(2l+1)!}{4\pi}}\left(\mp\frac{1}{2}\sin\theta e^{\pm\varphi}\right)^l \tag{5.61}$$

the final-state angular integral can be evaluated as

$$\begin{bmatrix} n & (n-n_A) & n_A \\ \mp n & \pm(n-n_A) & \pm n_A \end{bmatrix} = \frac{n!}{(n-n_A)!n_A!}\sqrt{\frac{(2(n-n_A)+1)!(2n_A+1)!}{4\pi(2n+1)!}}. \tag{5.62}$$

The coefficient now requires evaluating

$$A_{n_A}^{\pm n_A} K_{n_A}(k_n) X_{(n-n_A)}^{\pm(n-n_A)}(k_n) = (4\pi)^2 i^{(n+n_A)} j_{(n-n_A)}(k\xi)\overline{Y_{(n-n_A)}^{\pm(n-n_A)}(\hat{\boldsymbol{\xi}}_{\pm}(0))Y_{l_A}^{\pm n_A}(\hat{\mathbf{A}}_{\pm}(0))}. \tag{5.63}$$

Using the same spherical harmonic identity as earlier

$$\overline{Y^{\pm(n-n_A)}_{(n-n_A)}(\hat{\boldsymbol{\xi}}_{\pm}(0))Y^{\pm n_A}_{n_A}(\hat{\mathbf{A}}_{\pm}(0))} = \frac{(-i)^{n_A}}{(n-n_A)!n_A!}\left(\mp\frac{1}{2}\right)^n \frac{\sqrt{(2(n-n_A)+1)!(2n_A+1)!}}{4\pi} \tag{5.64}$$

and the weak field approximation

$$j_{l_S}(k_n\xi) \approx \frac{l_S!(2k_n\xi)^{l_S}}{(2l_S+1)!} \tag{5.65}$$

we have

$$A^{\pm n_A}_{n_A}K_{n_A}(k_n)X^{\pm(n-n_A)}_{(n-n_A)}(k_n) = 4\pi\left(\mp\frac{i}{2}\right)^n \frac{(2k_n\xi)^{(n-n_A)}}{n_A!}\sqrt{\frac{(2n_A+1)!}{(2(n-n_A)+1)!}}. \tag{5.66}$$

Applying

$$n_A!\,\Gamma(n_A+3/2) = \sqrt{\pi}(2n_A+1)!/2^{2n_A+1} \tag{5.67}$$

we finally have

$$C^{\pm n}_n(k_n) = 2(i/\hbar)\frac{(\mp i)^n\, n!\, C_{\kappa,l_i}}{\sqrt{(2n+1)!}}\sqrt{\frac{\kappa}{v_n}}\frac{(k_n\xi)^n}{(k_n^2+\kappa^2)}\sum_{n_A=0}^{n}\frac{(n_A\hbar\omega)}{(n-n_A)!}\left(\frac{2k_A/\xi}{k_n^2+\kappa^2}\right)^{n_A}. \tag{5.68}$$

The coefficient can be simplified using the exponential integral function

$$\sum_{n_A=0}^{n}\frac{n_A}{(n-n_A)!}z^{n_A} = \frac{1}{z\,n!}\left[1+e^{1/z}\left(n-\frac{1}{z}\right)E_{-n}\left(\frac{1}{z}\right)\right] \tag{5.69}$$

yielding

$$C^{\pm n}_n(k_n) = i\frac{C_{\kappa,l_i}(\mp ik_n\xi)^n}{\sqrt{(2n+1)!}}\sqrt{\frac{\hbar\kappa}{mk_n}}\left[1+\left(\frac{U_p}{\hbar\omega}\right)e^n E_{-n}(n)\right] \tag{5.70}$$

after the weak-field substitution

$$k_n^2+\kappa^2 = \left(\frac{2m}{\hbar^2}\right)(n\hbar\omega - U_p) \approx \left(\frac{2m}{\hbar^2}\right)n\hbar\omega. \tag{5.71}$$

Using the hypergeometric representation of $E_{-n}(1/z)$

$$C^{\pm n}_n(k_n) = i\frac{C_{\kappa,l_i}(\mp ik_n\xi)^n}{\sqrt{(2n+1)!}}\sqrt{\frac{\hbar\kappa}{mk_n}}\left[1+\left(\frac{U_p}{n\hbar\omega}\right){}_2F_0\left(-n,1;;-\frac{1}{n}\right)\right] \tag{5.72}$$

and $U_p \ll I_p < n\hbar\omega$ we see that the ${}_2F_0$ term is negligible leading to the simplified coefficient

$$C^{\pm n}_n(k_n) = i\frac{C_{\kappa,l_i}(\mp ik_n\xi)^n}{\sqrt{(2n+1)!}}\sqrt{\frac{\hbar\kappa}{mk_n}} \tag{5.73}$$

and the partial rate

$$w^{(s)}_{n,n\pm} = C^2_{\kappa,l_i} \frac{(\kappa\, v_n)\,(k_n\xi)^{2n}}{(2n+1)!} \tag{5.74}$$

which gives the expected near-threshold ($l = n$) scaling of $\sim k_n^{2l+1}$ [27, 29, 172] shown in section 2.2.

In Fig. 5.6 we demonstrate the accuracy of the above mentioned weak field approximations. The black (+) symbol represents the total ionization yield for $a = a_0/5$ obtained from the TDSE calculations, as in Fig. 5.3a). The cyan curve represents data when we keep only the dominant pathways described in this section. The green curve represents the results obtained by application of the first weak field approximation (Eq. (5.72)). Finally, the red curve represents predictions we get by applying the second simplified weak field approximation (Eq. (5.74)). We observe that the dominant pathways accurately describe ionization for all wavelengths considered. Additionally, both weak field approximations accurately reproduce the yield for one, two and three photon ionization while application of Eq. (5.74) holds well up to five photon ionization. This result is surprising since Eq. (5.74) is a further approximation of Eq. (5.72).

Since $k_A \ll \kappa$ we see that $j_{l_A}(k_A r)$ is approximated accurately by the lowest $(k_A r)^{l_A}$ term at short wavelengths. Similarly, since dominant contributions to ionization are described by the lowest energy near-threshold photo-electrons we have $k_n\xi \ll 1$ yielding that $j_{l_S}(k_n\xi)$ is approximated well by the term with order $(k_n\xi)^{l_S}$. The additional purple curve in Fig. 5.6 represents results obtained using the application of Eq. (5.74) where only the lowest order $n = n_{\text{th}}$ has been included to show accuracy of the near-threshold approximation for photon orders above the threshold value ($n > n_{\text{th}}$).

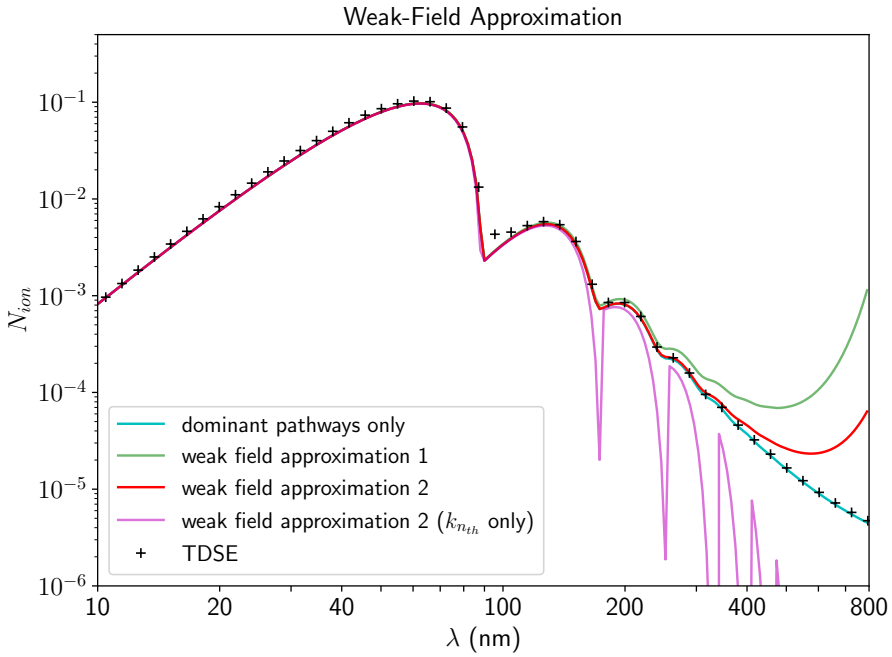

Figure 5.6: Comparison of the weak field approximations. The black (+) symbol represents the total ionization for $a = a_0/5$ obtained from the TDSE calculations, as in Fig. 5.3a. The cyan curve represents results for the dominant pathways described in this section. The green and red curves represent data obtained from Eq. (5.72) and Eq. (5.74), respectively. The purple curve shows data using the application of Eq. (5.74) where only the lowest order $n = n_{\text{th}}$ has been included.

5.3.2 Strong-Field Limit

The light blue curve in Fig. 5.6 demonstrates that the reduced set of pathways described in the prior weak-field subsection describe ionization up to the largest 800 nm wavelength considered. Other curves in Fig. 5.6 further approximate the rate from the lowest-order polynomial terms of $j_{l_A}(k_A r)$ and $j_{l_S}(k_n \xi)$. One would therefore expect that the weak-field approximations will tend towards TDSE predictions as higher contributions are used to approximate $j_{l_A}(k_A r)$ and $j_{l_S}(k_n \xi)$.

To demonstrate this trend we will expand the radial integrand as

$$j_{l_A}(k_A r) \approx (2k_A r)^{l_A} \sum_{\alpha=0}^{\alpha_{\max}} \frac{(-1)^\alpha (l_A + \alpha)!}{\alpha!(2l_A + 2\alpha + 1)!} (k_A r)^{2\alpha} \tag{5.75}$$

to express the radial integral as a series expansion

$$I_0^{l_k}(k_n) \approx \sum_{\alpha=0}^{\alpha_{\max}} z_1^{\alpha} I_0^{l_k(\alpha)}(k_n) \tag{5.76}$$

with respect to the bound-state intensity parameter $z_1 \equiv 2U_p/I_p$ [146, 148] (see section 2.3) which is related to the Keldysh parameter γ [98] by $z_1 = 1/\gamma^2$. In Fig. 5.7 we have compared predictions using Eq. (5.76) with orders $\alpha_{\max} = 0 - 4$ to the TDSE results which show that significantly higher order expansions are required to approximate the rate as the wavelength increases.

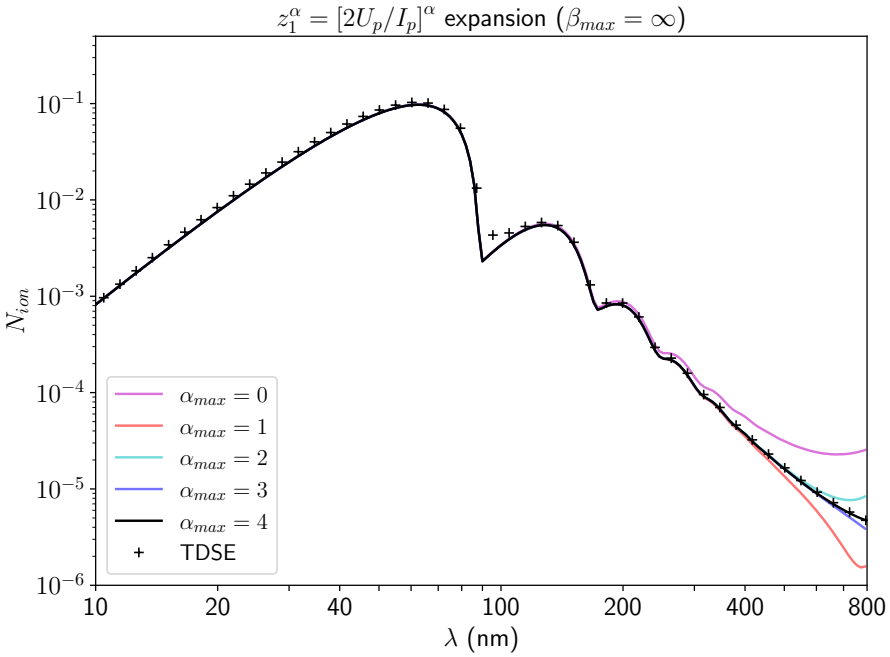

Figure 5.7: Dominant ionization pathway yield from Fig.(5.6) where $j_{l_S}(k_n\xi)$ is treated exactly and $j_{l_A}(k_A r)$ is expanded as in Eq.(5.76) to zeroth, first, second, third and fourth order $\alpha_{\max}$ (solid lines). Crosses correspond to the $a = a_0/5$ s-state TDSE data from Fig.(5.3).

We will express $j_{l_S}(k_n\xi)$ in a similar series expansion with respect to the non-perturbative intensity parameter $z = U_p/\hbar\omega$, yielding

$$j_{l_S}(k_n\xi) \approx \sum_{\beta=0}^{\beta_{\max}} z^{\beta} B_{l_S}^{(\beta)}(k_n) \quad \text{with} \quad B_{l_S}^{(\beta)}(k_n) \equiv \frac{(2k_n\xi)^{l_S}(l_S+\beta)!}{\beta!(2l_S+2\beta+1)!}\left[-4\left(\frac{E_{k_n}}{\hbar\omega}\right)\right]^{\beta}. \tag{5.77}$$

In Fig. 5.8 we have compare results using Eq. (5.77) with $\beta_{\max} = 0 - 7$ with the TDSE results. It is again clear that significantly higher order expansions are required to approximate the rate as the wavelength becomes large.

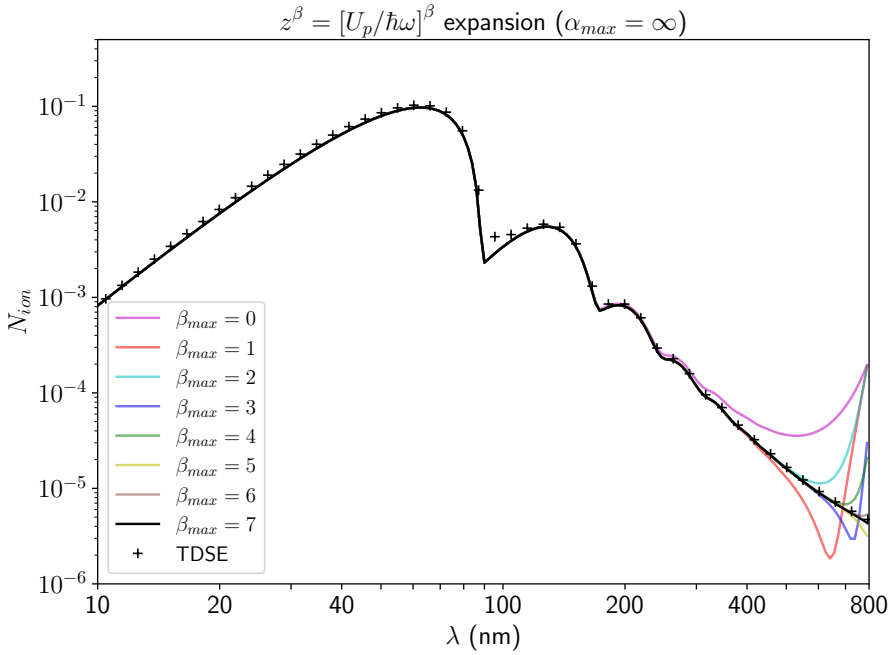

Figure 5.8: Dominant ionization pathway yield from Fig.(5.6) where $j_{l_A}(k_A r)$ is treated exactly and $j_{l_S}(k_n \xi)$ is expanded as in Eq.(5.77) from zeroth to seventh order $\beta_{\max}$ (solid lines). Crosses correspond to the $a = a_0/5$ s-state TDSE data from Fig.(5.3).

Combining these expansions it is obvious that probability amplitudes may be written as

$$C_n^{\pm n}(k_n) \approx \sum_{\alpha=0}^{\alpha_{\max}} \sum_{\beta=0}^{\beta_{\max}} z_1^\alpha z^\beta C_n^{\pm n(\alpha,\beta)}(k_n), \tag{5.78}$$

where an expansion is performed over both z_1 and z in disagreement with Reiss [147] who claimed that the length-gauge rate corresponds to an expansion over $z_1 = 1/\gamma^2$ only. To summarize, in this section we were able to evaluate the first-order Keldysh amplitude exactly for the case of arbitrary initial and final states. We described the importance of using correct atomic initial and final states at the shortest wavelengths and identified issues with the application of the saddle-point

approximation to p–states. We finished the section by finding simplified rates in the UV limit and appropriate strong-field corrections while transitioning into the strong-field IR limit.

5.4 Linear and elliptical polarization

5.4.1 Results

Expanding linearly and elliptically polarized laser pulses as a linear combination of both right-handed and left-handed circularly polarized fields exactly the same steps can be used to determine the ionization amplitude. The TDSE for ionization by an elliptically polarized field can be written as

$$i\hbar\frac{\partial}{\partial t}\Psi_\epsilon(\mathbf{r},t) = \left[H_a + |e|\mathbf{E}_\epsilon(t)\cdot\mathbf{r}\right]\Psi_\epsilon(\mathbf{r},t) \tag{5.79}$$

with

$$\mathbf{E}_\epsilon(t) = E\left[\cos(\omega t)\hat{\mathbf{x}} + \epsilon\sin(\omega t)\hat{\mathbf{y}}\right], \tag{5.80}$$

$$\mathbf{E}_\epsilon(t) = -\frac{1}{c}\frac{d\mathbf{A}_\epsilon}{dt}(t), \qquad \mathbf{A}_\epsilon(t) = -A\left[\sin(\omega t)\hat{\mathbf{x}} - \epsilon\cos(\omega t)\hat{\mathbf{y}}\right], \quad \text{and} \qquad A = \frac{cF}{\omega}. \tag{5.81}$$

The vector potential is now represented as

$$\mathbf{A}_\epsilon(t) = \left(\frac{1+\epsilon}{2}\right)\mathbf{A}_+(t) + \left(\frac{1-\epsilon}{2}\right)\mathbf{A}_-(t) \tag{5.82}$$

in terms of the right-handed (+) and left-handed (−) circularly polarized fields $\mathbf{A}_\pm(t)$. Expanding the exponential terms as in Eq. (5.28) and Eq. (5.15) a rate is determined exactly as in the last section dedicated to circular polarization. We will now give numerical comparisons of the predictions with the TDSE results before deriving the amplitude in the next subsection.

In Fig. 5.9 we reproduce the right panel of Fig. 5.4 where all laser parameters are the same except for the laser ellipticity. In the top panel (bottom panel) we show the good agreement with the TDSE results for the case of linear (elliptical $\epsilon = 0.5$) polarization at all wavelengths, where the best agreement is again found for the case when both atomic initial and final states are used. It is clear that the formulas yield a similar level of agreement for these cases as we have found earlier in the case of circular polarization.

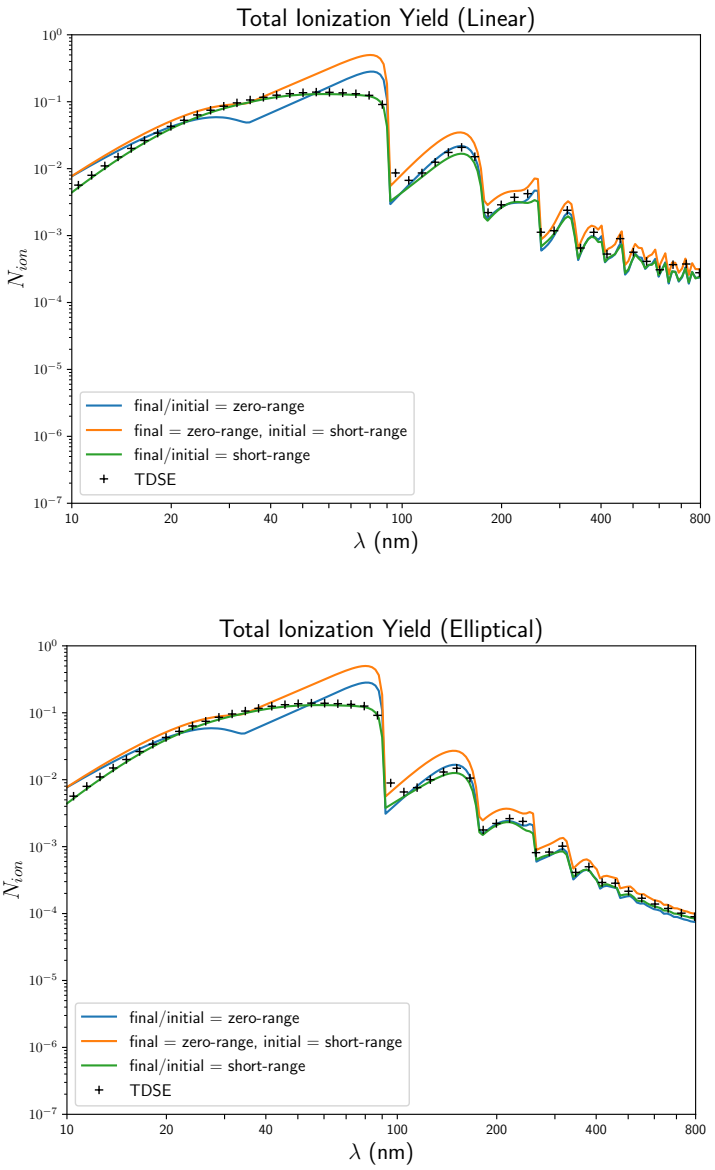

Figure 5.9: Comparison of the predictions of the p-state model with the TDSE results for exponential parameter $a = a_0/2$. The top (bottom) panel corresponds to interaction with a laser pulses with an ellipticity of $\epsilon = 0$ ($\epsilon = 0.5$). The blue line shows the predictions for zero-range initial and final states. The orange curve represents data for the asymptotic initial states with numerical states of the atomic Hamiltonian. The green curve corresponds to the application of the same numerical initial state, but now with Volkov states where the plane-wave scattering state has been replaced with scattering states of the atom.

5.4.2 Derivation

Using the partial wave expansion, Eq. (5.15), the amplitude

$$\mathcal{M}_\epsilon^{(1)}(\mathbf{k},t) = \int_0^t dt_1 e^{(i/\hbar)S_\epsilon(\mathbf{k},t_1)}\left(-\frac{\partial}{\partial t_1}\right)\int d\mathbf{r}_1 \overline{\phi_{\mathbf{k}}^{(-)}(\mathbf{r}_1)}\, e^{-\frac{i|e|}{\hbar c}\mathbf{A}_\epsilon(t_1)\cdot\mathbf{r}_1}\phi_i(\mathbf{r}_1) \tag{5.83}$$

is evaluated using

$$\begin{aligned}\left(-\frac{\partial}{\partial t_1}\right)\int d\mathbf{r}_1 \overline{\phi_{\mathbf{k}}^{(-)}(\mathbf{r}_1)}\, e^{-\frac{i|e|}{\hbar c}\mathbf{A}_\epsilon(t_1)\cdot\mathbf{r}_1}\phi_i(\mathbf{r}_1) &= \omega\sum_{l_{A_+}=0}^{\infty}\sum_{n_{A_+}=-l_{A_+}}^{l_{A_+}} \overline{Y_{l_{A_+}}^{n_{A_+}}(\hat{\mathbf{A}}_+(0))}\\ &\times\sum_{l_{A_-}=0}^{\infty}\sum_{n_{A_-}=-l_{A_-}}^{l_{A_-}} A_{l_{A_+},l_{A_-}}^{n_{A_+},n_{A_-}}\overline{Y_{l_{A_-}}^{-n_{A_-}}(\hat{\mathbf{A}}_-(0))}e^{-i(n_{A_+}+n_{A_-})\omega t_1}\sum_{l_k=0}^{\infty}\sum_{m_k=-l_k}^{l_k} K_{l_k}(k)Y_{l_k}^{m_k}(\hat{\mathbf{k}})\\ &\times I_{n_i,l_i}^{l_k,l_{A_-},l_{A_+}}(k,k_A,\epsilon)\begin{bmatrix} l_k & l_{A_-} & l_{A_+} & l_i\\ -m_k & -n_{A_-} & n_{A_+} & m_i\end{bmatrix},\end{aligned} \tag{5.84}$$

where

$$A_{l_{A_+},l_{A_-}}^{n_{A_+},n_{A_-}} = 16\pi^2 i(n_{A_+}+n_{A_-})(-i)^{l_{A_+}+l_{A_-}}, \qquad \text{and} \quad K_{l_k}(k) = (-i)^{l_k}e^{i\sigma_{l_k}(k)}. \tag{5.85}$$

Other contributions correspond to the angular integral

$$\begin{bmatrix} l_4 & l_3 & l_2 & l_1\\ -m_4 & m_3 & m_2 & m_1\end{bmatrix} \equiv \int d\mathbf{e}_r \overline{Y_{l_4}^{m_4}(\hat{\mathbf{r}})}Y_{l_3}^{m_3}(\hat{\mathbf{r}})Y_{l_2}^{m_2}(\hat{\mathbf{r}})Y_{l_1}^{m_1}(\hat{\mathbf{r}}) \tag{5.86}$$

expanded in terms of $3j$-symbols and the radial integral

$$I_{n_i,l_i}^{l_k,l_{A_-},l_{A_+}}(k,k_A,\epsilon) \equiv \frac{1}{k}\int_0^\infty dr_1\, r_1^2\, R_{k,l_k}(r_1)j_{l_{A_-}}\left(\left(\frac{1-\epsilon}{2}\right)k_A r_1\right)j_{l_{A_+}}\left(\left(\frac{1+\epsilon}{2}\right)k_A r_1\right)R_{n_i,l_i}(r_1) \tag{5.87}$$

which is evaluated numerically.

For asymptotic initial states and plane-wave Volkov states the radial integral becomes

$$\begin{aligned}I_{n_i,l_i}^{l_k,l_{A_-},l_{A_+}}(k,k_A,\epsilon) &= \frac{C_{\kappa l_i}}{2^{3/2-\nu}}\frac{\sqrt{\pi}}{\kappa^{3/2}}\frac{\Gamma\left(\frac{l_k+l_{A_-}+l_{A_+}+\nu+1}{2}\right)\Gamma\left(\frac{l_k+l_{A_-}+l_{A_+}+\nu+2}{2}\right)}{\Gamma\left(l_k+\frac{3}{2}\right)\Gamma\left(l_{A_-}+\frac{3}{2}\right)\Gamma\left(l_{A_+}+\frac{3}{2}\right)}\\ &\times\left(\frac{k}{\kappa}\right)^{l_k}\left[\left(\frac{1-\epsilon}{2}\right)\frac{k_A}{\kappa}\right]^{l_{A_-}}\left[\left(\frac{1+\epsilon}{2}\right)\frac{k_A}{\kappa}\right]^{l_{A_+}}F_C^{(3)}\left(\frac{l_k+l_{A_-}+l_{A_+}+\nu+1}{2},\frac{l_k+l_{A_-}+l_{A_+}+\nu+2}{2}\right.\\ &\left.;l_k+\frac{3}{2},l_{A_-}+\frac{3}{2},l_{A_+}+\frac{3}{2};-\left(\frac{k}{\kappa}\right)^2,-\left[\left(\frac{1-\epsilon}{2}\right)\frac{k_A}{\kappa}\right]^2,-\left[\left(\frac{1+\epsilon}{2}\right)\frac{k_A}{\kappa}\right]^2\right)\end{aligned} \tag{5.88}$$

where

$$F_C^{(3)}(a,b;c_1,c_2,c_3;x_1,x_2,x_3) \equiv \sum_{i_1,i_2,i_3=0}^{\infty} \frac{(a)_{i_1+i_2+i_3}(b)_{i_1+i_2+i_3}}{(c_1)_{i_1}(c_2)_{i_2}(c_3)_{i_3}} \frac{x_1^{i_1}}{i_1!}\frac{x_2^{i_2}}{i_2!}\frac{x_3^{i_3}}{i_3!} \tag{5.89}$$

is the Lauricella hypergeometric series [108] which may be evaluated past its radius of convergence $\sqrt{|x_1|}+\sqrt{|x_2|}+\sqrt{|x_3|}<1$ (or $k+k_A<\kappa$) through various analytic continuations. This exact solution allows for systematic approximations in the weak field limit ($k_A \ll \kappa$) just as we have shown it for circular polarization in section 5.3.

The amplitude is completed from the action

$$S_\epsilon(\mathbf{k},t) = \int_0^t d\tau \left[\frac{(\hbar\mathbf{k}+\frac{|e|}{c}\mathbf{A}_\epsilon(\tau))^2}{2m} + I_p\right] = (E_k+I_p)\,t + \hbar\mathbf{k}\cdot(\boldsymbol{\xi}_\epsilon(t)-\boldsymbol{\xi}_\epsilon(0)) + \frac{|e|^2}{2mc^2}\int_0^t d\tau \mathbf{A}_\epsilon(\tau)^2, \tag{5.90}$$

where the ponderomotive term

$$\frac{|e|^2}{2mc^2}\int_0^t d\tau \mathbf{A}_\epsilon(\tau)^2 = U_p t + \frac{|e|^2A^2(1-\epsilon^2)}{8\omega mc^2}\sin(-2\omega t) \qquad \text{with} \qquad U_p \equiv \frac{|e|^2A^2(1+\epsilon^2)}{4mc^2} \tag{5.91}$$

has additional time-dependent oscillations due to the presence of both right- and left-handed fields. The quiver motion

$$\boldsymbol{\xi}_\epsilon(t) = \left(\frac{1+\epsilon}{2}\right)\boldsymbol{\xi}_+(t) + \left(\frac{1-\epsilon}{2}\right)\boldsymbol{\xi}_-(t) \tag{5.92}$$

is separated into left- and right-handed contributions giving the exponential partitions

$$e^{(i/\hbar)S_\epsilon(\mathbf{k},t)} = e^{-i\mathbf{k}\cdot\boldsymbol{\xi}_\epsilon(0)}e^{iN(k)\omega t}e^{i\frac{|e|^2A^2(1-\epsilon^2)}{8\hbar\omega mc^2}\sin(-2\omega t)}e^{i\left(\frac{1-\epsilon}{2}\right)\mathbf{k}\cdot\boldsymbol{\xi}_-(t)}e^{i\left(\frac{1+\epsilon}{2}\right)\mathbf{k}\cdot\boldsymbol{\xi}_+(t)} \tag{5.93}$$

with

$$N(k) \equiv \frac{1}{\hbar\omega}\left(E_k+\tilde{I}_p\right). \tag{5.94}$$

The factors

$$e^{i\left(\frac{1\pm\epsilon}{2}\right)\mathbf{k}\cdot\boldsymbol{\xi}_\pm(t)} = \sum_{l_{S_\pm}=0}^{\infty}\sum_{n_{S_\pm}=-l_{S_\pm}}^{l_{S_\pm}} X_{l_{S_\pm}}(k,\xi,\epsilon)\overline{Y_{l_{S_\pm}}^{\pm n_{S_\pm}}(\hat{\boldsymbol{\xi}}_\pm(0))}Y_{l_{S_\pm}}^{\pm n_{S_\pm}}(\hat{\mathbf{k}})e^{-in_{S_\pm}\omega t} \tag{5.95}$$

are evaluated as before, where

$$e^{i\frac{|e|^2A^2(1-\epsilon^2)}{8\hbar\omega mc^2}\sin(-2\omega t)} = \sum_{a=-\infty}^{\infty} B_a(A,\omega,\epsilon)e^{-2ia\omega t} \tag{5.96}$$

completes the exponential with

$$X_{\pm}(k,\xi,\epsilon) \equiv 4\pi i^{l_{S_+/L}} j_{l_{S_+/L}}\left(\left(\frac{1\pm\epsilon}{2}\right)k\xi\right) \quad \text{and} \quad B_a(A,\omega,\epsilon) = J_a\left(\frac{|e|^2A^2(1-\epsilon^2)}{8\hbar\omega mc^2}\right). \tag{5.97}$$

Putting it all together the exponential action factor becomes

$$\begin{aligned} e^{(i/\hbar)S_\epsilon(\mathbf{k},t)} &= e^{-i\mathbf{k}\cdot\boldsymbol{\xi}_\epsilon(0)}\sum_{l_{S_+}=0}^{\infty}\sum_{n_{S_+}=-l_{S_+}}^{l_{S_+}} X_{l_{S_+}}(k,\xi,\epsilon)\overline{Y_{l_{S_+}}^{n_{S_+}}(\hat{\boldsymbol{\xi}}_+(0))}Y_{l_{S_+}}^{n_{S_+}}(\hat{\mathbf{k}}) \\ &\times\sum_{l_{S_-}=0}^{\infty}\sum_{n_{S_-}=-l_{S_-}}^{l_{S_-}} X_{l_{S_-}}(k,\xi,\epsilon)\overline{Y_{l_{S_-}}^{-n_{S_-}}(\hat{\boldsymbol{\xi}}_-(0))}Y_{l_{S_-}}^{-n_{S_-}}(\hat{\mathbf{k}})\sum_{a=-\infty}^{\infty}B_a(A,\omega,\epsilon)e^{i[N(k)-(n_{S_+}+n_{S_-}+2a)]\omega t}. \end{aligned} \tag{5.98}$$

Using

$$\int_0^t dt_1 e^{i[N(k)-(n_{A_+}+n_{A_-}+n_{S_+}+n_{S_-}+2a)]\omega t_1} = \delta_t([N(k)-(n_{A_+}+n_{A_-}+n_{S_+}+n_{S_-}+2a)]\omega/2) \tag{5.99}$$

the amplitude for a finite pulse becomes

$$\begin{aligned} \mathcal{M}_\epsilon^{(1)}(\mathbf{k},t) &= \omega e^{-i\mathbf{k}\cdot\boldsymbol{\xi}_\epsilon(0)}\sum_{l_{A_+}=0}^{\infty}\sum_{n_{A_+}=-l_{A_+}}^{l_{A_+}}\overline{Y_{l_{A_+}}^{n_{A_+}}(\hat{\mathbf{A}}_+(0))}\sum_{l_{A_-}=0}^{\infty}\sum_{n_{A_-}=-l_{A_-}}^{l_{A_-}}A_{l_{A_+},l_{A_-}}^{n_{A_+},n_{A_-}}\overline{Y_{l_{A_-}}^{-n_{A_-}}(\hat{\mathbf{A}}_-(0))} \\ &\times\sum_{l_k=0}^{\infty}K_{l_k}(k)I_{n_i,l_i}^{l_k,l_{A_-},l_{A_+}}(k,k_A,\epsilon)\begin{bmatrix} l_k & l_{A_-} & l_{A_+} & l_i \\ -(m_i+n_{A_+}-n_{A_-}) & -n_{A_-} & n_{A_+} & m_i\end{bmatrix} \\ &\times\sum_{l_{S_+}=0}^{\infty}\sum_{n_{S_+}=-l_{S_+}}^{l_{S_+}}X_{l_{S_+}}(k,\xi,\epsilon)\overline{Y_{l_{S_+}}^{n_{S_+}}(\hat{\boldsymbol{\xi}}_+(0))}\sum_{l_{S_-}=0}^{\infty}\sum_{n_{S_-}=-l_{S_-}}^{l_{S_-}}X_{l_{S_-}}(k,\xi,\epsilon)\overline{Y_{l_{S_-}}^{-n_{S_-}}(\hat{\boldsymbol{\xi}}_-(0))} \\ &\times\sum_{l=0}^{\infty}\begin{bmatrix} l & l_{S_-} & l_{S_+} & l_k \\ -(m_i+n_{A_+}-n_{A_-}+n_{S_+}-n_{S_-}) & -n_{S_-} & n_{S_+} & (m_i+n_{A_+}-n_{A_-})\end{bmatrix}Y_l^{m_i+n_{A_+}-n_{A_-}+n_{S_+}-n_{S_-}}(\hat{\mathbf{k}}) \\ &\times\sum_{a=-\infty}^{\infty}B_a(A,\omega,\epsilon)\delta_t([N(k)-(n_{A_+}+n_{A_-}+n_{S_+}+n_{S_-}+2a)]\omega/2). \end{aligned} \tag{5.100}$$

5.4.2.1 Long pulse limit

Next, we will compute the rate for a long pulse

$$W_\epsilon(\mathbf{k}) = \lim_{t\to\infty} t^{-1}|\mathcal{M}_\epsilon(\mathbf{k},t)|^2 \approx \lim_{t\to\infty} t^{-1}|\mathcal{M}_\epsilon^{(1)}(\mathbf{k},t)|^2. \tag{5.101}$$

To carry out the $t \to \infty$ limit we only need to consider properties of $\delta_t([N(k)-n]\omega/2)$ and known properties of the Dirac delta distribution

$$\lim_{t\to\infty} t^{-1}\delta_t([N(k)-n]\omega/2)\overline{\delta_t([N(k)-n']\omega/2)} = \lim_{t\to\infty} e^{i(n'-n)\omega t/2}\frac{\sin([N(k)-n]\omega t/2)\sin([N(k)-n']\omega t/2)}{t[N(k)-n][N(k)-n']\omega^2/4}$$
$$= \pi\,\delta([N(k)-n]\omega/2)\,\delta_{n,n'} = 2\pi\hbar\,\delta([N(k)-n]\hbar\omega)\,\delta_{n,n'}. \quad (5.102)$$

To finish the derivation of the rate we will replace the delta function in energy by a delta function in k-space where

$$2\pi\hbar\,\delta([N(k)-n]\hbar\omega)\,\delta_{n,n'} = \frac{2\pi m}{\hbar k_n}\,\delta(k-k_n)\,\delta_{n,n'}, \qquad \text{with} \qquad k_n \equiv \sqrt{\frac{2m}{\hbar^2}\left(n\hbar\omega - \tilde{I}_p\right)} \quad (5.103)$$

and

$$W_\epsilon(\mathbf{k}) = \lim_{t\to\infty} t^{-1}|\mathcal{M}_\epsilon^{(1)}(\mathbf{k},t)|^2 = \sum_{n=n_0}^{\infty} |\mathcal{M}_{n\epsilon}^{(1)}(\hat{\mathbf{k}})|^2\delta(k-k_n). \quad (5.104)$$

Using the selection rules

$$n = n_{A_+} + n_{A_-} + n_{S_+} + n_{S_-} + 2a \qquad \Rightarrow \qquad n_{S_-} = n - n_{A_+} - n_{A_-} - n_{S_+} - 2a \quad (5.105)$$

the sum over n_{S_-} is eliminated and we get the amplitude as

$$\mathcal{M}_{n\epsilon}^{(1)}(\hat{\mathbf{k}}) = \omega\sqrt{\frac{2\pi}{v_n}}e^{-i\mathbf{k}_n\cdot\boldsymbol{\xi}_\epsilon(0)}\sum_{l_{A_+}=0}^{\infty}\sum_{n_{A_+}=-l_{A_+}}^{l_{A_+}}\overline{Y_{l_{A_+}}^{n_{A_+}}(\hat{\mathbf{A}}_+(0))}\sum_{l_{A_-}=0}^{\infty}\sum_{n_{A_-}=-l_{A_-}}^{l_{A_-}}A_{l_{A_+},l_{A_-}}^{n_{A_+},n_{A_-}}\overline{Y_{l_{A_-}}^{-n_{A_-}}(\hat{\mathbf{A}}_-(0))}$$
$$\times\sum_{l_k=0}^{\infty}K_{l_k}(k)I_{n_i,l_i}^{l_k,l_{A_-},l_{A_+}}(k,k_A,\epsilon)\begin{bmatrix} l_k & l_{A_-} & l_{A_+} & l_i \\ -(m_i+n_{A_+}-n_{A_-}) & -n_{A_-} & n_{A_+} & m_i\end{bmatrix}$$
$$\times\sum_{l_{S_+}=0}^{\infty}\sum_{n_{S_+}=-l_{S_+}}^{l_{S_+}}X_{l_{S_+}}(k,\xi,\epsilon)\overline{Y_{l_{S_+}}^{n_{S_+}}(\hat{\boldsymbol{\xi}}_+(0))}\sum_{l_{S_-}=0}^{\infty}\sum_{a=-\infty}^{\infty}B_a(A,\omega,\epsilon)X_{l_{S_-}}(k,\xi,\epsilon)$$
$$\times\overline{Y_{l_{S_-}}^{n_{A_+}+n_{A_-}+n_{S_+}+2a-n}(\hat{\boldsymbol{\xi}}_-(0))}\sum_{l=0}^{\infty}Y_l^{m_i+2(n_{A_+}+n_{S_+}+a)-n}(\hat{\mathbf{k}})$$
$$\times\begin{bmatrix} l & l_{S_-} & l_{S_+} & l_k \\ -[m_i+2(n_{A_+}+n_{S_+}+a)-n] & (n_{A_+}+n_{S_+}+n_{A_-}+2a-n) & n_{S_+} & (m_i+n_{A_+}-n_{A_-})\end{bmatrix}. \quad (5.106)$$

The partial wave expansions used when expanding the ionization amplitude for circularly polarized fields apply directly to the case of linearly and elliptically polarized fields as well. Although

tedious, we believe that these formulas will prove to be an inexpensive alternative to numerical calculations by the TDSE. The amplitude can be greatly simplified in specific limits such as $\epsilon \approx \pm 1$ just as in section 5.3 where the right- (left-)handed circularly polarized fields may be non-perturbative with corrections by a perturbative field of opposite left- (right-)handed polarization.

Chapter 6

Strong-field processes involving polychromatic fields

6.1 Introduction[1]

The generation of ultrashort vacuum ultraviolet (VUV) and deep ultraviolet (DUV) laser pulses [41, 66, 145] is important since excitation and ionization energies of many atoms, molecules, nanoparticles, and materials lie in this spectral region. Such laser sources are used to trigger, steer, probe, and image physical processes and chemical reactions on the ultrafast time scale, down to the attosecond regime of electron dynamics [31, 55, 100, 109, 119, 127, 131, 156, 162]. Temporal pulse characterization is often required to enable the analysis of the spectroscopic data. Many ultrashort pulse characterization methods rely on the measurement of ions or photoelectrons via the autocorrelation or the cross correlation approach (for an overview, see [133]). In cross correlation methods the pulse to be characterized is used in superposition with a well-characterized infrared pulse [39, 73, 87, 121, 134, 159], while for autocorrelation measurements, two replicas of the unknown pulse are used [126, 130, 149, 160, 161].

In this Chapter we will derive semi-analytic perturbative two-photon amplitudes for the ionization of atoms by arbitrary polychromatic fields (section 6.2). These formulas are applied to reconstruct isolated attosecond pulses and pulse trains from a provided autocorrelation trace (ionization as a function of relative delay). A feedback loop is used and ionization is determined from a model laser parameterized by a set of variational parameters. The field is recovered by

[1] Part of the material presented in this Chapter has been previously published in S. Walker, R. Reiff, A. Jaron-Becker, and A. Becker, Optics Letters **46**, 3083–3086 (2021) [168].

determining variational parameters such that the exact autocorrelation trace agrees with the trace generated by the parameterized field. In the last section (section 6.3) of this Chapter we will extend the formulas into the non-perturbative limit. Time is partitioned into slices $(t_{m-1}, t_m]$ $(m \in \mathbb{Z})$ [63] narrow enough such that the formulas of section 6.2 may be applied. We see that time-slicing extends analytic perturbative principles into the nonperturbative limit. These formulas may prove to be useful for nonperturbative processes involving short pulses and electrons bound by long-range potentials.

6.2 Characterization of vacuum and deep ultraviolet pulses via two-photon autocorrelation signals

In an autocorrelation measurement, ion signals are recorded as a function of the time delay between the two replicas of the pulse. Generalized two-photon ionization cross sections for the interaction of a single Gaussian pulse with the target are then used to fit the autocorrelation trace and determine the pulse duration. This powerful method has been applied to estimate the duration of attosecond extreme ultraviolet (XUV) pulses [160, 161], VUV and DUV pulses [66, 149]. Overall, the application of current pulse characterization techniques in the important VUV and DUV spectral region is limited, since many methods, such as the widely used reconstruction of attosecond beating by interference of two-photon transitions (RABBITT) [134] or attosecond streaking technique [87], rely on the ionization of the target by absorption of a single photon from the unknown pulse.

We consider an extension of the single-Gaussian autocorrelation technique, which enables the characterization of the temporal pulse envelope of an isolated ultrashort VUV pulse or a pulse train, i.e. the time-dependent amplitude and phase variation of the electric field. The extension is based on the analytical solution of the time-dependent Schrödinger equation (TDSE) for the perturbative two-photon ionization of an atom by a Gaussian laser pulse in the single-active-electron approximation [86]. Since the solution includes both resonant and non-resonant pathways, it can be used for the characterization of broadband pulses with photon energies in the regime of typical

atomic excitation energies. The unknown pulse is approximated as a superposition of Gaussian pulses, for which the amplitudes and temporal widths are determined via fitting to the two-photon autocorrelation signal generated by the unknown laser pulse. We demonstrate this extension of the single-Gaussian autocorrelation technique via applications based on results for ultrashort VUV pulses from numerical simulations of macroscopic high harmonic generation (HHG).

6.2.1 Multi-color Gaussian approach

For the characterization, we use that the electric field of any arbitrary pulse can be written as the real part of an expansion in a basis of multi-color Gaussian functions (Hartree atomic units are used: $e = \hbar = m = 1$ a.u.):

$$\tilde{f}(t) = |\tilde{f}(t)|e^{-i\phi(t)} = \sum_{n,j} \tilde{f}_{n,j} \exp\left[-\frac{(t-\tau_{n,j})^2}{2T_{n,j}^2} - i\omega_j t\right], \tag{6.1}$$

where $|\tilde{f}(t)|$ and $\phi(t)$ are the time-dependent amplitude and phase of the unknown pulse. $\tilde{f}_{n,j}$ is the complex amplitude, $\tau_{n,j}$ is a translation in time, and $T_{n,j}$ is the width of a Gaussian pulse with central frequency ω_j. In the examples below, we consider linearly polarized pulses, but the expansion can be applied to other polarizations as well. Since each Gaussian has an independent phase factor, in the multi-Gaussian approach the nonlinear phase accumulation $\omega(t) \equiv \frac{d\phi}{dt}$ can be determined from the interferences in the two-photon autocorrelation trace. If a large frequency variation is expected, an alternative basis of linearly chirped Gaussian functions can be utilized by substituting $T_{n,j}^{-2} \to T_{n,j}^{-2} + i\alpha_{n,j}$, where $\alpha_{n,j}$ is an additional parameter. For all pulses considered in the present work, we have used $\alpha_{n,j} = 0$ to limit the number of fitting parameters.

Next, we utilize the analytic solution of the two-photon ionization amplitude for interaction of an atom in the single-active-electron approximation with two Gaussian laser pulses:

$$\begin{aligned} a_{f,i}^{(2)}(\tau_{n_2,j_2}, \tau_{n_1,j_1}) = -\frac{\pi}{4} \tilde{f}_{n_2,j_2} \tilde{f}_{n_1,j_1} T_{n_2,j_2} T_{n_1,j_1} \sum_{E_m<0} z_{f,m} z_{m,i} \\ \times \exp\left(-\frac{1}{2}T_{n_2,j_2}^2 \Delta_{f,m}^2 - \frac{1}{2}T_{n_1,j_1}^2 \Delta_{m,i}^2 + i\Delta_{f,m}\tau_{n_2,j_2} + i\Delta_{m,i}\tau_{n_1,j_1}\right) \\ \times \left\{1 + \mathrm{erf}\left[\frac{1}{\sqrt{2}\bar{T}}\left(\tau_{n_2,j_2} - \tau_{n_1,j_1} + i\left(T_{n_2,j_2}^2 \Delta_{f,m} - T_{n_1,j_1}^2 \Delta_{m,i}\right)\right)\right]\right\}. \end{aligned} \tag{6.2}$$

We note that Eq. (6.2) is a generalization of the solution for a single Gaussian pulse given in Ref. [86] and is derived in section 6.2.2. Here, $\bar{T}^2 = T_{n_2,j_2}^2 + T_{n_1,j_1}^2$, $\Delta_{m,i} = E_{m,i} - \omega_{j_1}$, and $\Delta_{f,m} = E_{f,m} - \omega_{j_2}$, where $E_{m,i}$ and $E_{f,m}$ are the energy differences between the field-free intermediate (m) states and the initial (i) and the final (f) states, respectively. $z_{f,m}$ and $z_{m,i}$ are the transition dipole moments between the respective states which can be obtained via various theoretical techniques for an atom. In the present applications, we restrict the sum to intermediate states with $E_m < 0$. To compute $\mathrm{erf}(x + iy)$, we have used a continued fraction approximation for the majority of the complex plane [43] and patched the (nonphysical) singularities near the origin with the global Padé approximation [173] and other singularities near the imaginary axis with the standard Padé approximation. Since we want to characterize ultrashort pulses with large bandwidths, we have also taken into account the one-photon ionization amplitude for interaction with the n-th Gaussian pulse which is given by

$$a_{f,i}^{(1)}(\tau_{n,j}) = -i\sqrt{\frac{\pi}{2}}\tilde{f}_{n,j}T_{n,j}z_{f,i}\,\exp\left(-\frac{1}{2}T_{n,j}^2\Delta_{f,i}^2 + i\Delta_{f,i}\tau_{n,j}\right). \tag{6.3}$$

The autocorrelation signal for the interaction with two replicas of the arbitrary pulse delayed by a time interval τ to each other can then be approximated by the multi-color Gaussian approach as:

$$P_{N_g}(\tau) = \int_{E_f>0}\left|A_{f,i}^{(1)}(\tau) + A_{f,i}^{(2)}(\tau)\right|^2 dE_f\,, \tag{6.4}$$

where the integral over E_f includes all final levels f for the one- and two-photon processes, respectively,

$$A_{f,i}^{(1)}(\tau) = \sum_n\sum_j a_{f,i}^{(1)}(\tau_{n,j})\left(1 + e^{iE_{f,i}\tau}\right)\,, \tag{6.5}$$

$$\begin{aligned} A_{f,i}^{(2)}(\tau) = &\sum_{n_2}\sum_{j_2}\sum_{n_1}\sum_{j_1} a_{f,i}^{(2)}(\tau_{n_2,j_2},\tau_{n_1,j_1})\left(1 + e^{iE_{f,i}\tau}\right) \\ &+\; a_{f,i}^{(2)}(\tau_{n_2,j_2}+\tau,\tau_{n_1,j_1})e^{i\omega_{j_2}\tau} + a_{f,i}^{(2)}(\tau_{n_2,j_2},\tau_{n_1,j_1}+\tau)e^{i\omega_{j_1}\tau} \end{aligned} \tag{6.6}$$

In order to characterize the envelope of the unknown ultrashort pulse, we introduce an objective function between the autocorrelation signal $P_{\mathrm{exact}}(\tau)$, measured with the unknown pulse, and the

approximate multi-Gaussian signal $P_{N_g}(\tau)$ as:

$$\mathrm{obj}_{N_g}(\tau) = \frac{|P_{\mathrm{exact}}(\tau) - P_{N_g}(\tau)|}{P_{\mathrm{exact}}(0)}, \tag{6.7}$$

where $P_{\mathrm{exact}}(0)$ is the maximum ionization yield for which the two replicas of the pulse perfectly overlap. For a given number of Gaussian pulses, N_g, the L^2 norm of the objective function is then minimized with respect to variation of $\tilde{f}_{n,j}$, $\tau_{n,j}$ and $T_{n,j}$ using the standard non-linear least squares approach, where the objective function has a complexity that scales as the square of the number of basis functions used. Without loss of generality, for exactly one n, j we chose $\tilde{f}_{n,j}$ real and fix $\tau_{n,j} = 0$.

6.2.2 Derivation of ionization amplitudes

Before applying the multi-color Gaussian approach we discuss the derivation of the one- and two-photon ionization amplitudes used in the approach. The perturbative ionization amplitude (Chapter 2) used in the previous section can be described by the Lippmann-Schwinger equation

$$\Psi(x) = \phi_i(x) + \int d^4x_1\, G(x;x_1) V_L(x_1) \phi_i(x_1), \tag{6.8}$$

where ϕ_i is the initial atomic state calculated from the time-independent Schrödinger equation for a single-active electron potential and V_L is the laser interaction. The exact Green's function G is now expanded as

$$G(x;x_1) = G_0(x;x_1) + \int d^4x_2\, G(x;x_2) V_L(x_2) G_0(x_2;x_1) \tag{6.9}$$

in terms of the atomic Green's function

$$G_0(x;x') = -i\,\theta\left(t-t'\right) \sum\!\!\!\!\!\!\int_j \phi_j(x)\, \overline{\phi_j(x')}, \tag{6.10}$$

where $\sum\!\!\!\!\!\!\int_j$ describes a sum over all bound and an integral over all continuum states $\phi_j(x)$.

The two photon ionization amplitude is then determined from the second order truncation

$$\begin{aligned}\Psi(x) \approx \phi_i(x) &+ \int d^4x_1\, G_0(x;x_1) V_L(x_1) \phi_i(x_1) \\ &+ \int d^4x_2 \int d^4x_1\, G_0(x;x_2) V_L(x_2) G_0(x_2;x_1) V_L(x_1) \phi_i(x_1)\end{aligned} \tag{6.11}$$

using the interaction potential

$$V_L(x) = \mathbf{F}(t)\cdot\mathbf{r} = \mathrm{Re}\left[f(t)\right]\hat{\mathbf{z}}\cdot\mathbf{r}, \tag{6.12}$$

where

$$\tilde{f}(t) = \left|\tilde{f}(t)\right| e^{-i\phi(t)} = \sum_{n,j}\tilde{f}_{n,j}\exp\left[-\frac{(t-\tau_{n,j})^2}{2T_{n,j}^2} - i\omega_j t\right] \tag{6.13}$$

is the laser field expanded in a basis of multi-color Gaussian functions. $\tilde{f}_{n,j}$ is the complex amplitude, $\tau_{n,j}$ is a translation in time, and $T_{n,j}$ is the width of a Gaussian pulse with central frequency ω_j. A detailed description of the first- and second-order terms are presented in sections 6.2.2.1 and 6.2.2.2.

6.2.2.1 One-photon ionization amplitude

The first-order term in Eq. (6.11), corresponds to the lowest order one-photon process

$$\Psi^{(1)}(x) = \int d^4x_1\, G_0(x;x_1)V_L(x_1)\phi_i(x_1). \tag{6.14}$$

Inserting the field interaction and taking $t_0 \to -\infty$ for a finite pulse the correction becomes

$$\Psi^{(1)}(x) = \frac{-i}{2}\sum\!\!\!\!\!\!\int_m \phi_m(x) z_{m,i}\sum_{n,j}\int_{-\infty}^{t} dt_1 \exp\left[-\frac{(t_1-\tau_{n,j})^2}{2T_{n,j}^2}\right] e^{i(E_m-E_i)t_1}\left(\tilde{f}_{n,j}e^{-i\omega_j t_1} + \overline{\tilde{f}_{n,j}}e^{i\omega_j t_1}\right)$$

and simplifies to

$$\Psi^{(1,\mathrm{abs})}(x) = \frac{-i}{2}\sum\!\!\!\!\!\!\int_m \phi_m(x) z_{m,i}\sum_{n,j}\tilde{f}_{n,j}\int_{-\infty}^{t} dt_1 \exp\left[-\frac{(t_1-\tau_{n,j})^2}{2T_{n,j}^2} + i\Delta_{m,i,j}t_1\right]. \tag{6.15}$$

for photon absorption processes. Taking the limit as $t \to \infty$ and projecting onto a continuum state $\phi_f(x)$ gives the contribution for each Gaussian in the laser field as

$$a_{f,i}^{(1)}(\tau_{n,m}) = -i\sqrt{\frac{\pi}{2}} z_{f,i} T_{n,j}\tilde{f}_{n,j}\exp\left(i\tau_{n,j}\Delta_{f,i} - \frac{\Delta_{f,i}^2}{2T_{n,j}^2}\right). \tag{6.16}$$

6.2.2.2 Two-photon ionization amplitude

The second-order, two photon term in Eq. (6.11) is given by

$$\Psi^{(2)}(x) = \int d^4x_2 \int d^4x_1\, G_0(x;x_2)V_L(x_2)G_0(x_2;x_1)V_L(x_1)\phi_i(x_1). \tag{6.17}$$

Inserting the field and following the same steps as the one-photon case before we obtain the $\phi_f(x)$ component

$$a_{f,i}^{(2)}\left(\tau_{n_2,j_2},\tau_{n_1,j_1}\right) = -\frac{\pi}{4}\sum\!\!\!\!\!\!\int_m z_{f,m}z_{m,i}\tilde{f}_{n_1,j_1}T_{n_1,j_1}\tilde{f}_{n_2,j_2}T_{n_2,j_2} \times \exp\left(i\tau_{n_1,j_1}\Delta_{m,i} + i\tau_{n_2,j_2}\Delta_{f,m} - \frac{\Delta_{m,i}^2}{2T_{n_1,j_1}^2} - \frac{\Delta_{f,m}^2}{2T_{n_2,j_2}^2}\right) \times \left\{\operatorname{erf}\left[\frac{1}{\sqrt{2}\sqrt{T_{n_1,j_1}^2+T_{n_2,j_2}^2}}\left(\tau_{n_2,j_2}-\tau_{n_1,j_1}-i\Delta_{m,i}T_{n_1,j_1}^2+i\Delta_{f,m}T_{n_2,j_2}^2\right)\right]+1\right\}$$

after Gaussian integration where photon absorption processes alone are considered.

In general, $\operatorname{erf}(x+iy)$, is poorly conditioned and expensive to compute in the standard integral form. We use a continued fraction approximation for the majority of the complex plane [43] and patch the nonphysical singularities near the origin with the global Padé approximate and other singularities near the imaginary axis with the standard Padé approximate. The evaluation involves defining $g(z,a) = e^a\operatorname{erf}(z)$, and approximating it as

$$g(z,a) \approx \begin{cases} e^a\left[5/5\right]_{\operatorname{erf}(\pm 2i)}(z) & |z\mp 2i| < 1.1 \\ \operatorname{sign}\left(\operatorname{Re}\left[z\right]\right)\sqrt{e^{2a}-e^{2a-z^2\frac{4/\pi+bz^2}{1+bz^2}}} & z\in\Omega \\ \operatorname{sign}\left(\operatorname{Re}\left[z\right]\right)e^a\left(1-\frac{ze^{-z^2}}{\sqrt{\pi}}\left(z^2+\frac{1/2}{1+\frac{1}{z^2+3/2}}\right)^{-1}\right) & \text{else,} \end{cases} \tag{6.18}$$

in the complex plane. Here $b \approx 0.14$, Ω is the set of all z such that $|z| < 1.4$ and $|z \pm 2i| \geq 1.1$, and $\left[m/n\right]_{f(z_0)}(z)$ is the Padé approximate of a function f centered around z_0 with order m in the numerator and order n in the denominator.

6.2.3 Application and results

To test the characterization with this multi-Gaussian approach, we have obtained ultrashort pulses using results of numerical macroscopic simulations of HHG spectra [144]. First, calculations of the microscopic single-atom response have been performed by solving the time-dependent Schrödinger equation within the dipole approximation with Hamiltonian

$$H(t) = -\frac{1}{2}\nabla^2 - \frac{1}{r} + \mathbf{E}(t)\cdot\mathbf{y}\,, \tag{6.19}$$

where $\mathbf{E}$(t) and $\mathbf{y}$ are the electric field and polarization direction of the driving laser pulse. The wavefunction has been expanded in 30 spherical harmonics and the radial part of the wavefunction and the potential have been discretized utilizing fourth order finite difference on a radial grid with spacing dr = 0.2 a.u. and grid sizes up to r_{max} = 100 a.u. [163]. As absorbing boundary, we have used exterior complex scaling (ECS), where the edge of the grid (10%) is rotated into complex space by an angle $\eta = \pi/4$. We have used the Crank-Nicolson method to propagate the wavefunction starting from the initial state of the hydrogen atom with time step dt = 0.1. To obtain the HHG spectra $P(\omega) = |\tilde{a}(\omega)|^2$, the dipole acceleration $a(t)$ has been evaluated using the Ehrenfest theorem $a(t) = \langle -\frac{\partial}{\partial y}\left(-\frac{1}{r}\right)\rangle$ and the complex harmonic response $\tilde{a}(\omega)$ is then obtained by taking the Fourier transform (without windowing).

For the macroscopic radiation signal, we have considered the low gas density regime that is free from longitudinal phase-matching effects. We then followed the approach used in Ref. [81], in which the macroscopic yield is obtained as the superposition of the fields generated at different points in the medium. Application of this approach requires single-atom simulations for a large number of intensities and phase factors. In the present simulations 5×10^5 single-atom results have been used via an interpolation scheme based on 100 exact TDSE results. The success of the interpolation method has been verified elsewhere [144].

In Fig. 6.1(a), we show the below- and near-threshold part of the numerical macroscopic HHG signal obtained for a gas jet of hydrogen atoms interacting with a 20-cycle, 800 nm pulse at peak intensity 4×10^{13} W/cm^2. From this spectrum, we have first extracted isolated ultrashort pulses by applying a Gaussian filter in the frequency domain centered about the harmonic H_0, i.e. $e^{-(H-H_0)^2/2\beta^2}$ where $\beta = 0.35$ in the present work. The temporal shape of the pulse filtered about the 9th harmonic varies significantly from that of a Gaussian pulse (Fig. 6.1(b)). For the application of the characterization method, we used replicas of the pulse with an intensity of 3.16×10^{11} W/cm^2 to determine the autocorrelation signal shown in Fig. 6.1(c). The signal has been obtained by solving the time-dependent Schrödinger equation for the interaction of a helium atom with the two pulses; a single-active-electron potential for the helium atom [143] has been used for these calculations.

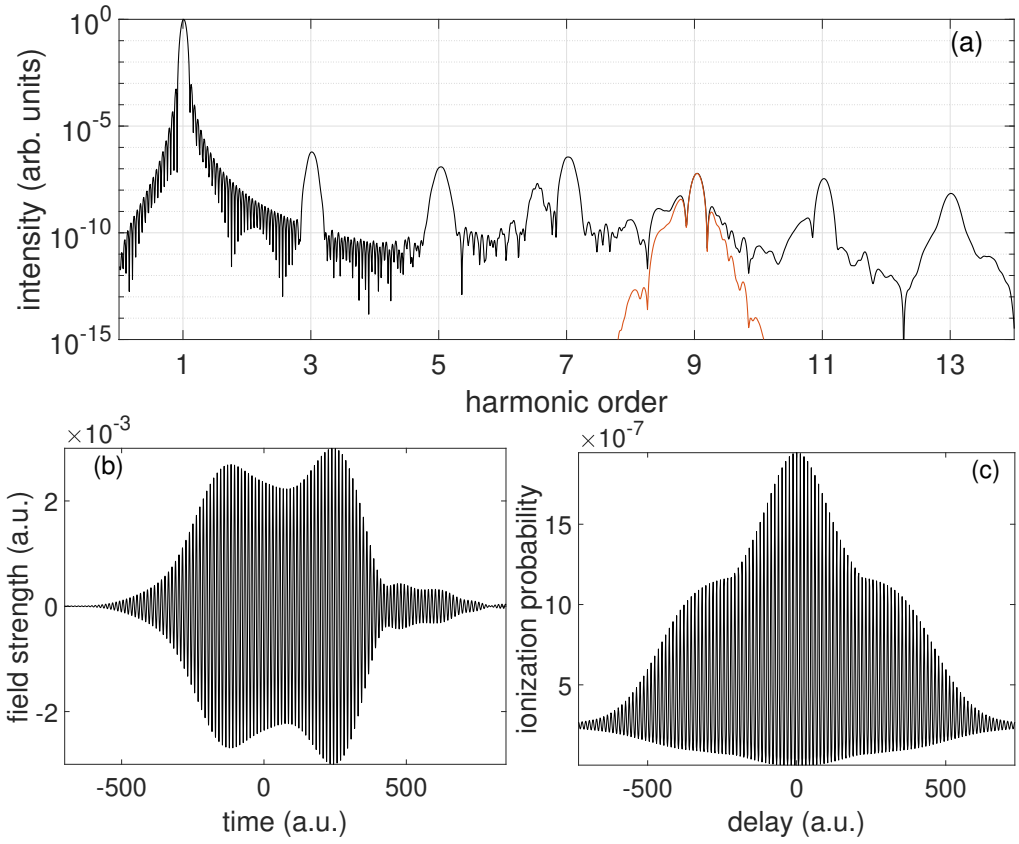

Figure 6.1: (a) Macroscopic high harmonic spectrum in hydrogen atom driven by 20-cycle, 800 nm laser pulse at 4×10^{13} W/cm^2: full spectrum (black line) and spectrum after application of a Gaussian filter about 9th harmonic (red line). (b) Temporal profile of filtered 9th harmonic and (c) autocorrelation signal using filtered 9th harmonic [168].

To characterize the filtered 9th harmonic, we have chosen a single-color approach in which all Gaussian pulses have the central frequency of the 9th harmonic. The results of the approximations for the time dependent amplitude $|\tilde{f}(t)|$ (blue) and phase variation $\omega(t)$ (red) using up to six Gaussian pulses (solid lines) are compared in Fig. 6.2 with the original pulse (dashed lines). The reconstruction with a single Gaussian (panel (a)) provides an estimate of the pulse width, but the double-hump structure in the amplitude and the phase variation is, of course, not reproduced. Already inclusion of a second Gaussian pulse (panel (b)) provides a significant improvement in this respect, however the minimum in between the two humps, the small post-pulse structure and most

of the phase variation is still not well reproduced. Using four (c) and six (d) Gaussian pulses, first the main part of the amplitude and then the post-pulse structure and even the phase variation in major parts of the pulse, is well reproduced. We however note that using autocorrelation signals, time-independent phases cannot be determined and a certain pulse cannot be distinguished from the pulse with time-reversed envelope.

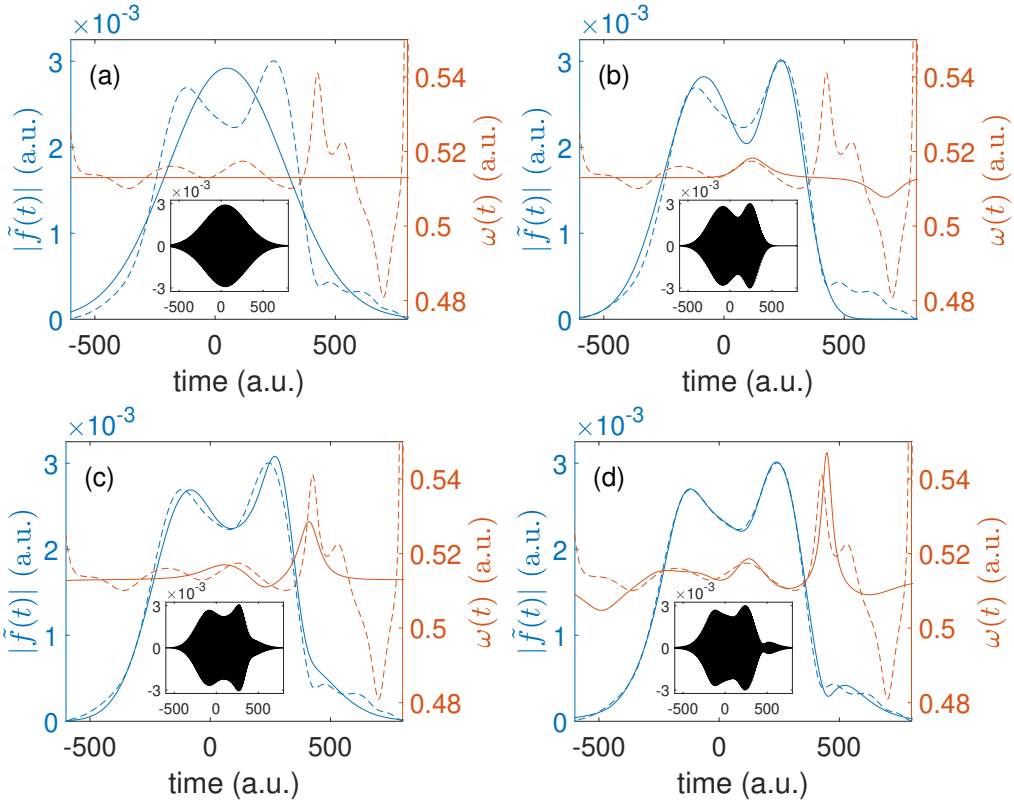

Figure 6.2: Comparison of time-dependent amplitude $|\tilde{f}(t)|$ (blue line) and phase variation $\omega(t)$ (red line) of the filtered 9th harmonic (dashed line) and reconstructed pulse with (a) 1, (b) 2, (c) 4 and (d) 6 Gaussians (solid line). The temporal profile is also provided as insets within each subplot [168].

While the results in Fig. 6.2 visualize the potential of the method, we quantify the convergence by errors for the ionization signal using the objective function as:

$$\mathrm{Error}_{N_g}[P_{\mathrm{ion}}] = \sqrt{\int d\tau \ \mathrm{obj}_{N_g}(\tau)^2}\,, \tag{6.20}$$

and the error in the field defined as:

$$\text{Error}_{N_g}[\tilde{f}] = \sqrt{\int dt \left|\tilde{f}_{\text{exact}}(t) - \tilde{f}_{N_g}(t)\right|^2} \tag{6.21}$$

in Fig. 6.3. Results for both the filtered 9th (blue) and the filtered 11th (red) harmonic are compared with each other. In both cases, the error in the ionization signal (panel (a)) drops smoothly with an increase of the number of Gaussians included in the method. The number of Gaussians necessary for similar degree of convergence is smaller for the 11th harmonic, since the pulse envelope (not shown) is less complex than that of the 9th harmonic. The convergence in the error for the ionization signal corresponds to a decrease of the error in the field (panel (b)) that reflects the observation in Fig. 6.2 that the pulse envelope is well reconstructed with just a few Gaussians. At the same time, we note that already two Gaussians are sufficient to provide an estimate of the FWHM pulse duration below 10 a.u. for for both harmonics.

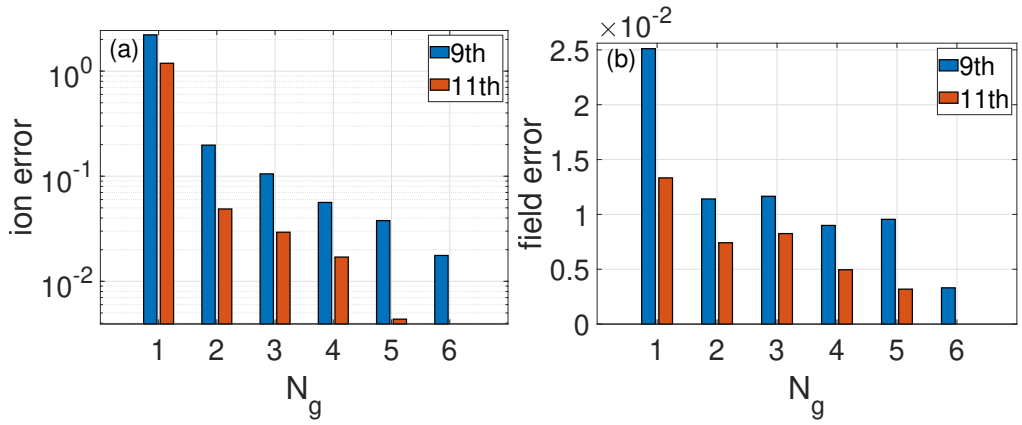

Figure 6.3: Error analysis of Gaussian pulse characterization method for filtered 9th (blue) and 11th harmonics (red): (a) $\text{Error}_{N_g}[P_{\text{ion}}]$ (Eq. 6.20), and (b) $\text{Error}_{N_g}[\tilde{f}]$ (Eq. 6.21) [168].

After applying the method to isolated ultrashort pulses by filtering the spectrum about a single harmonic, we consider the more complex temporal profile of a pulse train. To this end, we have used a flat top filter to the macroscopic HHG spectrum, where the leading edge is the same Gaussian filter used for the 9th harmonic and the trailing edge is a Gaussian filter applied to the 11th harmonic. The temporal shape of the resulting pulse train and the autocorrelation signal

obtained with the pulse train are shown in Fig. 6.4(a) and (b), respectively.

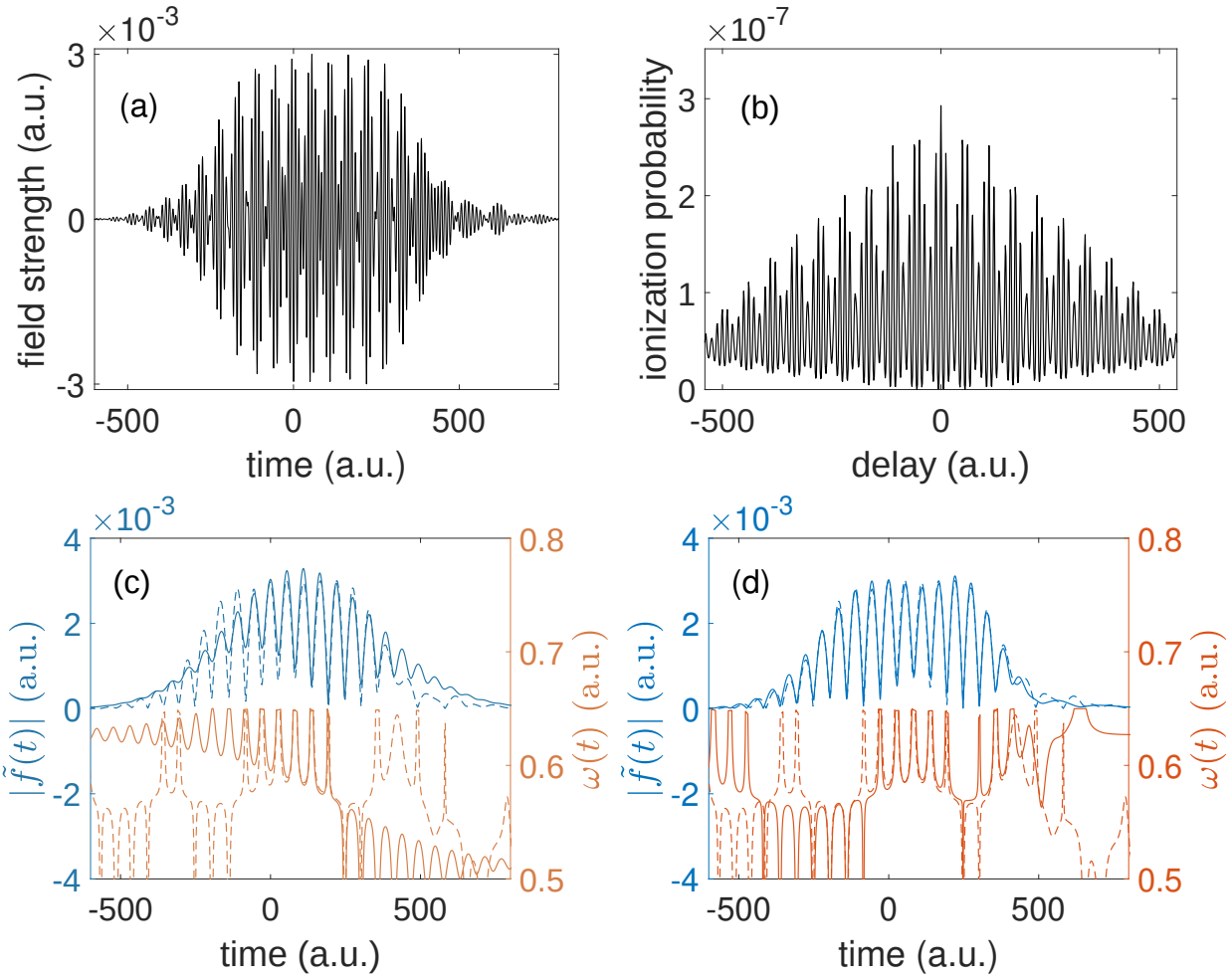

Figure 6.4: (a) Temporal profile of the filtered 9th to 11th harmonic spectral range, (b) autocorrelation signal, and comparison of time-dependent amplitude (blue) and phase variation (red) of the original pulse (dashed lines) and reconstructions (solid lines) obtained with one (c) and three (d) Gaussians per central frequencies at 9th and 11th harmonic [168].

Since the spectral filtering covers two harmonics, we have used a two-color approach with central frequencies equal to those of the 9th and 11th harmonics. Comparison of the original pulse train with the reconstructions shows that one Gaussian pulse per central frequency (panel (c)) provides a good approximation, including the duration of the train as well as the duration of the

individual pulses in the train. However, the rather flat overall envelope with several pulses in the train having similar amplitudes as well as most of the phase variation is not well reproduced. Using three Gaussian pulses per central frequency (panel (d)) improves the agreement with the original pulse in these aspects significantly.

Thus, using an extension of the two-photon autocorrelation technique based on multiple Gaussian pulses about one or several central frequencies enables a characterization of the amplitude and phase variation of isolated ultrashort pulses and pulse trains. The potential of the method is demonstrated using VUV pulses obtained from numerical simulations of macroscopic high harmonic spectra. We note that the method can be further improved by using alternative basis sets with more parameters or more sophisticated search algorithms in the fitting procedure. The same approach can also be applied to two-photon cross-correlation signals of two isolated ultrashort VUV pulses, e.g., if one of the two pulses is first characterized via autocorrelation. Furthermore, the analytic solutions of two-photon absorption may be extended to other techniques such as RABBITT for VUV and DUV pulse characterization. The accuracy of the method depends on the determination of one- and two-photon transition dipoles, for which several theoretical methods are available.

6.3 Non-perturbative limit

6.3.1 Time-slicing

In the prior section we derived efficient semi-analytical models for perturbative multiphoton processes via arbitrary polychromatic pulses. In this limit difficulties such as the long-range Coulomb potential are non-existent and there are no limitations on the properties of the incident radiation as long as the intensity is sufficiently weak and perturbation theory is extended to a sufficiently high order. Unfortunately, when transitioning into the strong field limit perturbation theory will break down (section 2.3) and alternative methods are required.

In the previous Chapters 3, 4 and 5 we explored various non-perturbative models for strong field processes, where each had unique benefits and difficulties. The first and most reliable method

is the direct numerical integration of the time dependent Schrödinger equation, which proves to be exact in the limit of converged parameters, but may become prohibitively computational expensive and requires additional models for analysis. The rest of the strong field approximations [57, 98, 136, 146] provide nearly exact analytic results for short-range potentials and long monochromatic pulses. For short polychromatic pulses these formulas either become cumbersome or require additional numerical time integration. Additionally, due to the lack of accurate Coulomb corrections across the entire electromagnetic spectrum (Chapter 5) application to electrons bound by long-range forces may be reliably approximated only in the limits $\gamma \gg 1$ and $\gamma \ll 1$. Higher order corrections such as in Ref. [58] may yield correct long-range threshold behavior for arbitrary γ, but those have not been systematically investigated.

In this section we will combine favorable properties of both perturbative and non-perturbative models in order to determine a semi-analytic strong field amplitude for processes involving arbitrary polychromatic fields and electrons bound by arbitrary (possibly long range) forces. Here, we decompose the interaction picture propagator $U_I(t_f, t_i)$ [151] defined by

$$|\Psi_I(t_f)\rangle = U_I(t_f, t_i)|\Psi_I(t_i)\rangle \tag{6.22}$$

into M different time-levels t_m between some initial time $t_i \equiv t_0$ and final time $t_f \equiv t_M$, where $t_0 < t_1 < \cdots < t_M$ [63, 75]. Taking final and initial matrix elements $|E_M\rangle$ and $|E_0\rangle$ we have

$$\langle E_M|U_I(t_M, t_0)|E_0\rangle = \langle E_M|\mathcal{T}\left[\prod_{m=1}^{M} U_I(m)\right]|E_0\rangle, \tag{6.23}$$

where we introduce the shorthand notation

$$U_I(m) \equiv U_I\left(t_m, t_{m-1}\right) \tag{6.24}$$

and $\mathcal{T}$ is the time-ordering operator.

Assuming each time-slice $\delta t_m \equiv t_m - t_{m-1}$ is sufficiently small, then the propagator $U_I(m)$ may be approximated perturbatively over the interval as it is done in numerical time integration schemes such as the Crank Nicolson method [42] which we have used for direct numerical solutions

of the TDSE. Each interval is perturbative, but the combined contribution from all intervals is non-perturbative. Instead of evaluating the propagator over δt_m numerically, we now choose U_I as the interaction picture propagator for a complete basis of atomic reference states $|E_m\rangle$ interacting with an external laser field $V_L(x) = \mathbf{E}(t) \cdot \mathbf{r}$ just as we have done for perturbative two-photon ionization by short pulses (section 6.2.2). We expand the external field as

$$\tilde{\mathbf{f}}(t) = \sum_n \sum_j \tilde{f}_{n,j}(t)\hat{\mathbf{z}} = \sum_n \sum_j \tilde{f}_{n,j} \exp\left[-\frac{(t-\tau_{n,j})^2}{2T_{n,j}^2} - i\omega_j t\right]\hat{\mathbf{z}}. \tag{6.25}$$

and

$$\mathbf{E}(t) = \mathrm{Re}[\tilde{\mathbf{f}}(t)] \tag{6.26}$$

as before. We will use $\mathbf{E}(t) = F(t)\hat{\mathbf{z}}$ to avoid confusion with what we will later call the energy at time t, $E(t)$.

The approximation involves finding sufficiently small time intervals δt_m such that

$$U_I(m) = 1 + \sum_{k=1}^{\infty} U_I^{(k)}(m) \approx 1 + U_I^{(1)}(m) \tag{6.27}$$

approximates the interval well. The last expression on the right is the first order Dyson approximation [51]. Here δt_m may be chosen independently for each m.

In this approximation we decompose the transition amplitude into a linear combination of Gaussian contributions

$$U_I^{(1)}(m) = \sum_{n,j} U_{n,j}^{(1)}(m)$$

with approximation

$$U_I^{(\mathrm{Dyson})}(m) \approx 1 + \sum_{n,j} U_{n,j}^{(1)}(m).$$

Next, one partitions the first order coefficient into a part responsible for absorption and one for emission of a photon

$$U_{n,j}^{(1)}(m) = U_{n,j}^{(\mathrm{abs})}(m) + U_{n,j}^{(\mathrm{emi})}(m),$$

where

$$\langle E_m|U_{n,j}^{(\mathrm{abs})}(m)|E_{m-1}\rangle = -i\sqrt{\frac{\pi}{8}}\tilde{f}_{n,j}T_{n,j}z_m\exp\left(-\frac{1}{2}T_{n,j}^2(\Delta_m^{(\mathrm{abs})})^2 + i\Delta_m^{(\mathrm{abs})}\tau_{n,j}\right) \times\left\{\mathrm{erf}\left[\frac{1}{\sqrt{2}T_{n,j}}\left(t_m-\tau_{n,j}-iT_{n,j}^2\Delta_m^{(\mathrm{abs})}\right)\right]-\mathrm{erf}\left[\frac{1}{\sqrt{2}T_{n,j}}\left(t_{m-1}-\tau_{n,j}-iT_{n,j}^2\Delta_m^{(\mathrm{abs})}\right)\right]\right\} \quad (6.28)$$

and

$$\langle E_m|U_{n,j}^{(\mathrm{emi})}(m)|E_{m-1}\rangle = -i\sqrt{\frac{\pi}{8}}\overline{\tilde{f}_{n,j}}T_{n,j}z_m\exp\left(-\frac{1}{2}T_{n,j}^2(\Delta_m^{(\mathrm{emi})})^2 + i\Delta_m^{(\mathrm{emi})}\tau_{n,j}\right) \times\left\{\mathrm{erf}\left[\frac{1}{\sqrt{2}T_{n,j}}\left(t_m-\tau_{n,j}-iT_{n,j}^2\Delta_m^{(\mathrm{emi})}\right)\right]-\mathrm{erf}\left[\frac{1}{\sqrt{2}T_{n,j}}\left(t_{m-1}-\tau_{n,j}-iT_{n,j}^2\Delta_m^{(\mathrm{emi})}\right)\right]\right\} \quad (6.29)$$

are the dipole-transition matrix elements for single photon absorption and emission process, respectively. The shorthand notations $\Delta_m^{(\mathrm{abs})} = E_m - E_{m-1} - \omega_j$ and $\Delta_m^{(\mathrm{emi})} = E_m - E_{m-1} + \omega_j$ are used.

6.3.2 Perturbation theory

The approximate propagator becomes

$$U_I(T/2,-T/2) = \mathcal{T}\left[\prod_{m=1}^{M}U_I(m)\right] \approx \mathcal{T}\left[\prod_{m=1}^{M}\left(1+U_I^{(1)}(m)\right)\right] \equiv \sum_{K=0}^{M}U_I^{(K,M)} \quad (6.30)$$

after each time-slice has been expanded in a first-order Dyson series. The sum over K on the right-hand side corresponds to terms containing K first-order Dyson contributions, where the zeroth-order term

$$U_I^{(0,M)} \equiv 1 = U_I^{(0)} \quad (6.31)$$

corresponds to the zeroth order of the standard Dyson series.

At first order

$$U_I^{(1,M)} \equiv \sum_{m=1}^{M}\sum_{n,j}U_{n,j}^{(1)}(m) = U_I^{(1)} \quad (6.32)$$

similarly represents the first-order Dyson series, where all "diagrams" containing a single photon are summed over. At second order

$$U_I^{(2,M)} \equiv \left[\sum_{m_2=m_1+1}^{M}\sum_{n_2,j_2}U_{n_2,j_2}^{(1)}(m_2)\right]\left[\sum_{m_1=1}^{M-1}\sum_{n_1,j_1}U_{n_1,j_1}^{(1)}(m_1)\right] \quad (6.33)$$

deviates from the Dyson result unless $\delta t_m \to 0$ $(M \to \infty)$ where

$$U_I^{(2)} = \lim_{M\to\infty} U_I^{(2,M)}. \tag{6.34}$$

Continuing now to the Kth order process

$$U_I^{(K,M)} \equiv \left[\sum_{m_K=m_{K-1}+1}^{M} \sum_{n_K,j_K} U^{(1)}_{n_K,j_K}(m_K)\right] \cdots \left[\sum_{m_2=m_1+1}^{M+2-K} \sum_{n_2,j_2} U^{(1)}_{n_2,j_2}(m_2)\right] \left[\sum_{m_1=1}^{M+1-K} \sum_{n_1,j_1} U^{(1)}_{n_1,j_1}(m_1)\right] \tag{6.35}$$

where the Dyson prediction

$$U_I^{(K)} = \lim_{M\to\infty} U_I^{(K,M)} \tag{6.36}$$

is again recovered for $\delta t_m \to 0$ $(M \to \infty)$.

Such an expansion extends analytic perturbative principles into a new non-perturbative limit where results agree with the time-dependent Schrödinger equation in the limit of converged parameters. The approximation is immediately applicable to problems involving short pulses and long-range interactions. Integration over each finite time-interval $(t_{m-1}, t_m]$ is performed analytically and may be interpreted in terms of photon absorption and emission processes. The propagator accounts for the temporal variation of the field over the interval in contrast to the Crank-Nicolson method which assumes a piecewise constant over each δt_m. Since the time-dependence of the field is approximated over the interval it is expected that significantly larger δt_m may be required yielding an improvement over the Crank-Nicholson method. We plan on exploring these ideas more in the future.

Chapter 7

Summary

Throughout this thesis we have explored ionization processes ranging from the x-ray and ultraviolet limit where electrons propagate as they would in an atomic system and applied radiation induces electronic transitions between atomic states before eventually transferring into the continuum to the opposite adiabatic infrared limit where large numbers of photons are required for ionization and electrons appear to tunnel through a static barrier. We summarized criteria responsible for the breakdown of perturbation theory and outlined key aspects of the non-perturbative theory. We discussed key steps responsible to derive the ionization amplitude of Keldysh and recognized its origins in the tunneling model of Oppenheimer. Additionally, we proved equivalence of Keldysh's amplitude with the model of Perelomov, Popov and Terent'ev for the case of a final plane-wave Volkov state and all possible combinations of initial states and applied radiation fields.

Numerical calculations were performed bridging the short wavelength limit of single photon perturbative ionization to the long wavelength limit of non-perturbative multiphoton ionization. These calculations found an optimal wavelength regime for generation of electron pulses for probing chiral systems in the intermediate wavelength limit where neither adiabatic tunneling theory nor perturbation theory are capable of describing the ionization process.

Breakdown was demonstrated of the asymptotic saddle point approximation for ionization of electrons bound to $p-$states. We overcame this issue by evaluating Keldysh's amplitude exactly. Our explorations recognized the intermediate wavelength limit where the asymptotic tail of the initial bound-state alone cannot determine ionization. Descriptions of ionization in this intermediate

wavelength regime prove difficult for electrons bound by long-range potentials both due to the inapplicability of perturbation theory and lack of sufficient Coulomb corrections to describe proper long-range threshold behavior in the strong field theories.

In the final Chapter we developed an analytic model for the perturbative two-photon ionization of atoms by arbitrary polychromatic radiation fields. As an application these formulas were applied to reconstruct isolated attosecond pulses and pulse trains from a provided autocorrelation trace generated in a pump probe ionization measurement. We generalized the amplitude to the non-perturbative limit by partitioning time into sufficiently small slices such that our perturbative formulas may be applied over each interval. We believe that this complementary approach may allow for an accurate semi-analytic physical description of strong-field processes involving long-range Coulomb potentials and short laser pulses.

Bibliography

[1] Felipe Zapata Abellan. Electron dynamics induced by single and multiphoton processes in atoms and molecules. PhD thesis, Sorbonne université, 2019.

[2] P Agostini and G Petite. Photoelectric effect under strong irradiation. Contemporary physics, 29(1):57–77, 1988.

[3] Pierre Agostini, F Fabre, Gérard Mainfray, Guillaume Petite, and N Ko Rahman. Free-free transitions following six-photon ionization of xenon atoms. Physical Review Letters, 42(17):1127, 1979.

[4] George Biddell Airy. On the intensity of light in neighbourhood of a caustic. Transactions of the Cambridge Philosophical Society, 6:379–402, 1838.

[5] Maxim V Ammosov, Nikolai B Delone, and Vladimir P Krainov. Tunnel ionization of complex atoms and of atomic ions in an alternating electromagnetic field. Soviet Journal of Experimental and Theoretical Physics, 64(6):1191, 1986.

[6] B Ananthanarayan, Samuel Friot, and Shayan Ghosh. Three-loop qed contributions to the g- 2 of charged leptons with two internal fermion loops and a class of kampé de fériet series. Physical Review D, 101(11):116008, 2020.

[7] B Ananthanarayan, Samuel Friot, Shayan Ghosh, and Anthony Hurier. New analytic continuations for the appell f_4 series from quadratic transformations of the gauss $\_\{2\}f\_1$ function. arXiv preprint arXiv:2005.07170, 2020.

[8] A. I. Andrjushin and A. E. Kazakov. Polarised electrons and two-photon-resonant ionisation of unpolarised atoms. Journal of Physics B: Atomic and Molecular Physics, 13(20):L609–L611, October 1980.

[9] Paul Appell. Sur les séries hypergéometriques de deux variables et sur des équations différentielles linéaires aux dérivées partielles. Comptes Rendus, 90:296–298, 1880.

[10] Luca Argenti and Roberto Moccia. K-matrix method with b-splines: σn, βn and resonances in he photoionization below n= 4 threshold. Journal of Physics B: Atomic, Molecular and Optical Physics, 39(12):2773, 2006.

[11] G. S. J. Armstrong, D. D. A. Clarke, J. Benda, A. C. Brown, and H. W. van der Hart. Electron correlation and short-range dynamics in attosecond angular streaking. Physical Review A, 101(4):041401, April 2020.

[12] G. S. J. Armstrong, D. D. A. Clarke, J. Benda, J. Wragg, A. C. Brown, and H. W. van der Hart. Enhancing spin polarization using ultrafast angular streaking. Phys. Rev. A, 103:053123, May 2021.

[13] G. S. J. Armstrong, D. D. A. Clarke, A. C. Brown, and H. W. van der Hart. Electron rotational asymmetry in strong-field photodetachment from F^- by circularly polarized laser pulses. Physical Review A, 99(2):023429, February 2019.

[14] David Ayuso, Alvaro Jiménez-Galán, Felipe Morales, Misha Ivanov, and Olga Smirnova. Attosecond control of spin polarization in electron–ion recollision driven by intense tailored fields. New Journal of Physics, 19(7):073007, July 2017.

[15] Henri Bachau, Eric Cormier, Piero Decleva, JE Hansen, and Fernando Martín. Applications of b-splines in atomic and molecular physics. Reports on progress in physics, 64(12):1815, 2001.

[16] G. Baravian, J. Godart, and G. Sultan. Resonant multiphoton ionization of neon. Experimental determination of the polarizability of the $3p'\left[\frac{1}{2}\right]_1$ level. Physical Review A, 14(2):761–767, August 1976.

[17] Ingo Barth and Manfred Lein. Numerical verification of the theory of nonadiabatic tunnel ionization in strong circularly polarized laser fields. Journal of Physics B: Atomic, Molecular and Optical Physics, 47(20):204016, October 2014.

[18] Ingo Barth and Olga Smirnova. Nonadiabatic tunneling in circularly polarized laser fields: Physical picture and calculations. Physical Review A, 84(6):063415, December 2011.

[19] Ingo Barth and Olga Smirnova. Comparison of theory and experiment for nonadiabatic tunneling in circularly polarized fields. Physical Review A, 87(6):065401, June 2013.

[20] Ingo Barth and Olga Smirnova. Nonadiabatic tunneling in circularly polarized laser fields. II. Derivation of formulas. Physical Review A, 87(1):013433, January 2013.

[21] Ingo Barth and Olga Smirnova. Spin-polarized electrons produced by strong-field ionization. Physical Review A, 88(1):013401, July 2013.

[22] Ingo Barth and Olga Smirnova. Hole dynamics and spin currents after ionization in strong circularly polarized laser fields. Journal of Physics B: Atomic, Molecular and Optical Physics, 47(20):204020, October 2014.

[23] Jarosław Bauer. Low-frequency–high-intensity limit of the keldysh-faisal-reiss theory. Physical Review A, 73(2):023421, 2006.

[24] Jarosław H. Bauer, Francisca Mota-Furtado, Patrick F. O'Mahony, Bernard Piraux, and Krzysztof Warda. Ionization and excitation of the excited hydrogen atom in strong circularly polarized laser fields. Physical Review A, 90(6):063402, December 2014.

[25] Jarosław H. Bauer and Zbigniew Walczak. Ionization and excitation of low-lying circular states of the hydrogen atom in strong circularly polarized laser fields. Physical Review A, 101(6):063409, June 2020.

[26] G. Baum, M. S. Lubell, and W. Raith. Spin-Orbit Perturbation in Heavy Alkali Atoms. Physical Review Letters, 25(5):267–270, August 1970.

[27] Alfred Ivanovich Baz, Iakov Borisovich Zeldovich, and Askold Mikhaĭlovich Perelomov. Scattering, Reactions and Decay in Nonrelativistic Quantum Mechanics, volume 510. Israel Program for Scientific Translations, 1969.

[28] R Bertoncini, AM Kriman, and DK Ferry. Airy-coordinate technique for nonequilibrium green's-function approach to high-field quantum transport. Physical Review B, 41(3):1390, 1990.

[29] John Markus Blatt and Victor Frederick Weisskopf. Theoretical nuclear physics. Courier Corporation, 1991.

[30] N Boroumand, A Thorpe, AM Parks, and T Brabec. Keldysh ionization theory of atoms: mathematical details. Journal of Physics B: Atomic, Molecular and Optical Physics, 55(21):213001, 2022.

[31] Rocío Borrego-Varillas, Lucia Ganzer, Giulio Cerullo, and Cristian Manzoni. Ultraviolet Transient Absorption Spectrometer with Sub-20-fs Time Resolution. Applied Sciences, 8(6):989, June 2018.

[32] B.H. Brandsen and C.J. Joachain. Physics of Atoms and Molecules. Addison-Wesley, 2003.

[33] Brian Harold Bransden and Charles Jean Joachain. Physics of atoms and molecules. Pearson Education India, 2003.

[34] L Brillouin. La mécanique ondulatoire de schrödinger: une méthode générale de resolution par approximations successives", comptes rendus de l'academie des sciences 183, 24 u26 (1926) ha kramers. Wellenmechanik und halbzählige Quantisierung", Zeit. f. Phys, 39(828):U840, 1926.

[35] B. Böning, P. Abele, W. Paufler, and S. Fritzsche. A strong-field approach with realistic wave functions to the above-threshold ionization of Ba^+. Journal of Physics B: Atomic, Molecular and Optical Physics, 54(2):025602, January 2021.

[36] Shaohao Chen, Xiang Gao, Jiaming Li, Andreas Becker, and Agnieszka Jaroń-Becker. Application of a numerical-basis-state method to strong-field excitation and ionization of hydrogen atoms. Physical Review A, 86(1):013410, 2012.

[37] Shaohao Chen, Xiang Gao, Jiaming Li, Andreas Becker, and Agnieszka Jaroń-Becker. Application of a numerical-basis-state method to strong-field excitation and ionization of hydrogen atoms. Physical Review A, 86(1):013410, July 2012.

[38] N. A. Cherepkov. Angular distribution and spin orientation of photoelectrons ejected by circularly polarized light. Physics Letters A, 40(2):119–121, July 1972.

[39] Michael Chini, Steve Gilbertson, Sabih D. Khan, and Zenghu Chang. Characterizing ultrabroadband attosecond lasers. Optics Express, 18(12):13006–13016, June 2010.

[40] D. D. A. Clarke, G. S. J. Armstrong, A. C. Brown, and H. W. van der Hart. *R*-matrix-with-time-dependence theory for ultrafast atomic processes in arbitrary light fields. Physical Review A, 98(5):053442, November 2018.

[41] David E. Couch, Daniel D. Hickstein, Daniel D. Hickstein, David G. Winters, Sterling J. Backus, Sterling J. Backus, Matthew S. Kirchner, Scott R. Domingue, Jessica J. Ramirez, Charles G. Durfee, Margaret M. Murnane, Henry C. Kapteyn, and Henry C. Kapteyn. Ultrafast 1 MHz vacuum-ultraviolet source via highly cascaded harmonic generation in negative-curvature hollow-core fibers. Optica, 7(7):832–837, July 2020.

[42] John Crank and Phyllis Nicolson. A practical method for numerical evaluation of solutions of partial differential equations of the heat-conduction type. In Mathematical proceedings of the Cambridge philosophical society, volume 43, pages 50–67. Cambridge University Press, 1947.

[43] A.A.M. Cuyt, V. Petersen, B. Verdonk, H. Waadeland, and W.B. Jones. Handbook of Continued Fractions for Special Functions. Springer, 2008.

[44] A. H. N. C. De Silva, T. Moon, K. L. Romans, B. P. Acharya, S. Dubey, K. Foster, O. Russ, C. Rischbieter, N. Douguet, K. Bartschat, and D. Fischer. Circular dichroism in atomic resonance-enhanced few-photon ionization. Phys. Rev. A, 103:053125, May 2021.

[45] A.H.N.C. De Silva, D. Atri-Schuller, S. Dubey, B.P. Acharya, K.L. Romans, K. Foster, O. Russ, K. Compton, C. Rischbieter, N. Douguet, K. Bartschat, and D. Fischer. Using Circular Dichroism to Control Energy Transfer in Multiphoton Ionization. Physical Review Letters, 126(2):023201, January 2021.

[46] Paul Adrien Maurice Dirac. The quantum theory of dispersion. Proceedings of the Royal Society of London. Series A, Containing Papers of a Mathematical and Physical Character, 114(769):710–728, 1927.

[47] Paul Adrien Maurice Dirac. The quantum theory of the emission and absorption of radiation. Proceedings of the Royal Society of London. Series A, Containing Papers of a Mathematical and Physical Character, 114(767):243–265, 1927.

[48] Paul Adrien Maurice Dirac. The principles of quantum mechanics. 1958.

[49] S. N. Dixit. ac-Stark-shift-induced photoelectron spin polarization in resonant multiphoton ionization. Physical Review A, 26(3):1505–1509, September 1982.

[50] S. N. Dixit, P. Lambropoulos, and P. Zoller. Spin polarization of electrons in two-photon resonant three-photon ionization. Physical Review A, 24(1):318–325, July 1981.

[51] Freeman J Dyson. The radiation theories of tomonaga, schwinger, and feynman. Physical Review, 75(3):486, 1949.

[52] S. Eckart, K. Fehre, N. Eicke, A. Hartung, J. Rist, D. Trabert, N. Strenger, A. Pier, L.Ph.H. Schmidt, T. Jahnke, M.S. Schöffler, M. Lein, M. Kunitski, and R. Dörner. Direct Experimental Access to the Nonadiabatic Initial Momentum Offset upon Tunnel Ionization. Physical Review Letters, 121(16):163202, October 2018.

[53] Sebastian Eckart, Maksim Kunitski, Martin Richter, Alexander Hartung, Jonas Rist, Florian Trinter, Kilian Fehre, Nikolai Schlott, Kevin Henrichs, Lothar Ph H. Schmidt, Till Jahnke, Markus Schöffler, Kunlong Liu, Ingo Barth, Jivesh Kaushal, Felipe Morales, Misha Ivanov, Olga Smirnova, and Reinhard Dörner. Ultrafast preparation and detection of ring currents in single atoms. Nature Physics, 14(7):701–704, July 2018.

[54] Albert Einstein. Über einem die erzeugung und verwandlung des lichtes betreffenden heuristischen gesichtspunkt. Annalen der physik, 4, 1905.

[55] Jennifer L. Ellis, Daniel D. Hickstein, Wei Xiong, Franklin Dollar, Brett B. Palm, K. Ellen Keister, Kevin M. Dorney, Chengyuan Ding, Tingting Fan, Molly B. Wilker, Kyle J. Schnitzenbaumer, Gordana Dukovic, Jose L. Jimenez, Henry C. Kapteyn, and Margaret M. Murnane. Materials Properties and Solvated Electron Dynamics of Isolated Nanoparticles and Nanodroplets Probed with Ultrafast Extreme Ultraviolet Beams. The Journal of Physical Chemistry Letters, 7(4):609–615, February 2016.

[56] H Exton. On the system of partial differential equations associated with appell's function f4. Journal of Physics A: Mathematical and General, 28(3):631, 1995.

[57] FHM Faisal. Multiphoton transitions. iv. bound-free transition integrals in compact forms. Journal of Physics B: Atomic and Molecular Physics, 6(3):553, 1973.

[58] FHM Faisal. Strong-field s-matrix theory with final-state coulomb interaction in all orders. Physical Review A, 94(3):031401, 2016.

[59] U. Fano. Spin Orientation of Photoelectrons Ejected by Circularly Polarized Light. Physical Review, 178(1):131–136, February 1969.

[60] P. S. Farago and D. W. Walker. Two-photon ionization of trivalent atoms as a source of polarized electrons. Journal of Physics B: Atomic and Molecular Physics, 6(10):L280–L283, October 1973.

[61] P. S. Farago, D. W. Walker, and J. S. Wykes. Remarks on photoelectron polarization in multiphoton ionization of alkali atoms. Journal of Physics B: Atomic and Molecular Physics, 7(1):59–68, January 1974.

[62] Enrico Fermi. Nuclear physics: a course given by Enrico Fermi at the University of Chicago. University of Chicago Press, 1950.

[63] Richard Phillips Feynman. Space-time approach to non-relativistic quantum mechanics. Reviews of modern physics, 20(2):367, 1948.

[64] Bengt Fornberg. Generation of finite difference formulas on arbitrarily spaced grids. Mathematics of computation, 51(184):699–706, 1988.

[65] R. R. Freeman, P. H. Bucksbaum, H. Milchberg, S. Darack, D. Schumacher, and M. E. Geusic. Above-threshold ionization with subpicosecond laser pulses. Phys. Rev. Lett., 59:1092–1095, Sep 1987.

[66] Mara Galli, Vincent Wanie, Diogo Pereira Lopes, Erik P. Månsson, Andrea Trabattoni, Lorenzo Colaizzi, Krishna Saraswathula, Andrea Cartella, Fabio Frassetto, Luca Poletto, François Légaré, Salvatore Stagira, Mauro Nisoli, Rebeca Martínez Vázquez, Roberto Osellame, and Francesca Calegari. Generation of deep ultraviolet sub-2-fs pulses. Optics Letters, 44(6):1308–1311, March 2019.

[67] Maria Göppert-Mayer. Über elementarakte mit zwei quantensprüngen. Annalen der Physik, 401(3):273–294, 1931.

[68] Edouard Goursat. A course in mathematical analysis, volume 1. Ginn, 1904.

[69] Izrail Solomonovich Gradshteyn and Iosif Moiseevich Ryzhik. Table of integrals, series, and products. Academic press, 2014.

[70] E. H. A. Granneman, M. Klewer, K. J. Nygaard, and M. J. Van der Wiel. Polarization effects in resonant two-photon ionization of caesium. Journal of Physics B: Atomic and Molecular Physics, 9(5):L87–L91, April 1976.

[71] E. H. A. Granneman, M. Klewer, and M. J. Van der Wiel. Two-photon ionization of caesium via the $6^2P_{3/2}$ intermediate state: analysis of photoelectron spin polarization and saturation effects. Journal of Physics B: Atomic and Molecular Physics, 9(16):2819–2838, November 1976.

[72] George Green et al. On the motion of waves in a variable canal of small depth and width. Transactions of the Cambridge Philosophical Society, 6:457, 1838.

[73] V. Gruson, L. Barreau, Á Jiménez-Galan, F. Risoud, J. Caillat, A. Maquet, B. Carré, F. Lepetit, J.-F. Hergott, T. Ruchon, L. Argenti, R. Taïeb, F. Martín, and P. Salières. Attosecond dynamics through a Fano resonance: Monitoring the birth of a photoelectron. Science, 354(6313):734–738, November 2016.

[74] E. V. Gryzlova, M. M. Popova, and A. N. Grum-Grzhimailo. Spin polarization of photoelectrons in bichromatic extreme-ultraviolet atomic ionization. Phys. Rev. A, 102:053116, Nov 2020.

[75] Brian C Hall. Quantum theory for mathematicians. Springer, 2013.

[76] Meng Han, Peipei Ge, Ming-Ming Liu, Qihuang Gong, and Yunquan Liu. Spatially and temporally controlling electron spin polarization in strong-field ionization using orthogonal two-color laser fields. Physical Review A, 99(2):023404, February 2019.

[77] Alexander Hartung, Felipe Morales, Maksim Kunitski, Kevin Henrichs, Alina Laucke, Martin Richter, Till Jahnke, Anton Kalinin, Markus Schöffler, Lothar Ph H. Schmidt, Misha Ivanov, Olga Smirnova, and Reinhard Dörner. Electron spin polarization in strong-field ionization of xenon atoms. Nature Photonics, 10(8):526–528, August 2016.

[78] F He, C Ruiz, and A Becker. Absorbing boundaries in numerical solutions of the time-dependent schrödinger equation on a grid using exterior complex scaling. Physical Review A, 75(5):053407, 2007.

[79] U. Heinzmann, J. Kessler, and J. Lorenz. Wavelength Dependence of the Fano Effect. Physical Review Letters, 25(19):1325–1325, November 1970.

[80] Thushani Herath, Lu Yan, Suk Kyoung Lee, and Wen Li. Strong-Field Ionization Rate Depends on the Sign of the Magnetic Quantum Number. Physical Review Letters, 109(4):043004, July 2012.

[81] C. Hernández-García, J. A. Pérez-Hernández, J. Ramos, E. Conejero Jarque, L. Roso, and L. Plaja. High-order harmonic propagation in gases within the discrete dipole approximation. Physical Review A, 82(3):033432, September 2010.

[82] J. Hofbrucker, A. V. Volotka, and S. Fritzsche. Fluorescence polarization as a precise tool for understanding nonsequential many-photon ionization. Physical Review A, 100(1):011401, July 2019.

[83] Markus Huber. Infrared behavior of vertex functions in d-dimensional Yang-Mills theory. na, 2007.

[84] Etienne Huens, Bernard Piraux, Alejandro Bugacov, and Mariusz Gajda. Numerical studies of the dynamics of multiphoton processes with arbitrary field polarization: Methodological considerations. Physical Review A, 55(3):2132, 1997.

[85] M. Ilchen, N. Douguet, T. Mazza, A.J. Rafipoor, C. Callegari, P. Finetti, O. Plekan, K.C. Prince, A. Demidovich, C. Grazioli, L. Avaldi, P. Bolognesi, M. Coreno, M. Di Fraia, M. Devetta, Y. Ovcharenko, S. Düsterer, K. Ueda, K. Bartschat, A.N. Grum-Grzhimailo, A.V. Bozhevolnov, A.K. Kazansky, N.M. Kabachnik, and M. Meyer. Circular Dichroism in Multiphoton Ionization of Resonantly Excited He^+ Ions. Physical Review Letters, 118(1):013002, January 2017.

[86] Kenichi L. Ishikawa and Kiyoshi Ueda. Photoelectron Angular Distribution and Phase in Two-Photon Single Ionization of H and He by a Femtosecond and Attosecond Extreme-Ultraviolet Pulse. Applied Sciences, 3(1):189–213, March 2013.

[87] J. Itatani, F. Quéré, G. L. Yudin, M. Yu. Ivanov, F. Krausz, and P. B. Corkum. Attosecond Streak Camera. Physical Review Letters, 88(17):173903, April 2002.

[88] I. A. Ivanov and A. S. Kheifets. Time delay in atomic photoionization with circularly polarized light. Physical Review A, 87(3):033407, March 2013.

[89] Harold Jeffreys. On certain approximate solutions of lineae differential equations of the second order. Proceedings of the London Mathematical Society, 2(1):428–436, 1925.

[90] Shih-Da Jheng, Tsin-Fu Jiang, Jen-Hao Chen, and Jinn-Liang Liu. Magnetic quantum number dependence of hydrogen photoelectron spectra under circularly polarized pulse in barrier suppression ionization regime. Physica Scripta, 93(8):085401, July 2018.

[91] WGCGB Kaiser and CGB Garrett. Two-photon excitation in ca f 2: Eu 2+. Physical review letters, 7(6):229, 1961.

[92] Jivesh Kaushal, Felipe Morales, and Olga Smirnova. Opportunities for detecting ring currents using an attoclock setup. Physical Review A, 92(6):063405, December 2015.

[93] Jivesh Kaushal, Felipe Morales, Lisa Torlina, Misha Ivanov, and Olga Smirnova. Spin–orbit Larmor clock for ionization times in one-photon and strong-field regimes. Journal of Physics B: Atomic, Molecular and Optical Physics, 48(23):234002, October 2015.

[94] Jivesh Kaushal and Olga Smirnova. Nonadiabatic Coulomb effects in strong-field ionization in circularly polarized laser fields. Physical Review A, 88(1):013421, July 2013.

[95] Jivesh Kaushal and Olga Smirnova. Looking inside the tunnelling barrier: I. Strong field ionisation from orbitals with high angular momentum in circularly polarised fields. Journal of Physics B: Atomic, Molecular and Optical Physics, 51(17):174001, August 2018.

[96] Jivesh Kaushal and Olga Smirnova. Looking inside the tunnelling barrier: II. Co- and counter-rotating electrons at the 'tunnelling exit'. Journal of Physics B: Atomic, Molecular and Optical Physics, 51(17):174002, August 2018.

[97] Jivesh Kaushal and Olga Smirnova. Looking inside the tunnelling barrier III: spin polarisation in strong field ionisation from orbitals with high angular momentum. Journal of Physics B: Atomic, Molecular and Optical Physics, 51:174001, September 2018.

[98] LV Keldysh. Ionization in the field of a strong electromagnetic wave. Sov. Phys. JETP, 20(5):1307–1314, 1965.

[99] J. Kessler. Polarized Electrons. Springer (Berlin), 1985.

[100] Takayoshi Kobayashi and Yuichiro Kida. Ultrafast spectroscopy with sub-10 fs deep-ultraviolet pulses. Physical Chemistry Chemical Physics, 14(18):6200–6210, April 2012.

[101] Vladimir P Krainov, Howard R Reiss, and Boris M Smirnov. Radiative processes in atomic physics. Wiley Online Library, 1997.

[102] VP Krainov and B Shokri. Energy and angular distributions of electrons resulting from barrier-suppression ionization of atoms by strong low-frequency radiation. Journal of Experimental and Theoretical Physics, 80(4):657–661, 1995.

[103] Hendrik Anthony Kramers. Wellenmechanik und halbzahlige quantisierung. Zeitschrift für Physik, 39(10-11):828–840, 1926.

[104] P. Lambropoulos. Spin-Orbit Coupling and Photoelectron Polarization in Multiphoton Ionization of Atoms. Physical Review Letters, 30(10):413–416, March 1973.

[105] P. Lambropoulos. On producing totally polarized electrons through multiphoton ionization. Journal of Physics B: Atomic and Molecular Physics, 7(2):L33–L35, February 1974.

[106] P. Lambropoulos and M. R. Teague. Two-photon ionization with spin-orbit coupling. Journal of Physics B: Atomic and Molecular Physics, 9(4):587–603, March 1976.

[107] L D Landau and E M Lifshits. Quantum Mechanics : Non-Relativistic Theory. Pergamon Press, 1965.

[108] Giuseppe Lauricella. Sulle funzioni ipergeometriche a piu variabili. Rendiconti del Circolo Matematico di Palermo, 7(Suppl 1):111–158, 1893.

[109] Stephen R. Leone, C. William McCurdy, Joachim Burgdörfer, Lorenz S. Cederbaum, Zenghu Chang, Nirit Dudovich, Johannes Feist, Chris H. Greene, Misha Ivanov, Reinhard Kienberger, Ursula Keller, Matthias F. Kling, Zhi-Heng Loh, Thomas Pfeifer, Adrian N. Pfeiffer, Robin Santra, Kenneth Schafer, Albert Stolow, Uwe Thumm, and Marc J. J. Vrakking. What will it take to observe processes in 'real time'? Nature Photonics, 8(3):162–166, March 2014.

[110] Yang Li, Pengfei Lan, Hui Xie, Mingrui He, Xiaosong Zhu, Qingbin Zhang, and Peixiang Lu. Nonadiabatic tunnel ionization in strong circularly polarized laser fields: counterintuitive angular shifts in the photoelectron momentum distribution. Optics Express, 23(22):28801–28807, November 2015.

[111] Joseph Liouville. Second mémoire sur le développement des fonctions ou parties de fonctions en séries dont les divers termes sont assujettis à satisfaire à une même équation différentielle du second ordre, contenant un paramètre variable. Journal de mathématiques pures et appliquées, 2:16–35, 1837.

[112] Bernard A Lippmann and Julian Schwinger. Variational principles for scattering processes. i. Physical Review, 79(3):469, 1950.

[113] Kunlong Liu and Ingo Barth. Nonadiabatic tunnel ionization of current-carrying orbitals of prealigned linear molecules in strong circularly polarized laser fields. Physical Review A, 94(4):043402, October 2016.

[114] Kunlong Liu and Ingo Barth. Spin-polarized photoelectrons produced by strong-field ionization of randomly aligned nitric oxide. Journal of Modern Optics, 64(10-11):987–994, June 2017.

[115] Kunlong Liu, Hongcheng Ni, Klaus Renziehausen, Jan-Michael Rost, and Ingo Barth. Deformation of Atomic $p_{\pm}$ Orbitals in Strong Elliptically Polarized Laser Fields: Ionization Time Drifts and Spatial Photoelectron Separation. Physical Review Letters, 121(20):203201, November 2018.

[116] Kunlong Liu, Klaus Renziehausen, and Ingo Barth. Producing spin-polarized photoelectrons by using the momentum gate in strong-field ionization experiments. Physical Review A, 95(6):063410, June 2017.

[117] Ming-Ming Liu, Min Li, Yun Shao, Meng Han, Qihuang Gong, and Yunquan Liu. Effects of orbital and Coulomb potential in strong-field nonadiabatic tunneling ionization of atoms. Physical Review A, 96(4):043410, October 2017.

[118] Ming-Ming Liu, Yun Shao, Meng Han, Peipei Ge, Yongkai Deng, Chengyin Wu, Qihuang Gong, and Yunquan Liu. Energy- and Momentum-Resolved Photoelectron Spin Polarization in Multiphoton Ionization of Xe by Circularly Polarized Fields. Physical Review Letters, 120(4):043201, January 2018.

[119] Franck Lépine, Misha Y. Ivanov, and Marc J. J. Vrakking. Attosecond molecular dynamics: fact or fiction? Nature Photonics, 8(3):195–204, March 2014.

[120] TH MAIMAN. Stimulated optical radiation in ruby. Nature, 187(4736):493–494, 1960.

[121] Y. Mairesse and F. Quéré. Frequency-resolved optical gating for complete reconstruction of attosecond bursts. Physical Review A, 71(1):011401, January 2005.

[122] F. Mauger and A. D. Bandrauk. Electronic dynamics and frequency effects in circularly polarized strong-field physics. Journal of Physics B: Atomic, Molecular and Optical Physics, 47(19):191001, September 2014.

[123] C William McCurdy and Fernando Martin. Implementation of exterior complex scaling in b-splines to solve atomic and molecular collision problems. Journal of Physics B: Atomic, Molecular and Optical Physics, 37(4):917, 2004.

[124] Héctor Mera, Thomas G Pedersen, and Branislav K Nikolić. Nonperturbative quantum physics from low-order perturbation theory. Physical Review Letters, 115(14):143001, 2015.

[125] Eugen Merzbacher. Quantum mechanics. John Wiley & Sons, 1998.

[126] Katsumi Midorikawa, Yasuo Nabekawa, and Akira Suda. XUV multiphoton processes with intense high-order harmonics. Progress in Quantum Electronics, 32(2):43–88, January 2008.

[127] Benoit Mignolet, Basile F. E. Curchod, Francoise Remacle, and Todd J. Martínez. Sub-Femtosecond Stark Control of Molecular Photoexcitation with Near Single-Cycle Pulses. The Journal of Physical Chemistry Letters, 10(4):742–747, February 2019.

[128] D. B. Milošević. Possibility of introducing spin into attoscience with spin-polarized electrons produced by a bichromatic circularly polarized laser field. Phys. Rev. A, 93:051402, May 2016.

[129] Nimrod Moiseyev. Non-Hermitian quantum mechanics. Cambridge University Press, 2011.

[130] Yasuo Nabekawa, Toshihiko Shimizu, Tomoya Okino, Kentaro Furusawa, Hirokazu Hasegawa, Kaoru Yamanouchi, and Katsumi Midorikawa. Conclusive Evidence of an Attosecond Pulse Train Observed with the Mode-Resolved Autocorrelation Technique. Physical Review Letters, 96(8):083901, February 2006.

[131] Mauro Nisoli, Piero Decleva, Francesca Calegari, Alicia Palacios, and Fernando Martín. Attosecond Electron Dynamics in Molecules. Chemical Reviews, 117(16):10760–10825, August 2017.

[132] J Robert Oppenheimer. Three notes on the quantum theory of aperiodic effects. Physical review, 31(1):66, 1928.

[133] I. Orfanos, I. Makos, I. Liontos, E. Skantzakis, B. Förg, D. Charalambidis, and P. Tzallas. Attosecond pulse metrology. APL Photonics, 4(8):080901, August 2019.

[134] P. M. Paul, E. S. Toma, P. Breger, G. Mullot, F. Augé, Ph Balcou, H. G. Muller, and P. Agostini. Observation of a Train of Attosecond Pulses from High Harmonic Generation. Science, 292(5522):1689–1692, June 2001.

[135] AM Perelomov and VS Popov. Ionization of atoms in an alternating electrical field. iii. Sov. Phys. JETP, 25(2), 1967.

[136] AM Perelomov, VS Popov, and MV Terent'Ev. Ionization of atoms in an alternating electric field. Sov. Phys. JETP, 23(5):924–934, 1966.

[137] AM Perelomov, VS Popov, and MV Terent'Ev. Ionization of atoms in an alternating electric field: ii. Sov. Phys. JETP, 24(1):207–217, 1967.

[138] Guillaume Petite, Pierre Agostini, and François Yergeau. Intensity, pulse width, and polarization dependence of above-threshold-ionization electron spectra. JOSA B, 4(5):765–769, 1987.

[139] Josip Plemelj and Jens Rainer Maria Radok. Problems in the sense of Riemann and Klein, volume 16. Interscience Publishers New York, 1964.

[140] SV Popruzhenko, VD Mur, VS Popov, and D Bauer. Strong field ionization rate for arbitrary laser frequencies. Physical review letters, 101(19):193003, 2008.

[141] R. H. Pratt, Akiva Ron, and H. K. Tseng. Atomic Photoelectric Effect Above 10 keV. Reviews of Modern Physics, 45(2):273–325, April 1973.

[142] V Privman. New method of perturbation-theory calculation of the stark effect for the ground state of hydrogen. Physical Review A, 22(5):1833, 1980.

[143] R. Reiff, T. Joyce, A. Jaroń-Becker, and A. Becker. Single-active electron calculations of high-order harmonic generation from valence shells in atoms for quantitative comparison with TDDFT calculations. Journal of Physics Communications, 4(6):065011, June 2020.

[144] R. Reiff, J. Venzke, A. Jaron-Becker, and A. Becker. Interference effects in harmonic generation induced by focal phase distribution. submitted for publication.

[145] Jan Reislöhner, Christoph Leithold, and Adrian N. Pfeiffer. Characterization of weak deep ultraviolet pulses using cross-phase modulation scans. Optics Letters, 44(7):1809–1812, April 2019.

[146] Howard R Reiss. Effect of an intense electromagnetic field on a weakly bound system. Physical Review A, 22(5):1786, 1980.

[147] HR Reiss. Complete keldysh theory and its limiting cases. Physical Review A, 42(3):1476, 1990.

[148] HR Reiss. Theoretical methods in quantum optics: S-matrix and keldysh techniques for strong-field processes. Progress in Quantum electronics, 16(1):1–71, 1992.

[149] Florentin Reiter, Ulrich Graf, Martin Schultze, Wolfgang Schweinberger, Hartmut Schröder, Nicholas Karpowicz, Abdallah Mohammed Azzeer, Reinhard Kienberger, Ferenc Krausz, and Eleftherios Goulielmakis. Generation of sub-3 fs pulses in the deep ultraviolet. Optics Letters, 35(13):2248–2250, July 2010.

[150] Kazimierz Rzazewski and Bernard Piraux. Circular Rydberg orbits in circularly polarized microwave radiation. Physical Review A, 47:R1612–R1615, March 1993.

[151] J Sakurai and J Napolitano. Modern quantum mechanics. 2-nd edition. Person New International edition, page 35, 2014.

[152] Ramamurti Shankar. Principles of quantum mechanics. Springer Science & Business Media, 2012.

[153] Colin JR Sheppard. Multiphoton microscopy: a personal historical review, with some future predictions. Journal of biomedical optics, 25(1):014511–014511, 2020.

[154] Yu W Sokhotskii. On definite integrals and functions used in series expansions. St. Petersburg, 1873.

[155] Elias M Stein and Rami Shakarchi. Princeton lectures in analysis. Princeton University Press Princeton, 2003.

[156] Albert Stolow, Arthur E. Bragg, and Daniel M. Neumark. Femtosecond Time-Resolved Photoelectron Spectroscopy. Chemical Reviews, 104(4):1719–1758, April 2004.

[157] M. R. Teague and P. Lambropoulos. Three-photon ionization with spin-orbit coupling. Journal of Physics B: Atomic and Molecular Physics, 9(8):1251–1262, June 1976.

[158] D. Trabert, A. Hartung, S. Eckart, F. Trinter, A. Kalinin, M. Schöffler, L.Ph.H. Schmidt, T. Jahnke, M. Kunitski, and R. Dörner. Spin and Angular Momentum in Strong-Field Ionization. Physical Review Letters, 120(4):043202, January 2018.

[159] Sergei A. Trushin, Kyriaki Kosma, Werner Fuß, and Wolfram E. Schmid. Sub-10-fs supercontinuum radiation generated by filamentation of few-cycle 800 nm pulses in argon. Optics Letters, 32(16):2432–2434, August 2007.

[160] P. Tzallas, D. Charalambidis, N. A. Papadogiannis, K. Witte, and G. D. Tsakiris. Direct observation of attosecond light bunching. Nature, 426(6964):267–271, November 2003.

[161] P. Tzallas, E. Skantzakis, L. A. A. Nikolopoulos, G. D. Tsakiris, and D. Charalambidis. Extreme-ultraviolet pump–probe studies of one-femtosecond-scale electron dynamics. Nature Physics, 7(10):781–784, October 2011.

[162] J. Venzke, A. Becker, and A. Jaron-Becker. Imaging ring-current wave packets in the helium atom. Phys. Rev. A, 103:042808, Apr 2021.

[163] J. Venzke, A. Jaroń-Becker, and A. Becker. Ionization of helium by an ultrashort extreme-ultraviolet laser pulse. Journal of Physics B: Atomic, Molecular and Optical Physics, 53(8):085602, April 2020.

[164] J. Venzke, T. Joyce, Z. Xue, A. Becker, and A. Jaron-Becker. Central frequency of few-cycle laser pulses in strong-field processes. Physical Review A, 98(6):063409, December 2018.

[165] DM Volkov. On a class of solutions of the dirac equation. Z. Phys, 94(3-4):250–260, 1935.

[166] S. Walker, L. Kolanz, J. Venzke, and A. Becker. Enhanced ionization of counter-rotating electrons via doorway states in ultrashort circularly polarized laser pulses. Physical Review A, 103(6):L061101, June 2021.

[167] S Walker, L Kolanz, J Venzke, and A Becker. Selectivity in electron emission induced by ultrashort circularly polarized laser pulses. Physical Review Research, 3(4):043051, 2021.

[168] S. Walker, R. Reiff, A. Jaron-Becker, and A. Becker. Characterization of vacuum and deep ultraviolet pulses via two-photon autocorrelation signals. Optics Letters, 46(13):3083–3086, July 2021.

[169] Jun-Ping Wang and Feng He. Tunneling ionization of neon atoms carrying different orbital angular momenta in strong laser fields. Physical Review A, 95(4):043420, April 2017.

[170] Tian Wang, Xin-Lei Ge, Jing Guo, and Xue-Shen Liu. Sensitivity of strong-field double ionization to the initial ensembles in circularly polarized laser fields. Physical Review A, 90(3):033420, September 2014.

[171] Gregor Wentzel. Eine verallgemeinerung der quantenbedingungen für die zwecke der wellenmechanik. Zeitschrift für Physik, 38(6-7):518–529, 1926.

[172] Eugene P Wigner. On the behavior of cross sections near thresholds. Physical Review, 73(9):1002, 1948.

[173] Serge Winitzki. Uniform approximations for transcendental functions. In International conference on computational science and its applications, pages 780–789. Springer, 2003.

[174] Dan Wu, Fu-Ming Guo, Ji-Gen Chen, Jun Wang, and Yu-Jun Yang. Ionization of an atom with different initial angular momenta in an intense circular polarized laser field. Journal of Physics B: Atomic, Molecular and Optical Physics, 53(23):235601, November 2020.

[175] J. Wätzel and J. Berakdar. Discerning on a sub-optical-wavelength the attosecond time delays in electron emission from magnetic sublevels by optical vortices. Physical Review A, 94(3):033414, September 2016.

[176] Shengliang Xu, Qingbin Zhang, Xianglong Fu, Xiang Huang, Xu Han, Min Li, Wei Cao, and Peixiang Lu. Towards atom-scale spin-selective electron emitters based on strong-field Freeman resonant ionization. Physical Review A, 102(6):063128, December 2020.

[177] Tokio Yamabe, Akitomo Tachibana, and Harris J Silverstone. Theory of the ionization of the hydrogen atom by an external electrostatic field. Physical Review A, 16(3):877, 1977.

[178] Youliang Yu and BD Esry. An optimized absorbing potential for ultrafast, strong-field problems. Journal of Physics B: Atomic, Molecular and Optical Physics, 51(9):095601, 2018.

[179] MingHu Yuan, GuangJiu Zhao, and HongPing Liu. Influence of wavelength on nonadiabatic effects in circularly polarized strong-field ionization. Physical Review A, 92(5):053405, November 2015.

[180] Jakub Zakrzewski, Dominique Delande, Jean-Claude Gay, and Kazimierz Rzazewski. Ionization of highly excited hydrogen atoms by a circularly polarized microwave field. Physical Review A, 47(4):R2468–R2471, April 1993.

[181] Qingbin Zhang, Gihan Basnayake, Alexander Winney, Yun Fei Lin, Duke Debrah, Suk Kyoung Lee, and Wen Li. Orbital-resolved nonadiabatic tunneling ionization. Physical Review A, 96(2):023422, August 2017.

[182] Xiaosong Zhu, Pengfei Lan, Kunlong Liu, Yang Li, Xi Liu, Qingbin Zhang, Ingo Barth, and Peixiang Lu. Helicity sensitive enhancement of strong-field ionization in circularly polarized laser fields. Optics Express, 24(4):4196–4209, February 2016.